Imaging Cerebral (Patho-)Physiology - merits from functional brain imaging

Wyss, Matthias

MEDIZINISCHE FAKULTÄT ZÜRICH
UNIVERSITÄTSSPITAL ZÜRICH

Institut für Pharmakologie und Toxikologie (Direktor: Prof. Dr. Hanns Ulrich Zeilhofer)
Labor für funktionelle Bildgebung und Neurovaskuläre Kopplung (Prof. Dr. Bruno Weber)

‚Imaging Cerebral (Patho-)Physiology' –

merits from functional brain imaging

Kumulative Habilitationsschrift zur Erlangung der Venia Legendi
der Medizinischen Fakultät der Universität Zürich
im Fach Pharmakologische Bildgebung

Der Medizinischen Fakultät der Universität Zürich vorgelegt von

Dr. med. et. sc. nat. Matthias T. Wyss
von Zürich ZH und Alchenstorf BE, Schweiz

Zürich, 2012

Matthias Wyss
mwyss@pharma.uzh.ch
Institute for Pharmacology and Toxicology
Laboratory for functional Neuroimaging
University Hospital of Zürich
Rämistrasse 100
CH-8091 Zürich

for Simon

"In the Brain the appearance is so peculiar, and so little capable of illustration from other parts of the body, the surfaces are so soft, and so easily destroyed by rude dissection, and it is so difficult to follow an abstract description merely, that this part of Anatomy cannot be studied without the help of Engravings."

Charles Bell
(from *The Anatomy of the Brain, Explained in a Series of Engravings*, 1802)

Acknowledgements

When I started working in a research laboratory, I did not intend to stay for longer than was necessary to collect data for my MD thesis. However, during this time I discovered the excitement of research in a laboratory environment and, more specifically, the beauty of imaging physiological processes. Thanks to Professors Alfred Buck and Bruno Weber in the Department of Nuclear Medicine at the University Hospital of Zurich, I realized the importance of basic brain research and functional neuroimaging. Equally, I would like to thank Prof. Gustav von Schulthess, firstly for arranging the opportunity for me to work in this laboratory, and secondly for the enormous support and access to the imaging facility at the PET Center.

Many people have crossed my path during my years in research, and it is impossible to refer to them all by name. Therefore, I mention only a few here as representatives for the whole group. Special thanks must go to Gerrit Westera, Konstantin Drandarov, Tibor Cservenyak and Rolf Hesselmann from the Center for Radiopharmaceutical Sciences. Without their extremely competent radiotracer production, it would not have been possible to perform numerous studies. They constantly improved tracer synthesis and radiochemical yield, and regularly produced radiotracers specifically for my studies in addition to their daily clinical requirements. Furthermore, they always fulfilled my special requests concerning the particular requirements for radiotracers to be used in the laboratory for small animal experiments.

I am also indebted to Nicolas Späth, Michael Honer, Prof. Ulrich Roelcke, Florent Haiss, Novella Calcinaghi, Prof. Boris Quednow, Arko Gosh, Christian Matter, Prof. Pierre Magistretti and many others working either alongside me or in groups with which I have had/still have fruitful collaborations. With the help of these colleagues and collaborators, many ambitious projects were realized and led to well-received publications.

I also want to thank Prof. Jean-Marc Fritschy and Hanns Ulrich Zeilhofer from the Institute of Pharmacology and Toxicology to which the Laboratory of Functional Imaging and Neurovascular Coupling has been affiliated with for several years. One of the many opportunities they kindly provided was to gain experience in teaching. In addition, Prof. Fritschy was a member of my PhD committee several years ago.

Finally, I am grateful to my friends in- and outside of research, and my family. Their support and encouragement has helped me to manage the daily challenges and the ups and downs of science.

Table of contents

Summary

During the last few decades, *in vivo* brain imaging has undergone substantial changes. The first brain images, obtained using X-ray-computed tomography, could only provide structural information. Subsequently, magnetic resonance tomography provided a better understanding of the brain's anatomy. Nowadays, functional information can also be measured, dramatically improving the understanding of brain physiology and pathophysiology. It has been demonstrated in numerous studies that the ability to capture functional readouts from the brain is of considerable benefit in a range of situations. Detecting the accumulation of radioactive ligands is one of the most common functional imaging modalities. Among these modalities, the most prominent detection method is positron emission tomography (PET).

When performed with suitably labeled agents, PET allows the detection of biochemical processes such as glucose utilization and ligand-receptor interactions, and other physiological processes such as blood flow and amino acid transport. In the brain, one of the most frequently used radionuclide techniques is the glucose utilization measurement made with radiolabeled 2-deoxyglucoses (2-DG). This technique was first used in autoradiographic studies using a carbon-14-labeled 2-DG compound in the late 1970s, and then a few years later with PET as fluorine-18-labeled fluorodeoxyglucose. Since then, countless studies have been performed. The notion that increases in brain activity are tightly linked to the rate of 2-DG uptake has made it a precious tool for neuroscience.

Despite extensive use of the method for studying brain energy metabolism, the precise mechanisms involved in processing glucose in the brain are not well understood. It is widely accepted that glucose constitutes the main exogenous cerebral energy substrate, but the exact allocation of the total glucose uptake to different cell types remains uncertain. Neurons and astrocytes are the two main cell groups in the mammalian brain. The classic view is that neurons adjust their glucose uptake to match their energy needs. In contrast, a concept introduced 17 years ago postulates that activity-dependent uptake of glucose occurs mainly in astrocytes, leading to increased production of lactate. Lactate is then transported via specific monocarboxylate transporters from astrocytes to neurons. In neurons, lactate is then used as an energy substrate. This concept is known as the astrocyte-neuron lactate shuttle (ANLS) hypothesis, and remains a significant controversy in the literature. One of the main reasons for the ongoing debate is the lack of *in vivo* data, as most of the available evidence is derived from *in vitro* studies, which by their nature do not reflect normal physiology.

A major focus of my recent research has been exploring different aspects of cerebral energy metabolism in the intact animal using a multimodal approach. Using radiolabeled acetate, we were able to demonstrate an activity-dependent oxidative metabolism in astrocytes. The active involvement of astrocytes in neuroenergetics is a new finding and we were the first to

demonstrate the feasibility of using label clearance as a measure of astrocytic oxidative metabolism. The radiotracer approach using a PET nuclide allowed us to transfer the experiment directly into a human setting and to reproduce the findings obtained in animals. If the ANLS hypothesis is valid, it is essential that neurons are able to use lactate as an energy source. However, at the time, only limited *in vitro* data were available that suggested neurons were using lactate. In a further study, we demonstrated the ability of lactate to sustain neuronal activity in the intact animal. We showed activity-dependent cerebral lactate oxidation and a preference for lactate over glucose in the brain.

Of course, functional imaging is not only used for basic neuroscience but also for clinical applications. PET is a powerful tool in the diagnosis of neurological disorders. In particular, its use in the diagnosis of glioma has gained considerable interest during the last few years. The most widely used radiotracer for brain (tumor) imaging, ^{18}F-fluorodeoxyglucose, has a number of limitations, mainly due to the high intrinsic cerebral glucose utilization and the consequent difficulty of differentiating normal from pathological tissue. An additional shortcoming of ^{18}F-fluorodeoxyglucose is its uptake in inflammatory tissue, which aggravates the difficulty of differentiation of e.g. radiation necrosis from tumor recurrence, one of the major clinical indications of PET imaging. Therefore, the development of more specific radiotracers is a general aim of nuclear medicine research. However, thorough validation is required prior to the introduction of a new molecular probe for clinical application. In this context, one aim of my work has been to evaluate the tracers ^{18}F-fluoroethyl-L-tyrosine, ^{18}F-fluorocholine and ^{18}F-fluorodeoxyglucose in several animal models to determine the tracers' specificity for brain tumor imaging, and to quantify the impact of several factors on the tracers. We tested the uptake of the three tracers in an experimentally induced radiation necrosis model and in cryolesions. Based on these measurements, we showed that the amino acid analog ^{18}F-fluoroethyl-L-tyrosine and the choline analog ^{18}F-fluorocholine are feasible tracers for the differentiation of radiation necrosis from tumor recurrence. In addition, we measured the accumulation of ^{18}F-fluorocholine and of ^{18}F-fluorodeoxyglucose in an abscess model to assess the uptake of these tracers in inflammatory tissue. Notably, we observed pronounced ^{18}F-fluorocholine accumulation in infectious tissue, which clearly reduces the specificity of this tracer for applications in oncology. On the basis of these and other studies, ^{18}F-fluoroethyl-L-tyrosine PET is now used in patients who have been treated for glioma to discriminate between treatment residuals and recurrent glioma tissue. This important distinction allows better treatment decisions.

Metabolic changes often precede structural alterations. Therefore, we hypothesized that tracer imaging may also be helpful for refining therapy monitoring in brain tumor patients. In low-grade glioma patients, we observed an early metabolic response to temozolomide treatment, which preceded detectable changes in magnetic resonance images, the standard

imaging modality for treatment control. By demonstrating that molecular imaging has an advantage over structural imaging in low-grade gliomas in terms of the early identification of response to treatment, we proposed that PET data could be used to define and adjust the duration of chemotherapy.

In summary, my work encompasses a broad range of applications of radiotracer techniques ranging from basic brain research purposes, to preclinical radiotracer testing in animal models, and finally to clinically relevant problems. In the future, new imaging modalities and novel combinations of imaging techniques such as hybrid PET systems (e.g. PET/MR scanners) may further enhance the clinical impact of radiotracer techniques.

Background

In 1802, the Scottish anatomist Sir Charles Bell portrayed the anatomy of the human brain in a famous series of lifelike watercolor plates demonstrating the beauty of our brains (Bell 1802). At the time, no one could have imagined that it would be possible in the future to image brains in living organisms. Less than a century later, the demonstration of the first radiograph by Wilhelm Roentgen in 1895 opened a new window to medical diagnosis (Röntgen 1898). His discovery was the starting point for even more amazing advances in imaging during the following century. In 1961, William Oldendorf developed the theoretical bases for computerized tomography (Oldendorf 1961). Two years later, his idea of a new instrument incorporating the principles and hardware eventually used by modern CT scanners was patented. However, manufacturers of X-ray equipment were not aware of the potential at this time. Only Sir Godfrey Hounsfield acknowledged Oldendorf's studies in his own work which led to the invention of the X-ray CT scanner (and the Nobel Prize for Medicine in 1979 (Hounsfield 1973)). Since then, technical advances have been rapid and the next milestone was achieved as quickly as the mid-1970s when magnetic resonance imaging (MRI) was introduced by the chemist Paul Lauterbur (Lauterbur 1973). The same decade also saw the development of positron emission tomography (PET), which became a tool for medical diagnosis by the mid-1980s (Phelps *et al* 1975; Phelps and Mazziotta 1985). This impressive progression in the development of neuroimaging methods has continued until today. In this regard, *in vivo* optical brain imaging methods should be mentioned. *In vivo* imaging using light has seen 30 years of intense development and provides sensitivity to functional changes and temporal and spatial resolution not so far seen. Currently, a wide range of approaches is applied such as intrinsic optical imaging for the detection of variations in the oxygenation state of hemoglobin (Dunn *et al* 2003), voltage-sensitive dye imaging for the measurement of neuronal activity using fluorescent dyes bound to neuronal membranes that report changes in transmembrane potentials (Petersen and Sakmann 2001), laser speckle imaging for cerebral blood flow (CBF) measurements (Dunn *et al* 2001) and two-photon laser scanning microscopy with its subcellular resolution (Helmchen and Denk 2005). All these developments have started to satisfy the interest in investigating the brain *in situ*. The more traditional imaging methods such as computed X-ray tomography, ultrasound and especially structural MRI allow the imaging of the central nervous system with ever-increasing spatial resolution, allowing the identification of very small structural alterations. However, information about the morphology alone is clearly not enough to obtain a complete picture of the (patho)physiology of the brain. In this regard, functional imaging methods such

as the nuclear imaging techniques (e.g. PET) and optical brain imaging methods mentioned above are playing a significant role. In my work over recent years, I have mainly made use of radiotracer techniques which I will focus on in the following sections.

Functional imaging of the brain using PET tracers

PET measures the accumulation and distribution of radiolabeled biologically active substrates in the tissue over time. The radiotracers are injected into the bloodstream at micromolar or nanomolar concentrations. These low concentrations have the advantage that systemic effects can be excluded. The nuclides used for radiolabeling decay by the emission of positrons which combine with nearby electrons (annihilation reaction), leading to the emission of two 511 keV gamma rays traveling at 180°. The emitted gamma rays penetrate the head allowing detection by the scintillation crystals of the PET scanner. In addition, the most commonly used nuclides have short half-lives, minimizing radiation burden. The most widely used radioactive nuclides are fluorine-18 ($T_{1/2}$ = 110 min), which is used as a substitute for hydrogen, carbon-11 ($T_{1/2}$ = 20.4 min), nitrogen-13 ($T_{1/2}$ = 10.1 min) and oxygen-15 ($T_{1/2}$ = 2 min), which are used to replace natural isotopes of carbon, nitrogen and oxygen, respectively. In theory, this affords an unlimited number of biologically active substrates which can be labeled (for more details about basic aspects of PET see (von Schulthess 2007)). Together with tracer kinetic models that represent mathematical descriptions of transport and biochemical reaction sequences, PET images allow non-invasive access to the local biochemistry of the intact brain. All these properties make PET an ideal tool for both *in vivo* research and clinical imaging. This is reflected by the increasing number of brain studies using PET over the last 15 years (Figure 1).

With the advance of PET, the term molecular imaging has become increasingly important. As recommended by a task force of the Molecular Imaging Center of Excellence in 2007 (Mankoff 2007), molecular imaging includes the "visualization, characterization, quantification and measurement of biological processes at the molecular and the cellular levels in humans and other living systems in space and over time". Molecular imaging instrumentation comprises tools that enable visualization and quantification in space and over time of signals from molecular imaging agents. Apart from radiotracer techniques, MRI, MR spectroscopy, optical imaging, ultrasound and other techniques also offer the capability for molecular imaging. However, for human use, PET imaging is still one of the most prevalent modalities for functional imaging. In addition to its use in research, molecular imaging has enormous clinical relevance because it reveals information about the biology of the disease process and characterizes specific disease processes in individual patients. By accurately characterizing tumor processes or biological processes, molecular imaging may help to refine the treatment (monitoring, treatment decisions, etc.) and evaluate prognosis.

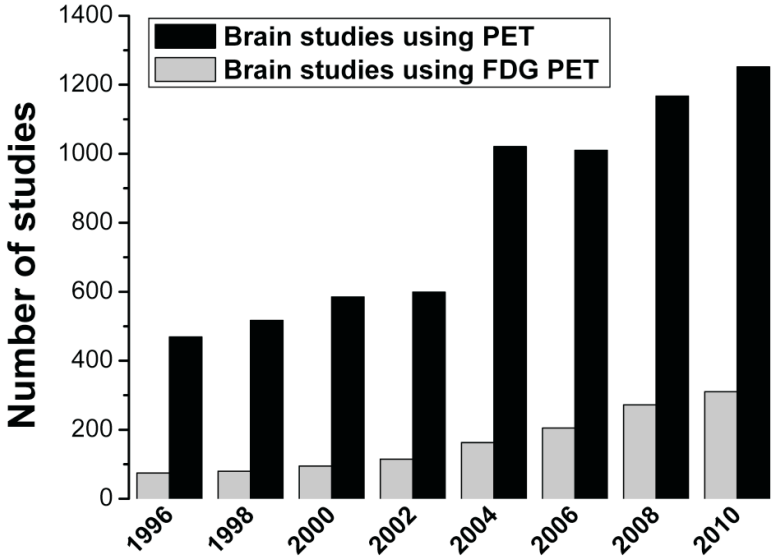

Figure 1. **Brain studies using positron emission tomography.**

Number of brain studies using PET between 1996 and 2010 cited by PubMed (www.ncbi.nlm.nih.gov/pubmed) searching for 'brain positron emission tomography' (black bars). Gray bars represent brain studies performed using radiolabeled fluorodeoxyglucose (PubMed search 'brain positron emission tomography fluorodeoxyglucose').

Aims of my work

My work can be divided into two fields. One major focus was the application of nuclear techniques to investigate fundamental physiological processes in the brain and, where possible, to combine them with complementary imaging methods (see the two articles in Section 1). We aimed to disentangle the specific processes involved in the energy production of the brain and to measure them in the intact brain. Specifically, we intended to demonstrate the feasibility of 1-^{11}C-acetate kinetics for quantitative measurements of astrocytic oxidative metabolism and then to translate the approach to a human set-up. With this work, we wanted to show whether astrocytes also exhibit activity-dependent oxidative energy metabolism as is the case with neurons. In the second study submitted with this work, we aimed to measure neuronal lactate oxidation with an analogous approach using ^{11}C-L-lactate. This is of general interest because of the ongoing debate regarding cerebral lactate oxidation (see below). Combining the radiotracer approach with additional imaging modalities, we further tested the hypothesis that the intact brain can sustain its electrical activity with lactate as the only substrate.

The second pillar of my research over the last decade has been the evaluation of new tracers for their application *in vivo*, mainly for brain tumor imaging. In the technically oriented part of this work (see Section 2 – Part I (three articles)), we aimed at improving a preclinical imaging system, the so-called beta-probe, for radiotracer evaluation in the intact animal. The aims were: 1) to test the beta-probe methodology together with ^{15}O-H_2O for CBF measurements, 2) to evaluate a novel beta-scintillator system for *in vivo* brain cortex measurements and 3) to demonstrate the system's feasibility for the evaluation of novel PET tracers.

Furthermore, we examined PET tracers already established for other indications in terms of their potential for imaging brain tumors (see Section 2 – Part II (four articles)). In the first two studies, we aimed to assess the uptake of ^{18}F-fluoroethyl-L-tyrosine, ^{18}F-fluorocholine and ^{18}F-fluorodeoxyglucose in induced radiation injury and of ^{18}F-fluorocholine in experimentally induced abscesses. We wanted to test in detail the tracers' feasibility for use as brain tumor imaging agents, specifically for their ability to distinguish radiation necrosis from tumor recurrence. In the next study submitted with this work, we focused on the *in vivo* characterization of microvessel distribution and CBF in low-grade gliomas using PET. A better understanding of tumor biology may enable better assessment and planning of individual treatment. In the last study, we investigated the time course of low-grade tumor metabolism in patients during temozolomide chemotherapy, and compared metabolic responses as measured with PET with volume responses as revealed by MRI.

Section 1 –
Understanding brain physiology: example of cerebral energy metabolism

The importance of functional imaging in clinical situations is continually increasing and will further accelerate with ongoing technical improvements and combinations of imaging modalities.

However, apart from clinical applications, the neuroscience field has also profited considerably from the technical developments in brain imaging. One field where *in vivo* imaging has accounted for significant new insights is brain energy metabolism. Traditionally, glucose metabolism has been used as a surrogate marker for neuronal activity (e.g. glucose utilization measurement using ^{18}F-fluorodeoxyglucose (^{18}F-FDG)), due to the close and reliable correlation between brain electrical activity and glucose metabolism (Sokoloff 1999). Surprisingly, despite its extensive use as an indirect measure of brain activity, the precise mechanisms underlying the energy supply of the brain and the coupling of brain activity and glucose utilization are still not well understood. However, in order to draw valid conclusions from functional imaging signals, it is crucial to understand not only the mechanisms of the methods and imaging agents used, but also the exact nature of the underlying physiological processes. The brain is a high energy-consuming organ, having a signaling-related energy use equivalent to that of leg muscle running a marathon (Hochachka PW cited in (Attwell and Laughlin 2001)). While it constitutes only about 2% of the body's weight, it uses around 20% of the whole body glucose consumption (Magistretti 2008). It is widely accepted that glucose represents the main exogenous energy substrate for the healthy brain, providing 95% of the total energy (Barros and Deitmer 2010). These numbers are well accepted, but exactly how glucose is processed in the brain remains heavily debated. The main cell types found in the brain are neurons and astrocytes. The classic view of brain energy metabolism assumed that each of these cells use glucose directly as an energy substrate in proportion to its demand. However, about two decades ago this perspective was challenged by the suggestion of an interaction between neurons and glia in brain energy metabolism. The hypothesis proposed a tight spatial and temporal interplay between astrocytes and neurons (Magistretti *et al* 1999; Pellerin and Magistretti 1994), and discussed a major activity-dependent astrocytic glucose uptake and glycolysis leading to a high lactate production (Figure 2). Most of this astrocytic lactate is then released into the extracellular space, and from there it is taken up by neurons via specialized monocarboxylate transporters (MCT 2; (Pierre *et al* 2002)) to serve as a neuronal oxidative fuel. The concept was termed the astrocyte-neuron lactate shuttle (ANLS) hypothesis, based on the processes involved.

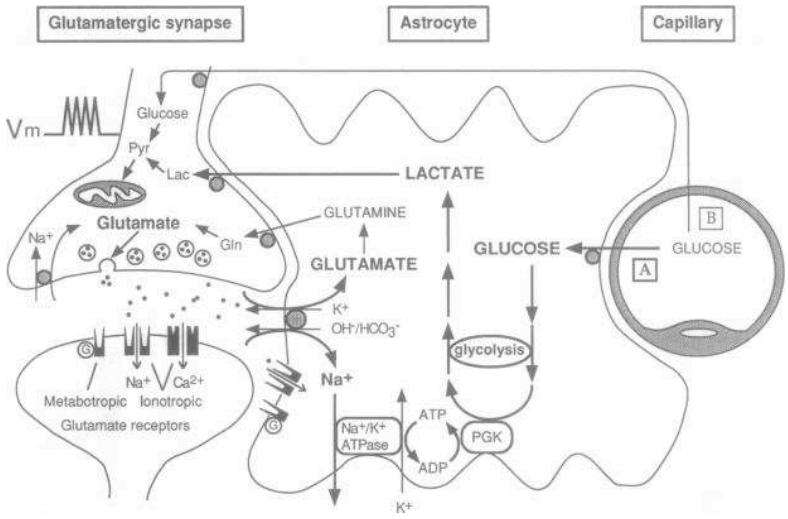

Figure 2. **Glutamate uptake into astrocytes stimulates glycolysis: a mechanism coupling neuronal activity to glucose utilization.**

This scheme was the first representation of the astrocyte-neuron lactate shuttle model postulated by Pellerin and Magistretti (1994). Upon neuronal activity, glutamate is released from presynaptic terminals and induces glycolysis in astrocytes. Glutamate is co-transported with sodium (Na^+), resulting in an increased astrocytic Na^+ concentration. Increased $[Na^+]_i$ leads to activation of the Na^+/K^+ ATPase which is fueled by ATP. The pump activates glycolysis, i.e. glucose utilization and lactate production, in astrocytes. The released lactate can be used by neurons as an energy substrate after its uptake. Pyr = pyruvate, Lac = lactate, Gln = glutamine, PGK = phoshoglycerate kinase, Figure taken from Pellerin and Magistretti (1994).

However, the controversy is still ongoing regarding the validity of the concept (for review see (Pellerin and Magistretti 2011)), largely due to a lack of *in vivo* evidence for the processes proposed to be involved. The main reason for this is the difficulty of measuring the participating physiological steps with reasonable temporal and spatial (i.e. cellular) resolution.

Investigating aspects of brain energy metabolism down to the cellular level

Only during the last few years have methods emerged that allow measurements of cellular processes in the intact animal. The purpose of one of the articles submitted with this work was to investigate the feasibility of non-invasively measuring oxidative metabolism specifically in astrocytes using ^{11}C-acetate (Wyss *et al* 2009c). Labeled acetate was chosen as a promising candidate for this purpose due to its selective uptake and metabolism in astrocytes (Waniewski and Martin 1998). For the first time, this study used label clearance as a measure for oxidative astrocytic metabolism *in vivo*. During electrical nerve stimulation, an increase of k_2 (the parameter describing radiolabel washout) from 0.014 ± 0.007 min^{-1} (mean ± SD) to 0.027 ± 0.006 min^{-1} was found in rats, supporting the notion of an activity-related astrocytic oxidative metabolism. Of note, the experiments were first performed in rats using a dedicated beta-probe (see below for further details about this technology) and were subsequently translated in a straightforward manner in a human PET study. In healthy volunteers, astrocytic oxidative metabolism increased upon stimulation to a similar degree,

confirming the animal results. Due to acetate's cell specificity, with this approach it is possible to investigate aspects of brain metabolism on a cellular level despite the use of acquisition tools that intrinsically do not reach cellular resolution.

Using an analogous approach, the aim of the second work of Section 1 was to investigate whether neurons are able to oxidize exogenous lactate (Wyss *et al* 2011). Using ^{11}C-L-lactate, we tested the hypothesis that k_2 (in the one-tissue compartment model applied, this parameter reflects lactate oxidation) increases during increased brain activity. Indeed, we found an increase of k_2 from 0.077 ± 0.009 to 0.105 ± 0.007 min^{-1} when brain work was increased by electrical infraorbital nerve stimulation. Making use of optical imaging in combination with voltage-sensitive dyes, we further examined the ability of the brain to use lactate as a source of energy. For the first time, we demonstrated *in vivo* the maintenance of neuronal activity measured by voltage-sensitive dye imaging in the presence of lactate as the primary energy substrate. The advantages of a multimodal imaging approach were evident in this study, as various aspects could be addressed in the same animal model using different methods. In summary, we demonstrated for the first time that lactate is capable of maintaining neuronal integrity to a large degree in the absence of glucose in the intact animal. Furthermore, we found that 1) lactate is preferred over glucose if both substrates are available, 2) lactate is readily metabolized by the intact adult brain and 3) its metabolism is activity-dependent.

These examples from basic neurophysiology research demonstrate how radiotracer methods can provide helpful insights into principle mechanisms. In particular, combining radiotracer methods with additional imaging modalities increases the impact of these experiments and significantly enhances the interpretation of the findings.

Section 2 –
Evaluation of PET tracers to establish clinical usefulness

Newly designed PET radiotracers require rigorous testing before they can be used in the clinical setting. First, new radioligands are tested *in vitro*, e.g. binding studies with membrane fractions, metabolism studies with (human) plasma and/or hepatocytes, etc. However, the predictive value of *in vitro* experiments remains limited and is not sufficient to evaluate whether a new tracer is suited for application in human subjects. For this purpose, *in vivo* experiments are mandatory.

Part I: Establishment and advancements of novel imaging techniques for preclinical *in vivo* radiotracer testing

Before a PET tracer can be applied in humans, considerable preclinical evaluation in intact organisms is required. One of the prerequisites for economical and conclusive testing of novel radiotracers is the appropriate *in vivo* imaging technology. Ideally, such techniques should be relatively inexpensive, preferably non-invasive and exhibit good temporal and spatial resolution. For a long time, autoradiography was the only established method to test radiolabeled tracers in experimental animals. This method is appropriate for the characterization of tracer uptake with sufficient spatial resolution and for organ bio-distribution studies. However, an autoradiographic study is a 'one-shot method', yielding the distribution of a given radioligand at one time point only. Thus, using this method to obtain temporal information concerning a radiotracer's kinetic behavior requires a large number of animals.

The development of small animal PET scanners (Ambrosini *et al* 2009; Dupont and Warwick 2009; Riemann *et al* 2008) unequivocally helped to close the gap between the evaluation of novel tracers in preclinical animal experiments and their final clinical application. These dedicated scanners allow imaging of the whole rodent – if necessary, several times in a longitudinal design. However, small animal PET scanners are expensive, need considerable servicing and have a limited temporal and spatial resolution. Despite significant improvements over the last few years with respect to sensitivity, the temporal resolution is still a problem for radiotracers exhibiting fast kinetics. Another drawback of small animal PET is the requirement of anesthesia, which inevitably alters normal physiology.

In this regard, the development of so-called beta-probes (Zimmer *et al* 2002) has added additional possibilities to the field of preclinical radioligand testing in small laboratory animals, further accelerating the clinical translation of potential tracer candidates. In two of the articles submitted with this work, we substantially improved the performance of original beta-scintillators. First, we developed for the first time completely light-tight systems, which improve usability because experiments no longer have to be performed in darkness.

Secondly, the system was tested in response to very fast kinetics with ^{15}O-H_2O, a tracer used for perfusion measurements that has a very short physical half-life ($t_{1/2}$ = 122 seconds; (Weber *et al* 2003)). To overcome the invasiveness of classic intracortical probes, and with them the need for anesthesia, we later developed and introduced a highly sensitive beta-scintillator for measurements in the intact rodent cortex (Wyss *et al* 2009b). We demonstrated the feasibility of using this device in non-anesthetized, head-fixed rats. Remarkable changes in tracer kinetics were detected between awake and anesthetized animals, demonstrating the need for methods that can be applied in awake animals to overcome the unfavorable effects of anesthetic agents. In addition, the higher sensitivity increased the practicability of study protocols with repeated injections in the same animal. This is especially helpful in combination with tracers with short half-lives where the radioactivity concentration declines quickly (e.g. carbon-11-labeled compounds with $T_{1/2}$ = 20.4 min). Apart from the higher sensitivity and the ability to perform experiments in the absence of any tissue damage, this device still shares the advantages of a low price and a high temporal resolution with the classic beta-probe.

The justification of this methodology for the testing of novel radiotracers for human application is shown in the third article of Section 2 – Part I. In that project, the aim was to quantitatively evaluate a novel receptor ligand for the metabotropic glutamate receptor subtype 5 (mGluR5), ^{11}C-ABP688, for its application in brain studies (Wyss *et al* 2007a). In antecedent *in vitro* experiments, it exhibited ideal properties such as high affinity and specificity for the target receptor (mGluR5), high stability of the radioligand in plasma and brain, and sufficient passage through the blood-brain barrier (Ametamey *et al* 2006). Altogether, the preclinical profile of ^{11}C-ABP688 suggested that the tracer would have reasonable potential for *in vivo* use. However, in the past, numerous candidates passed *in vitro* evaluation but failed in the following testing in the living organism. We demonstrated the feasibility of mGluR5 quantification in intact brains of 13 animals using a beta-scintillator (Wyss *et al* 2007a). Directly following from this kinetic validation in rats, the tracer was transferred to human use in a straightforward manner. Notably, ^{11}C-ABP688 exhibited very similar kinetic characteristics in the human central nervous system as found in the rodent experiments (Ametamey *et al* 2007). This clearly demonstrates the importance of proper preclinical imaging for the efficient introduction of new imaging agents into a human set-up ('from bench-to-bedside'). A congruent example, discussed earlier, is the study using 1-^{11}C-acetate where we also found similar results in healthy volunteers as previously measured using the beta-probe in animals (Wyss *et al* 2009c).

Part II: Evaluation of radiotracers for the management of brain tumor patients

Overall, the labeled glucose analog ^{18}F-FDG is the most commonly used radiotracer in clinical PET. FDG is transported and phosphorylated in a similar manner as native glucose but it is trapped within the tissue and is not further metabolized after being transformed to FDG-6-P by the enzyme hexokinase. The accumulation of the label in the tissue is then proportional to the cellular glucose utilization rate. In the daily routine for whole body tumor staging, FDG is by far the most often used PET tracer. PET imaging has always played an important role in patients suffering from cerebral pathologies, e.g. diagnosis of brain tumors was the first oncological application of ^{18}F-FDG PET (Di Chiro *et al* 1982). However, in these patients, the use of ^{18}F-FDG is more problematic (see below for more details). Nowadays, ^{18}F-FDG is used in only about one fifth of all brain studies (Figure 1). On the other hand, the variety of tracers used for brain studies is large and continuously increasing. Already, numerous different compounds have been used to target a wide range of processes, e.g. blood flow, glucose metabolism, receptor occupancy of various types of receptors, amino acid transport, cellular proliferation, etc. Consequently, PET imaging is becoming increasingly helpful in the differential diagnosis of numerous neurological conditions such as dementias, movement disorders, seizure disorders, perfusion impairments and psychiatric disorders. Amongst all these pathologies, glioma patients still form a considerable fraction of the routine diagnostic workout of brain PET examinations.

A) Uptake characteristics in various pathologies

In glioma patients, PET found a major application for the differentiation of tumor recurrence from residual tissue lesions due to treatment, such as cerebral radiation necrosis. However, as described in one of the articles submitted with this work, and by others, more and more studies suggest that PET may find its niche in the monitoring of treatment response in brain tumor patients ((Piroth *et al* 2011; Schiepers *et al* 2010; Wyss *et al* 2009a), see also below).

Over the last 25 years, PET has become a useful diagnostic tool for the evaluation of the biologic activity of brain tumors (for review see (Chen 2007; Heiss *et al* 2011; Waldman *et al* 2009)). One of the main indications for PET in brain tumor patients is the differentiation of post-therapy radiation necrosis and pseudoprogression from tumor recurrence (Okamoto *et al* 2011; Terakawa *et al* 2008), as direct diagnosis is crucial for correct patient management. Although the usefulness of ^{18}F-FDG in tumor imaging is beyond doubt, there are several drawbacks which reduce the accuracy of ^{18}F-FDG in these situations. One problem is the high intrinsic uptake of ^{18}F-FDG in normal brain gray matter. A second issue is the wide range of ^{18}F-FDG uptake in different brain tumors and third, the significant uptake of ^{18}F-FDG by inflammatory cells (Kaim *et al* 2002a). Collectively, these problems render the differentiation of brain lesions difficult and make the separation of radiation necrosis and

brain tumor imprecise. Also, conventional MRI and CT often cannot reliably separate these two pathologies (Del Sole *et al* 2001; Mullins *et al* 2005).

In this regard, the development of more specific radiotracers with low intrinsic uptake in normal brain tissue and no accumulation in inflammatory cells was and still is a major aim of nuclear medicine research. Establishment of the validity of a novel tracer *in vivo* is an indispensable prerequisite for later clinical application. Two promising radiotracers, ^{18}F-fluorocholine (^{18}F-FCH) and ^{18}F-fluoroethyl-L-tyrosine (^{18}F-FET), were introduced about 10 years ago. Using classic autoradiography, we compared the accumulation of ^{18}F-FCH and ^{18}F-FET with the accumulation of ^{18}F-FDG in a radiation necrosis model of the rat (Spaeth *et al* 2004). In the same study, we uncovered the effect of a blood-brain barrier disruption on radiotracer uptake by using a cryolesion model. ^{18}F-FCH and ^{18}F-FET revealed themselves to be superior to ^{18}F-FDG for separating radiation necrosis from tumor recurrence. We found that ^{18}F-FET uptake is most likely due to a disruption of the blood-brain barrier and no uptake was observed in macrophages. This is in agreement with previous work which also showed that ^{18}F-FET is not taken up in inflammatory lesions (Kaim *et al* 2002b). In contrast, no data were available regarding the uptake of ^{18}F-FCH in inflammatory tissue. For each oncological tracer, it is crucial to know the uptake behavior in non-tumorous lesions, of which inflammatory and/or infectious foci are amongst the most important. In the second article of this section, we assessed ^{18}F-FCH uptake using small animal PET imaging in an animal abscess model established in our laboratory (Wyss *et al* 2004). In addition, autoradiographic analysis was performed on a subsequent day for exact correlation with histology. Pronounced accumulation of ^{18}F-FCH was found in inflammatory infiltrates, with tracer uptake three or more times higher than the accumulation in healthy muscle tissue. This finding considerably limits the specificity of labeled choline for tumor detection and has to be incorporated into the evaluation of clinical PET scans using ^{18}F-FCH.

B) Target tumor biology with the help of functional imaging and estimate merits of functional PET imaging for treatment monitoring

A better understanding of tumor biology may help to better understand the tumor response to treatment. For example, low-grade gliomas have long been regarded as resistant to chemotherapy; however, several studies have shown remarkable responses to various regimens (Hoang-Xuan *et al* 2004; Peyre *et al* 2010). Nevertheless, it is difficult to predict the outcome of treatment. Adequate delivery of drugs is a main prerequisite for effective chemotherapy. On the one hand drug delivery is a function of drug concentration in the blood, but on the other hand it depends on blood flow through tumor microvasculature and the transport of drugs across capillaries. In another article submitted with this work, we investigated the perfusion and the vascular density in low-grade gliomas (Wyss *et al* 2007b)

using ^{15}O-H_2O for CBF measurements and ^{18}F-FET as a tracer for amino acid transport. Earlier studies using the amino acid analog ^{11}C-methionine demonstrated that amino acid PET serves as an indirect measure of the number of microvessels (Kracht *et al* 2003). Together with the notion that ^{18}F-FET and ^{11}C-methionine provide comparable information (Grosu *et al* 2011; Weber *et al* 2000), it can be assumed that ^{18}F-FET is a surrogate marker of the microvascular density. The spatial distribution of the amino acid carrier, which is located at the brain capillaries, and tumor CBF were determined in a group of 17 patients. In 82% of the patients, increased global CBF and FET uptake were determined. The volumes of increased CBF and FET uptake spatially coincided (Spearman rank rho = 0.944, $p < 0.01$). However, we found that CBF only started to increase when ^{18}F-FET uptake increased above a certain level, suggesting that CBF increases follow the formation of new microvessels. Irrespective of increased capillary density, CBF increases were more confined to the tumor center. In many patients, intratumoral heterogeneity on the PET scans was also observed. The observed variation of CBF and amino acid uptake within single tumors and within the whole group did not depend on the lesion size determined from MR tomographies. Taken together, these findings may help to better understand the differences in treatment response and aid treatment decisions. Based on these findings and the fact that microvascular density constitutes a significant independent prognostic factor (Abdulrauf *et al* 1998; Leon *et al* 1996), we initiated a parallel prospective study addressing the effect of chemotherapy on amino acid uptake and examining the potential to use PET for the identification of early treatment response in low-grade glioma patients (Wyss *et al* 2009a). ^{18}F-FET PET scans were performed at six-month intervals in a homogeneous population of 11 patients with progressive supratentorial LGG WHO II and treated with 75 mg/m^2 temozolomide per day over three weeks followed by one week off. None of the patients showed blood-brain barrier disruption as revealed by gadolinium-enhanced MR (Figure 3).

Comparing metabolic (PET) and structural (MRI) responses, we observed a mean delay in MRI tumor volume reduction of seven months compared to the PET response. Most interestingly, with regard to the identification of patients who benefit most from treatment, we found that the magnitude of the first ^{18}F-FET volume response correlated with the best MRI tumor volume response obtained later during chemotherapy (Spearman rank rho = 0.731, $p = 0.01$). Due to the small sample size, final conclusions cannot be drawn concerning the degree to which the magnitudes of the PET and MR responses relate to the subsequent clinical course and to the time until tumor progression. However, we clearly demonstrated the advantage of having additional molecular information for low-grade glioma patients in terms of the time window of identifying treatment response.

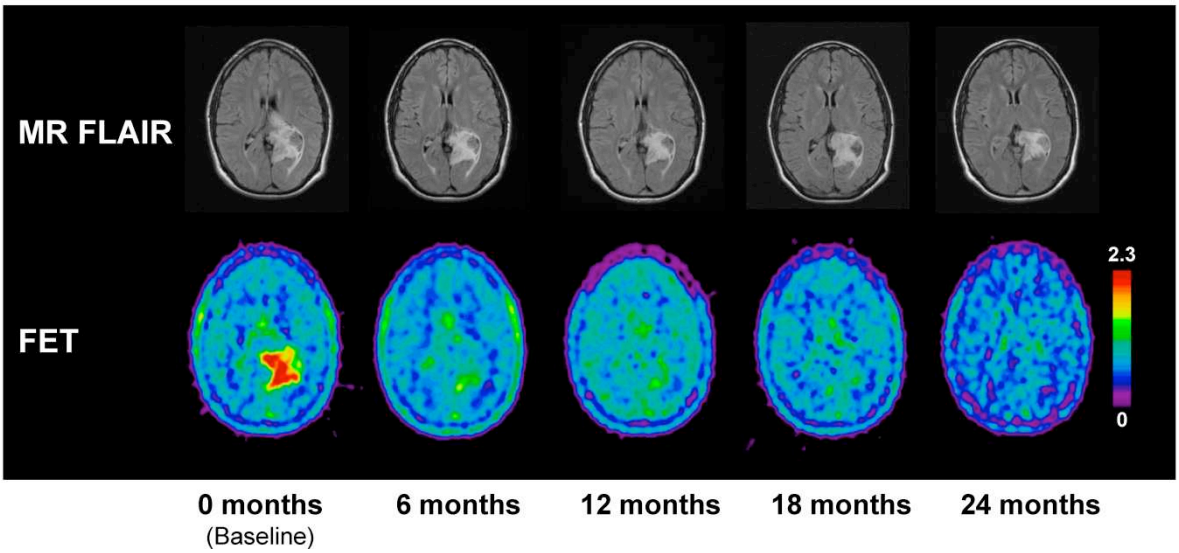

Figure 3. **Metabolic response precedes structural reaction.**

Example of a patient undergoing chemotherapy using temozolomide. Imaging studies were performed before and 6, 12, 18, 24 months after initiation of treatment. The color scale represents the tumor:cerebellum ^{18}F-FET uptake ratio. Figure modified from Wyss et al. (2009a).

Functional brain imaging using techniques from nuclear medicine now has a broad field of application, which is exemplified by my work ranging from basic neuroscience research to applications for patient management. In the future, with the advance of novel radioligands and technical improvements of the measurement devices such as the introduction of hybrid systems (e.g. PET/MR systems (Heiss 2009)), the field may further expand.

Section 1 –
Understanding brain physiology: example of cerebral energy metabolism

1. Stimulation-induced increases of astrocytic oxidative metabolism in rats and humans investigated with 1-^{11}C-acetate

Journal of Cerebral Blood Flow and Metabolism, 2009, Vol 29 (1), Pages 44-56

2. *In vivo* evidence for lactate as a neuronal energy source

Journal of Neuroscience, 2011, Vol 31 (20), Pages 7477-7485

Journal of Cerebral Blood Flow & Metabolism (2009) 29, 44–56

www.jcbfm.com

Stimulation-induced increases of astrocytic oxidative metabolism in rats and humans investigated with 1-^{11}C-acetate

Matthias T Wyss[1], Bruno Weber[1,2], Valerie Treyer[1], Stefan Heer[1], Luc Pellerin[3], Pierre J Magistretti[4] and Alfred Buck[1]

[1]*PET Center, Division of Nuclear Medicine, University Hospital, Zürich, Switzerland;* [2]*Institute of Pharmacology and Toxicology, University of Zürich, Zürich, Switzerland;* [3]*Physiology Department, University of Lausanne, Lausanne, Switzerland;* [4]*Brain Mind Institute, École Polytechnique Fédérale de Lausanne (EPFL), Lausanne, Switzerland*

The purpose of this study was to investigate astrocytic oxidative metabolism using 1-^{11}C-acetate. 1-^{11}C-acetate kinetics were evaluated in the rat somatosensory cortex using a β-scintillator during different manipulations (test–retest, infraorbital nerve stimulation, and administration of acetazolamide or dichloroacetate). In humans a visual activation paradigm was used and kinetics were measured with positron emission tomography. Data were analyzed using a one-tissue compartment model. The following features supported the hypothesis that washout of radiolabel (k_2) is because of ^{11}C-CO_2 and therefore related to oxygen consumption ($CMRO_2$): (1) the onset of ^{11}C washout was delayed; (2) k_2 was not affected by acetazolamide-induced blood flow increase; (3) k_2 demonstrated a significant increase during stimulation in rats (from 0.014 ± 0.007 to 0.027 ± 0.006 per minute) and humans (from 0.016 ± 0.010 to 0.026 ± 0.006 per minute); and (4) dichloroacetate led to a substantial decrease of k_2. In the test–retest experiments K_1 and k_2 were very stable. In summary, 1-^{11}C-acetate seems a promising tracer to investigate astrocytic oxidative metabolism *in vivo*. If the washout rate indeed represents the production of ^{11}C-CO_2, then its increase during stimulation would point to a substantially higher astrocytic oxidative metabolism during brain activation. However, the quantitative relationship between k_2 and $CMRO_2$ needs to be determined in future experiments.
Journal of Cerebral Blood Flow & Metabolism (2009) **29,** 44–56; doi:10.1038/jcbfm.2008.86; published online 20 August 2008

Keywords: 1-^{11}C-acetate; astrocytes; β-scintillator; oxidative metabolism; positron emission tomography; washout

Introduction

There is increasing evidence that astrocytes and neurons constitute a tightly coupled metabolic unit. Already early studies of brain metabolism using ^{14}C-labeled precursors such as glucose or acetate led to the concept of two distinct tricarboxylic acid (TCA) cycle compartments, that is, two separate pools for glutamate and glutamine (Berl and Frigyesi, 1969; Cremer, 1970; Minchin and Beart, 1975; Van den Berg *et al*, 1969). Later histochemical work on the restricted localization of glutamine synthetase to glial cells (Martinez-Hernandez *et al*, 1977; Norenberg and Martinez-Hernandez, 1979) further supported the idea on the glial and neuronal site of these distinct pools. Simplification of these data has sometimes led to the wrong assumption that the oxidative activity of astrocytes is negligible. However, studies using mainly nuclear magnetic resonance spectroscopy have suggested that astrocytic energy metabolism indeed contains a substantial oxidative component which may account for up to 30% of total oxidative metabolism in brain under resting conditions (for review see Hertz and Kala, 2007; Hertz *et al*, 2007; Hyder *et al*, 2006). Recent transcriptome analysis has revealed a pattern of gene expression in astrocytes consistent with a significant oxidative activity (Lovatt *et al*, 2007).

Another question is how astrocytic metabolism behaves during activation. A recent study using *ex vivo* autoradiography with ^{14}C-labeled acetate at the carbon 2 position suggested that astrocytic oxidative metabolism increases with brain activity

Correspondence: Dr A Buck, Division of Nuclear Medicine, Rämistrasse 100, University Hospital, Zürich CH-8091, Switzerland. E-mail: fred.buck@usz.ch
The study was supported by the Swiss National Science Foundation (Grants 3100A0-105804/1 and PP00B-110751/1) and by the OPO-Stiftung Zürich.
Received 16 November 2007; revised and accepted 27 June 2008; published online 20 August 2008

(Cruz *et al*, 2005). Labeled acetate is a promising candidate to investigate astrocytic oxidative metabolism *in vivo* because it is selectively taken up and metabolized by astrocytes (Hassel *et al*, 1992; Muir *et al*, 1986; Waniewski and Martin, 1998). Earlier studies in the heart muscle have further revealed that quantitative measures for oxygen consumption can be derived from the washout rate of label after injection of radiolabeled acetate (Buck *et al*, 1991). Acetate can be labeled in the 1- or 2-carbon position. Whole-body studies using ^{13}C-labeled acetate demonstrated that labeled CO_2 is produced during the second or third turn in the TCA cycle, depending on whether 1-^{13}C-acetate or 2-^{13}C-acetate was used (Wolfe and Jahoor, 1990). However, these results reflect whole-body metabolism, brain-specific reactions cannot be directly derived from them. In brain, with 1- and 2-labeled acetate there was substantial labeling of amino acids, such as glutamate, glutamine, and aspartate and further TCA cycle intermediates as shown in older and more recent literature (Badar-Goffer *et al*, 1990; Berl and Frigyesi, 1969; Lebon *et al*, 2002; Tyce *et al*, 1981; Tyson *et al*, 2003; Van den Berg *et al*, 1969; Van den Berg and Ronda, 1976). However, the static measurement of metabolites at single time points yields only limited information on astrocytic oxidative metabolism.

In this study we applied 1-^{11}C-acetate and dynamic measurements to investigate astrocytic oxidative metabolism. Specific questions were (1) what is the extraction fraction (EF) of the tracer, (2) what is the kinetic behavior at baseline and during stimulation, (3) how does dichloroacetate, an agent that increases the production of acetyl-coenzyme A (CoA) from pyruvate in the cell, change the kinetics of 1-^{11}C-acetate, and (4) is the loss of radiolabel dependent on blood flow. Studies were performed in rats and humans. In rats data were acquired using a β-scintillator, in humans we applied positron emission tomography (PET).

Materials and methods

Automated Radiosynthesis of Sodium 1-^{11}C-Acetate

^{11}C-CO_2 was produced by the ^{14}N(p,α)^{11}C nuclear reaction using a nitrogen gas (N_2/0.5% O_2) target. ^{11}C-CO_2 was bubbled at room temperature in a mixture of methylmagnesium bromide (3 mol/L solution in diethyl ether; Fluka, 70 μL, 0.21 mmol) and dry diethyl ether (3 mL) placed in the reactor, where the chemical trapping of the ^{11}C-CO_2 by C-carboxylation of the Grignard reagent takes place instantly. After delivery (10 mins) the reaction was quenched by automated addition of nearly equimolar amount of acid (1 mL 0.2 mol/L aqueous HCl, 0.2 mmol HCl) and the diethyl ether from the bilayer mixture was removed by evaporation in a stream of nitrogen (100 mL/min) for approximately 10 mins. The residual water solution of 1-^{11}C-acetic acid was automatically drawn into the loop of the preparative chromatograph (Merck-Hitachi chromatograph equipped with L-4000A UV detector at 254 nm, isocratic pump L-6000A, 5 mL loop, and radiation detector Radiation Monitor; Eberline Instrument Corporation, Santa Fe, NM, USA), injected into a semipreparative reversed phase column (Polymerx, 10 μm, 250 $\times$ 10 mm, Phenomenex) and eluted with a mixture of sterile salt physiologic solution as the mobile phase. The fraction corresponding to the 1-^{11}C-acetic acid (t_R = 7 mins) was collected to give up to 10 GBq activity of no-carrier-added sodium 1-^{11}C-acetate with over 99% radiochemical purity and specific activity of approximately 400 GBq/μmol at the end of the synthesis in 10 mL sterile isotonic, buffered at physiological pH solution. The radiolabeling was performed in a lead shielded cell using a computer-assisted homemade automatic apparatus controlled by LabVIEW software (National Instruments) via Modulink and RS232 interfaces.

Radiotracer Experiments

Experiments were performed in animals using the β-scintillator and in humans using PET. All animal experiments were approved by the local veterinary authorities and were performed in accordance with their guidelines. The experiments were performed by licensed investigators. The animals were kept in cages in a ventilated cabinet with standardized conditions of light (night/day cycle 12/12 h) and temperature and free access to food and water. Before the experiment the animals were fasted overnight. A total of 29 Sprague–Dawley rats (5 for the EF determination, 24 for the different experimental paradigms (for details see below)) weighing $310 \pm 41\,g$ (mean $\pm$ s.d.) were included in the study.

The human study population was composed of 6 healthy male volunteers aged between 24 and 36 years without any known neurological impairments. All subjects were studied at the University Hospital Zurich. Informed written consent was obtained from all subjects before the beginning of the experiment. The protocol was approved by the Local Ethics Committee.

Magnetic resonance scanning was performed on each subject (Twin Speed; GE Medical Systems, Milwaukee, WI, USA) to rule out any cerebral pathologies and for anatomical coregistration of the PET scan.

Animal Preparation

Surgery was performed under isoflurane anesthesia and involved the placement of an arteriovenous shunt from the right femoral artery to the right femoral vein, tracheotomy for mechanical ventilation, and exposition of the skull with subsequent thinning of the bone above the primary somatosensory cortex using a dental drill. The actual experiment was then performed under urethane anesthesia (1400 mg/kg, i.p.). The arteriovenous shunt was used for the injection of the tracer, collection of blood samples for metabolite analysis, the monitoring of arterial blood pressure, and the continuous measurement of total arterial ^{11}C activity. For the latter purpose, the shunt was run through a coincidence counter (GE Medical Systems) that stored the whole blood radioactivity concentration at

1-sec intervals. The online arterial sampling procedure is described in detail elsewhere (Weber *et al*, 2002).

β-Scintillator

The β-scintillator (Swisstrace, Zurich, Switzerland) has been described in detail earlier (Weber *et al*, 2003; Wyss *et al*, 2007). In short, it consists of a scintillation tip (Bicron, BF12, Newbury, OH, USA) with a length of 1 mm and a diameter of 0.25 mm attached to a high numerical aperture glass fiber. The scintillator was made light tight by applying a uniform coating of silver particles. The scintillations were measured using a photomultiplier tube and counting electronics (Perkin Elmer, MA, USA). The limited range of β-particles within biological tissues leads to a limited detection volume centered around the scintillating tip of the probe. Monte Carlo simulations demonstrated that for C-11 the distance required to detect 90% of the β-particles around the probe is 2.0 mm (Pain *et al*, 2002). The sensitivity of the used β-scintillator was in the range of 0.036 to 0.047 cps/kBq/cc.

The scintillator was inserted into the cortex using a stereotactic frame (David Kopf Instruments, Tujunga, CA, USA). At the insertion point, which was approximately (according to Bregma) 1 mm posterior and 5 mm lateral, the thinned bone was removed and the dura was carefully incised. The scintillator tip was decreased 1.4 mm below the dura. In the stimulation experiments, the correct position was verified by Laser Doppler flowmetry (Periflux System 5000; Perimed AB, Järfälla, Sweden). This position was adjusted to avoid large superficial blood vessels. Only one scintillator penetration was performed per animal. The count rate was stored on a personal computer using a bin width of 1 sec yielding tissue time–activity curves.

Positron Emission Tomography

All subjects were scanned on a whole-body PET/computer tomography-scanner (Discovery ST-RX; GE Medical Systems, Waukesha, WI, USA). This is a scanner with an axial field of view of 14.6 cm and a reconstructed in-plane resolution of approximately 7 mm. Before the positioning of the subjects in the scanner, a radial artery was cannulated for timed arterial blood sampling. An additional catheter for administration of the radiotracers was placed in the contralateral antecubital vein. At the beginning of each study, a low-dose computer tomogram for attenuation correction was performed.

Experimental Protocols

Cerebral blood flow measurements using $H_2{}^{15}O$: First Pass Extraction Fraction: The first pass EF of 1-^{11}C-acetate at baseline was determined according to the relationship $EF = K_1/CBF$, where K_1 is the transport parameter of the one-tissue compartment model and CBF is cerebral blood flow. Cerebral blood flow was determined in five animals using ^{15}O-labeled water injected before measurement of 1-^{11}C-acetate kinetics. In the human study CBF was measured in all subjects 10 mins before the 1-^{11}C-acetate injections. The visual stimulation was interrupted between CBF and acetate measurements. Approximately 300 MBq $H_2{}^{15}O$ was injected intravenously using an automatic injection device. After the arrival of the bolus in the brain, the acquisition of a series of 18 frames (10 secs each frame) was started.

Measurements of 1-^{11}C-Acetate Kinetics During Different Conditions

In the animal experiments, two injections spaced 30 mins apart were administered. Data were acquired for 20 mins after the injection (slow injection over a period of 30 secs) of 230 to 260 MBq (diluted in 0.5 mL) of radiotracer. This part of the study included 24 animals, which were distributed among the following experimental subgroups: (1) in this group the baseline was followed by electrostimulation (bas–stim); (2) the order was reversed (stim–bas). Groups (1) and (2) were examined with respect to a potential order effect. (3) To evaluate the reproducibility two consecutive baseline measurements were performed (bas–bas). (4) In four animals the effect of acetazolamide (Diamox, 66 mg/kg), a carbonic anhydrase inhibitor increasing CBF but not oxygen consumption ($CMRO_2$; Okazawa *et al*, 2001), on the kinetics of 1-^{11}C-acetate was examined. After 20 mins of baseline acquisition, acetazolamide was intravenously injected over 1 min. Ten minutes later the same amount of 1-^{11}C-acetate was injected for the second time. In a last group (5) the effect of dichloroacetate was investigated. Four hours after the injection of dichloroacetate (50 mg/kg, Sigma-Aldrich Product No. 347795, Buchs, Switzerland) a baseline study was followed by electrostimulation (dichloroacetate challenge). Dichloroacetate was dissolved in physiological saline and was adjusted to pH 7.4.

To activate the whisker-to-barrel pathway the infraorbital branch of the trigeminal nerve was electrically stimulated with two stainless steel electrodes. The cathode was inserted through the infraorbital hiatus and the anode was positioned in the masticatory muscle on the ipsilateral side. The current was adjusted to 2 mA, and 2 Hz stimulation frequency was chosen because previous measurements using ^{18}F-fluorodeoxyglucose-autoradiographies demonstrated this frequency to be optimal eliciting a maximal increase in glucose consumption of 70% to 80% (unpublished data). The stimulation started 30 secs before the tracer injections. To check the effectivity of the applied stimulation and the effect of acetazolamide in group (4) animals, a Laser Doppler flowmetry probe was fixed just above the primary somatosensory cortex to follow regional CBF changes.

In humans, PET was performed under baseline conditions with eyes closed and during visual stimulation using different video clips presented on a screen (Charlie's Angels and Rolling Stones). In three subjects the baseline examinations preceded the stimulation studies and in the other three subjects the order was reversed to rule out any order effect. The visual stimulation was started 20 secs before scan start and continued during complete PET

acquisition. After the intravenous injection of 250 MBq 1-^{11}C-acetate, administered as a slow bolus over approximately 60 s, data were recorded for 20 mins (25 frames: 6×20, 3×40, and 16×60 secs).

Time–activity curves were derived from volumes of interest defined on three consecutive slices on the anatomical magnetic resonance scans and subsequently transferred to the PET data. Volumes of interest were drawn in the visual cortex as the target region and in the frontal cortex and cerebellum as references.

Statistics

The Wilcoxon signed rank test for dependent samples was used to evaluate differences between within-subject conditions and the Mann–Whitney *U*-test was used for group differences. The criterion for significance was set at $P < 0.05$. Values are expressed as mean ± s.d.

Data Acquisition and Analysis

The details are described in the appendix.

Results

Animal Studies

Metabolites of 1-^{11}C-acetate in the blood: High-pressure liquid chromatography identified ^{11}C-CO_2 as the only metabolite in blood. The time course of the fraction of authentic ^{11}C-acetate in arterial plasma is demonstrated in Figure 1. The pH and arterial blood gases were all in the physiological range (pH = 7.35 to 7.45; $pCO_2 = 35$ to 45 mm Hg; $pO_2 = 70$ to 100 mm Hg). Plasma lactate levels were also determined as lactate competes with acetate for the uptake into brain. They ranged between 1.4 and 2.1 mmol/L. However, no relationship between plasma lactate levels and changes in the kinetics of 1-^{11}C-acetate could be found. Only in group 5 (dichloroacetate challenge) there was a statistically significant difference in plasma levels between the two different modalities (see below).

First pass extraction fraction: CBF was measured in 5 baseline experiments and was 56 ± 16 mL/min/100 *g*. The first pass EF of 1-^{11}C-acetate calculated in these experiments was 18% ± 5%.

Reproducibility of the 1-^{11}C-acetate measurements: The reproducibility of the time–activity curves and of the parameters K_1 and k_2 is demonstrated in the top graphs of Figures 2 and 3. In contrast to trigeminal nerve stimulation, the tissue time–activity curves in the two sequential baseline experiments look identical. The difference of the mean K_1 ($K_{1\,\text{experiment}\,2} - K_{1\,\text{experiment}\,1}$) was −0.001, and for k_2 the difference was 0.002 per minute.

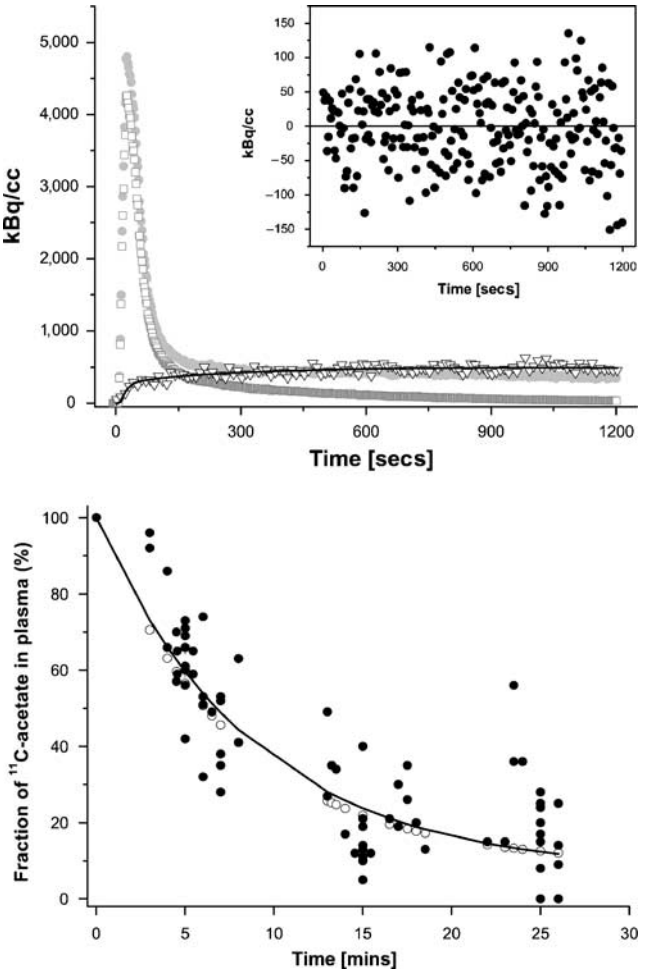

Figure 1 In the upper panel the time course of ^{11}C radioactivity in whole blood (●), plasma (□), and brain tissue (▼) acquired over 20 mins is shown. In addition the model fit is demonstrated (straight line, $K_1 = 0.085$ mL/min/mL tissue, $k_2 = 0.015$ per minute). The goodness-of-fit is demonstrated by the random distribution of the residuals, demonstrated in the insert. In the lower panel the fraction f of true 1-^{11}C-acetate in plasma in animal and human studies is plotted. The filled circles represent data points from animal studies (anesthetized rats) and the solid line is the corresponding fit of the function $f = 100\text{-}\alpha(1-\exp(-\mu t))$. Least squares fitting yielded $\alpha = 93\%$ and $\mu = 0.11$ per minute. In the human study (open circles; conscious humans), α and μ were taken from previous experiments which had yielded very similar values ($\alpha = 91\%$, $\mu = 0.13$ per minute) (Buck *et al*, 1991).

1-^{11}C-Acetate kinetics during infraorbital nerve stimulation: The electrical infraorbital nerve stimulation increased the washout of 1-^{11}C-acetate as shown in the middle graph of Figure 2. The order of the experiments (baseline–stimulation or stimulation–baseline) had no significant effect on the changes of the kinetic parameters (Figures 3C and 3D). Therefore the two groups (1) and (2) (bas–stim and stim–bas) were pooled. During stimulation, k_2 increased by 93% from 0.014 ± 0.007 to 0.027 ± 0.006 per minute ($P < 0.01$) in the primary somatosensory cortex. In parallel, K_1 increased from

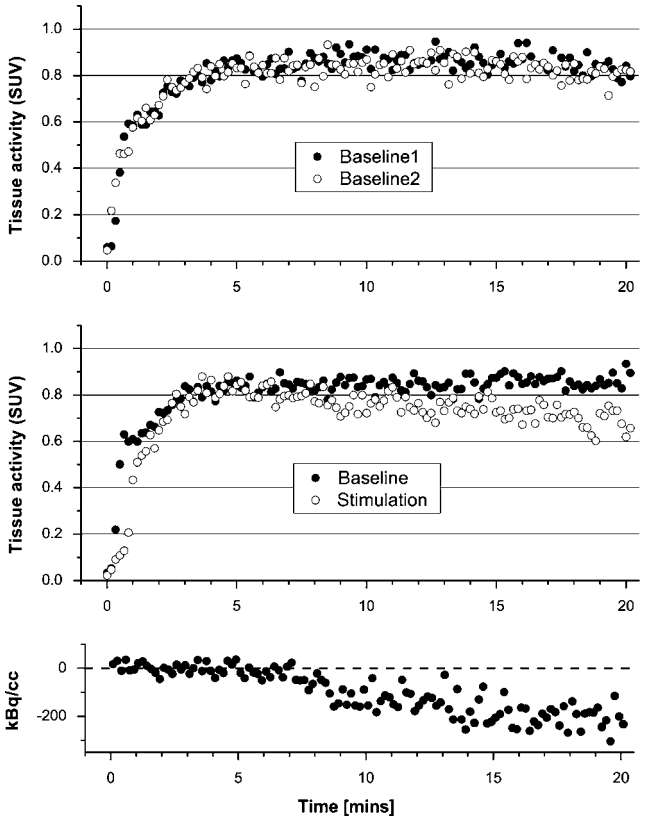

Figure 2 The top and middle graph demonstrate time–activity curves of ^{11}C activity in rat brain tissue normalized to injected activity per g bodyweight yielding standardized uptake values (SUV). The curves represent mean data from five experiments. In the baseline–baseline experiments (top panel) the curves appear identical. In contrast, the washout of ^{11}C activity is remarkably larger during stimulation (middle panel). The bottom panel illustrates the residuals between fit and data if only the first 5 mins of data are fitted. Such a short fit yields substantially lower initial washout rates than a 20 mins fit, demonstrating that the onset of the washout of radiolabel from tissue is delayed.

0.080 ± 0.015 at baseline to 0.095 ± 0.017 ($P < 0.01$). The efficacy of the stimulation was confirmed by the increase of the laser Doppler flowmetry signal by 20 to 25% (data not shown).

To check for a delayed onset of the radioactivity washout, the first 5 mins of data were refitted with only k_2 as a free parameter. In this dataset, k_2 decreased from 0.014 ± 0.007 to 0.001 ± 0.002 in the baseline experiments and from 0.027 ± 0.006 to 0.003 ± 0.004 in the stimulation experiments. An example of a 5 mins fit is illustrated at the bottom of Figure 2. The low k_2 of 0.001 fits the initial data well, then the washout is clearly increased.

Effect of acetazolamide on k_2: In the 4 experiments k_2 was 0.016 ± 0.002 at baseline and 0.016 ± 0.002 per minute 10 mins after acetazolamide injection. Laser Doppler flowmetry showed a signal increase of $61.1\% \pm 8.1\%$.

Effect of dichloroacetate on k_2 during baseline and stimulation: Dichloroacetate pretreatment decreased arterial plasma lactate from 1.5 ± 0.1 to 1.25 ± 0.2 mmol/L (mean ± s.d.; $P < 0.05$) but exerted no change of arterial blood gases which stayed in the physiological range. Four hours after intravenous dichloroacetate administration, k_2 was less at baseline and during stimulation, compared with the experiments without dichloroacetate. At baseline the values were on average 36% less (0.009 ± 0.002 compared with 0.014 ± 0.007), however, this difference failed to reach significance ($n = 5$; $P = 0.15$). During stimulation k_2 was 26% less ($n = 5$; $P < 0.05$) than that in the experiments without administration of dichloroacetate (0.020 ± 0.004 compared with 0.027 ± 0.006). There was still a significant 122% increase of k_2 from baseline to electrostimulation (from 0.009 ± 0.002 to 0.020 ± 0.004; $n = 5$; $P < 0.05$; Figure 3E).

Relationship of the tissue activity and changes of the washout rate k_2: This relationship is a measure of the parameter identifiability. A larger change of the tissue activity with a unit change of k_2 is associated with a better parameter identifiability. The sensitivity analysis demonstrated that at 20 mins, a 10% change in k_2 led to a 2.1% change in tissue activity at baseline ($k_2 = 0.014$ per minute) and to a 3.8% change during stimulation ($k_2 = 0.027$ per minute). Furthermore, the activity change in tissue was linear in the investigated range 0 to 30% k_2 change.

Human Studies

1-^{11}C-Acetate kinetics present the same characteristics as in animal studies: In all subjects the blood gas parameters were always in the physiological range (pH = 7.35 to 7.45; $pCO_2 = 35$ to 45 mm Hg; $pO_2 = 70$ to 100 mm Hg). An illustration of the effect of the visual activation on the kinetic of 1-^{11}C-acetate is demonstrated in Figure 4 and the quantitative values are shown in Figure 5. The calculated EF of 1-^{11}C-acetate in visual cortex was $19 \pm 4\%$ at baseline and $13 \pm 3\%$ during stimulation. The visual stimulation increased mean CBF in visual cortex by 64% ($P < 0.05$). In the control regions, 'cerebellum' and 'frontal cortex,' no significant change of the CBF was noticed. In visual cortex mean K_1 and k_2 values of 1-^{11}C-acetate were 11% and 62% ($P < 0.05$ for both) higher during stimulation as shown in Figures 5F and 5I. No significant changes of K_1 or k_2 were noted in frontal cortex and cerebellum. However, in frontal cortex K_1 and k_2 data are somewhat distorted by a single subject, which showed a decrease of the values in this region in response to visual stimulation.

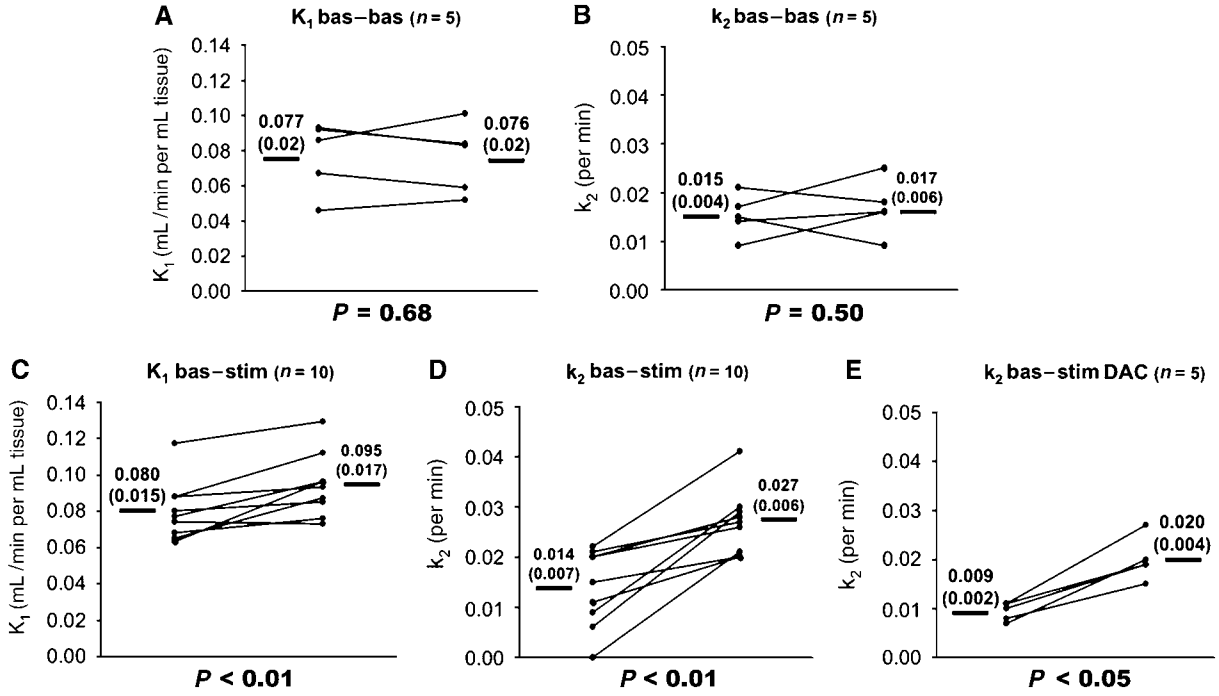

Figure 3 Summary of animal data. Panels (**A** and **B**) demonstrate the reproducibility of parameters K_1 and k_2. There was no significant change of K_1 and k_2 between sequential baseline experiments. Panels (**C** and **D**) show the increase of K_1 and k_2 during infraorbital nerve stimulation. The values of k_2 after the administration of dichloroacetate (DAC, 50 mg/kg) at baseline and during infraorbital nerve stimulation are demonstrated in panel (**E**). The *P*-values were calculated using the Wilcoxon signed rank test. Values are given as mean ± s.d.

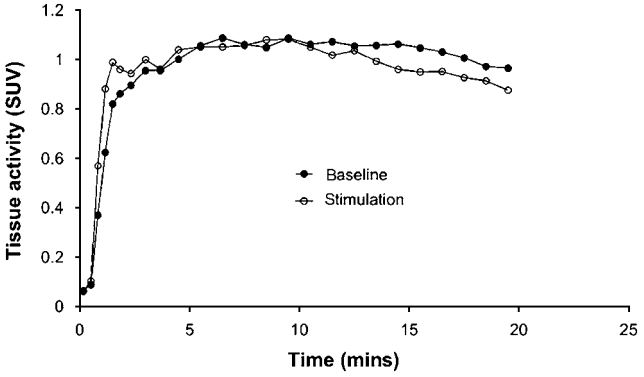

Figure 4 Time–activity curves of 1-^{11}C-acetate uptake in the human visual cortex normalized to injected activity per kg bodyweight yielding standardized uptake values (SUV). The curves represent mean data from all six human experiments. During visual stimulation the clearance of ^{11}C activity is larger compared with baseline. Note also the modestly faster wash-in of radioactivity during stimulation.

Discussion

It was previously suggested that the astrocyte-specific substrate acetate allows to measure metabolism in human brains *in vivo* (Hosoi *et al*, 2004; Muir *et al*, 1986). However, to our knowledge this is the first study using label clearance from brain after 1-^{11}C-acetate administration for the investigation of astrocytic oxidative metabolism *in vivo*. Labeled acetate was already used in various studies to illuminate certain aspects of astrocytic metabolism. Some groups used autoradiographical determination of ^{14}C-acetate uptake (Cruz *et al*, 2005; Muir *et al*, 1986), other groups measured the metabolic fate of acetate by measuring the appearance of labeled compounds as the label traveled through the TCA cycle (e.g., Badar-Goffer *et al*, 1990; Berl and Frigyesi, 1969; Lebon *et al*, 2002; Van den Berg and Ronda, 1976).

Our study demonstrates for the first time the changes of 1-^{11}C-acetate kinetics during stimulation *in vivo*, which are thought to be correlated with the changes of astrocytic oxidative metabolism. Although total cerebral $CMRO_2$ can be successfully measured *in vivo* using PET and inhaled $^{15}O_2$ (Mintun *et al*, 1984; Yee *et al*, 2006), a direct *in vivo* measurement of $CMRO_2$ in astrocytes alone is not available.

K_1 and Extraction Fraction

Compared with the heart where 1-^{11}C-acetate is almost 100% extracted, the cerebral EF is approximately 5-fold less. Nevertheless, brain uptake is large enough to allow quantification. One consequence of the lower EF is the blunted increase of K_1 compared with CBF during stimulation. In the

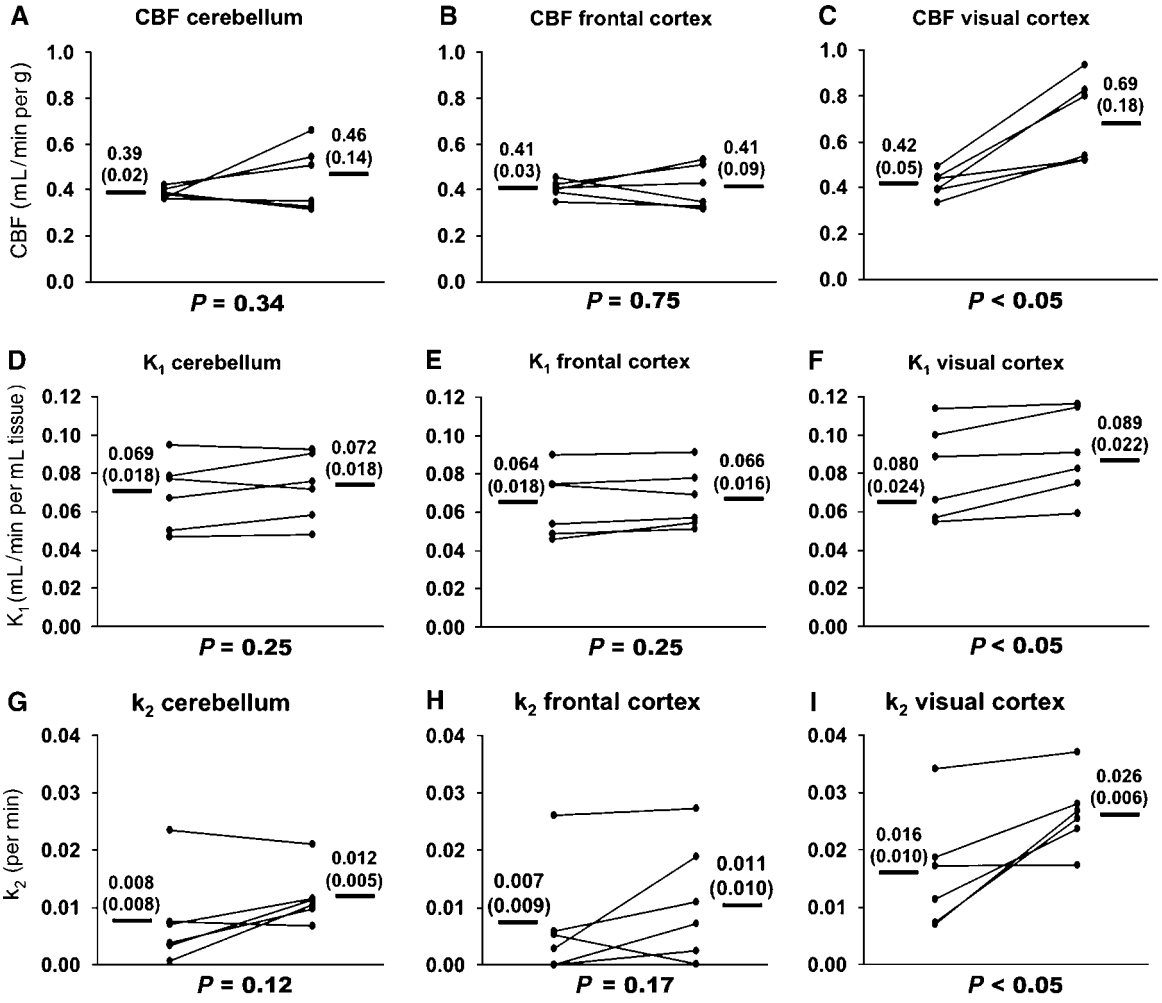

Figure 5 Summary of human data. The change of CBF from baseline to visual stimulation in the three examined brain areas is demonstrated in the top panels (**A–C**), the one of K_1 and k_2 of 1-^{11}C-acetate in the middle (**D–F**) and bottom panels (**G–I**), respectively. The *P*-values were calculated using Wilcoxon signed rank test. Values are given as mean ± s.d.

human study K_1 increased 11% compared with a 64% increase in CBF (visual cortex).

Quantitative Relationship Between k_2 and Astrocytic $CMRO_2$

In the following discussion about the meaning of the rate constant k_2 we provide arguments that k_2 may be strongly related to $CMRO_2$. However, it is clear that a direct proof is not given and would be difficult to establish, as there is actually no data available to prove this conclusion directly. One major reason is that a direct measurement of astrocytic $CMRO_2$ is yet impossible *in vivo*.

We hypothesize that k_2 is directly related to $CMRO_2$ in the astrocytes as has been demonstrated in the heart for the myocytes (Buck *et al*, 1991). Prerequisites for this hypothesis are (1) the washout of radioactivity from the volume of interest is indeed because of the loss of $^{11}C\text{-}CO_2$ and (2) the rate-limiting step determining k_2 is the production of $^{11}C\text{-}CO_2$ and not its removal.

Prerequisite (1): There seems to be no doubt that at least part of the radioactivity loss is because of $^{11}C\text{-}CO_2$, because the production of labeled CO_2 from exogenous 1-^{14}C-acetate has been proven in astrocyte cultures (Waniewski and Martin, 1998). However, a quantitative proof of prerequisite (1) would be difficult. One theoretical possibility would be the measurement of the arterio-venous difference of $^{11}C\text{-}CO_2$. However, a first order estimation of this difference demonstrates that it would be in the order of 4% of the total blood counts. The conclusive demonstration of such a small difference would require a prohibitively large amount of animals.

Prerequisite (2): It is well known that CO_2 diffuses practically freely across the blood–brain barrier (Paulson, 2002). It could therefore theoretically be possible that the removal of CO_2 by the blood is a

limiting factor for the washout of CO_2. However, the lack of a change of k_2 after the acetazolamide-induced blood flow increases demonstrates that the removal of the radioactivity from the volume of interest is not a limiting factor.

Other arguments which point at a strong relationship between k_2 and astrocytic $CMRO_2$ are (1) the increase of k_2 during stimulation, (2) the delay of the onset of the label washout and the decrease of the K_1/k_2 ratio during stimulation, (3) the behavior of k_2 under dichloroacetate, and (4) reasonable values of astrocytic $CMRO_2$ can be obtained by applying the calibration established in the dog heart.

Changes of k_2 During Increased Brain Activity

Parameter k_2 significantly increased during stimulation. In the animal study, k_2 almost doubled from baseline to infraorbital nerve stimulation, indicating a substantial increase in oxygen consumption. In the human study, the increase in the visual cortex was 63%. Although not significant, there also seemed to be a trend toward higher values in cerebellum and frontal cortex. In fact, omitting the subject with a decreased value during stimulation, the increase became significant, not surprising considering the connectivity in the brain.

Delay of the Washout Onset and the Decrease of the K_1/k_2 Ratio During Stimulation

Another result pointing at ^{11}C-CO_2 as the washout agent is the delay of the washout onset (bottom graph of Figure 2). Such a delay for the appearance of labeled CO_2 was demonstrated by Waniewski and Martin (1998) in cultured astrocytes and is explained by the fact that labeled CO_2 is only produced in the second turn of the label in the TCA cycle. If the loss of label was substantially because backdiffusion of labeled acetate, one would not expect a delay. Furthermore, if backdiffusion of labeled acetate was the main factor determining k_2, one would expect the same effect of stimulation on K_1 and k_2, that is, the ratio K_1/k_2 would remain constant. However, the data demonstrate a markedly lower ratio during stimulation. In the anesthetized rat studies, the mean ratio dropped 44% ($P=0.08$), in the studies with dichloroacetate the decrease was 53% ($P=0.001$) and in the human visual cortex the ratio dropped 44% ($P=0.048$). This behavior suggests that the labeled compounds entering and leaving the brain tissue are different. The mentioned points are all consistent with the hypothesis that the washed out compound is indeed ^{11}C-CO_2. However, we cannot completely exclude that some label loss is because of release of other labeled substrates, particularly because of efflux of glutamine, which is quickly labeled after injection of radiolabeled acetate (Cremer, 1970). Despite the fact that the blood–brain barrier is closed for the passage of glutamate and glutamine from blood to brain, the reverse direction seems possible. Glutamine is taken up by endothelial cells and intracellularly converted by the enzyme glutaminase to glutamate. When the glutamate concentration within endothelial exceeds the one in plasma net transport of glutamate takes place through facilitative transporters (Hawkins *et al*, 2006). The high number of steps involved in this process and the fact that normal plasma concentration of glutamate is approximately 10 times higher than glutamate concentration in the extracellular fluid of the brain (Hawkins *et al*, 2006) indicate that this process is slow and probably not of relevance during our acquisition period of 20 mins.

Pharmacological Interventions Using Dichloroacetate and Acetazolamide

The dichloroacetate experiments are also consistent with the hypothesis that k_2 is related to $CMRO_2$. This compound activates pyruvate dehydrogenase (Abemayor *et al*, 1984) by inhibiting its phosphorylation by the PDH kinase (Whitehouse *et al*, 1974). As a consequence more pyruvate is converted to acetyl-CoA and less to lactate and the concentration of acetyl-CoA is expected to increase. If the rate constants in the following chain of acetyl-CoA oxidation, which are expected to be related to k_2, remained the same, the rate of the acetyl-CoA metabolism would increase and with it most likely $CMRO_2$. However, as the energetic demand is unchanged there is no reason why $CMRO_2$ should increase. Consequently one would expect a decrease in k_2 and this is exactly what was observed, at baseline as well as during stimulation. A good candidate for regulation at this stage is citrate synthase, which condenses acetyl-CoA and oxaloacetate into citrate. It has been documented that this enzyme is inhibited by increased concentrations of acetyl-CoA (Bayer *et al*, 1981). This inhibition could be a major reason for the observed decrease of k_2 after dichloroacetate. Furthermore, the suggested increase of the cold acetyl-CoA concentration under dichloroacetate is itself indirect evidence for the ability of astrocytes to completely oxidize glucose, as is the work by Lovatt *et al* (2007), which confirmed significantly higher relative expression of almost all TCA-cycle enzymes in freshly isolated astrocytes than neurons and showed that the oxidative pathways were active in astrocytes.

Analogy with Previous Heart Studies

The idea to use the washout rate k_2 of 1-^{11}C-acetate as a marker of $CMRO_2$ was inspired by earlier studies performed in the heart (Armbrecht *et al*, 1990; Buck *et al*, 1991; Lindner *et al*, 2006). In those studies it was clearly established that k_2 reflects myocardial oxygen consumption in a linear fashion. One rough indication that this approach may also be

valid in the brain is derived from the following estimation. In the dog heart, the relationship between $CMRO_2$ and k_2 was $CMRO_2$ (mL/min/100 g) = 48.8 mL/100 g $\times$ k_2, (per minute). Application of this relationship to this study yields an astrocytic $CMRO_2$ of 0.7 mL/min per 100 g in rats and humans at baseline. This amounts to approximately 20% of whole brain oxygen consumption (3.4 ± 0.28 mL/min per 100 g in humans (Kety and Schmidt, 1948)). This value compares favorably to the published values for the fraction of astrocytic ATP generation by oxidative processes (Hertz and Kala, 2007; Hertz *et al*, 2007; Oz *et al*, 2004) which are in the range of 14% to 30%.

Is k_2 Specific for Astrocytic Metabolism?

One important observation in this regard is that labeled acetate is taken up only by astrocytes and not neurons (Waniewski and Martin, 1998). However, a fraction of the label will eventually end up in neurons as labeled glutamine/glutamate (via the glutamate/glutamine cycle), which was produced via the α-ketoglutarate-glutamate step in the astrocytes. Nevertheless, the transfer of labeled glutamine to neurons is slow relative to the 20 mins acquisition time of this study. Lebon *et al* (2002) investigated astrocytic energy metabolism using nuclear magnetic resonance spectroscopy and 2-^{13}C-acetate in humans. They concluded that the labeled glutamine/glutamate observed during the first 20 mins after the start of the 2-^{13}C-acetate infusion reflected astrocytic glutamate only. It therefore seems reasonable to assume that most of the ^{11}C activity measured in our study was originating from astrocytes. Even if a small fraction of labeled glutamine/glutamate had reached the neurons, the contribution of neuronal ^{11}C-CO_2 production could be expected to have been small. Hertz *et al* (1988) demonstrated in cell cultures, that glutamate oxidation of neurons was at most 25% of the one in astrocytes. In addition, a recent work found a 4.3-fold higher expression of the enzyme glutamate dehydrogenase Glud1 in astrocytes, also suggesting a substantially higher capacity for astrocytes to metabolize glutamate (Lovatt *et al*, 2007).

Comparison of the k_2 Method with Autoradiography

Cruz *et al* (2005) investigated the accumulation of 2-^{14}C-acetate during acoustic stimulation in rats using autoradiography performed 5 mins after tracer injection. They reported a 15 to 18% increase of 2-^{14}C-acetate uptake in the stimulated compared with the contralateral structures. These results are in line with our experiments. At 5 mins, the uptake of 1-^{11}C-acetate was 14% higher in the stimulation compared with the baseline experiments (Supplementary Figure S1). This value was calculated by simulating tissue time–activity curves with a mean input curve and the mean K_1 and k_2 values of the stimulation and baseline experiments. Here, it is crucial to point to an important difference in the methodology. By evaluating just one time point as in autoradiographic studies, it is not easy to determine to what degree the differential uptake is influenced by increased blood flow, although this influence seems to be low for acetate (Dienel *et al*, 2007), but probably not negligible as our demonstration of a small K_1 increase during stimulation suggests. To separate delivery and washout, a kinetic approach as chosen in this study seems advantageous. However, autoradiographic studies deliver images and, when using the long-lived ^{14}C, allow an easier determination of metabolites.

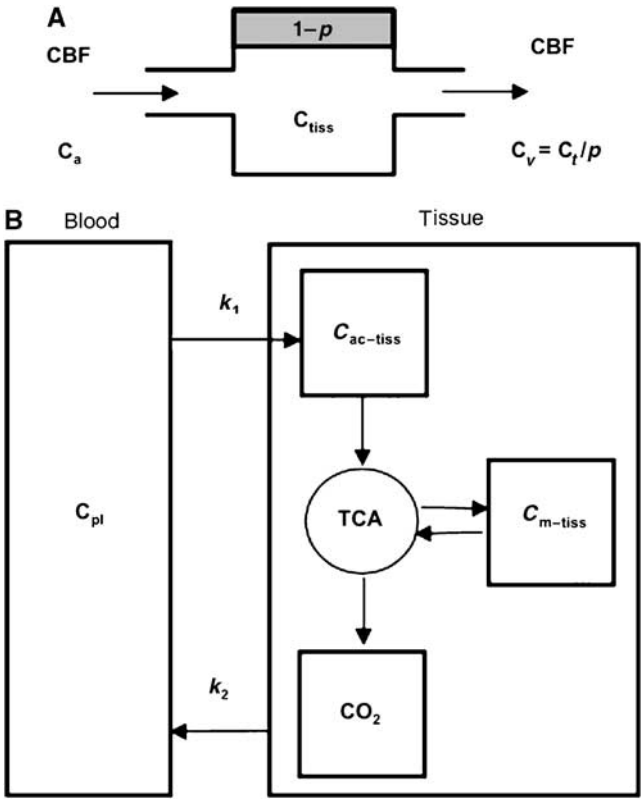

Figure 6 One-tissue compartment models used in animal and human studies to analyze CBF using $H_2{}^{15}O$ (**A**) and the kinetics of 1-^{11}C-acetate respectively (**B**). K_1 describes the transfer of acetate from blood to tissue whereas k_2 corresponds to the flux of radiolabel from tissue to blood. Labeled acetate in tissue ($C_{ac-tiss}$) is converted to acetyl-CoA, catalyzed by acetyl-CoA synthetase. Acetyl-CoA then enters the TCA cycle, where the label can either be transferred to CO_2 or metabolites (C_{m-tiss}) such as glutamine and glutamate which were produced via α-keto-glutarate. Some labeled metabolites will reenter the TCA cycle at the α-keto-glutarate level and in this way yield more labeled CO_2. In theory, k_2 denotes the backdiffusion of all labeled species from tissue. However, as discussed in the main text, we argue that the loss of label is mainly because of backdiffusion of ^{11}C-CO_2, and that the rate of this label loss, described by k_2, is reflecting the production of CO_2 and is therefore closely related to oxidative metabolism.

Using the short-lived isotope ^{11}C we simply concentrated on two aspects of the label kinetics, delivery, and washout. We cannot deliver any data concerning the fate of the label between these steps, which may be very complex. An indication of this complexity is demonstrated in the model of Figure 6. Previous work by Berl and Frigyesi (1969) demonstrated (1) that 5 mins after injection of 1-^{14}C-acetate most label is found in amino acids and (2) that there is a decline of their concentration afterwards. This may indicate that most acetate oxidation happens indirect via amino acids. More extended information on the fate of the label are found elsewhere (Dienel *et al*, 2007; Berl and Frigyesi, 1969). Nevertheless, still more studies are needed to identify the contribution of acetate and TCA cycle metabolites as direct substrates for oxidative metabolism.

General Remarks

Because of the delay of the onset of the label washout, k_2 is smaller during the first few minutes after injection. This effect was not taken into account in the tracer kinetic modeling, for example, k_2 was assumed constant. To estimate the resulting error we calculated simulated tissue time–activity curves with $k_2 = 0$ (during the first 5 mins) and 0.027 per minute thereafter. The refit of these curves using a constant k_2 demonstrated only a 1.5% change of k_2.

Another point concerns parameter identifiability. The sensitivity analysis demonstrated that the dependence of tissue activity on k_2 is more pronounced at the higher values, implying that the k_2 values during baseline are less reliable than during stimulation. This aspect and the fact that k_2 at baseline is relatively small may lead to a relatively large error margin in the ratio $k_{2\,simulation}/k_{2\,baseline}$. We also did not consider the effect of blood-borne ^{11}C-CO_2 on K_1 and k_2. Most of the CO_2 in blood is converted to HCO_3^-, which does not cross the blood–brain barrier. Approximately 5% of total HCO_3^-/CO_2 is present as dissolved ^{11}C-CO_2 (Brooks *et al*, 1984) which freely penetrates the brain. We constructed simulated tissue time–activity curves using the one-tissue compartment model and the blood-borne ^{11}C-CO_2 as a second input curve. K_1 and k_2 values for this fraction of CO_2 were taken from Brooks *et al* (1984). These tissue time–activity curves were then refitted using the standard one-tissue compartment model not considering blood borne ^{11}C-CO_2. The deviation of the K_1 and k_2 values was less than 1.5%, demonstrating that the effect of blood-borne ^{11}C-CO_2 on K_1 and k_2 is negligible.

Summary

1-^{11}C-acetate seems a promising tracer to investigate astrocytic oxidative metabolism in animals and humans. If the washout rate indeed represents the production of ^{11}C-CO_2, then its increase during stimulation would point to a substantially higher astrocytic oxidative metabolism during brain activation. However, the quantitative relationship between k_2 and $CMRO_2$ needs to be determined in future experiments.

Acknowledgements

The authors acknowledge the important laboratory and editorial help by Prateep Beed and John Mc Clacken, respectively, and thank Tibor Cservenyàk and Konstantin Drandarov for radiosynthesis of the tracer. The authors also thank Rolf Grütter for valuable discussions.

References

Abemayor E, Kovachich GB, Haugaard N (1984) Effects of dichloroacetate on brain pyruvate dehydrogenase. *J Neurochem* 42:38–42

Alpert NM, Eriksson L, Chang JY, Bergstrom M, Litton JE, Correia JA, Bohm C, Ackerman RH, Taveras JM (1984) Strategy for the measurement of regional cerebral blood flow using short-lived tracers and emission tomography. *J Cereb Blood Flow Metab* 4:28–34

Armbrecht JJ, Buxton DB, Schelbert HR (1990) Validation of [1-^{11}C]acetate as a tracer for noninvasive assessment of oxidative metabolism with positron emission tomography in normal, ischemic, postischemic, and hyperemic canine myocardium. *Circulation* 81:1594–605

Badar-Goffer RS, Bachelard HS, Morris PG (1990) Cerebral metabolism of acetate and glucose studied by ^{13}C-n.m.r. spectroscopy. A technique for investigating metabolic compartmentation in the brain. *Biochem J* 266:133–9

Bayer E, Bauer B, Eggerer H (1981) Evidence from inhibitor studies for conformational changes of citrate synthase. *Eur J Biochem* 120:155–60

Berl S, Frigyesi TL (1969) The turnover of glutamate, glutamine, aspartate and GABA labeled with [1-^{14}C]acetate in caudate nucleus, thalamus and motor cortex (cat). *Brain Res* 12:444–55

Brooks DJ, Lammertsma AA, Beaney RP, Leenders KL, Buckingham PD, Marshall J, Jones T (1984) Measurement of regional cerebral Ph in human-subjects using continuous inhalation of (Co2)-C-11 and positron emission tomography. *J Cereb Blood Flow Metab* 4:458–65

Buck A, Wolpers HG, Hutchins GD, Savas V, Mangner TJ, Nguyen N, Schwaiger M (1991) Effect of carbon-11-acetate recirculation on estimates of myocardial oxygen consumption by PET. *J Nucl Med* 32:1950–7

Cremer JE (1970) Selective inhibition of glucose oxidation by triethyltin in rat brain *in vivo*. *Biochem J* 119:95–102

Cruz NF, Lasater A, Zielke HR, Dienel GA (2005) Activation of astrocytes in brain of conscious rats during acoustic stimulation: acetate utilization in working brain. *J Neurochem* 92:934–47

Dienel GA, Schmidt KC, Cruz NF (2007) Astrocyte activation *in vivo* during graded photic stimulation. *J Neurochem* 103:1506–22

Hassel B, Paulsen RE, Johnsen A, Fonnum F (1992) Selective inhibition of glial cell metabolism *in vivo* by fluorocitrate. *Brain Res* 576:120–4

Hawkins RA, O'Kane RL, Simpson IA, Vina JR (2006) Structure of the blood-brain barrier and its role in the transport of amino acids. *J Nutr* 136: 218S–226S

Hertz L, Drejer J, Schousboe A (1988) Energy metabolism in glutamatergic neurons, GABAergic neurons and astrocytes in primary cultures. *Neurochem Res* 13:605–10

Hertz L, Kala G (2007) Energy metabolism in brain cells: effects of elevated ammonia concentrations. *Metab Brain Dis* 22:199–218

Hertz L, Peng L, Dienel GA (2007) Energy metabolism in astrocytes: high rate of oxidative metabolism and spatiotemporal dependence on glycolysis/glycogenolysis. *J Cereb Blood Flow Metab* 27:219–49

Hosoi R, Okada M, Hatazawa J, Gee A, Inoue O (2004) Effect of astrocytic energy metabolism depressant on ^{14}C-acetate uptake in intact rat brain. *J Cereb Blood Flow Metab* 24:188–90

Hyder F, Patel AB, Gjedde A, Rothman DL, Behar KL, Shulman RG (2006) Neuronal-glial glucose oxidation and glutamatergic-GABAergic function. *J Cereb Blood Flow Metab* 26:865–77

Kety SS, Schmidt CF (1948) The nitrous oxide method for the quantitative determination of cerebral blood flow in man—theory, procedure and normal values. *J Clin Invest* 27:476–83

Lebon V, Petersen KF, Cline GW, Shen J, Mason GF, Dufour S, Behar KL, Shulman GI, Rothman DL (2002) Astroglial contribution to brain energy metabolism in humans revealed by ^{13}C nuclear magnetic resonance spectroscopy: elucidation of the dominant pathway for neurotransmitter glutamate repletion and measurement of astrocytic oxidative metabolism. *J Neurosci* 22: 1523–1531

Lindner O, Sorensen J, Vogt J, Fricke E, Baller D, Horstkotte D, Burchert W (2006) Cardiac efficiency and oxygen consumption measured with ^{11}C-acetate PET after long-term cardiac resynchronization therapy. *J Nucl Med* 47:378–83

Lovatt D, Sonnewald U, Waagepetersen HS, Schousboe A, He W, Lin JHC, Han X, Takano T, Wang S, Sim FJ, Goldman SA, Nedergaard M (2007) The transcriptome and metabolic gene signature of protoplasmic astrocytes in the adult murine cortex. *J Neurosci* 27:12255–66

Martinez-Hernandez A, Bell KP, Norenberg MD (1977) Glutamine synthetase: glial localization in brain. *Science* 195:1356–8

Mikolajczyk K, Szabatin M, Rudnicki P, Grodzki M, Burger C (1998) A JAVA environment for medical image data analysis: initial application for brain PET quantitation. *Med Inform (Lond)* 23:207–14

Minchin MC, Beart PM (1975) Compartmentation of amino acid metabolism in the rat dorsal root ganglion; a metabolic and autoradiographic study. *Brain Res* 83:437–49

Mintun MA, Raichle ME, Martin WR, Herscovitch P (1984) Brain oxygen utilization measured with O-15 radiotracers and positron emission tomography. *J Nucl Med* 25:177–87

Muir D, Berl S, Clarke DD (1986) Acetate and fluoroacetate as possible markers for glial metabolism *in vivo*. *Brain Res* 380:336–40

Norenberg MD, Martinez-Hernandez A (1979) Fine structural localization of glutamine synthetase in astrocytes of rat brain. *Brain Res* 161:303–10

Okazawa H, Yamauchi H, Sugimoto K, Toyoda H, Kishibe Y, Takahashi M (2001) Effects of acetazolamide on cerebral blood flow, blood volume, and oxygen metabolism: a positron emission tomography study with healthy volunteers. *J Cereb Blood Flow Metab* 21: 1472–1479

Oz G, Berkich DA, Henry PG, Xu Y, LaNoue K, Hutson SM, Gruetter R (2004) Neuroglial metabolism in the awake rat brain: CO2 fixation increases with brain activity. *J Neurosci* 24:11273–9

Pain F, Laniece P, Mastrippolito R, Pinot L, Charon Y, Glatigny A, Guillemin MT, Hantraye P, Leviel V, Menard L, Valentin L (2002) SIC, an intracerebral radiosensitive probe for *in vivo* neuropharmacology investigations in small laboratory animals: prototype design, characterization, and *in vivo* evaluation. *IEEE Trans Nucl Sci* 49:822–6

Paulson OB (2002) Blood-brain barrier, brain metabolism and cerebral blood flow. *Eur Neuropsychopharmacol* 12:495–501

Tyce GM, Ogg J, Owen Jr CA (1981) Metabolism of acetate to amino acids in brains of rats after complete hepatectomy. *J Neurochem* 36:640–50

Tyson RL, Gallagher C, Sutherland GR (2003) C-Labeled substrates and the cerebral metabolic compartmentalization of acetate and lactate. *Brain Res* 992:43–52

Van den Berg CJ, Krzalic L, Mela P, Waelsch H (1969) Compartmentation of glutamate metabolism in brain. Evidence for the existence of two different tricarboxylic acid cycles in brain. *Biochem J* 113:281–90

Van den Berg CJ, Ronda G (1976) The incorporation of double-labelled acetate into glutamate ad related amino acids from adult mouse brain: compartmentation of amino acid metabolism in brain. *J Neurochem* 27: 1443–1448

Waniewski RA, Martin DL (1998) Preferential utilization of acetate by astrocytes is attributable to transport. *J Neurosci* 18:5225–33

Weber B, Burger C, Biro P, Buck A (2002) A femoral arteriovenous shunt facilitates arterial whole blood sampling in animals. *Eur J Nucl Med Mol Imaging* 29:319–23

Weber B, Spath N, Wyss M, Wild D, Burger C, Stanley R, Buck A (2003) Quantitative cerebral blood flow measurements in the rat using a beta-probe and H_2 ^{15}O. *J Cereb Blood Flow Metab* 23:1455–60

Whitehouse S, Cooper RH, Randle PJ (1974) Mechanism of activation of pyruvate dehydrogenase by dichloroacetate and other halogenated carboxylic acids. *Biochem J* 141:761–74

Wolfe RR, Jahoor F (1990) Recovery of labeled CO_2 during the infusion of C-1- versus C-2-labeled acetate: implications for tracer studies of substrate oxidation. *Am J Clin Nutr* 51:248–52

Wyss MT, Ametamey SM, Treyer V, Bettio A, Blagoev M, Kessler LJ, Burger C, Weber B, Schmidt M, Gasparini F, Buck A (2007) Quantitative evaluation of ^{11}C-ABP688 as PET ligand for the measurement of the metabotropic glutamate receptor subtype 5 using autoradiographic studies and a beta-scintillator. *Neuroimage* 35:1086–92

Yee SH, Lee K, Jerabek PA, Fox PT (2006) Quantitative measurement of oxygen metabolic rate in the rat brain using microPET imaging of briefly inhaled ^{15}O-labelled oxygen gas. *Nucl Med Commun* 27:573–81

Appendix

Details of β-Probe Experiments and Human PET Measurements

Blood and Tissue Processing

(1) Physiological blood parameters: Several blood gas variables (pH, pCO_2, pO_2) relevant to cerebral energy metabolism were measured with a pH/blood gas analyzer (AVL, Compact 3, Roche Diagnostics, Switzerland) before the start of tracer kinetic measurements. Plasma lactate levels were determined before the first tracer injection in 24 animals (Ektachem DT, Kodak, USA). In animals of group 5 (dichloroacetate challenge) lactate levels were determined twice, before and 4 h after injection of dichloroacetate respectively (Ektachem DT, Kodak, USA). In five animals there were technical problems with the analyzer rendering a measurement impossible.

(2) Determination of the arterial plasma input curve: For the CBF measurements arterial blood was continuously drawn during scanning and the activity in the catheter was measured in a coincidence counter (GE Medical Systems), which was cross calibrated with the β-scintillator and the PET scanner respectively. During the 1-^{11}C-acetate scan arterial radioactivity was also measured online for the total scan time in the animal experiments (for an example of acquired time–activity curves see Supplementary Figure S2). In the human study, it was acquired online only for the first 5 mins so as not to miss the peak of the arterial input curve, thereafter for the remaining 15 mins 4 single samples were taken manually at different time points (around 3, 6, 15 and 25 mins) and processed as described below. Whole-blood activity was then corrected for (1) a different tracer concentration in whole blood and plasma and (2) the build up of labeled metabolites. The ratio '$^{11}C_{plasma}/^{11}C_{whole\ blood}$' was determined in all animals at different time points (three blood samples per injection). The data of all animals were then pooled and the time course of the ratio was approximated by fitting a quadratic polynomial to the data. This function was then used to convert counts in whole blood to counts in plasma. In humans, the ^{11}C concentration in whole blood (C_B) was first converted to ^{11}C concentration in plasma (C_{PL}) using the same conversion function as determined in rats.

Secondly, plasma activity was corrected for the build-up of labeled metabolites using data from previous 1-^{11}C-acetate studies in the human heart (Buck *et al*, 1991).

(3) Metabolite analysis in blood: Three blood samples (approximately 400 μL each) were collected at different time points during each 20-min acquisition for analysis of authentic tracer and metabolites. These samples were first centrifuged for 3 mins at 2000*g*. Proteins were then precipitated with 75 μL acetonitrile in 50 μL plasma. After a second centrifugation for 3 mins at 2000*g*, the composition of the ^{11}C-derived radioactivity in the supernatant (80 μL) was analyzed by high-pressure liquid chromatography on a polymeric column (PRP-1, 5-μm, 250 × 4.1 mm i.d.; Hamilton, USA) with 3 mmol/L phosphoric acid in water (pH 2.67) as the mobile phase (1 mL/min). The amount of authentic tracer was expressed as a fraction of total plasma ^{11}C counts (f).

The fraction data of all animals was then pooled and the time-course of the fraction was approximated by a decaying exponential function of the form function $f = 1-\alpha(1-\exp(-\mu t))$. This function was subsequently used to convert the total plasma activity to the time course of authentic 1-^{11}C-acetate (= input curve).

Data Analysis

In the animal and human studies the analytical and statistical methods were similar as described below. All calculations were performed using the software package PMOD (Mikolajczyk *et al*, 1998; PMOD Technologies, Adliswil, Switzerland).

(1) Cerebral blood flow measurements: The basis of the calculation for CBF measurements was the one-tissue compartment model including a partition coefficient for $H_2{}^{15}O$ (see Figure 6A). The change of the radioactivity concentration in tissue C_T is then defined by the following differential equation

$$dC_T/dt = CBF(C_A(t) - C(t)/p) \qquad (1)$$

where C_A is the arterial tracer concentration and p is the tissue partition coefficient, for example, that fraction of tissue that is permeable for $H_2{}^{15}O$. In this configuration C_{TISS} is the concentration of $H_2{}^{15}O$ in 1 mL of brain and it is assumed that $H_2{}^{15}O$ immediately reaches a homogeneous concentration in permeable space and no division into a vascular and a tissue compartment is necessary. The analytical solution of Equation 1 is

$$C_T = CBF \exp(-CBF/p\,t) \otimes C_A \qquad (2)$$

where $\otimes$ means mathematical convolution.

Equation 2 was fitted to the data using least squares fitting (Marquardt algorithm) implemented in the software PMOD (Mikolajczyk *et al*, 1998). Before that data analysis tissue TACs and arterial input curves were corrected for physical decay of ^{15}O.

With the human $H_2{}^{15}O$ PET data we calculated quantitative parametric maps representing regional CBF using the integration method described by Alpert *et al* (1984). This method yielded maps of K_1 and k_2 which represent regional CBF and regional CBF/p respectively (p = partition coefficient). Before calculation of the parametric

maps, the input curve was corrected for delay and dispersion.

(2) 1-^{11}C-acetate experiments: The investigated method consisted of standard compartmental modeling using an arterial input function. Tracer kinetic modeling was performed using the one-tissue compartment model depicted in Figure 6B.

K_1 describes uptake of tracer across the blood–brain barrier. K_1 is related to the first pass EF and CBF through the following equation: $K_1 = \mathrm{EF} \times \mathrm{CBF}$. This equation was used to determine EF in the animal and human experiments.

k_2 represents back diffusion of radioactivity from tissue to vascular space.

Tracer exchange between the compartments is described by the following differential equation:

$$\frac{dC_T}{dt} = K_1 C_p - k_2 C_T \quad (3)$$

As the total activity measured in a region is composed of counts from tissue and blood, all models contained a parameter (α) correcting for blood activity.

$$C_{vol} = (1 - \alpha) C_T + \alpha C_{blood} \quad (4)$$

where C_{VOI}, in the human PET study is the ^{11}C activity concentration in the defined volume of interest, in the animal study it is the ^{11}C activity measured by the tip of the β-scintillator; α, percentage of intravascular space in tissue; C_T, activity in the extra vascular compartment; C_B, total blood activity.

C_T was calculated by numerical integration of the differential equations. The correction for the contribution of blood in the brain (α) was fixed at 0.05. This value considers that signals originating from large superficial pial vessels impact the β-scintillator measurements.

Delay of Onset of Radiolabel Washout

To check whether the start of the radioactivity washout from tissue was delayed, the first 5 mins of data after tracer injection were refitted with only k_2 as a free parameter and K_1 fixed to the full length fit.

Supplementary Information accompanies the paper on the Journal of Cerebral Blood Flow & Metabolism website (http://www.nature.com/jcbfm)

Cellular/Molecular

In Vivo Evidence for Lactate as a Neuronal Energy Source

Matthias T. Wyss,[1,2] Renaud Jolivet,[1] Alfred Buck,[2] Pierre J. Magistretti,[3] and Bruno Weber[1]

[1]Institute of Pharmacology and Toxicology, University of Zürich, 8091 Zürich, Switzerland, [2]Department of Nuclear Medicine, University Hospital, 8091 Zürich, Switzerland, and [3]Brain Mind Institute, Ecole Polytechnique Fédérale de Lausanne, 1015 Lausanne, Switzerland

Cerebral energy metabolism is a highly compartmentalized and complex process in which transcellular trafficking of metabolites plays a pivotal role. Over the past decade, a role for lactate in fueling the energetic requirements of neurons has emerged. Furthermore, a neuroprotective effect of lactate during hypoglycemia or cerebral ischemia has been reported. The majority of the current evidence concerning lactate metabolism at the cellular level is based on *in vitro* data; only a few recent *in vivo* results have demonstrated that the brain preferentially utilizes lactate over glucose. Using voltage-sensitive dye (VSD) imaging, beta-probe measurements of radiotracer kinetics, and brain activation by sensory stimulation in the anesthetized rat, we investigated several aspects of cerebral lactate metabolism. The present study is the first *in vivo* demonstration of the maintenance of neuronal activity in the presence of lactate as the primary energy source. The loss of the voltage-sensitive dye signal found during severe insulin-induced hypoglycemia is completely prevented by lactate infusion. Thus, lactate has a direct neuroprotective effect. Furthermore, we demonstrate that the brain readily oxidizes lactate in an activity-dependent manner. The washout of 1-[^{11}C]L-lactate, reflecting cerebral lactate oxidation, was observed to increase during brain activation from 0.077 ± 0.009 to 0.105 ± 0.007 min^{-1}. Finally, our data confirm that the brain prefers lactate over glucose as an energy substrate when both substrates are available. Using [^{18}F]fluorodeoxyglucose (FDG) to measure the local cerebral metabolic rate of glucose, we demonstrated a lactate concentration-dependent reduction of cerebral glucose utilization during experimentally increased plasma lactate levels.

Introduction

For a long time, it was considered that blood-borne glucose is the sole energy substrate in the adult healthy brain. However, several studies have reported a different situation in the developing and diseased brain. For example, in breast-fed newborns and suckling rats, the utilization of monocarboxylates, such as lactate, and ketone bodies is increased (Cremer, 1982; Dombrowski et al., 1989; Nehlig and Pereira de Vasconcelos, 1993). In addition, a neuroprotective role for exogenous lactate in pathologic situations, such as prolonged starvation, diabetes, and cerebral ischemia, has been documented on several occasions (Gjedde and Crone, 1975; Schurr et al., 2001; Mason et al., 2006; Berthet et al., 2009). However, it is still unclear whether the neuroprotective effect of lactate is indirect [e.g., via increased cerebral blood flow (CBF) caused by hyperlactemia (Shackford et al., 1994)] or whether lactate can serve as a direct neuronal energy substrate.

One of the first indications that lactate is not only a product of the metabolic chain but also a potentially important alternative neuronal energy substrate was documented more than two decades ago from the demonstration that lactate is able to support synaptic function in the absence of glucose in rat hippocampal slices (Schurr et al., 1988). For the living brain, the situation is less clear. No information about the capability of lactate to sustain neuronal action *in vivo* could be provided. Recently, independent groups have reported lactate utilization by the brain in humans (Gallagher et al., 2009; van Hall et al., 2009; Boumezbeur et al., 2010). There is also evidence that lactate oxidation is preferentially located in neurons. Bouzier et al. (2000) used 3-[^{13}C]lactate to investigate cerebral lactate metabolism. From the accumulation of labeled metabolites, they concluded that lactate metabolism is located in a compartment devoid of pyruvate carboxylase, e.g., neurons.

Furthermore, astrocytic production of lactate, which serves as an energy pool for neurons, was proposed (Pellerin and Magistretti, 1994), but neuronal lactate use has still to be demonstrated *in situ*.

In the present study, we followed a multimodal approach. First, using optical voltage-sensitive dye (VSD) imaging to directly monitor the synaptic activity in the somatosensory cortex, we report for the first time that lactate is capable of sustaining neuronal activity for a time period of hours in the quasi-absence of glucose in the living organism. Second, applying radiotracer kinetic measurements of 1-[^{11}C]L-lactate accumulation and classical cerebral glucose utilization measurements using FDG, we demonstrate that lactate is metabolized by the intact brain in an activity-dependent manner.

Materials and Methods

Animal preparation

All the animal experiments were approved by the local veterinary authorities and were performed by licensed investigators. In total, 64 animals (male adult Sprague Dawley rats; weighing 220–350 g) were included in the study. Before measurements, the animals were fasted overnight to

Received Jan. 17, 2011; revised March 10, 2011; accepted April 1, 2011.

Author contributions: M.T.W., A.B., and B.W. designed research; M.T.W. performed research; M.T.W. and A.B. analyzed data; M.T.W., R.J., A.B., P.J.M., and B.W. wrote the paper.

M.T.W. and B.W. are supported by Swiss National Foundation Grants 31003A-124739/1 and PP0033-110751. R.J. is supported by grants from the Hartmann Müller Foundation, the Olga Mayenfisch Foundation, and the EMDO Foundation. We thank Florent Haiss for help in setting up the voltage-sensitive dye instrument and Felipe Barros for valuable discussions.

Correspondence should be addressed to Dr. Bruno Weber, Institute of Pharmacology and Toxicology, University of Zürich, Rämistrasse 100, 8091 Zürich, Switzerland. E-mail: bweber@pharma.uzh.ch.

DOI:10.1523/JNEUROSCI.0415-11.2011

 0270-6474/11/317477-09$15.00/0

standardize plasma levels of glucose. Surgery was performed under 2.5–3.5% isoflurane anesthesia and involved the placement of an arterial and a venous catheter and tracheotomy for mechanical ventilation. For the cortical beta-probe acquisitions, the cranial bone above somatosensory cortices was thinned to translucency. For the voltage-sensitive dye imaging experiments, a craniotomy was performed. Staining with the voltage-sensitive dye RH1691 (Optical Imaging) was done through the intact dura mater for 90 min. Leaving the dura intact reduces the movement artifact during recording and decreases the risk of cortex irritations (Lippert et al., 2007). After staining, the dye was removed by washing with dye-free Ringer's solution. Plasma glucose and lactate levels were determined periodically (Ektachem DT; Eastman Kodak). The actual experiments were performed under α-chloralose anesthesia (44 mg/kg bodyweight, s.c.). Several blood gas variables (pH, P_{CO_2}, P_{O_2}) (AVL, Compact 3; Roche Diagnostics) and metabolic measures such as plasma glucose and lactate levels (Ektachem DT; Eastman Kodak), which are relevant parameters influencing lactate uptake in the brain, were measured in all animals before the start of measurements. Ventilation was adjusted to reach physiological blood gas values.

Voltage-sensitive dye imaging

The VSD was excited with 630 nm light from an LED (Aculed; PerkinElmer Life and Analytical Sciences). A custom-built tandem lens system consisting of two 50 mm objectives and dichroic and emission filters was used. Data were collected with a high-speed CMOS-based camera (Micam Ultima; Scimedia). Images were collected with 1 ms temporal resolution. Images were analyzed using custom-written Matlab routines and the software package PMOD (Mikolajczyk et al., 1998). Bleaching of fluorescence was corrected by subtraction of a best-fit double exponential. Time courses of fluorescence changes were quantified as $\Delta F/F_0$ from circular regions of interest of constant diameter manually placed over the activated area. To compare VSD signal from different animals, region of interests (ROIs) were centered on the location of the earliest responses. In addition, to estimate the spatial extent of the neuronal activation at the time point of the highest activation (peak amplitude), the area containing voxels >70% of the maximum within the experiment was determined. The amplitudes of sensory-evoked responses were calculated as the change in the VSD signal ($\Delta F/F_0$) over a fixed time interval for each experiment. Finally, the time until peak response was determined as the time span between stimulation onset and peak amplitude within the ROI. Baseline was the 10 ms period immediately before the stimulus.

In VSD experiments, five experimental groups were examined: (1) effect of hyperlactemia ($n = 4$) on neuronal integrity, (2–4) evolution of the VSD signal after induction of severe hypoglycemia (insulin at 20 IU/kg, i.p.) and subsequent continuous infusion of saline ($n = 5$), glucose ($n = 5$), or lactate ($n = 5$), respectively, and (5) control experiments with saline infusion only ($n = 3$).

Radiotracer experiments

Radiotracer synthesis: production of 1-[^{11}C]L-lactate. Racemic 1-[^{11}C]lactic acid was made by [^{11}C]cyanohydrine synthesis starting from [^{11}C]HCN (trapped as [^{11}C]KCN) and acetaldehyde bisulfite adduct. The quantitatively formed 1-[^{11}C]DL-lactonitrile was hydrolyzed by reflux in concentrated HCl, and the reaction mixture was introduced directly into a semipreparative polymeric HPLC column (250 × 10 mm, 0.03% H_3PO_4 as the mobile phase; Polymerx 10μ; Phenomenex) in which the product was isolated from the aggressive reaction matrix. Then the collected racemic 1-[^{11}C]lactic acid was automatically introduced into a preparative chiral HPLC column coated with a penicillamine-derived chiral selector and eluted with 1 mM $CuSO_4$ solution as the mobile phase in which both enantiomers were separated by ligand exchange chromatography. The fractions corresponding to [^{11}C]D-lactic acid or [^{11}C]L-lactic acid were passed through anion exchanger Sep-Pak cartridges (Accell Plus QMA, in CO_3^{2} form) in which the Cu^{2+} ions (as insoluble carbonate) and the [^{11}C]lactate are retained. The latter was selectively washed out from the cartridges with 2 mmol/L sodium phosphate buffer, pH 7.4, to obtain injectable solutions of pure Na-[^{11}C]D-lactate and L-lactate enantiomers. The quality control of the final product was done by chiral ligand exchange HPLC. The procedure led to a product of >99% chemical and enantiomeric purity. The specific activity at the end of synthesis was ~400 GBq/μmol. FDG was obtained from the daily in-house production by the Radiochemistry Department of the University Hospital Zurich.

Beta-probe experiments using 1-[^{11}C]L-lactate and FDG. A recently developed two-channel system with surface probes was used for the measurement of the radioactivity concentration in brain cortices (Wyss et al., 2009). The used devices consist of scintillator crystals with a thickness of 0.2 mm and a diameter of 3 mm. The beta scintillators were made light-tight by applying a uniform coating of silver particles. The scintillations were measured using a photomultiplier tube and counting electronics (PerkinElmer Life and Analytical Sciences). The limited range of beta particles within biological tissues leads to a limited detection volume centered around the scintillating tip of the probe (Wyss et al., 2009). The sensitivities of the used scintillators were 0.31–0.60 cps/kBq/cc.

For beta-probe measurements, the arterial and venous lines were connected to form an arterio-venous (av) shunt. The av shunt was used for continuous monitoring of arterial blood pressure, injection of the radiotracers, continuous measurement of the total arterial blood radioactivity, and the collection of blood samples. For the recording of the total blood radioactivity, the shunt ran through a coincidence counter (GE Medical Systems) (for details, see Weber et al., 2002). Before the actual experimental measurements for 1-[^{11}C]L-lactate, the kinetic properties and the buildup of metabolites of the novel radiotracer were characterized in 10 animals. In addition, in four of these animals, the first pass extraction fraction was determined with additional measurements of CBF (see below). All subsequent 1-[^{11}C]L-lactate experiments consisted of two acquisitions. For each acquisition, 100–150 MBq of radiotracer was intravenously injected. First, the change of 1-[^{11}C]L-lactate kinetics from baseline conditions to increased neuronal activity [electrical infraorbital nerve stimulation (ION): 2 mA, 2 Hz, 1 ms pulses applied during the whole acquisition period; $n = 5$] and the effect of monocarboxylic acid transporter blockade using α-cyano-4-hydroxy-cinnamate (CIN) ($n = 5$) was investigated. CIN was injected intraperitoneally (90 mg/kg) 30 min before tracer injection.

FDG was used to determine the local cerebral metabolic rate of glucose ($LCMR_{glu}$). For each FDG acquisition, 50–80 MBq of tracer was injected. All FDG experiments consisted of two measurements. Accumulation of FDG was measured at baseline (SAL) and at artificially increased plasma lactate levels (LAC) (100 $\mu mol \cdot kg^{-1} \cdot min^{-1}$ during the first 20 min; thereafter, 50 $\mu mol \cdot kg^{-1} \cdot min^{-1}$, i.v.) during rest conditions ($n = 4$ for SAL; $n = 13$ for LAC) and during activation ($n = 2$ for SAL; $n = 5$ for LAC).

Characterization of 1-[^{11}C]lactate. The total radioactivity in arterial blood was continuously recorded over 40 min using a coincidence counter (GE Medical Systems). Whole blood activity was then corrected for (1) a different tracer concentration in whole blood and plasma and (2) the buildup of labeled metabolites. The ratio $^{11}C_{plasma}/^{11}C_{whole\ blood}$ was determined in all animals at different time points (three to four blood samples per animal). The data of all animals were then pooled, and the time course of the ratio was approximated by fitting a quadratic polynomial to the data. This function was then used to convert counts in whole blood to counts in plasma.

Samples (about 400 μl) were collected at different time points after tracer injection, with a maximum of four blood samples per animal, to determine the time course of the ratio of the ^{11}C activity in plasma to whole blood and for analysis of authentic tracer and metabolites. These samples were first centrifuged for 3 min at 2000 rpm. Proteins were then precipitated with 75 μl of acetonitrile in 50 μl of plasma. After centrifugation for 3 min at 2000 rpm, the composition of the ^{11}C-derived radioactivity in the supernatant (80 μl) was analyzed by HPLC on a polymeric column (5 μm, 250 × 4.1 mm inner diameter; PRP-1; Hamilton) with 3 mmol/L phosphoric acid in water, pH 2.67, as the mobile phase (1 ml/min). The retention times of [^{11}C]HCO_3^- (3.3 min) and lactic acid (5.1 min) were determined by using aqueous solution of $NaHCO_3$ and DL-lactic acid as reference compounds, detected by UV absorption at 220 nm. The amount of authentic tracer was expressed as a fraction of total plasma ^{11}C counts.

The fraction data of all animals was then pooled, and the time course of the fraction was approximated by a decaying biexponential function. This function was subsequently used to convert the total plasma activity

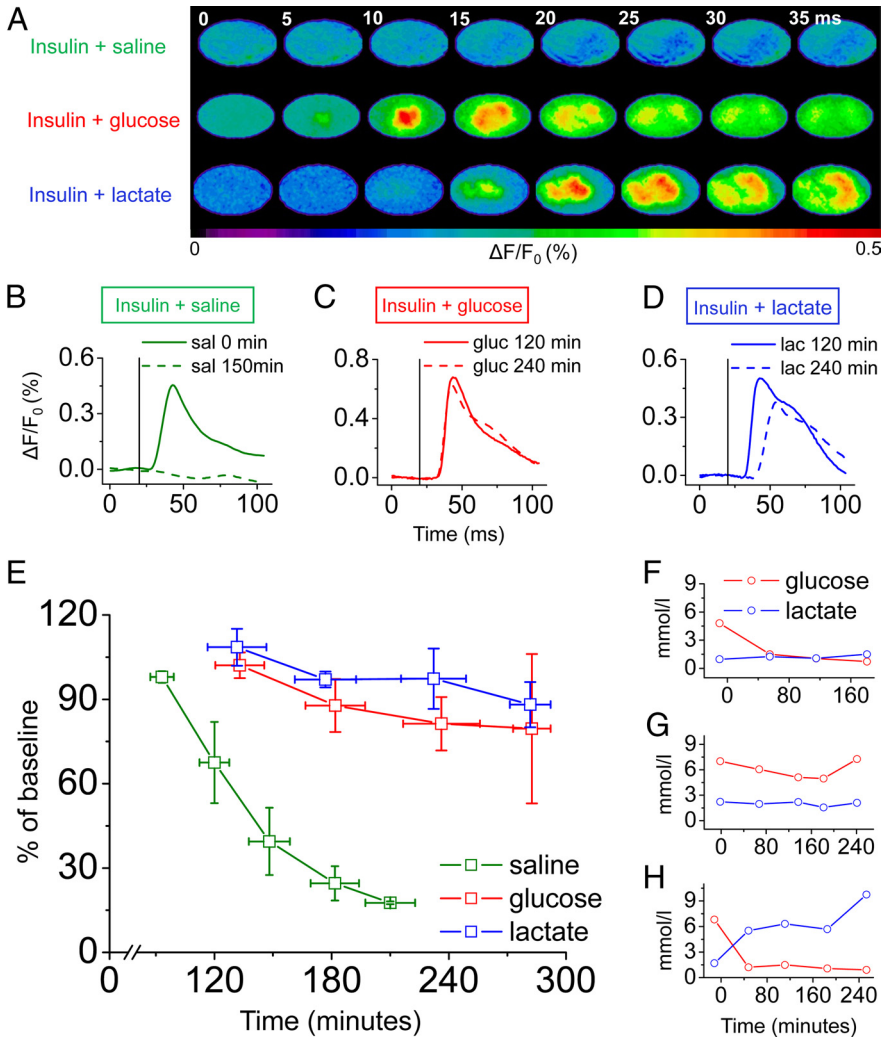

Figure 1. Lactate is able to sustain neuronal activity in the absence of glucose. ***A***, A single electrical pulse applied to the rat's hindpaw evoked a transient increase in VSD fluorescence in the primary somatosensory cortex that was abolished after only 150 min in animals receiving saline after the insulin injection (top row) but remained stable in animals infused with glucose (middle row) or lactate (bottom row) after 240 min. ***B–D***, The time courses of the VSD signal displayed a similar result in animals supplied with glucose (***C***; gluc) or lactate (***D***; lac) with sustained amplitude 240 min after insulin injection. In contrast, removal of the signal was observed in animals receiving saline infusion only (***B***; sal). In the group supplied with lactate, the signal onset was delayed (example shown in ***D***). The vertical black line represents the time point of hindpaw stimulation. ***E***, Comparison of amplitudes in all three groups injected with insulin at 0 min (mean ± SE; $n = 5$). ***F–H***, Mean plasma levels of glucose and lactate plotted for saline (***F***), glucose (***G***), and lactate (***H***) animals.

to the time course of authentic [^{11}C]lactate (input curve). At the end of these experiments, the rats were perfused with PBS, and brains were prepared for measurements with the HPLC system. Each brain was first homogenized before adding acetonitrile (150%). The subsequent procedure was the same as with the blood samples described above, except that the amount of supernatant injected into the HPLC system was 200 μl.

CBF measurements (used for estimating the first-pass extraction fraction of lactate). The basis of the CBF calculation was the one-tissue compartment model, including a partition coefficient for $H_2{}^{15}O$. The change of the radioactivity concentration in tissue C_{tiss} is then defined by the following differential equation:

$$dC_{tiss}/dt = CBF(C_a(t) - C_{tiss}(t)/p), \quad (1)$$

where C_a is the arterial tracer concentration, and p is the tissue partition coefficient, e.g., the fraction of tissue that is $H_2{}^{15}O$ permeable. In this configuration, C_{tiss} is the concentration of $H_2{}^{15}O$ in 1 ml of brain, and it is assumed that $H_2{}^{15}O$ immediately reaches a homogeneous concentration in permeable space and no division into a vascular and a tissue compartment is necessary. The analytical solution of Equation 1 is as follows:

$$C_{tiss} = CBF * e^{(-CBF/pt)} \otimes C_a, \quad (2)$$

where ⊗ represents mathematical convolution.

Equation 2 was fitted to the data using least-squares fitting (Marquardt algorithm) implemented by the software PMOD (Mikolajczyk et al., 1998). Before data analysis, tissue time activity curves and arterial input curves were corrected for the physical decay of ^{15}O.

Analysis of the radiotracer data

The calculations and parameter fitting were performed using the software PMOD (Mikolajczyk et al., 1998). Data were corrected for physical decay and multiplied by a calibration factor taking into account differences in sensitivities of the probe system and the coincidence counter. Before analysis, data were downsampled to obtain a 10 or 30 s resolution for ^{11}C and ^{18}F data, respectively. The investigated methods consisted of standard compartmental modeling using an arterial input function.

1-[^{11}C]L-Lactate. Tracer kinetic modeling was performed using the one-tissue compartment model. The parameters are as follows: K_1 describes the uptake of tracer across the blood–brain barrier and is related to CBF and the first-pass extraction fraction EF ($K_1 = CBF * EF$); and k_2 represents the back-diffusion of label from the tissue to the vascular compartment.

Label exchange between the compartments is described by the following differential equation:

$$dC_{tiss}/dt = K_1 C_{plasma}(t) - k_2 C_{tiss}(t). \quad (3)$$

Because the total activity measured in a region is composed of counts from tissue and blood, all models contained a parameter (α) correcting for blood activity:

$$C_{VOI} = (1-\alpha)C_{tiss} + \alpha C_{blood}, \quad (4)$$

where C_{VOI} is ^{11}C activity measured by the tip of the beta scintillator, α is the percentage of intravascular space in the tissue, C_{tiss} is activity in the extravascular compartment, C_{blood} is total blood activity, and C_{tiss} was calculated by numerical integration of the differential equations. The vascular fraction α was included as a fit parameter that improved the least-squares fit.

The kinetic model was adjusted in two ways for the analysis of dual-injection data arising from use of the surface probe. (1) Two sets of rate constants (K_1, k_2) were used in the calculation of the operational equation: the first set for the time until the second injection, and the second set thereafter. The least-squares fit procedure resulted in estimates for all four rate constants (K_1-1, k_2-1 and K_1-2, k_2-2) and the vascular fraction. (2) The correction function to derive plasma activity from whole blood activity was adjusted to distinguish between the contributions from the two injections. To this end, the blood activity from the first injection was extrapolated using an exponential function, which was fitted to the blood activity 10 min before the second injection.

The interpretation of the 1-[^{11}C]L-lactate experiments is based on the following assumptions, which are discussed in detail below: (1) parameter k_2 is reflecting the activity of the enzyme lactate dehydrogenase (LDH), and (2) the total amount of lactate that is oxidized is the product of k_2 and intracellular lactate concentration.

FDG. FDG data were used for calculating $LCMR_{glu}$. The procedure for the quantification of the probe studies followed the [^{14}C]deoxyglucose method described by Sokoloff et al. (1977). A compartmental model with two tissue compartments and four kinetic rate constants (K_1 to k_4) was used. The operational equation, which was fitted to the probe time activity curve, additionally included a vascular fraction α as a fit parameter. This improved the least-squares fit compared with a fixed value of α = 5%. $LCMR_{glu}$ values were calculated from the fitted rate constants: $LCMR_{glu} = K_1 * k_3/(k_2 + k_3)C_{plasma}/LC$, where C_{plasma} represents the plasma glucose concentration, and LC represents the lumped constant (LC of 0.437).

The kinetic model was adjusted in two ways for the dual-injection data analysis. (1) Two sets of four rate constants (K_1 to k_4) were used in the operational equation calculation: the first set for the time until the second injection, and the second set thereafter. The least-squares fit procedure resulted in estimates for all eight rate constants and the vascular fraction. (2) The correction function to derive plasma activity from whole blood activity was adjusted to distinguish between the contributions from the two injections. To this end, the blood activity from the first injection was extrapolated using an exponential function that was fitted to the blood activity 10 min before the second injection.

Statistics

Results are presented as mean ± SD if not otherwise stated. To test differences between different interventions for inter-individual comparisons, the nonparametric Wilcoxon's signed rank test was applied. A p value of 0.05 was taken as the significance limit.

Results

Lactate can sustain neuronal integrity as an alternative energy substrate

Severe glucose deprivation was induced by insulin injection (20 IU/kg, injection at time 0 min) while monitoring neural activity with VSD imaging. In three experimental groups, infusion of saline, glucose, or lactate was immediately initiated after the insulin injection. The total recording time for VSD imaging is limited because of dye washout and excitation light-related amplitude reductions of the signal (Lippert et al., 2007). Therefore, imaging commenced with delay, ~100 min after the insulin injection. In animals infused with saline only, blood glucose levels reached 1.5 mmol/L already after 60 min. Plasma lactate levels varied on average between 1.0 and 1.5 mmol/L throughout the whole experimental period (Fig. 1*F*). Severe hypoglycemia reduced the amplitude of the VSD signal by >50% from the baseline after only 140 min after the application of insulin (Fig. 1*A*,*B*,*E*). Thereafter, the signal was further decreased as a result of severe glucose deprivation. In animals supplied continuously with glucose, plasma levels of glucose were not reduced by insulin action and remained at normoglycemic values (Fig. 1*G*). Not surprisingly, the neuronal signal did not show a significant decline throughout the period of data acquisition [270 min after the insulin injection; n = 5; not significant (n.s.) compared with baseline acquisition at 120 min (Fig. 1*A*,*C*,*E*)]. In the group in which sodium lactate was infused over the whole time period (plasma lactate levels between 5.5 and 9.7 mmol/L), plasma levels of glucose also exhibited a rapid decline to values ~1 mmol/L within 60 min (Fig. 1*H*). Nevertheless, the amplitude of the VSD signal reflecting neuronal activity remained high (n = 5; n.s. compared with the 120 min time point) (Fig. 1*A*,*D*,*E*). The spread of activation remained constant in the glucose- and lactate-treated animals within the 240 min after the insulin injection, whereas the extent of activation in the animals receiving saline infusion only decreased considerably (data not shown). In the latter group, four of five animals showed no pixels surpassing 70% of the maximal amplitude after 150 min. In the fifth, the number decreased by >50%. The time course of the VSD signal revealed an accentuated delay of the signal in animals receiving lactate infusion compared with glucose-infused rats (Fig. 1*C*,*D*). In the animals receiving glucose infusion after insulin injection (n = 5), the times-to-peak were 21.8 ± 1.6, 21.6 ± 1.9, and 20.7 ± 1.5 ms after 120, 180, and 240 min, respectively. In the lactate group (n = 5), delays at the corresponding time points were 21.2 ± 0.9, 23.5 ± 4.4, and 36.2 ± 10.7 ms. The difference after 240 min was significant between the two groups ($p < 0.05$).

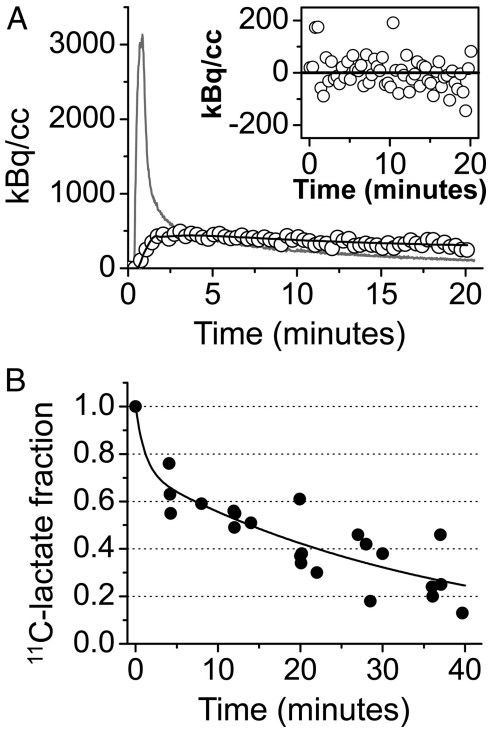

Figure 2. 1-[^{11}C]L-lactate is a suitable tracer to study cerebral lactate oxidation. ***A***, Measured radioactivity concentration in the brain (open circles), model fit (black line), and arterial input curve (gray line). The inset displays the residuals of the fitting to a one-tissue compartment model. The absence of any distribution bias supports the adequacy of the applied one-tissue compartment model. ***B***, Fraction of native radiolabeled lactate over 40 min after intravenous injection of 1-[^{11}C]L-lactate in blood. The filled circles represent data points from baseline experiments (n = 7) performed to characterize the radiotracer, and the solid line is the corresponding fit of a biexponential curve.

Lactate is oxidized by the brain in an activity-dependent manner

To directly assess lactate use in the adult rodent brain *in vivo*, we synthesized radiolabeled 1-[^{11}C]L-lactate. Characterization of 1-[^{11}C]L-lactate revealed suitable properties for use in brain studies, allowing cerebral tracer kinetic measurements with high temporal resolution. An extraction fraction (EF = K_1/CBF) of 30 ± 10% (n = 4) was calculated, which is sufficient to study physiological processes in the brain and is in good agreement with previous studies reporting the uptake of L-lactate to be 25–50% of that of glucose (Knudsen et al., 1991; Hassel and Bråthe, 2000). Kinetic modeling showed that a one-tissue compartment model was sufficient for the analysis of 1-[^{11}C]L-lactate data, yielding K_1 and k_2 values measuring the uptake and the release of radiolabel, respectively. The time courses of the fraction of authentic tracer and metabolites in plasma are shown in Figure 2. As in brain, the main metabolite detected in blood was [^{11}C]CO_2. After 20 min, the fraction of true tracer fell to ~40%. In the brain,

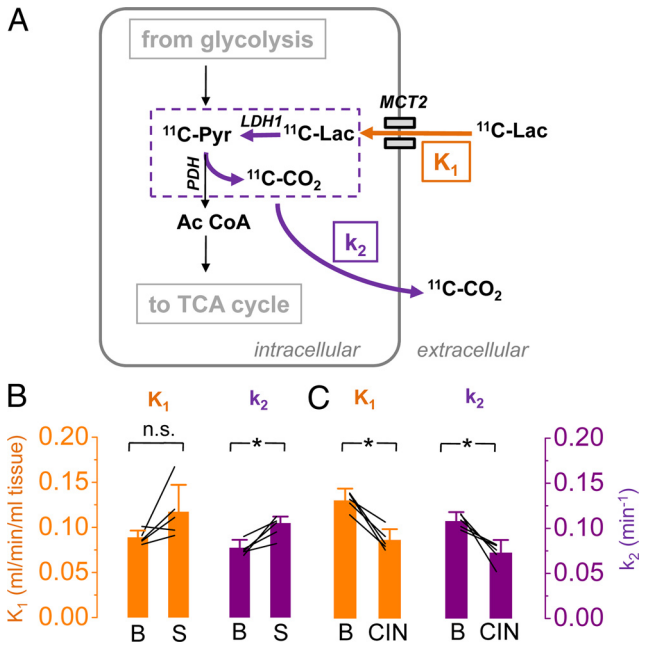

Figure 3. The brain oxidizes lactate in an activity-dependent manner. ***A***, Schematic of the biochemical pathways involved in the degradation of 1-[^{11}C]L-lactate (^{11}C-Lac) and the proposed interpretation of the rate constants K_1 and k_2 describing the kinetics of the radiotracer (for details, see Results). Briefly, K_1 represents delivery of 1-[^{11}C]L-lactate (orange arrow), and k_2 reflects kinetically the loss of radiolabel after conversion of lactate to pyruvate and of pyruvate to acetyl-coenzyme A (purple arrows). During activation (***B***; S; $n = 5$), delivery (K_1) and washout (k_2) increased, whereas during MCT blockade (***C***; CIN; $n = 5$), the transfer of 1-[^{11}C]L-lactate slowed down in both directions (Pyr, pyruvate; Ac CoA, acetyl coenzyme A; TCA cycle, tricarboxylic acid cycle). *$p < 0.05$, n.s., not significant.

Table 1. 1-[^{11}C]L-lactate kinetics

	K_1 (ml · min^{-1} · ml^{-1} tissue)		k_2 (min^{-1})	
Animal number	Baseline	Stimulation	Baseline	Stimulation
1	0.081	0.091	0.073	0.082
2	0.085	0.111	0.074	0.105
3	0.097	0.101	0.09	0.107
4	0.086	0.12	0.069	0.112
5	0.111	0.128	0.076	0.095
Mean	0.092	0.110	0.076	0.100
SD	0.01	0.01	0.01	0.01
	Baseline	CIN	Baseline	4-CIN
6	0.138	0.076	0.116	0.052
7	0.139	0.083	0.115	0.071
8	0.132	0.107	0.102	0.082
9	0.128	0.091	0.109	0.076
10	0.115	0.08	0.098	0.081
Mean	0.130	0.087	0.108	0.072
SD	0.01	0.01	0.01	0.01

the analysis revealed 58 ± 8% lactate and 42 ± 8% CO_2 after 40 min ($n = 7$). Using for the first time ^{11}C-radiolabeled lactate to measure cerebral lactate oxidation, we observed a noticeable increase of both rate constants K_1 and k_2 during increased neuronal activity (Fig. 3*B*, Table 1). Delivery of the tracer increased during electrostimulation of the infraorbital nerve as reflected by an increase of the CBF-dependent K_1 from 0.09 ± 0.01 to 0.12 ± 0.03 ml · min^{-1} · ml^{-1} tissue ($n = 5$; change n.s.).

In parallel to the elevated delivery, radioactivity washout (k_2) increased from 0.077 ± 0.009 to 0.105 ± 0.007 min^{-1} ($n = 5$; $p < 0.05$). In Discussion, we will argue that this is most likely related to increased LDH activity during stimulation.

Table 2. Plasma lactate levels and calculated cerebral lactate uptake

	Plasma lactate level (mmol/L)		Calculated cerebral lactate uptake (K_1*lac; μmol · g^{-1} · min^{-1}	
Animal number	Baseline	Stimulation	Baseline	Stimulation
1	2	2.2	0.162	0.200
2	2	2.9	0.170	0.322
3	2	2.1	0.194	0.212
4	1.7	1.6	0.146	0.192
5	1.5	1.5	0.167	0.192
Mean	1.84	2.06	0.17	0.22
SD	0.2	0.6	0.02	0.06

lac, Plasma lactate level.

There is strong evidence in our and other studies that the label leaves the tissue as CO_2, which is cleaved off during the conversion of pyruvate to acetyl-CoA by pyruvate dehydrogenase (PDH) (Fig. 3*A*). In the present study, the metabolite analysis revealed only lactate and CO_2 as labeled metabolites. This is in line with a study by van Hall et al. (2009). Using 1-[^{13}C]lactate, they reported that 86 ± 15% of the label was released as CO_2. The situation is completely different, if lactate is labeled at position 2 or 3. In that case, most of the label ends up in metabolites of the TCA cycle (van Hall, 1999; Bouzier et al., 2000; van Hall et al., 2009).

Increased uptake of blood-borne lactate and efficiency of lactate transport during activation

It is possible to calculate cerebral uptake of blood-borne lactate as the product of K_1 and blood lactate concentration (in this group of experiments, plasma lactate levels ranged from 1.7 to 2.8 mmol/L) (Table 2). Based on these values, baseline mean cerebral lactate uptake was estimated to be 0.17 μmol · g^{-1} · min^{-1} and increased to 0.22 μmol · g^{-1} · min^{-1} during stimulation.

A detailed analysis of K_1 revealed furthermore that the stimulation-induced increase cannot be completely explained by an increase in CBF only but must at least be partly attributable to an increased transport rate for lactate. We estimated this increase to be in the order of 30% using the following relationships:

$$K_1 = \mathrm{CBF} * \mathrm{EF}, \quad (5)$$

where EF can be expressed according to Renkin (1959) and Crone (1963), and

$$EF = 1 - e^{-\mathrm{PS/CBF}}. \quad (6)$$

Combining Equations 5 and 6 yields the following:

$$PS = -\mathrm{CBF} * \ln(1 - K_1/\mathrm{CBF}), \quad (7)$$

where PS is the permeability–surface area product. We performed a simulation assuming a constant PS from baseline to ION stimulation. In previous experiments, the applied electrostimulation of the ION led to a mean increase of CBF from 0.35 to 0.50 ml · min^{-1} · ml^{-1} tissue (Weber et al., 2003). In the present series of 1-[^{11}C]L-lactate experiments, K_1 increased from 0.09 ± 0.01 to 0.12 ± 0.03 ml · min^{-1} · ml^{-1} tissue during ION. Inserting these numbers into Equation 7 demonstrates a 32% increase of PS, from 0.104 to 0.137 ml · min^{-1} · ml^{-1}. This suggests that monocarboxylate transporter (MCT) efficiency increases during increased demand.

Effect of MCT blockade on lactate uptake

Injection of CIN 30 min before [^{11}C]lactate tracer kinetic measurements reduced K_1 from 0.13 ± 0.01 to 0.09 ± 0.01

ml · min^{-1} · ml^{-1} tissue ($n = 5$; $p < 0.05$) and k_2 from 0.11 ± 0.01 to 0.07 ± 0.01 min^{-1} ($n = 5$; $p < 0.05$) (Fig. 3*C*, Table 1). CIN has been shown to permeate the blood–brain barrier and to be effective 30 min after intraperitoneal injection (Schurr et al., 2001). The reduction in K_1 after CIN administration is most likely attributable to the reduction of lactate transport by a partial blockade of MCTs. The concomitant reduction in k_2 cannot be reliably interpreted without additional biochemical measurements. The fact that the relative decrease of k_2 is of the same magnitude as the decrease of K_1 (−33%) points to the possibility that k_2 under CIN blockade represents back-diffusion of lactate into vascular space.

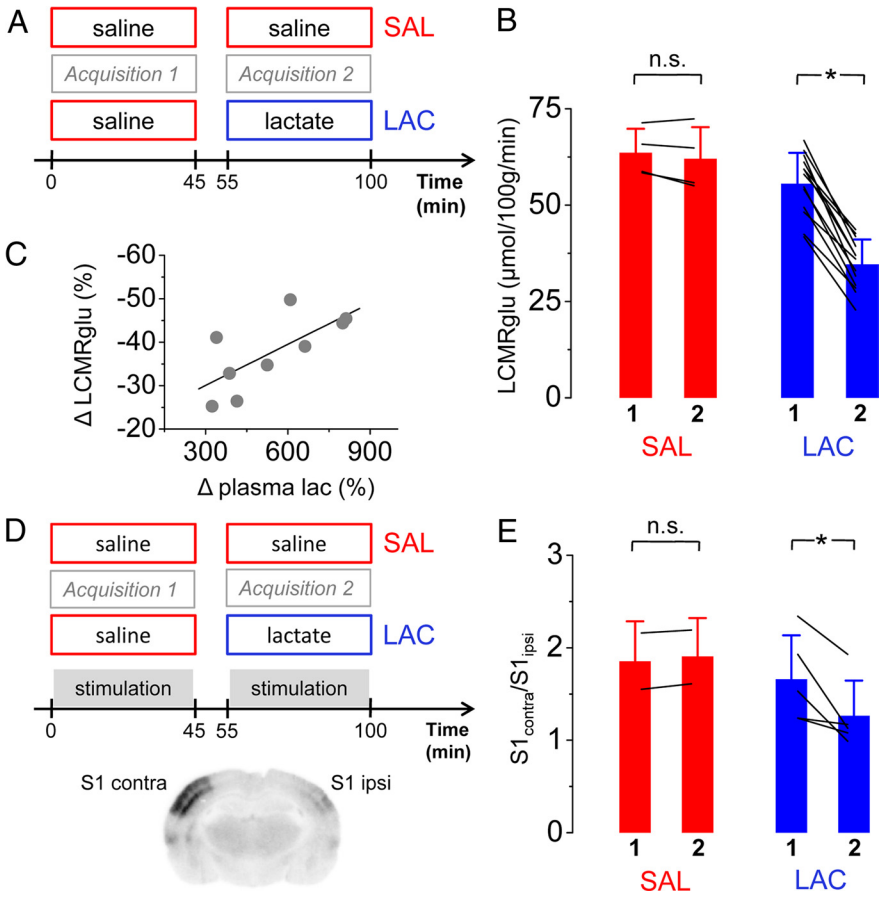

Figure 4. Lactate is preferred over glucose by the brain. ***A*** and ***D*** detail the protocol during baseline (***A***) and stimulation (***D***) conditions. Overall, hyperlactemia reduced $LCMR_{glu}$ by on average 38% in a dose-dependent manner (***B***, ***C***) during baseline conditions. In activated cortex ($S1_{contra}$), cerebral glucose utilization was further decreased. The effectiveness of stimulation was controlled autoradiographically (***D***). The ratio $S1_{contra}/S1_{ipsi}$ decreased from 1.65 ± 0.47 to 1.26 ± 0.37 (***E***). 1, Acquisition 1; 2, acquisition 2; LAC, hyperlactemia; SAL, saline. *$p < 0.05$, n.s., not significant. $n = 13$ for LAC group, $n = 4$ for SAL group at baseline conditions, $n = 5$ for LAC group, and $n = 2$ for SAL at stimulation conditions.

Increased blood lactate reduces the local metabolic rate of glucose

To address the question of how the brain processes blood-borne lactate compared with glucose, we artificially increased the supply of lactate to the brain by continuous intravenous infusion of sodium lactate (Fig. 4*A*). This led to a significant increase of plasma lactate levels (from 1.3 ± 0.6 to 5.8 ± 1.6 mmol/L; $n = 10$; $p < 0.05$). Plasma glucose levels were not affected by the continuous lactate infusions. In all examined animals, a clear reduction of $LCMR_{glu}$ was observed at resting conditions (decreases ranging from −25 to −49%; $n = 13$; $p < 0.05$) (Fig. 4*B*). The reduction of the cerebral glucose utilization was attributable to both a decreased delivery of glucose into the tissue (reflected by a change of K_1 from 0.16 ± 0.05 to 0.12 ± 0.03 ml · min^{-1} · ml^{-1} tissue; $n = 13$; $p < 0.05$) and a reduced phosphorylation by hexokinase (k_3 decreased from 0.04 ± 0.02 to 0.03 ± 0.01 min^{-1}; $n = 13$; $p < 0.05$). The replacement of glucose by lactate as an energy substrate occurred in a dose-dependent manner (Fig. 4*C*).

Reduction in glucose utilization is balanced by the excess of lactate consumption

The observed mean reduction in glucose utilization was 21 μmol/100 g/min (Fig. 4*B*). Because glucose has a six-carbon skeleton, this corresponds to 42 μmol/100 g/min three-carbon substrates such as pyruvate. The following estimation demonstrates that the decrease in glucose utilization is quantitatively matched by an increase in lactate use. For this purpose, we made the following assumptions: (1) lactate transport from blood into the brain equals K_1 * plasma lactate concentration ([Lac]), (2) K_1 (= 0.09 min^{-1} at baseline) does not markedly change within the range of lactate concentrations found in our experiments, and (3) all the lactate, which is taken up, is ultimately oxidized by the brain.

Thus, lactate uptake during baseline conditions in the FDG experiments was 12 μmol/100 g/min (= 0.09 min^{-1} * 1.3 mmol/L; mean K_1 determined in baseline 1-[^{11}C]lactate experiments (Fig. 3*B*) and mean [Lac] from FDG experiments during saline infusion) and 52 μmol/100 g/min during hyperlactemia (= 0.09 min^{-1} * 5.8 mmol/L; mean [Lac] during lactate infusion). The difference of lactate uptake between baseline and hyperlactemia conditions is therefore 40 μmol/100 g/min (52 μmol/100 g/min − 12 μmol/100 g/min). This matches the above mentioned reduction of three-carbon constituents derived from glucose during hyperlactemia.

Reduction of glucose consumption during hyperlactemia is more pronounced during activation

Our results further demonstrate that the reduction of glucose utilization is not only dependent on blood lactate levels but also on the level of activation. As shown in Figure 4, *D* and *E*, the decrease of glucose utilization was more pronounced on the activated side, as reflected by the decrease of the ratio contralateral/ipsilateral in the primary somatosensory cortex (i.e., $S1_{contra}$ vs $S1_{ipsi}$). During normolactemia, this ratio was 1.65 ± 0.47, but during hyperlactemia, it decreased to 1.26 ± 0.37 ($n = 5$; $p < 0.05$) (Fig. 4*E*). In two control animals, in which both acquisitions were performed under saline infusion, the ratio of $LCMR_{glu}$ between $S1_{contra}$ and $S1_{ipsi}$ remained the same during the first and the second acquisition (Fig. 4*E*). Plasma levels of glucose and lactate behaved in a similar manner as in the baseline group.

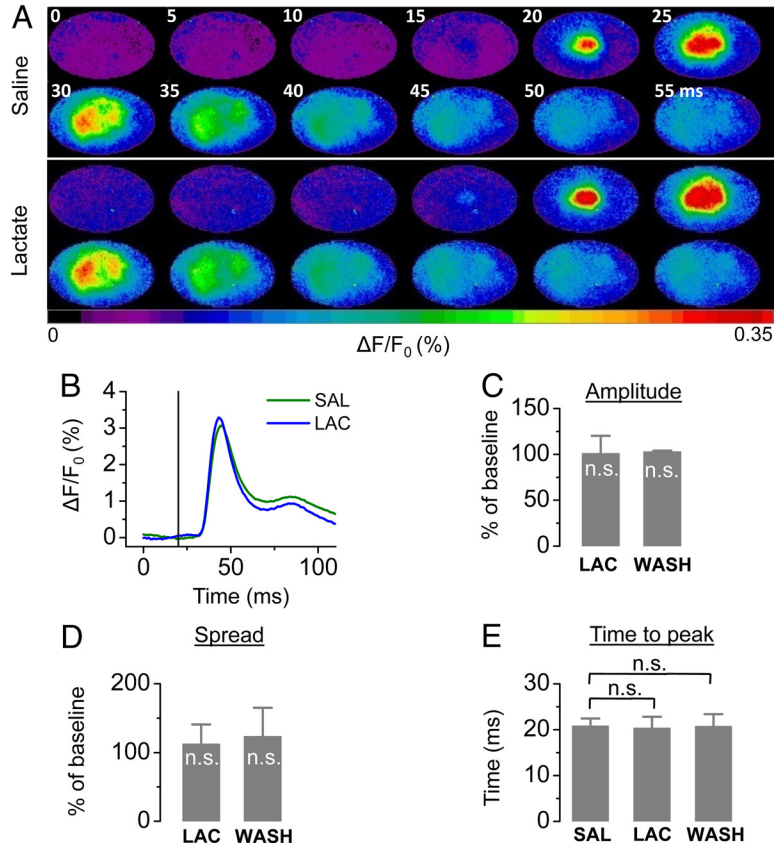

Figure 5. Cerebral integrity is not disrupted during hyperlactemia. ***A***, ***B***, A single example demonstrating the spread (***A***) and the amplitude over time (***B***) during saline (SAL) and lactate (LAC) infusion is shown. ***C–E***, Mean results of changes in amplitude (***C***), spread (***D***), and time-to-peak (***E***) ($n = 4$; n.s., not significant compared with baseline).

Neuronal activity is not reduced by lactate

To verify that the observed reduction in glucose utilization does not originate from a reduced requirement for energy of the brain attributable to impaired neural activity, we performed an additional series of VSD experiments during hyperlactemia. Under these conditions, increased lactate levels did not affect neuronal excitability (Fig. 5).

Discussion

For a long time, no functional role has been assigned to cerebral lactate. Contrarily, the presence of lactate in the brain has been interpreted as a sign of cerebral harm and of hypoxia (Siesjö, 1981). Over the past few decades, this perspective has changed and it has been postulated that lactate may also possess physiological functions relevant to the CNS. Important roles have been attributed to lactate such as the modulation of CBF (Gordon et al., 2008), as a buffer to sustain neuronal energy supply (Kasischke et al., 2004) and most prominently as a pivotal element in the neuron–glia metabolic cooperation to regulate energy supply in an activity-dependent manner (for review, see Pellerin and Magistretti, 2003; Magistretti, 2006). Furthermore, it has been shown recently that lactate levels are sensed by a specific type of neuron (orexin neurons in the lateral hypothalamus) to coordinate the balancing of brain activity and energy supply (Lam et al., 2005; Shimizu et al., 2007; Erlichman et al., 2008; Parsons and Hirasawa, 2010). Nevertheless, the details of brain energy metabolism in general and of lactate as a cerebral energy substrate in particular are still highly debated.

Lactate serves as a metabolic source for neurons

It has been shown *in vitro* that lactate oxidation is able to sustain excitatory synaptic activity (Schurr et al., 1988; Rouach et al., 2008), and there have been reports about lactate protecting cerebral function during hypoglycemia (Maran et al., 1994; King et al., 1998). However, the latter *in vivo* studies did not use direct neuronal readouts to assess synaptic activity, and glucose levels were above 2.5 mmol/L. The present study is the first *in vivo* demonstration of the maintenance of neuronal excitability in the presence of lactate as the primary energy source. The amplitude of the stimulation-induced increase in neuronal activity was maintained when lactate was supplied during severe hypoglycemia (Fig. 1). However, the increased delay of the VSD signal may indicate that lactate alone may not quite suffice to completely sustain neuronal functioning. Indeed, it has been shown that glucose is used by neurons to maintain their antioxidant status via the pentose phosphate pathway (PPP), which cannot be fueled by lactate (Magistretti, 2008; Herrero-Mendez et al., 2009). Because of the low plasma glucose levels and subsequent small glucose concentration gradient, the transport into neurons is inadequate (Barros and Deitmer, 2010) and presumably not enough substrate is available for the neurons to efficiently stimulate their antioxidant PPP. Neurons, which are thought to be especially vulnerable against reactive oxygen and nitrogen species, might not be capable of completely avoiding oxidative damage, which may lead to the observed delay of the electrical signal in the absence of glucose. Furthermore, this finding supports the important role in functional neuroenergetics dedicated to glucose because glucose is required by the astrocyte to pump glutamate (Magistretti et al., 1999). Second, lactate is transported by MCTs in a cotransport with protons (Hertz and Dienel, 2005). Lactate elevations as performed in our study may lead to changes in lactate influx that result in alterations of intracellular and extracellular pH in nerve tissue. These changes of the proton gradient could disturb the conductance of action potentials along nerve axons and lead to a delayed response.

Physiological meaning of k_2

Using 1-[^{11}C]L-lactate, we demonstrated that the brain readily oxidizes lactate at normal plasma lactate levels in accordance with recent work using 1- and 3-[^{13}C]L-lactate (Bouzier et al., 2000; van Hall et al., 2009; Boumezbeur et al., 2010). Our radiotracer approach enables the measurement of cerebral lactate oxidation without altering blood and tissue concentrations of lactate. In this respect, it is important to consider the physiological meaning of k_2. By definition, it represents the loss of label from tissue (Fig. 3*A*). The model depicted in Figure 3*A* demonstrates that the label can be lost by back-diffusion of labeled lactate into vascular space and as labeled CO_2. The latter pathway is more interesting because it is related to the oxidation of lactate, unless the diffusion of CO_2 across the blood–brain barrier is rate limiting. This is

unlikely because CO_2 back-diffusion does not seem restricted (Paulson, 2002). Radiolabeled lactate is processed by LDH and PDH before the label is lost as CO_2. Parameter k_2 can therefore be related to either of them or to both, depending on whether one of these steps is rate limiting. A flux estimation suggests that the processing by LDH and not PDH is the rate-limiting step.

If k_2 represented the conversion of pyruvate to acetyl-CoA, it would closely be related to the flux of pyruvate ($Flux_{PDH}$), which in this model would be expressed as follows: $Flux_{PDH} = k_2 * C_{pyr}$, or $C_{pyr} = Flux_{PDH}/k_2$, where C_{pyr} is the intracellular pyruvate concentration. Inserting a measured $Flux_{PDH}$ value of 1.13 $\mu mol \cdot g^{-1} \cdot min^{-1}$ (Oz et al., 2004) and the mean k_2 from our [^{11}C]L-lactate experiments (0.077 min^{-1}) yields an unphysiological pyruvate concentration of ~15 mmol/L. Measured pyruvate concentrations are in the range of 0.1–0.2 mmol/L (McIlwain, 1985).

In analogy, the conversion of lactate to pyruvate by LDH yields $Flux_{LDH} = k_2 * C_{lac}$, where C_{lac} is the intracellular lactate concentration. Using the numbers measured in humans by magnetic resonance spectroscopy [$Flux_{LDH} = 0.06\ \mu mol \cdot g^{-1} \cdot min^{-1}$) (Boumezbeur et al., 2010)], the above equation yields an intracellular lactate concentration of 0.06/0.077 = 0.78 mmol/L. This is in the same range as the reported number [1 mmol/L at plasma lactate levels of 1.5 mmol/L (Boumezbeur et al., 2010)]. These estimations suggest that k_2 is more related to the activity of LDH than PDH.

Evidence for increased lactate oxidation during stimulation

The increase of k_2 can be seen as a facilitation of the flux of substrates through the oxidative chain. However, an effective increase of the lactate flux furthermore requires that there is no relevant stimulation-induced drop in another factor driving lactate oxidation, e.g., the intracellular lactate concentration. However, such a drop seems unlikely for two reasons. First, the extracellular lactate concentration has been shown to increase during stimulation (Hu and Wilson, 1997; Caesar et al., 2008). Second, there is evidence for a translocation of MCT2 to the membrane surface during stimulation (Pierre et al., 2009), which would augment lactate transport and lead to higher intracellular lactate concentration. Such a translocation could also explain the increased permeability surface product during stimulation observed in this study.

There is another line of evidence supporting an elevated neuronal lactate oxidation during increased neuronal activity. An increased conversion of lactate to pyruvate is facilitated by an increase of the lactate/pyruvate ratio. Besides the increase in the lactate concentration (see above), a decrease of the pyruvate concentration or both causes a drop in this ratio. A reduced pyruvate concentration is achieved by a reduced glycolytic flux. Indeed, there is evidence from experiments in cell cultures that glutamate inhibits neuronal glucose uptake (Porras et al., 2004; Castro et al., 2009) and that upregulation of glycolysis under stress conditions is prevented (Herrero-Mendez et al., 2009). Recently, it has been found *in vivo* that increased neuronal firing mediates inhibition of glucose transport in neurons while stimulating astrocytic glucose uptake (Chuquet et al., 2010).

Concluding remarks

The results presented demonstrate *in vivo* that lactate is metabolized by neurons. Indeed, VSD imaging enabled us to follow a neuronal readout, which is supported by the supplied lactate during the experimental period. Considering the facts that intracerebral glycogen stores are relatively limited and consumed in the absence of exogenous glucose within a few minutes (Brown and Ransom, 2007) and that gluconeogenic activity in the brain is negligible (Nelson et al., 1985), it is evident that the neurons must rely on lactate as an energy substrate under hypoglycemic conditions. In addition, hepatic gluconeogenesis is suppressed by the insulin action. Thus, it can be suggested that the neuroprotective effect of lactate observed in previous studies (Gjedde and Crone, 1975; Schurr et al., 2001; Mason et al., 2006; Berthet et al., 2009) is attributable to direct lactate oxidation in neurons. However, we cannot exclude astrocytic lactate uptake and oxidation.

It is important to note that the data reported here using radiolabeled lactate provide evidence for the ability of neurons to increase lactate use during stimulation. During increased activation, we observed an increased turnover of 1-[^{11}C]lactate also under normoglycemia. Considering the fact that all the experiments were performed under anesthesia, thus reducing the overall metabolic rate by a factor of twofold to threefold (Hyder et al., 2006), it is reasonable to assume that an even larger contribution of lactate to brain metabolism may occur in the awake animal.

In summary, our multimodal experiments demonstrate that (1) lactate is capable of maintaining neuronal integrity to a large degree in the absence of glucose, (2) lactate is preferred over glucose if both substrates are available, (3) lactate is readily metabolized by the intact adult rodent brain, and (4) its metabolism is activity dependent.

References

Barros LF, Deitmer JW (2010) Glucose and lactate supply to the synapse. Brain Res Rev 63:149–159.

Berthet C, Lei H, Thevenet J, Gruetter R, Magistretti PJ, Hirt L (2009) Neuroprotective role of lactate after cerebral ischemia. J Cereb Blood Flow Metab 29:1780–1789.

Boumezbeur F, Petersen KF, Cline GW, Mason GF, Behar KL, Shulman GI, Rothman DL (2010) The contribution of blood lactate to brain energy metabolism in humans measured by dynamic 13C nuclear magnetic resonance spectroscopy. J Neurosci 30:13983–13991.

Bouzier AK, Thiaudiere E, Biran M, Rouland R, Canioni P, Merle M (2000) The metabolism of [3-(13)C]lactate in the rat brain is specific of a pyruvate carboxylase-deprived compartment. J Neurochem 75:480–486.

Brown AM, Ransom BR (2007) Astrocyte glycogen and brain energy metabolism. Glia 55:1263–1271.

Caesar K, Hashemi P, Douhou A, Bonvento G, Boutelle MG, Walls AB, Lauritzen M (2008) Glutamate receptor-dependent increments in lactate, glucose and oxygen metabolism evoked in rat cerebellum in vivo. J Physiol 586:1337–1349.

Castro MA, Beltrán FA, Brauchi S, Concha II (2009) A metabolic switch in brain: glucose and lactate metabolism modulation by ascorbic acid. J Neurochem 110:423–440.

Chuquet J, Quilichini P, Nimchinsky EA, Buzsáki G (2010) Predominant enhancement of glucose uptake in astrocytes versus neurons during activation of the somatosensory cortex. J Neurosci 30:15298–15303.

Cremer JE (1982) Substrate utilization and brain development. J Cereb Blood Flow Metab 2:394–407.

Crone C (1963) The permeability of capillaries in various organs as determined by use of the indicator diffusion method. Acta Physiol Scand 58:292–305.

Dombrowski GJ Jr, Swiatek KR, Chao KL (1989) Lactate, 3-hydroxybutyrate, and glucose as substrates for the early postnatal rat brain. Neurochem Res 14:667–675.

Erlichman JS, Hewitt A, Damon TL, Hart M, Kurascz J, Li A, Leiter JC (2008) Inhibition of monocarboxylate transporter 2 in the retrotrapezoid nucleus in rats: a test of the astrocyte-neuron lactate-shuttle hypothesis. J Neurosci 28:4888–4896.

Gallagher CN, Carpenter KL, Grice P, Howe DJ, Mason A, Timofeev I, Menon DK, Kirkpatrick PJ, Pickard JD, Sutherland GR, Hutchinson PJ (2009) The human brain utilizes lactate via the tricarboxylic acid cycle: a 13C-labelled microdialysis and high-resolution nuclear magnetic resonance study. Brain 132:2839–2849.

Gjedde A, Crone C (1975) Induction processes in blood-brain transfer of ketone bodies during starvation. Am J Physiol 229:1165–1169.

Gordon GR, Choi HB, Rungta RL, Ellis-Davies GC, MacVicar BA (2008) Brain metabolism dictates the polarity of astrocyte control over arterioles. Nature 456:745–749.

Hassel B, Bråthe A (2000) Cerebral metabolism of lactate in vivo: evidence for neuronal pyruvate carboxylation. J Cereb Blood Flow Metab 20: 327–336.

Herrero-Mendez A, Almeida A, Fernández E, Maestre C, Moncada S, Bolaños JP (2009) The bioenergetic and antioxidant status of neurons is controlled by continuous degradation of a key glycolytic enzyme by APC/C-Cdh1. Nat Cell Biol 11:747–752.

Hertz L, Dienel GA (2005) Lactate transport and transporters: general principles and functional roles in brain cells. J Neurosci Res 79:11–18.

Hu Y, Wilson GS (1997) A temporary local energy pool coupled to neuronal activity: fluctuations of extracellular lactate levels in rat brain monitored with rapid-response enzyme-based sensor. J Neurochem 69:1484–1490.

Hyder F, Patel AB, Gjedde A, Rothman DL, Behar KL, Shulman RG (2006) Neuronal-glial glucose oxidation and glutamatergic-GABAergic function. J Cereb Blood Flow Metab 26:865–877.

Kasischke KA, Vishwasrao HD, Fisher PJ, Zipfel WR, Webb WW (2004) Neural activity triggers neuronal oxidative metabolism followed by astrocytic glycolysis. Science 305:99–103.

King P, Kong MF, Parkin H, MacDonald IA, Barber C, Tattersall RB (1998) Intravenous lactate prevents cerebral dysfunction during hypoglycaemia in insulin-dependent diabetes mellitus. Clin Sci (Lond) 94:157–163.

Knudsen GM, Paulson OB, Hertz MM (1991) Kinetic analysis of the human blood-brain barrier transport of lactate and its influence by hypercapnia. J Cereb Blood Flow Metab 11:581–586.

Lam TK, Gutierrez-Juarez R, Pocai A, Rossetti L (2005) Regulation of blood glucose by hypothalamic pyruvate metabolism. Science 309:943–947.

Lippert MT, Takagaki K, Xu W, Huang X, Wu JY (2007) Methods for voltage-sensitive dye imaging of rat cortical activity with high signal-to-noise ratio. J Neurophysiol 98:502–512.

Magistretti PJ (2006) Neuron-glia metabolic coupling and plasticity. J Exp Biol 209:2304–2311.

Magistretti PJ (2008) Brain energy metabolism. In: Fundamental neuroscience (Squire L, Berg D, Bloom FE, du Lac S, Ghosh A, Spitzer N, eds), pp 271–293. San Diego: Academic.

Magistretti PJ, Pellerin L, Rothman DL, Shulman RG (1999) Energy on demand. Science 283:496–497.

Maran A, Cranston I, Lomas J, Macdonald I, Amiel SA (1994) Protection by lactate of cerebral function during hypoglycaemia. Lancet 343:16–20.

Mason GF, Petersen KF, Lebon V, Rothman DL, Shulman GI (2006) Increased brain monocarboxylic acid transport and utilization in type 1 diabetes. Diabetes 55:929–934.

McIlwain H, Bachelard HS (1985) Biochemistry and the central nervous system, Ed 5. New York: Churchill Livingstone.

Mikolajczyk K, Szabatin M, Rudnicki P, Grodzki M, Burger C (1998) A JAVA environment for medical image data analysis: initial application for brain PET quantitation. Med Inform (Lond) 23:207–214.

Nehlig A, Pereira de Vasconcelos A (1993) Glucose and ketone body utilization by the brain of neonatal rats. Prog Neurobiol 40:163–221.

Nelson T, Lucignani G, Atlas S, Crane AM, Dienel GA, Sokoloff L (1985) Reexamination of glucose-6-phosphatase activity in the brain in vivo: no evidence for a futile cycle. Science 229:60–62.

Oz G, Berkich DA, Henry PG, Xu Y, LaNoue K, Hutson SM, Gruetter R (2004) Neuroglial metabolism in the awake rat brain: CO_2 fixation increases with brain activity. J Neurosci 24:11273–11279.

Parsons MP, Hirasawa M (2010) ATP-sensitive potassium channel-mediated lactate effect on orexin neurons: implications for brain energetics during arousal. J Neurosci 30:8061–8070.

Paulson OB (2002) Blood-brain barrier, brain metabolism and cerebral blood flow. Eur Neuropsychopharmacol 12:495–501.

Pellerin L, Magistretti PJ (1994) Glutamate uptake into astrocytes stimulates aerobic glycolysis: a mechanism coupling neuronal activity to glucose utilization. Proc Natl Acad Sci U S A 91:10625–10629.

Pellerin L, Magistretti PJ (2003) Food for thought: challenging the dogmas. J Cereb Blood Flow Metab 23:1282–1286.

Pierre K, Chatton JY, Parent A, Repond C, Gardoni F, Di Luca M, Pellerin L (2009) Linking supply to demand: the neuronal monocarboxylate transporter MCT2 and the alpha-amino-3-hydroxyl-5-methyl-4-isoxazole-propionic acid receptor GluR2/3 subunit are associated in a common trafficking process. Eur J Neurosci 29:1951–1963.

Porras OH, Loaiza A, Barros LF (2004) Glutamate mediates acute glucose transport inhibition in hippocampal neurons. J Neurosci 24:9669–9673.

Renkin EM (1959) Transport of potassium-42 from blood to tissue in isolated mammalian skeletal muscles. Am J Physiol 197:1205–1210.

Rouach N, Koulakoff A, Abudara V, Willecke K, Giaume C (2008) Astroglial metabolic networks sustain hippocampal synaptic transmission. Science 322:1551–1555.

Schurr A, West CA, Rigor BM (1988) Lactate-supported synaptic function in the rat hippocampal slice preparation. Science 240:1326–1328.

Schurr A, Payne RS, Miller JJ, Tseng MT, Rigor BM (2001) Blockade of lactate transport exacerbates delayed neuronal damage in a rat model of cerebral ischemia. Brain Res 895:268–272.

Shackford SR, Schmoker JD, Zhuang J (1994) The effect of hypertonic resuscitation on pial arteriolar tone after brain injury and shock. J Trauma 37:899–908.

Shimizu H, Watanabe E, Hiyama TY, Nagakura A, Fujikawa A, Okado H, Yanagawa Y, Obata K, Noda M (2007) Glial Nax channels control lactate signaling to neurons for brain [Na+] sensing. Neuron 54:59–72.

Siesjö BK (1981) Cell damage in the brain: a speculative synthesis. J Cereb Blood Flow Metab 1:155–185.

Sokoloff L, Reivich M, Kennedy C, Des Rosiers MH, Patlak CS, Pettigrew KD, Sakurada O, Shinohara M (1977) The [14C]deoxyglucose method for the measurement of local cerebral glucose utilization: theory, procedure, and normal values in the conscious and anesthetized albino rat. J Neurochem 28:897–916.

van Hall G (1999) Correction factors for 13C-labelled substrate oxidation at whole-body and muscle level. Proc Nutr Soc 58:979–986.

van Hall G, Strømstad M, Rasmussen P, Jans O, Zaar M, Gam C, Quistorff B, Secher NH, Nielsen HB (2009) Blood lactate is an important energy source for the human brain. J Cereb Blood Flow Metab 29:1121–1129.

Weber B, Burger C, Biro P, Buck A (2002) A femoral arteriovenous shunt facilitates arterial whole blood sampling in animals. Eur J Nucl Med Mol Imaging 29:319–323.

Weber B, Späth N, Wyss M, Wild D, Burger C, Stanley R, Buck A (2003) Quantitative cerebral blood flow measurements in the rat using a beta-probe and H2 15O. J Cereb Blood Flow Metab 23:1455–1460.

Wyss MT, Obrist NM, Haiss F, Eckert R, Stanley R, Burger C, Buck A, Weber B (2009) A beta-scintillator for surface measurements of radiotracer kinetics in the intact rodent cortex. Neuroimage 48:339–347.

Section 2 –
Evaluation of PET tracers to establish clinical usefulness

Part I: Establishment and advancements of novel imaging techniques for preclinical *in vivo* radiotracer testing

I.1. Quantitative cerebral blood flow measurements in the rat using a beta-probe and $H_2{}^{15}O$

Journal of Cerebral Blood Flow and Metabolism, 2003, Vol 23 (12), Pages 1455-1460

I.2. A beta-scintillator for surface measurements of radiotracer kinetics in the intact rodent cortex

Neuroimage, 2009, Vol 48 (2), Pages 339-347

I.3. Quantitative evaluation of ^{11}C-ABP688 as PET ligand for the measurement of the glutamate receptor subtype 5 using autoradiographic studies and a beta-scintillator

Neuroimage, 2007, Vol 35 (3), Pages 1086-1092

Journal of Cerebral Blood Flow & Metabolism
23:1455–1460 © 2003 The International Society for Cerebral Blood Flow and Metabolism
Published by Lippincott Williams & Wilkins, Inc., Baltimore

Quantitative Cerebral Blood Flow Measurements in the Rat Using a Beta-Probe and $H_2{}^{15}O$

*Bruno Weber, *Nicolas Späth, *Matthias Wyss, *Damian Wild, *Cyrill Burger, †Ross Stanley, and *Alfred Buck

**PET Center, Division of Nuclear Medicine, University Hospital Zurich, Zurich, and †Center Suisse d'Electronique et de Microtechnique SA, Neuchatel, Switzerland*

Summary: Beta-probes are a relatively new tool for tracer kinetic studies in animals. They are highly suited to evaluate new positron emission tomography tracers or measure physiologic parameters at rest and after some kind of stimulation or intervention. In many of these experiments, the knowledge of CBF is highly important. Thus, the purpose of this study was to evaluate the method of CBF measurements using a beta-probe and $H_2{}^{15}O$. CBF was measured in the barrel cortex of eight rats at baseline and after acetazolamide challenge. Trigeminal nerve stimulation was additionally performed in five animals. In each category, three injections of 250 to 300 MBq $H_2{}^{15}O$ were performed at 10-minute intervals. Data were analyzed using a standard one-tissue compartment model (K_1 = CBF, k_2 = CBF/p, where *p* is the partition coefficient). Values for K_1 were 0.35 ± 0.09, 0.58 ± 0.16, and 0.49 ± 0.03 mL · min^{-1} · mL^{-1} at rest, after acetazolamide challenge, and during trigeminal nerve stimulation, respectively. The corresponding values for k_2 were 0.55 ± 0.12, 0.94 ± 0.16, and 0.85 ± 0.12 min^{-7}, and for p were 0.64 ± 0.05, 0.61 ± 0.07, and 0.59 ± 0.06.The standard deviation of the difference between two successive experiments, a measure for the reproducibility of the method, was 10.1%, 13.0%, and 5.7% for K_1, k_2, and p, respectively. In summary, beta-probes in conjunction with $H_2{}^{15}O$ allow the reproducible quantitative measurement of CBF, although some systematic underestimation seems to occur, probably because of partial volume effects. **Key Words:** Cerebral blood flow—Beta-probe—Positron emission tomography.

Beta-probes have recently been introduced to measure the time course of tracer uptake with high temporal resolution (Pain et al., 2002, 2000; Woody et al., 2002; Zimmer et al., 2002). The applications of the method are widespread. Examples are blocking and displacing experiments with receptor ligands or the measurement of glucose metabolism using ^{18}fluorodeoxyglucose under different conditions. Compared to an animal positron emission tomography (PET) system, they are relatively cheap, the temporal resolution is much higher and measurements can potentially be performed in the awake animal. However, simultaneous information can only be obtained from a few locations, whereas the PET systems cover the whole brain. In some applications of the beta-probe, the knowledge of CBF is important. The purpose of this study was to evaluate a beta-probe with regard to CBF measurements in conjunction with $H_2{}^{15}O$.

Received June 24, 2003; final version received August 19, 2003; accepted August 21, 2003.

This work was supported by the Vision-Stiftung für bildgebende Verfahren in der Medizin, the OPO Stiftung, and the Radium Stiftung.

Address correspondence and reprint requests to Dr. Buck, University Hospital Zurich, Division of Nuclear Medicine, Rämistrasse 100, 8091 Zurich, Switzerland; e-mail: buck@nuklearmed.unizh.ch

MATERIALS AND METHODS

Animal preparation

The study included eight male rats (Sprague-Dawley) weighing approximately 300 g. Surgery was performed under isoflurane anesthesia and involved the placement of an arteriovenous shunt from the right femoral artery to the right femoral vein, tracheotomy for mechanical ventilation and craniotomy for the placement of the beta-probe. The actual experiment was then performed under alpha-chloralose anesthesia. 25 mg kg^{-1} body weight was injected in the axillary fatty tissue immediately after the induction of the anesthesia. After surgery, alpha chloralose (made soluble at room temperature by mixing it with 2-hydroxypropyl-beta-cyclodextrin (Storer et al., 1997) was constantly infused at 20 mg · kg^{-1} · h^{-1}. The shunt was used for the continuous monitoring of arterial blood pressure, the infusion of $H_2{}^{15}O$, α-chloralose, acetazolamide, and lethal dose of pentobarbital at the end of the experiment, and for the continuous measurement of ^{15}O activity for the arterial input curve. For the latter purpose, the shunt was run through a coincidence probe that stored the data at 1-second intervals. The online arterial sampling procedure is described in detail elsewhere (Weber et al., 2002).

DOI: 10.1097/01.WCB.0000095799.98378.7D

Electrical stimulation

For the stimulation of the whisker-to-barrel pathway, the infraorbital branch of the trigeminal nerve was stimulated with two stainless steel electrodes. The cathode was inserted through the infraorbital hiatus and the anode was positioned in the masticatory muscle. The current of the stimulation was adjusted to produce whisker movements (pulses of 1-millisecond duration at 1.2-mA, 2-Hz stimulation frequency, using an isolated constant-current stimulator). The stimulation started 30 seconds before the $H_2{}^{15}O$ bolus injection and lasted 210 seconds.

Acetazolamide challenge

Acetazolamide is a carbonic anhydrase inhibitor that leads to vasodilatation and can thus be used to induce a global increase in cerebral blood flow. Acetazolamide (66 mg/kg) was intravenously injected in 0.3 mL saline during a 30-second period.

Automated $H_2{}^{15}O$ bolus injection

For the administration of the short-living $H_2{}^{15}O$ (half-life, 122 seconds) in high concentrations, a special injection instrumentation is mandatory. ^{15}O was produced continuously in the cyclotron and transferred to the synthesis/injection device. (More information on this device can be found at http://www.swisstrace.com.) The injection/synthesis device continuously delivered $H_2{}^{15}O$ at a rate of 60 mL/h in a closed loop. For the bolus injections, a peristaltic precision pump (Ismatec SA, Glattbrugg, Switzerland) drew approximately 300 MBq $H_2{}^{15}O$ from this loop at a rate of 0.4 mL/min during a 40-second period. This high radioactivity concentration requires careful lead shielding, not only for the experimenters but also to reduce background counts in the photomultiplier tube and coincidence counter.

Beta-probe

The beta-probe used is a modification of the sensor developed by Pain et al (2000) (for further information, see http://www.swisstrace.com). It consists of a scintillation tip (Bicron, BF12, Newbury, OH, U.S.A.) with a length of 0.8 mm and a diameter of 0.25 mm attached to a high numerical aperture glass fiber. The probe was made light-tight by applying a uniform coating of silver particles. The scintillations were measured using a photomultiplier tube and counting electronics (PMT 9131/350B, Package P30CWAD5–08, Electron Tubes Limited). The main contributions to unwanted counts are (1) the dark count of the PMT, (2) background light, and (3) Cerenkov radiation. Dark counts below 1 cps were achieved with the system. Background light is a serious problem that can be eliminated by working in total darkness or by using light-tight probes. Photons can also be created by fast-moving β particles. A particle moving through a medium faster than the speed of light in that medium will radiate light. This light is known as Cerenkov radiation; its spectrum follows the inverse of the wavelength, so it appears blue. Cerenkov radiation is created both in the tissue of the animal and theoretically in the fiber itself. To overcome the problem of Cerenkov radiation, some investigators use a double-probe system where the reference probe has no scintillating fiber and is located close to the scintillating probe so that the contribution from Cerenkov can be subtracted (Pain et al., 2000). This has the drawback of increased complexity, and increased dark noise. A coated probe has an advantage in that the Cerenkov light coming from outside the probe cannot enter it. To determine the signal not originating from the scintillating tip, the following experiment was performed. The probe was lowered into a homogeneous solution of $H_2{}^{15}O$ (50 MBq/mL) to various depths: 2 mm (tip just covered), 7 mm, and 12 mm. Although lowering the probe from position a to b increased the count rate by 34.0%, there was only a 3.5% further increase from position b to c. The first increase is easily explained by a partial volume effect. If Cerenkov radiation is created inside the fiber, the signal should increase linearly with depth. However, the small second increase demonstrates that this is unlikely and that potential Cerenkov radiation produced in the fiber is therefore negligible.

After each experiment, position c was also used to cross-calibrate the beta-probe with the coincidence counter used to measure the arterial input curve. For this purpose, the shunt tubing was additionally filled with the same $H_2{}^{15}O$ solution and counted with the coincidence counter. For data analysis, all data were background corrected, converted to kBq/mL, and decay corrected to the time point of injection.

The probe was inserted in the brain using a stereotactic frame (David Kopf Instruments, Tujunga, CA, U.S.A.). The skull was exposed and a craniotomy was performed using a dental drill. The dura was carefully incised at the insertion position, which was (according to bregma) 2 mm posterior and 6 mm lateral for the barrel cortex and 3 mm posterior and 3 mm lateral for the combined thalamic/cortical penetrations. This position was adjusted to avoid large superficial blood vessels. The probe was carefully lowered to a depth of 1.4 mm for cortical and 6 mm for thalamic recordings. Only one probe penetration was performed per animal. The count rate was stored on a personal computer using a bin width of 1 second.

Experimental protocols

After each $H_2{}^{15}O$ injection, 180 seconds of data were recorded. Injections were spaced at least 10 minutes apart to let the activity decay to background level. Each experimental block started under baseline conditions (barrel cortex, $n = 8$). Then, measurements were performed during electrical stimulation of the trigeminal nerve (in five animals only). The final measurements were acquired starting 10 minutes after administration of acetazolamide. Thalamic experiments were performed in three animals. After measurements in the cortex at baseline, the probe was advanced to the thalamus leaving the surface position unchanged. Acetazolamide was then injected and additional thalamic measurements were taken. The last measurements were acquired shortly after the probe was retracted to the original cortical depth. Three consecutive injections were made in each condition.

Model

The basis of the calculation of the CBF measurements was the one-tissue compartment model including a partition coefficient for $H_2{}^{15}O$. The change of the radioactivity concentration in tissue Ct is then defined by the following differential equation:

$$dCt/dt = CBF(Ca(t) - Ct(t)/p) \quad (1)$$

where *Ca* is the arterial tracer concentration and *p* is the tissue partition coefficient (that fraction of tissue that is permeable for $H_2{}^{15}O$). In this configuration, Ct is the concentration of $H_2{}^{15}O$ in 1 mL of brain and it is assumed that $H_2{}^{15}O$ immediately reaches a homogeneous concentration in permeable space and no division into a vascular and a tissue compartment is necessary. The analytical solution of Eq. 1 is

$$Ct = CBF \exp(-CBF/p\ t) \otimes Ca \quad (2)$$

where $\otimes$ signifies mathematical convolution. In a K_1, k_2 notation, Eq. 2 becomes

$$Ct = K_1 \exp(-k_2 t) \otimes Ca \quad (3)$$

where K_1 = CBF and $k_2 = K_1/p$.

Equation 3 was fitted to the data using least squares fitting (Marquardt algorithm) implemented in the software PMOD (http://www.pmod.com; Mikolajczyk et al., 1998). Before data analysis, tissue time–activity curves and arterial input curves were corrected for physical decay.

Statistical analysis

The means of K_1, k_2, and p at baseline and after acetazolamide challenge were statistically compared using the signed rank test. Bland-Altman analysis was used to assess the reproducibility (Bland and Altman, 1986). In this method, the standard deviation of the difference of consecutive experiments (in this study, experiment 2 and 3 of each block) is a measure for the reproducibility. The differences were expressed as percentage of the mean of the two measurements. A total of 21 differences were evaluated. Only the cortical experiments were included in this analysis.

RESULTS

The high reproducibility of the shape of the input curves is demonstrated in Figure 1. The peak, which was reached at 50 seconds was followed by a rapid decline, lasting until 60 seconds. The further time-course was flat due to recirculating $H_2{}^{15}O$.

A typical blood and tissue curve and the model fit after injection of acetazolamide are shown in Fig. 2. The absence of any bias in the residuals demonstrates the goodness-of-fit.

The result of the model fitting is summarized in Table 1. In each animal there was a marked and reproducible increase of K_1 and k_2 after acetazolamide challenge. The percentage increase (mean ± SD) from baseline was 66 ± 27 ($T = 0$; $P < 0.01$) and 72 ± 22 ($T = 0$; $P < 0.01$) for K_1 and k_2, respectively. All five animals in which trigeminal stimulation was performed displayed a pronounced increase of K_1 and k_2 in the corresponding barrel cortex. Because of the small sample size ($n = 5$), no statistical analysis was performed. The percentage increase from baseline was 47 ± 29 for K_1 and 59 ± 44 for k_2. No significant change in the partition coefficient p was noticed between the different conditions. In the eight baseline experiments, p in cortex was 0.64 ± 0.05. In the three animals with a thalamic measurement, p in thalamus was higher than in cortex (18%, 13%, and 8% higher than in cortex).

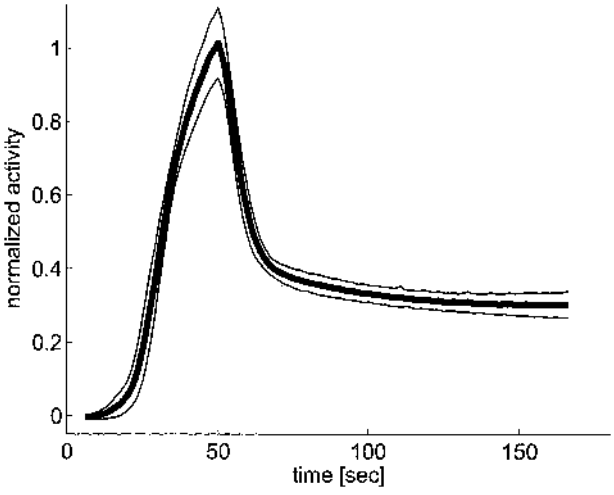

FIG. 1. Decay-corrected arterial input functions measured in the arteriovenous shunt. The graph displays mean ± SD of all injections performed in this study. Before averaging, all curves were normalized to the integrated activity between 0 and 160 seconds and time-shifted. The peak of the resulting average curve was then scaled to 1.

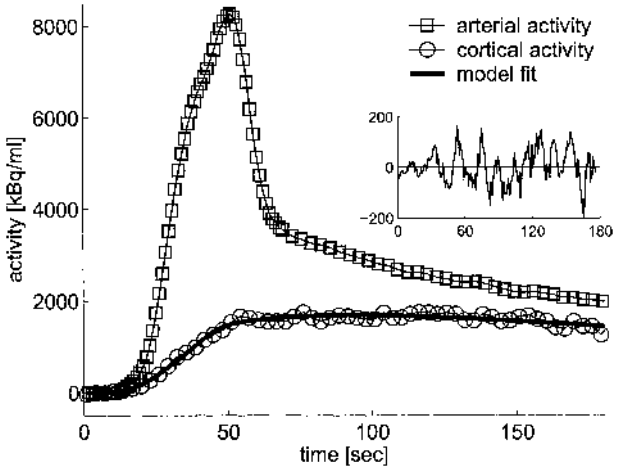

FIG. 2. A typical example of a tissue time–activity curve, an arterial input curve, and the model fit of an experiment after administration of acetazolamide. All data are corrected for ^{15}O decay. The insert represents the residuals. In this experiment, the values of K_1 and k_2 were 0.48 mL · min^{-1} · mL^{-1} and 0.71 min^{-1}. Note that the ratio of counts in tissue and blood at 180 seconds is 0.89, which is higher than the equilibrium value of 0.68 because equilibrium is not yet reached at 180 seconds. Exp, experiment.

The Bland-Altman plots of the reproducibility are summarized in Fig. 3. The highest reproducibility (lowest standard deviation between successive measurements 2 and 3) was achieved for p, followed by K_1 and k_2. For all parameters, all except one data point were contained in the range mean ± 2 SD.

DISCUSSION

The purpose of this work was to validate the quantification of CBF measurements using a beta-probe and $H_2{}^{15}O$. The validation is focused on three major aspects: (1) the magnitude of the CBF values; (2) the response to stimulation; and (3) the reproducibility.

Magnitude of K_1, k_2, and p

The K_1 values seem to systematically underestimate the true CBF. Compared with ^{14}C iodoantipyrine autoradiography data published by Nakao et al. (2001), who used a similar anesthetic protocol, our values in the barrel cortex are approximately 40% lower (0.35 vs. 0.6

TABLE 1. *Summarized results of the model fitting*

Animal	Location	Type	K1 (mL·min^{-1}·mL^{-1})	k2 (min^{-1})	p (K1/k2) (mL/mL)
1	ctx	base	0.245	0.402	0.611
1	ctx	stim	0.485	0.955	0.508
1	ctx	ACZ	0.443	0.786	0.564
2	ctx	base	0.393	0.687	0.572
2	ctx	stim	0.539	0.994	0.547
2	ctx	ACZ	0.526	1.008	0.522
3	ctx	base	0.347	0.582	0.598
3	ctx	stim	0.480	0.806	0.595
3	ctx	ACZ	0.591	0.883	0.669
4	ctx	base	0.353	0.543	0.650
4	ctx	stim	0.491	0.787	0.624
4	ctx	ACZ	0.466	0.823	0.567
5	ctx	base	0.384	0.533	0.722
5	ctx	stim	0.468	0.705	0.669
5	ctx	ACZ	0.600	0.998	0.601
6	ctx	base	0.309	0.496	0.636
6	ctx	ACZ	0.672	1.032	0.651
6	thal	base	0.375	0.513	0.754
7	ctx	base	0.532	0.738	0.720
7	ctx	ACZ	0.933	1.239	0.754
7	thal	base	0.837	1.021	0.818
8	ctx	base	0.270	0.434	0.622
8	ctx	ACZ	0.440	0.728	0.604
8	thal	base	0.382	0.565	0.677
n = 8	ctx	mean (SD) base	0.354 (0.089)	0.552 (0.116)	0.641 (0.055)
n = 5	ctx	mean (SD) stim	0.493 (0.027)	0.849 (0.121)	0.589 (0.063)
n = 8	ctx	mean (SD) ACZ	0.584 (0.164)	0.937 (0.165)	0.616 (0.073)

The values represent the mean of three successive experiments.
base, baseline; stim, trigeminal nerve stimulation; ACZ, acetazolamide challenge; ctx, cortex; thal, thalamus.

min^{-1}). This discrepancy is most likely due to an underestimation of the true cortical $H_2{}^{15}O$ concentration because of partial volume effects. The maximum free path length of a positron emitted from ^{15}O in water is 8.2 mm and the most probable free path length is approximately 2.7 mm, indicating that most of the signal picked up by the beta-probe originates from a sphere that is approximately 5 mm in diameter. During calibration, this sphere contains a homogeneous radioactivity concentration. Because the rat cortex is approximately 2 mm thick, the volume contributing to signal in a probe positioned in the cortex is heterogeneous and includes not only gray matter, but also white matter and air above the cortex. This leads to an underestimation of the true cortical $H_2{}^{15}O$

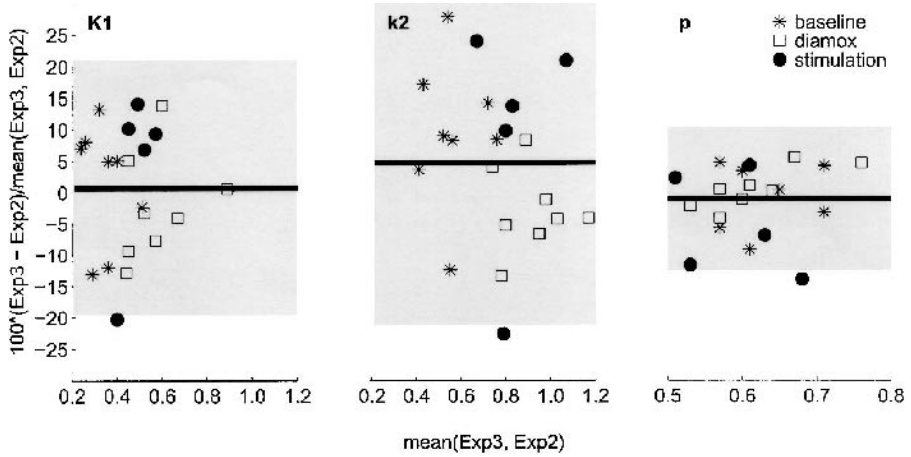

FIG. 3. Bland-Altman plot of the reproducibility of K_1, k_2, and p. The analysis included eight animals for baseline and acetazolamide and five animals for the trigeminal stimulation. In each experimental block (i.e., baseline, acetazolamide, and trigeminal nerve stimulation) there were three consecutive injections 10 minutes apart. The important parameter for reproducibility is the standard deviation of the difference between the second and third experiments (experiment 3 – experiment 2), which is indicated as percentage of the mean. The middle line represents the mean difference; the top and bottom of the gray rectangle are mean ± 2 SD of the pooled differences of all types of experiments. The respective values (mean ± SD) for K_1, k_2, and p respectively were 0.6 ± 10.1%, 4.7 ± 13.0%, and −1.1 ± 5.7%.

concentration and, consecutively, K_1. This underestimation would also explain the low value of p (K_1/k_2, 0.64 ± 0.055 at baseline). One would expect a value in the order of 0.95 mL/mL (Ginsberg et al., 1982). This reasoning is supported by the result that K_1 and p are higher in the thalamus than in the cortex. There the gray matter volume surrounding the probe is larger, leading to smaller partial volume effects. The situation is considerably more favorable for ^{11}C and ^{18}F with maximum free path lengths of 4.1 and 2.4 mm.

While K_1 describes the delivery of $H_2{}^{15}O$, k_2 is determined by the washout. The baseline value (0.55 ± 0.11 min^{-1}) is closer to the autoradiographically determined CBF values reported by Nakao et al. (2001). Considering the relationship CBF = k_2 p, one could use k_2 multiplied by an estimated p as an indicator of CBF. If one assumes a p value of 0.95, the baseline CBF would be 0.52 $mL \cdot min^{-1} \cdot mL^{-1}$. This value probably still underestimates true CBF, because k_2 is also affected by the partial volume effects (tissue heterogeneity), although to a lesser degree than K_1 (Blomqvist et al., 1995; Herholz and Patlak, 1987). In our view, there is no simple way to correct for the partial volume effects. The problem is the heterogeneity in the volume contributing to signal in the probe. The different time course of the counts in the compartments of this volume render a simple correction by a constant factor inaccurate.

Response of K_1 and k_2 to stimulation

The increase of K_1 (43%) in the barrel cortex during trigeminal stimulation is in line with the results of Nielsen and Lauritzen (2001). Using laser-Doppler flowmetry in the chloralose-anesthetized rat, they found an approximately 40% change during trigeminal nerve stimulation at 2 Hz. These values are somewhat higher than the 28% increase reported by Nakao et al. (2001). The discrepancy can be explained by the different stimulation methods (mechanical whisker stimulation vs. electrical trigeminal nerve stimulation). The mean of k_2 increased from 0.54 to 0.84 min^{-1}, corresponding to 54%.

All animals also displayed a marked increase of K_1 and k_2 after acetazolamide challenge; the increase of the mean was 65% and 70%, respectively.

Reproducibility

The Bland-Altman plots demonstrate that the standard deviation of two successive measurements is in the order 10%, 13%, and 6% for K_1, k_2, and p, respectively. A direct comparison with the hydrogen-clearance method, the only other quantitative method allowing serial measurements in the same animal, is difficult. However, it is in line with human (Carroll et al., 2002; Matthew et al., 1993) and monkey (Iida et al., 2000) $H_2{}^{15}O$ PET measurements, for which the reproducibility is in the order of 10%.

The data suggest that K_1 and k_2 are reasonable measures of CBF. Compared with k_2, K_1 is somewhat more reproducible but underestimates true CBF to a higher degree.

Comparison with alternative methods

In small animals, probably the most accurate quantitative method for CBF measurement is ^{14}C-iodoantipyrine autoradiography (Nakao et al., 2001; Ohno et al., 1979; Sakurada et al., 1978). This method also has the highest spatial resolution. The obvious disadvantage is the need to kill the animals after one experiment, which renders serial experiments in the same animal impossible. Other possibilities that allow serial measurements are the methods based on laser-Doppler flowmetry (Dirnagl et al., 1989; Skarphedinsson et al., 1988) and hydrogen clearance (Haining et al., 1968; Moskalenko et al., 1996; Moskalenko Yu et al., 1995; von Kummer and Herold, 1986; von Kummer et al., 1986). Laser-Doppler flowmetry has become very popular, one reason being that brain tissue is not injured. However, it is not a quantitative method. The hydrogen clearance method yields theoretically quantitative CBF values with high temporal, but relatively low spatial resolution, as does the beta-probe. Another method is the use of the newly introduced animal PET scanners. However, with the present systems the temporal resolution seems to be too low to allow CBF measurements with $H_2{}^{15}O$, and studies using other potential PET flow tracers have not been published.

Applications of beta-probes include neuropharmacologic experiments, blocking and displacing experiments with receptor ligands, or the measurement of glucose metabolism using ^{18}fluorodeoxyglucose under different physiologic conditions and pharmacological interventions. In such experiments, the additional measurement of CBF may contribute important information. For instance, one important parameter of radioligands is the first-pass extraction fraction (EF). In compartmental models the first parameter K_1 describes transport of tracer from blood into tissue; it is determined by the relationship K_1 = CBF EF. Thus, EF can be calculated from K_1 and CBF. An important advantage of $H_2{}^{15}O$ is the short physical half-life of ^{15}O of 122 seconds, meaning that experiments can be performed at 10-minute intervals. A disadvantage of the presented method is its complexity and the requirement of a cyclotron. However, in centers where the necessary equipment is available, it offers an elegant technique for CBF measurements, especially in situations where the beta-probe is used for other experiments that additionally require the knowledge of CBF. Another disadvantage is the relatively large diameter of the beta-probe (0.25 mm). It is possible that new, more sensitive scintillator materials may allow a reduction in this diameter. Furthermore, because of the

high radioactivity concentrations used, radiation safety issues have to be considered. In the present study, movable lead shielding was used.

In summary, the beta-probe and $H_2{}^{15}O$ allow quantitative, reproducible, and serial measurements of CBF, although true flow values in cortex are systematically underestimated. The reproducibility is comparable to human $H_2{}^{15}O$ PET.

REFERENCES

Bland JM, Altman DG (1986) Statistical methods for assessing agreement between two methods of clinical measurement. *Lancet* 1:307–310

Blomqvist G, Lammertsma AA, Mazoyer B, Wienhard K (1995) Effect of tissue heterogeneity on quantification in positron emission tomography. *Eur J Nucl Med* 22:652–663

Carroll TJ, Teneggi V, Jobin M, Squassante L, Treyer V, Hany TF, Burger C, Wang L, Bye A, Von Schulthess GK, Buck A (2002) Absolute quantification of cerebral blood flow with magnetic resonance, reproducibility of the method, and comparison with H2(15)O positron emission tomography. *J Cereb Blood Flow Metab* 22:1149–1156

Dirnagl U, Kaplan B, Jacewicz M, Pulsinelli W (1989) Continuous measurement of cerebral cortical blood flow by laser-Doppler flowmetry in a rat stroke model. *J Cereb Blood Flow Metab* 9:589–596

Ginsberg MD, Lockwood AH, Busto R, Finn RD, Butler CM, Cendan IE, Goddard J (1982) A simplified *in vivo* autoradiographic strategy for the determination of regional cerebral blood flow by positron emission tomography: theoretical considerations and validation studies in the rat. *J Cereb Blood Flow Metab* 2:89–98

Haining JL, Turner MD, Pantall RM (1968) Measurement of local cerebral blood flow in the unanesthetized rat using a hydrogen clearance method. *Circ Res* 23:313–324

Herholz K, Patlak CS (1987) The influence of tissue heterogeneity on results of fitting nonlinear model equations to regional tracer uptake curves: with an application to compartmental models used in positron emission tomography. *J Cereb Blood Flow Metab* 7:214–229

Iida H, Law I, Pakkenberg B, Krarup-Hansen A, Eberl S, Holm S, Hansen AK, Gundersen HJ, Thomsen C, Svarer C, Ring P, Friberg L, Paulson OB (2000) Quantitation of regional cerebral blood flow corrected for partial volume effect using O-15 water and PET: I. Theory, error analysis, and stereologic comparison. *J Cereb Blood Flow Metab* 20:1237–1251

Matthew E, Andreason P, Carson RE, Herscovitch P, Pettigrew K, Cohen R, King C, Johanson CE, Paul SM (1993) Reproducibility of resting cerebral blood flow measurements with H2(15)O positron emission tomography in humans. *J Cereb Blood Flow Metab* 13:748–754

Mikolajczyk K, Szabatin M, Rudnicki P, Grodzki M, Burger C (1998) A JAVA environment for medical image data analysis: initial application for brain PET quantitation. *Med Inform (Lond)* 23:207–214

Moskalenko YE, Dowling JL, Liu D, Rovainen CM, Semernia VN, Woolsey TA (1996) LCBF changes in rat somatosensory cortex during whisker stimulation monitored by dynamic H2 clearance. *Int J Psychophysiol* 21:45–59

Moskalenko Yu E, Rovainen C, Woolsey TA, Dowling J, Liu D, Semernia VN (1995) Combinations of methods for monitoring the microcirculation of the brain. *Neurosci Behav Physiol* 25:266–272

Nakao Y, Itoh Y, Kuang TY, Cook M, Jehle J, Sokoloff L (2001) Effects of anesthesia on functional activation of cerebral blood flow and metabolism. *Proc Natl Acad Sci U S A* 98:7593–7598

Nielsen AN, Lauritzen M (2001) Coupling and uncoupling of activity-dependent increases of neuronal activity and blood flow in rat somatosensory cortex. *J Physiol* 533:773–785

Ohno K, Pettigrew KD, Rapoport SI (1979) Local cerebral blood flow in the conscious rat as measured with 14C-antipyrine, 14C-iodoantipyrine and 3H-nicotine. *Stroke* 10:62–67

Pain F, Besret L, Vaufrey F, Gregoire MC, Pinot L, Gervais P, Ploux L, Bloch G, Mastrippolito R, Laniece P, Hantraye P (2002) In vivo quantification of localized neuronal activation and inhibition in the rat brain using a dedicated high temporal-resolution beta +-sensitive microprobe. *Proc Natl Acad Sci U S A* 99:10807–10812

Pain F, Laniece P, Mastrippolito R, Charon Y, Comar D, Leviel V, Pujol JF, Valentin L (2000) SIC, an intracerebral radiosensitive probe for *in vivo* neuropharmacology investigations in small laboratory animals: theoretical considerations and physical characteristics. *IEEE Transactions on Nuclear Science* 47:25–32

Sakurada O, Kennedy C, Jehle J, Brown JD, Carbin GL, Sokoloff L (1978) Measurement of local cerebral blood flow with iodo [14C] antipyrine. *Am J Physiol* 234:H59–66

Skarphedinsson JO, Harding H, Thoren P (1988) Repeated measurements of cerebral blood flow in rats. Comparisons between the hydrogen clearance method and laser Doppler flowmetry. *Acta Physiol Scand* 134:133–142

Storer RJ, Butler P, Hoskin KL, Goadsby PJ (1997) A simple method, using 2-hydroxypropyl-beta-cyclodextrin, of administering alpha-chloralose at room temperature. *J Neurosci Methods* 77:49–53

von Kummer R, Herold S (1986) Hydrogen clearance method for determining local cerebral blood flow. I. Spatial resolution. *J Cereb Blood Flow Metab* 6:486–491

von Kummer R, von Kries F, Herold S (1986) Hydrogen clearance method for determining local cerebral blood flow. II. Effect of heterogeneity in cerebral blood flow. *J Cereb Blood Flow Metab* 6:492–498

Weber B, Burger C, Biro P, Buck A (2002) A femoral arteriovenous shunt facilitates arterial whole blood sampling in animals. *Eur J Nucl Med Mol Imaging* 29:319–323

Woody CL, Stoll SP, Schlyer DJ, Gerasimov M, Vaska P, Shokouhi S, Volkow N, Fowler JS, Dewey SL (2002) A study of scintillation beta microprobes. *IEEE Transactions on Nuclear Science* 49:2208–2212

Zimmer L, Hassoun W, Pain F, Bonnefoi F, Laniece P, Mastrippolito R, Pinot L, Pujol JF, Leviel V (2002) SIC, an intracerebral beta(+)-range-sensitive probe for radiopharmacology investigations in small laboratory animals: binding studies with (11)C-raclopride. *J Nucl Med* 43:227–233

NeuroImage 48 (2009) 339–347

Contents lists available at ScienceDirect

NeuroImage

journal homepage: www.elsevier.com/locate/ynimg

A beta-scintillator for surface measurements of radiotracer kinetics in the intact rodent cortex☆,☆☆

Matthias T. Wyss [a,b,1], Nicolas M. Obrist [a,1], Florent Haiss [b], Rolf Eckert [c], Ross Stanley [c], Cyrill Burger [a], Alfred Buck [a], Bruno Weber [b,*]

[a] PET Center, Department of Nuclear Medicine, University Hospital Zürich, Switzerland
[b] Institute of Pharmacology and Toxicology, University Hospital Zurich, Nuclear Medicine, Rämistrasse 100, 8091 Zürich, Switzerland
[c] Swiss Center for Electronics and Microtechnology, Inc., Neuchâtel, Switzerland

ARTICLE INFO

Article history:
Received 12 January 2009
Revised 3 June 2009
Accepted 29 June 2009
Available online 8 July 2009

Keywords:
Awake animal
Radiotracer experiments
Surface beta probe

ABSTRACT

β^+-sensitive probes are useful tools for the measurement of radiotracer kinetics in small animals. They allow the cost-effective development of new PET tracers and offer the possibility to investigate a variety of cerebral processes. The study's main aim was the in vivo evaluation of a probe system for cerebral surface acquisitions. The detector system is a 0.2-mm thick scintillating disk of 3-mm diameter, positioned close to the cerebral surface. The study consists of 4 subparts: (1) simulation of the detection volume, (2) direct comparison with the classic intracortical beta probe regarding its capability to acquire kinetic data, (3) test of the ability to detect local tracer accumulations during infraorbital nerve (ION) electrostimulation and (4) demonstration of the feasibility to measure tracer kinetics in awake animals. Kinetic data acquired with ^{18}F-fluorodeoxyglucose and ^{15}O-H_2O were fitted with standard compartment models. The surface probe measurements were in good agreement with those obtained using the intracortical scintillator. ION electrostimulation induced a marked increase in tracer accumulation adequately detected by the surface probe. In the head-fixed animal, a marked change in FDG kinetics was detected between the awake and anesthetized state. The novel surface probe system proved to be a valuable instrument for in vivo radiotracer studies of the cerebral cortex. Its main advantage is the absence of any tissue damage. In addition, serial acquisitions of tracer kinetics in the awake animal turned out to be feasible.

Introduction

Despite the rapid development of new functional neuroimaging tools, radiotracer experiments are still considered the gold standard if absolute quantification is needed. Radiotracer methods are widely used for the investigation of physiological and biochemical processes in the brain, such as receptor binding, hemodynamics, substrate use and transport processes as well as for studies in early drug development. The progress of research in these fields during the last few years is in part due to the advance of methods applicable in small animals. At present, positron emission tomography (PET) and beta probe measurements are the two available methods for the acquisition of tracer kinetics in small animals (Chatziioannou, 2002; Hume and Myers, 2002; Pain et al., 2000; Pain et al., 2002b; Rowland and Cherry, 2008; Weber et al., 2003; Weber and Bauer, 2004; Wyss et al., 2007; Wyss et al., 2009). The cost of PET is substantial and the temporal resolution is still limited, due to which kinetic analysis of animal PET data is often difficult. The recently introduced beta probes demonstrate a valuable and cost-effective alternative for the detection of positrons with high temporal and reasonable spatial resolution. They allow the precise in vivo evaluation of the kinetics of radiotracers labeled with a variety of PET nuclides (e.g. O-15, C-11, F-18). A disadvantage of most available beta detectors is their invasiveness. The systems consist of a scintillating crystal of 0.25 to 1 mm in diameter, which are introduced into the tissue, which may lead to tissue irritation or even damage.

In this study, we present a detection system designed for cerebral surface acquisitions in vivo. The probe is positioned close to the cerebral surface and thus does not cause any cerebral tissue irritation or damage. The aims of the present study were: (1) to estimate the detection volume of the surface probe using simulation, (2) to directly compare the novel system with the classic intracortical beta probe regarding its capability to acquire kinetic data, (3) to test the ability to detect local tracer accumulations during infraorbital nerve (ION) electrostimulation and (4) to demonstrate the feasibility to measure tracer kinetics in awake animals.

☆ http://www.pharma.uzh.ch/research/functionalimaging/introduction.html.

☆☆ The study was supported by the Swiss National Science Foundation (Grants 3100A0-105804/1 and PP00B-110751/1), by the OPO-Stiftung Zürich and the Novartis Research Foundation.

* Corresponding author. Fax: +41 44 255 4428.
E-mail address: bweber@pharma.uzh.ch (B. Weber).

[1] These authors contributed equally to this work.

1053-8119/$ – see front matter © 2009 Elsevier Inc. All rights reserved.
doi:10.1016/j.neuroimage.2009.06.077

Material and methods

Design/specifications of the system

We used a twin probe system (Swisstrace GmbH, Zurich, Switzerland) with two photomultiplier tubes (Perkin Elmer, Massachusetts, USA) allowing simultaneous acquisitions of the radioactivity concentration in two separate brain regions. The detectors were connected with the PMTs via two high numerical aperture glass fibers. The detector of the surface probe consisted of organic scintillating crystal disks (Bicron, BF12, Newbury, OH, USA) with a thickness of 0.2 mm and a diameter of 3 mm embedded in a brass collimator (Fig. 1A). The intracortical system consisted of a scintillation tip (Bicron, BF412, Newbury, OH, USA) with a length of 1 mm and a diameter of 0.25 mm. The probes were made light-tight by applying a uniform black polymer coating (thickness of 50–60 μm). The limited range of beta particles within biological tissues limits detection volume to a small sphere centered on the scintillating tip of the probe. Monte Carlo simulations demonstrated that for F-18 the distance required to detect 90% of the beta particles around the probe is ~1.0 mm (Pain et al., 2002b). Measuring the decay of a radioactive phantom containing F-18 over the course of several hours allowed us to measure the linearity of our system. Kinetic data was stored on a personal computer using a bin width of 1 s. In the in vivo experiments acquisitions of radioactivity count rates began 10–30 s before tracer injection to evaluate dark counts. Thereafter, mean background counts were subtracted from raw data before data analysis. PMTs were allowed to warm up at least for 1 h before each experiment in order to reach stable background counts.

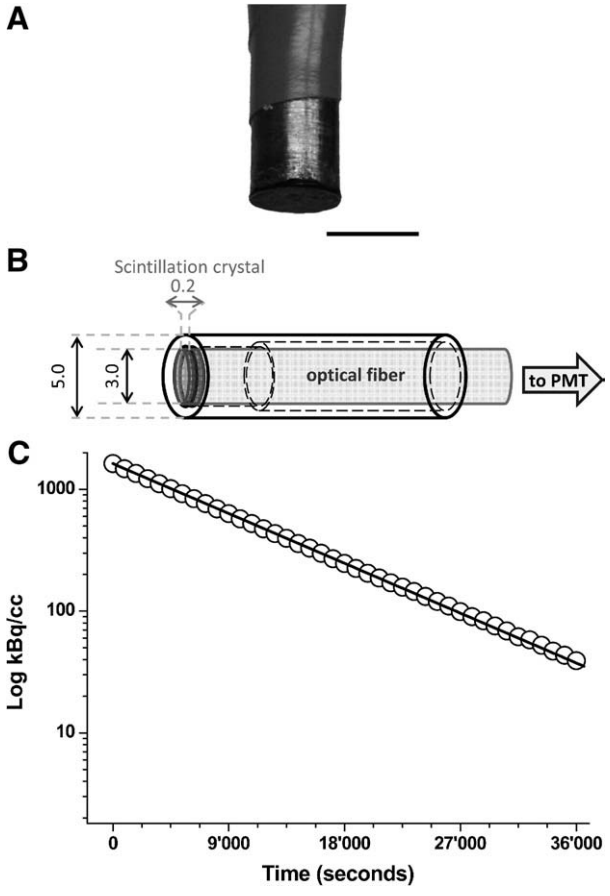

Fig. 1. (A) Photograph of the novel detector tip. Scale bar represents 5 mm. (B) Schematic of the novel probe. Dimensions are given in mm. The scintillation crystal and the optical fiber are covered by a brass shell. (C) Semi-logarithmic plot of the physical decay of F-18 detected by the novel surface probe. Linearity of the device is evident from the high agreement of the measured data (open circles) with the theoretical decay (black line).

Calibration procedure

Calibration measurements were performed after each experiment. A homogeneous solution with a known radioactivity concentration (range: 5.7 MBq/ml to 6.8 MBq/ml for F-18 and 7.1 MBq/ml to 8.0 MBq/ml for O-15) was prepared. For the intracortical probe the calibration was performed by lowering the scintillating tip 1.5 mm into the solution. To calibrate the surface probe the solution was covered with an ultra-thin plastic foil to prevent adhesion of solution to the detector surface. For the actual calibration measurement the radioactivity of the test source was measured with the surface probe in close contact. The factors obtained by this procedure were used to convert the raw data reflecting counts per second (cps) to the apparent radioactivity concentration (kBq/cc) measured in the experiments. Furthermore, for the surface probe, the fraction of recorded events attributable to gamma radiation was estimated by counting the test source additionally with the interposition of a 4 mm thick brass disk sufficient to absorb the ^{18}F positrons but not attenuating 511 keV gamma photons.

Simulation of the detection volume

Since the calibration procedure demonstrated a relatively small contribution of (gamma) photons to the measured signal ($\leq$15%), only positrons were considered. We also assumed that positrons only enter the scintillator through the end surface and not through the side (metal shielding). For the simulation the space below the scintillator was sparsed into a 3D grid (P_{xyz}) and the scintillator surface was divided into discrete squares (SQ_{x1y1}). For each point in space P_{xyz}, the probability that a positron emitted at location P would enter square SQ_{x1y1} on the detector was calculated, yielding Q_{x1y1} (xyz). This probability depends on the spatial angle of SQ_{x1y1} as seen from P_{xyz} and the probability that the positron reaches SQ_{x1y1}. This probability, which depends on the distance, the material and the emission energy of the positrons was taken from recently published data derived from a Monte Carlo simulation (Le Loirec and Champion, 2007). The total signal recorded from location P_{xyz} is then the sum of all Q_{x1y1}. We simulated the situation, in which the scintillator is placed 0.2 mm from the surface of water containing O-15, C-11 and F-18 (0.2 mm distance was chosen to match the distance between the scintillator crystal and the cortical surface in a real experiment). The sum of Q_{x1y1} (xyz) in the simulated volume was normalized to 100.

Animals and radiotracer production

All animal experiments were approved by the local veterinary authorities and were performed by licensed investigators. 16 female Sprague–Dawley rats (^{18}F-fluorodeoxyglucose experiments: $n=14$; ^{15}O-H_2O: experiments $n=2$; weighing between 220 g to 280 g) were used for this study. The animals were kept in cages in a ventilated cabinet with standardized conditions of light (night/day-cycle 12 h/12 h) and temperature and free access to food and water. Animals used for the FDG experiments were fasted overnight.

^{18}F-fluorodeoxyglucose (FDG) was obtained from the daily in-house production by the Radiochemistry Department of the University Hospital Zurich. For the administration of the short-living ^{15}O-H_2O (half-life, 122.2 s) in high concentrations, O-15 was produced continuously in the cyclotron and transferred to the synthesis device. The synthesis device delivered ^{15}O-H_2O at a concentration of about 1 GBq/ml into a glass vial from where 0.5 ml were drawn into a syringe for injection.

Animal preparation

Surgery was performed under 2.5–3.5% isoflurane anesthesia and involved for experiments of Paradigm 1 and 2 the placement of an arterio-venous shunt from the right femoral artery to the right femoral vein and tracheotomy for mechanical ventilation. In experiments where the intracortical probe was used, a craniotomy and small incision of the dura was performed for the placement of the beta-scintillator. This was not needed for the surface probe measurements, where the cranial bone was merely thinned to translucency. The actual experiments were performed under α-chloralose anesthesia (44 mg/kg bodyweight s.c.) according to the protocol of Bonvento et al. (1994). The shunt was used for continuous monitoring of arterial blood pressure, the injection of the radiotracers, the continuous measurement of the total arterial blood radioactivity, the collection of blood samples and the administration of a lethal dose of pentobarbital at the end of the experiment. For the recording of the total blood radioactivity the shunt ran through a coincidence counter (GE Medical Systems). The online arterial sampling procedure was established earlier and is described in detail elsewhere (Weber et al., 2002a). During the experiments arterial blood gases were determined regularly (AVL, Compact 3, Roche Diagnostics, Switzerland) and ventilation was adjusted as necessary to keep the animals within physiological ranges. Blood glucose levels were determined before and after each 45 min acquisition (Ektachem DT, Kodak, USA). For the experiment with the head-fixed animal (Paradigm 3), after surgery and 1 week of recovery, the animal was trained to accept head fixation (Haiss and Schwarz, 2005). Implantation of a head post for later head fixation was undertaken under 3% isoflurane anesthesia. After fixation of micro skull screws (Medartis, Basel, Switzerland) a base was built with dental cement for the final fixation of a standard M5 screw.

No dental cement was applied above the right primary somatosensory cortex and the cranial bone was thinned at this location using a dental drill. To prevent bacterial infections after surgery the chronically implanted animal received oral antibiotic treatment added to the drinking water for 1 week, starting 1 day before surgery (Baytril® 10% oral solution, Bayer, Germany, 1 ml/1 l).

Experimental protocols

The experiments were divided into three groups:

Paradigm 1) Comparison of the surface probe with the intracortical probe to measure cortical time–activity curves

In a total of 8 animals the novel probe system was directly compared to our classic intracortical system. For this purpose the surface probe was positioned over the primary somatosensory cortex on one side (S1; 2 mm posterior and 6 mm lateral according to Bregma; Paxinos and Watson, 1998). The intracortical probe was stereotactically positioned in the corresponding contralateral S1 and lowered 1.5 mm below the dura avoiding large blood vessels. For this paradigm two different radiotracers were used. In 6 animals local cerebral metabolic rates of glucose ($LCMR_{glu}$) were determined using ^{18}F-fluorodeoxyglucose. Only one radiotracer injection per animal was performed in this group (injected activity: 90–145 MBq). Kinetic data was acquired for a period of 45 min. In 2 more animals the quantitative capability of the novel system was compared to the classical intracortical device performing cerebral blood flow (CBF) measurements. 180 s of data were recorded after each ^{15}O-H_2O injection. In each animal a total of 4 injections were performed 15 min apart to allow for sufficient activity decay to background level. After two acquisitions under baseline conditions the carbonic anhydrase inhibitor acetazolamide (Diamox®; 66 mg/kg i.v.) was injected. Acetazolamide leads to vasodilation and thus induces a global increase in cerebral blood flow. Ten minutes after drug application the last two measurements were started.

Paradigm 2) Quantification of localized increases of $LCMR_{glu}$ using the surface probe

In a second group ($n=5$) the ability of the novel system to detect local metabolic activations was evaluated. For this purpose a surface probe was positioned over S1 of each hemisphere. Two subsequent radiotracer injections were performed in these experiments (injection 1: 25–35 MBq in 0.5 ml saline; injection 2: 80–100 MBq in 0.5 ml saline). Each data acquisition took 45 min. One of the two acquisitions of ^{18}F time-course served as the baseline, whereas the other FDG injection was performed immediately after initiation of electrical infraorbital nerve stimulation (2 Hz, 2 mA, pulse length 1 ms, continuous stimulation over 45 min). The order of baseline/activation conditions was balanced across the animals. An autoradiography was performed after the second tracer injection as a control for the effectiveness of the applied stimulation (only in animals with electrostimulation performed during the second injection; $n=3$). Autoradiographic studies were performed as described in detail earlier (Weber et al., 2002b). In short, brains were removed directly after the probe measurements, frozen in chilled isopentane and cut in 10 μm slices. Brain slices were subsequently placed on a phosphor imaging screen (Fuji TR2025). In two additional animals both injections were performed during baseline conditions to control for possible drift during the experiment.

Paradigm 3) Surface probe measurement in an awake head-fixed animal

The aim of this experiment was to demonstrate the feasibility of the system for measurements in head-fixed non-anesthetized animals. First, the animal was carefully trained to tolerate head fixation. The training started 1 week after surgery and involved handling during the first week and habituation to the head holding device in the second week. In the third week, fixation of the animal in the head holding device started. Over the following 2 weeks, the duration of fixation was gradually increased up to 30 min. Finally, the tracer experiment was performed during head fixation. The acquisition started at the time of intraperitoneal tracer injection. After about 20 min, anesthesia was induced with sevoflurane 3% in a mixture of oxygen and air (30%/70%) and data acquisition was continued until 45 min after tracer injection. Two days later the measurement was repeated in the same animal.

Data analysis

Calculations were performed using the software PMOD (Mikolajczyk et al., 1998); PMOD Technologies, Adliswil, Switzerland) and Matlab (Mathworks, Natick MA, USA).

All time–activity curves (TACs) presented are corrected for physical decay and multiplied by the calibration factor taking into account the respective experimental configuration for each probe (scintillating crystal above cortical surface or scintillating tip inside cerebral cortex). Data from FDG experiments were resampled before analysis to obtain 30-second frames, whereas TACs from blood flow measurements were taken with the 1-second time frame duration.

Calculation of the local cerebral metabolic rate of glucose ($LCMR_{glu}$)

The procedure for the quantification of the probe studies follows the [^{14}C]-deoxyglucose method described by Sokoloff et al. (1977). It employs a compartmental model with two-tissue compartments and three kinetic rate constants (K_1 to K_4). The operational equation, which was fitted to the probe time–activity curve additionally included a vascular fraction α as a fit parameter which was in the range of 3 to 9%. This improved the least square fit as compared to a fixed value of $\alpha = 5\%$. $LCMR_{glu}$ values were calculated from the fitted rate constants by: $LCMR_{glu} = (K_1 * K_3/(K_2 + K_3))/(LC/C_{plasma})$, where C_{plasma} represents the plasma glucose concentration and LC the lumped constant ($LC = 0.437$).

Model adjustments for the dual-injection paradigm

The kinetic model was adjusted in two ways for the analysis of the dual-injection data: (1) two sets of rate constants (K_1 to K_4) were used in the calculation of the operational equation, the first set for the time until the second injection, and the second set thereafter. The least-squares fit procedure resulted in estimates for all 6 rate constants and the vascular fraction. (2) The correction function to derive plasma activity from whole blood activity was adjusted to distinguish between the contributions from the two injections. To this end, blood activity from the first injection was extrapolated using an exponential function, which was fitted to the blood activity 10 min before the second injection.

Analysis of the two-condition experiment

Relative values for $LCMR_{glu}$ were estimated for the awake and anesthetized state by applying a standard FDG model adapted to allow the estimation of 2 parameter sets, one for each state. The input curve was based on measurements in other experiments with intraperitoneal injections in the awake and anesthetized rat. It was constructed by taking the first part of the awake state input curve and the tail of the anesthetized state input curves. This is taken as a first approximation of the true input curve. This approach yields only relative values for $LCMR_{glu}$ since input and tissue curve are not truly scaled. However, it allows estimating the fractional change of $LCMR_{glu}$ from the awake to the anesthetized state.

Calculation of cerebral blood flow measurements (CBF)

The basis of the calculation using the one-tissue compartment model included a partition coefficient for ^{15}O-H_2O. Before data analysis, tissue time–activity curves and arterial input curves were corrected for radioactive decay. Further details of the analysis procedure were described previously (Weber et al., 2003).

Statistics

Bland–Altman tests were used to assess the agreement of $LCMR_{glu}$ values obtained by kinetic beta probe measurements using the two different systems and by the static autoradiographic method (Bland and Altman, 1986). Values are given as mean ± sd.

Results

Performance characteristics of the new probe system

The agreement of the decay of F-18 monitored with the beta probe and a monoexponential function as shown in Fig. 1B demonstrates the linearity of the detector response. This is in accordance to previous reports showing linearity for scintillating plastic and LSO crystals (Pain et al., 2002b; Woody et al., 2001). The mean sensitivity of the novel surface probe system was 0.83 ± 0.04 cps/kBq/ml. The background (dark counts) ranged from 2–8 cps. Stopping the positrons using the brass disk between the ^{18}F source and the detector tip reduced the count rate to 14.7 ± 4.4% of the initial value. Accordingly, the contribution of gamma radiation (originating from positron annihilation) to the total acquired count rate was about 15% for the new probe system.

Simulation of detection volume

The simulation yielded the detection volumes depicted in Figs. 2A–C. For F-18, 95% of the signal was detected from within an isosurface with a maximum depth of about 1 mm. This range is considerably larger for C-11 and O-15, due to the higher positron

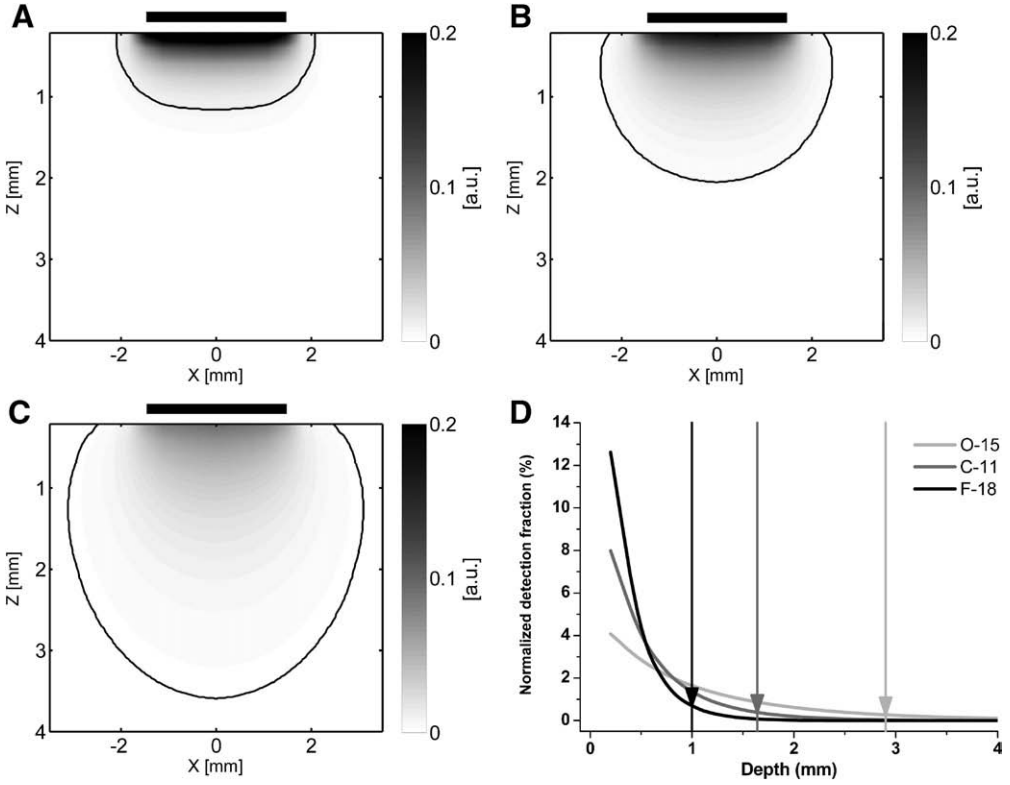

Fig. 2. Results from the detection volume simulations. (A)–(C): Detection fraction from a plane representing the sum projection along the Y-direction for F-18 (A), C-11 (B) and O-15 (C). The thin black lines represent the 95% isolines. The sum of all values in the simulated volume was set to 100. (D) The curves depict the normalized detection fraction for sums in planes along the depth (Z-direction) for the simulated isotopes. The vertical straight lines represent the 95% thresholds.

Table 1
Rate constants determined using a two-tissue compartment model during baseline.

	Animal number	K_1 (ml min^{-1} ml tissue^{-1})	K_2 (min^{-1})	K_3 (min^{-1})	K_4 (min^{-1})	LCMRglu (μmol 100 g^{-1} min^{-1})
Right somatosensory cortex surface probe	1	0.080	0.196	0.075	0	43.21
	2	0.107	0.256	0.070	0.019	45.37
	3	0.122	0.304	0.098	0.017	55.88
	4	0.111	0.264	0.060	0.009	35.67
	5	0.106	0.304	0.108	0.023	61.90
	6	0.128	0.269	0.058	0.018	45.89
	mean ± sd	0.109 ± 0.02	0.266 ± 0.04	0.078 ± 0.02	0.014 ± 0.008	47.99 ± 9.4
Left somatosensory cortex intracortical probe	1	0.081	0.165	0.094	0.010	57.56
	2	0.103	0.204	0.069	0.017	51.6
	3	0.131	0.266	0.067	0.004	49.26
	4	0.089	0.156	0.063	0	45.63
	5	0.116	0.270	0.149	0.018	92.13
	6	0.173	0.224	0.060	0.014	72.06
	mean ± sd	0.116 ± 0.03	0.214 ± 0.05	0.084 ± 0.03	0.011 ± 0.007	61.37 ± 17.69

emission energy. As can be seen in Figs. 2A–D, the sensitivity rapidly decays with depth.

Animal experiments

Paradigm 1) Direct comparison of the two probe systems

Local cerebral metabolic rates of glucose consumption ($LCMR_{glu}$) based on measurements with the two probe systems are shown in Table 1 ($n=6$). The data of both probes were adequately fitted by the standard two-tissue compartment FDG model, as the lack of bias in the residuals indicates (Figs. 3A and B). However, the higher sensitivity of the novel surface probe system led to a marked decrease in the relative residual size. The Bland–Altman plot in Fig. 4 shows that all differences in $LCMR_{glu}$ are in the range defined by the mean ± 2 SD. Nevertheless, the values measured with the surface probe were on average 22% lower than the ones determined with the intracortical probe.

A typical example of FDG time–activity curves recorded simultaneously with the 2 probe systems is demonstrated in Fig. 5. In order to illustrate the similarity of the shape, the curves were normalized to the integral of the tissue activity between 0 and 45 min.

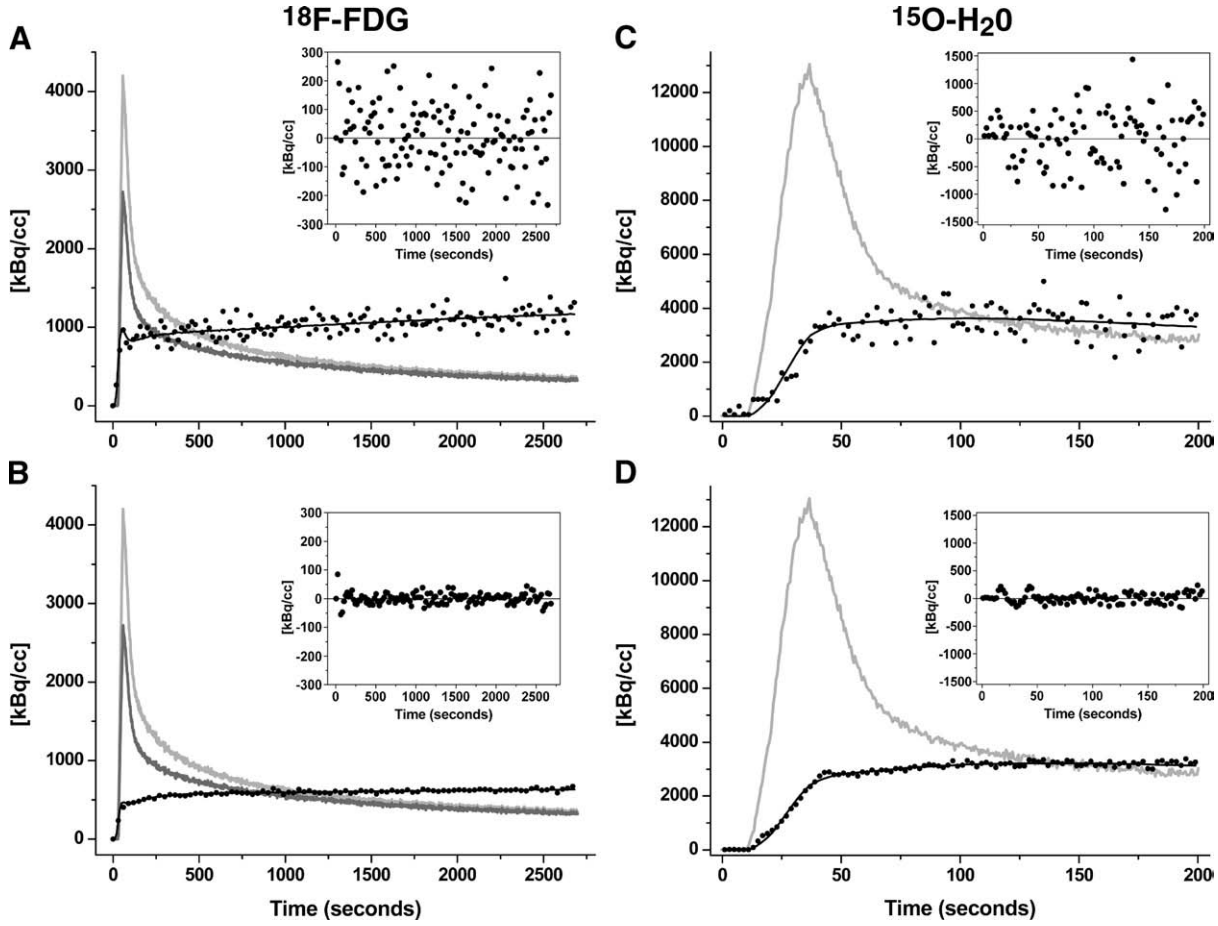

Fig. 3. Typical examples of tissue time–activity curves acquired by the original intracortical probe (A, C) and the surface probe (B, D) using two different radiotracers, ^{18}F-FDG (A, B) and ^{15}O-H_2O (C, D). The radioactivity concentration in plasma (light gray line) in whole blood (dark gray line) and the model fit (black line) are also shown. The goodness-of-fit is demonstrated by the random distribution of the residuals (inset). Due to the increased sensitivity of the new system, signal-to-noise ratio is increased leading to an improved model fit illustrated by the narrower range of variability of the residuals.

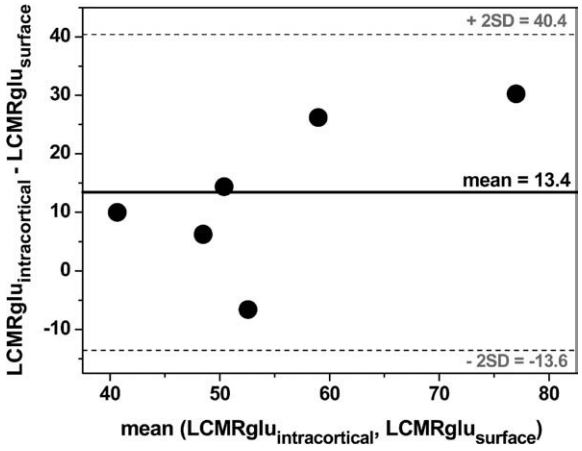

Fig. 4. Bland–Altman plot to evaluate the agreement of the probe measurements in 6 animals using ^{18}F-FDG. The middle line represents the mean of two measurements in the same animal using the two different probe systems, the border dashed lines the mean ± 2 sd, respectively.

For the CBF measurements ($n=2$) a typical example of tissue time–activity curves acquired with the two probe systems is shown in Fig. 3 (panel C and D). Again the surface probe yielded a considerably improved signal-to-noise ratio. CBF data are shown in Table 2.

In Fig. 6 the reproducibility of the detection of O-15 and F-18 in the surface probe measurements is shown illustrating the high stability of the measurement obtained with this device.

The acetazolamide induced CBF increase was 51% when measured with the surface probe and 48% with the intracortical probe. As with FDG, the absolute CBF values were somewhat smaller with the surface probe.

Paradigm 2) ION electrostimulation

To assess whether the surface probe is able to detect local increases in metabolic activity in the brain, electrical stimulation of the right infraorbital branch of the trigeminal nerve (ION) was applied. The stimulation of the ION caused the expected circumscribed increase of tracer uptake in the contralateral primary somatosensory cortex (S1) as shown by the autoradiographic slice in Fig. 7. Only a weak increase in tracer uptake is noticed on the ipsilateral side. The increase was correctly recorded by the surface probe in all 5 experiments and was on average 60.7% at 45 min. The subsequent autoradiographic evaluation showed a mean increase of 64.9%. A typical example of a

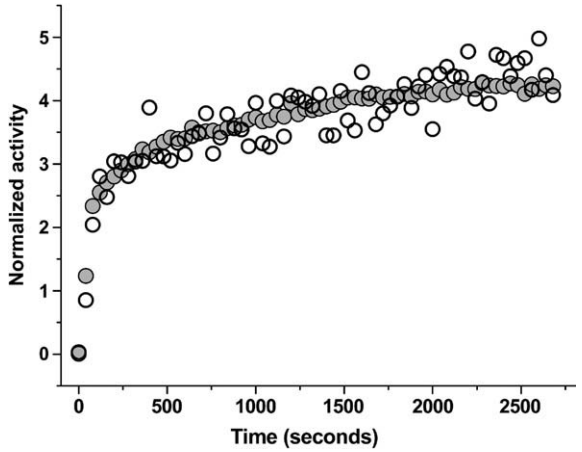

Fig. 5. Time–activity curves of ^{18}F-FDG accumulation in the rat's somatosensory cortex normalized to the integral of plasma activity between 0 and 45 min. Shown is the measurement in a single animal acquired on one side with the intracortical system (open circles) and homotopically on the contralateral hemisphere with the surface probe system (filled gray circles).

Table 2
Rate constants determined using a two-tissue compartment model during baseline.

	Condition	Animal number	CBF (ml min^{-1} 100 ml tissue^{-1})	
Right somatosensory cortex surface probe	Baseline	1	35.14	
		1	34.58	
		2	34.04	
		2	34.21	34.49 ± 0.5
	Acetazolamide	1	50.82	
		1	50.4	
		2	53.87	
		2	54.07	52.29 ± 1.9
Left somatosensory cortex intracortical probe	Baseline	1	37.38	
		1	38.92	
		2	39.53	
		2	39.20	38.76 ± 0.9
	Acetazolamide	1	55.02	
		1	56.14	
		2	59.94	
		2	58.97	57.52 ± 2.3

probe acquisition during ION stimulation is presented in Fig. 7. In the 2 animals with two FDG injections during baseline conditions stable radiotracer accumulation was observed. The difference in $LCMR_{glu}$ between the first and the second injection was 8.7% and − 14.9% in the two animals, verifying the stability of the double-injection protocol.

Paradigm 3) Determination of FDG kinetics in the awake head-fixed rat

The animal was successfully trained for 5 weeks to tolerate the head fixation for up to 30 min. Fig. 8 shows the constant increase of cerebral FDG uptake during the first 20 min in the awake animal. After induction of sevoflurane anesthesia LCMRglu was reduced by 46.8%. The repetition of the acquisition 2 days later precisely reproduced these results (data not shown), demonstrating the feasibility to perform serial experiments in the same animal.

Discussion

An increasing number of molecular imaging studies are performed with PET scanners. These devices allow imaging of the whole animal, if necessary several times in a longitudinal design. However, these PET scanners suffer from drawbacks, such as a high price and limited temporal resolution. The latter makes it difficult to use them in a dynamic imaging design coupled with kinetic modeling. Another drawback of small animal PET is the requirement for anesthesia, which inevitably alters normal physiology. The recently introduced small beta probes for intracortical measurements in small animals overcame some of these problems (Ginovart et al., 2004; Pain et al., 2000; Pain et al., 2002b; Weber et al., 2003; Zimmer et al., 2002a; Zimmer et al., 2002b) and the combination with other methods turned out to be more straightforward (Desbree et al., 2004; Desbree et al., 2007). They offer a cost-effective alternative whenever the measurement at a few locations in the brain is sufficient. They already found application in blood flow studies (Weber et al., 2003), metabolic studies (Millet et al., 2004; Pain et al., 2002a), receptor occupancy studies (Ginovart et al., 2004; Zimmer et al., 2002a; Zimmer et al., 2002b) and the evaluation of new radiotracers (Galineau et al., 2006; Wyss et al., 2007; Wyss et al., 2009). All these studies were performed using thin probes designed for direct acquisition within the structure of interest. However, a disadvantage of these intracerebral probes is the potential tissue disturbance caused by their insertion. This was already noted in a previous study by Pain et al. (2002a) and as a consequence a beta probe of 1 mm diameter was positioned on the brain surface. However, no results were shown and no subsequent publications concerning this issue followed according to our knowledge.

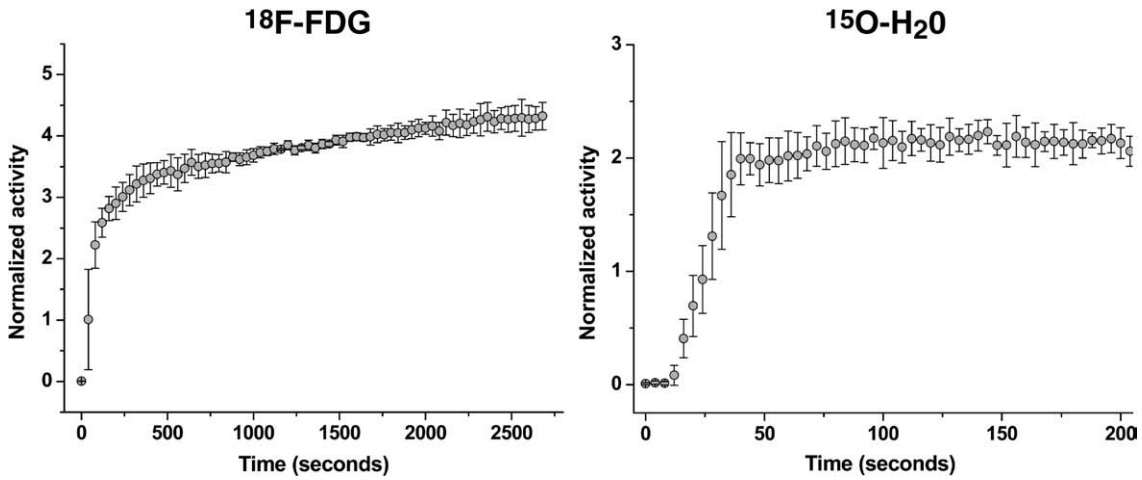

Fig. 6. Mean tissue time–activity curves normalized to the integral of plasma radioactivity between 0 and 210 s for ^{15}O-H_2O ($n=4$) and between 0 and 45 min for ^{18}F-FDG ($n=6$). The narrow range of standard deviations supports the high reproducibility of the measurements.

The present study demonstrates the suitability of the surface probe for reliable measurements of tracer kinetics in the rat cerebral cortex through the thinned skull. The fact that there is no need for craniotomy facilitates and shortens the surgery and does not cause any tissue disturbance. The dura and brain remain untouched, leaving the cortex in a physiological state. However, the design of the probe system does not allow acquisitions from deep brain areas and measurements are restricted to superficial structures. This limitation can be overcome by complementary use of intracerebral beta probes for non-cortical measurements.

This novel probe system was able to reliably measure kinetic data using radiotracers labeled with nuclides of different energies. However, values for $LCMR_{glu}$ and CBF were both lower in the surface probe measurements compared to the intracortical acquisitions. Several factors could contribute to these differences which include probe calibration procedures, differences in the geometry and size of the detection volume. In addition, tissues between the surface probe and cortical surface, such as dura, cerebrospinal fluid and thinned bone may affect the signal measured. For the performed simulations we assumed a gap of 200 μm between cortical surface and the scintillator surface. This gap is mainly filled by cerebrospinal fluid. Dura mater and bone add at maximum 50–100 μm. Therefore the assumption of water instead of bone absorbing the positrons in our simulations will lead only to a minor error. Gamma radiation may be yet another source for error (Pain et al., 2000; Pain et al., 2002b; Weber et al., 2003). In the case of the here presented surface probe the contribution of 511 keV gamma rays was evaluated to be about 15% in the calibration experiments. The exact contribution depends on factors such as geometry of the volume containing radioactivity and the temporal and spatial distribution in that volume. This factor is difficult to assess quantitatively.

The reason we used F-18 and O-15 was the different emission energy of the positrons and that FDG and ^{15}O-H_2O display a very different kinetic behavior. The higher emission energy of O-15 leads to a different geometry and size of the volume of the detected positrons, as is demonstrated in Fig. 2C. Furthermore, the kinetic of ^{15}O-H_2O is much faster than that of FDG. It was therefore relevant to demonstrate the suitability of the surface probe for both tracers. One of the most

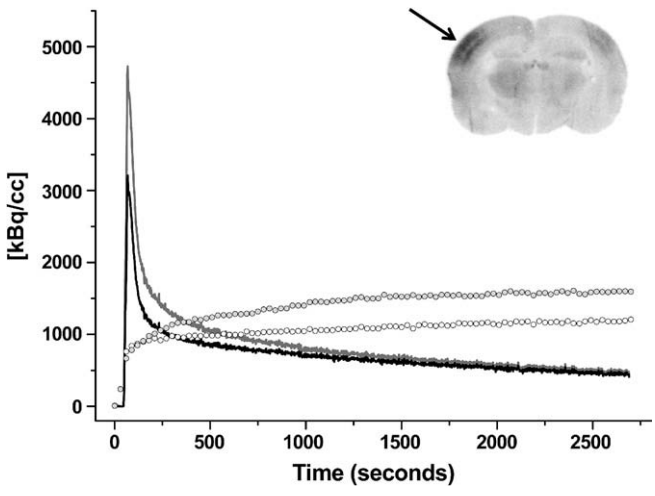

Fig. 7. Decay-corrected tissue time–activity curves acquired by the surface probe system during electrical infraorbital nerve stimulation in one animal are demonstrated. As shown in the autoradiogram, contralateral to the stimulation site (arrow, gray squares in the graph) accumulation of ^{18}F-FDG was increased compared to the ipsilateral hemisphere (open circles in the graph). The radioactivity concentration in plasma (gray line) and in whole blood (black line) is also shown.

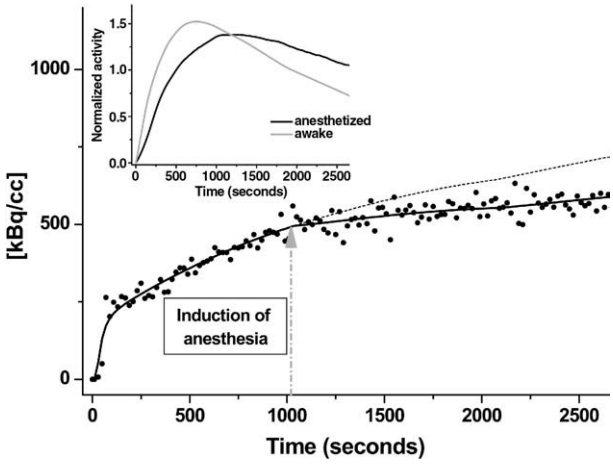

Fig. 8. Acquisition in the awake, head-fixed animal. Tissue accumulation of FDG clearly slowed down after induction of sevoflurane anesthesia (gray arrow). Shown are measured tissue activity (circles), the model fit to the actually measured data (black line) and the putative model fit if the curve was continued using the same rate constants from the period before anesthesia induction (dotted black line). LCMRglu decreased by 46.8%. The inset shows the two mean input curves obtained in awake ($n=4$) and in sevoflurane anesthetized animals ($n=4$) from which the applied input curve was constructed (see Materials and methods).

critical issues with regard to absolute quantification is the precise calibration of instruments. The calibration procedure should also adequately mimic the in vivo situation. It can be assumed, that this is somewhat more difficult in the case of the surface detector as compared to the intracortical probe, mainly because the position of the surface detector cannot be perfectly reproduced from experiment to experiment (e.g., due to the thinning of the bone, angle and distance of the probe relative to brain surface). Therefore the accuracy of the surface probe is expected to be inferior to the one of the intracortical probe regarding absolute quantification. However, in many situations it is the change following some kind of intervention, which is of more interest than absolute values, and that is where we see the major application of the surface probe. This is illustrated by the stimulation experiments where the surface probe registered a similar percentage change as the autoradiography.

Besides beta sensitive probes, alternative radiotracer probes were developed in the past. The principle of detection of gamma probes is either excitation (scintillator) or ionization (semiconductor) and their major application is intra-operative radio-guided surgery (Classe et al., 2005; Zanzonico and Heller, 2000). Their spatial resolution is however at least one order of magnitude poorer as compared to beta probes (Haigh et al., 2000), which severely limits their applicability in small animal research.

Finally, another valuable feature of the surface system is its use in awake animals. This clearly broadens the applicability of the device given the fact that an increasing number of studies are performed in awake animals to avoid the disturbing effect of anesthetics on brain function (Austin et al., 2005; Lindauer et al., 1993; Martin et al., 2006; Nakao et al., 2001). Our preliminary data acquired in one animal at two different days demonstrates a marked effect of sevoflurane inhalation on brain metabolism and shows the feasibility of serial experiments. However, no arterial input curves were measured in these experiments, which would be mandatory to obtain reliable absolute values.

Summary

In this work, we demonstrated the feasibility of a surface probe system for the measurement of radiotracer kinetics from the cerebral cortex of the rat. The system yielded reproducible results in the anesthetized rat. Its potential use in the awake animal was demonstrated in preliminary experiments. The surface probe is thus a valuable tool for tracer kinetic experiments where data from only a few cortical locations are needed. The major advantage of the system in comparison to intracortical probes is that the brain tissue is not injured or disturbed.

Acknowledgments

The authors want to thank the Center for Radiopharmaceutical Science of the ETH, PSI and USZ for tracer production. In addition, we are grateful to Dr. Wynne K. Schiffer for providing us with arterial input curves from intraperitoneal injection in awake rats. The study was supported by the Swiss National Science Foundation (Grants 3100A0-105804/1 and PP00B-110751/1), by the OPO-Stiftung Zürich, the Zurich Center for Integrative Human Physiology and the Novartis Research Foundation.

References

Austin, V.C., Blamire, A.M., Allers, K.A., Sharp, T., Styles, P., Matthews, P.M., Sibson, N.R., 2005. Confounding effects of anesthesia on functional activation in rodent brain: a study of halothane and alpha-chloralose anesthesia. Neuroimage 24, 92–100.

Bland, J.M., Altman, D.G., 1986. Statistical methods for assessing agreement between two methods of clinical measurement. Lancet 1, 307–310.

Bonvento, G., Charbonne, R., Correze, J.L., Borredon, J., Seylaz, J., Lacombe, P., 1994. Is alpha-chloralose plus halothane induction a suitable anesthetic regimen for cerebrovascular research? Brain Res. 665, 213–221.

Chatziioannou, A.F., 2002. PET scanners dedicated to molecular imaging of small animal models. Mol. Imaging Biol. 4, 47–63.

Classe, J.M., Fiche, M., Rousseau, C., Sagan, C., Dravet, F., Pioud, R., Lisbona, A., Ferrer, L., Campion, L., Resche, I., Curtet, C., 2005. Prospective comparison of 3 gamma-probes for sentinel lymph node detection in 200 breast cancer patients. J. Nucl. Med. 46, 395–399.

Desbree, A., Pain, F., Gurden, H., Zimmer, L., Pinot, L., Laniece, P., Mastrippolito, R., 2004. Combining the radiosensitive Beta MicroProbe to nuclear magnetic resonance: theoretical approach for in vivo studies in small animals. J. Neurosci. Methods 140, 47–52.

Desbree, A., Rbah, L., Langlois, J.B., Grenier, D., Mastrippolito, R., Pain, F., Pinot, L., Laniece, P., Zimmer, L., Gurden, H., 2007. Simultaneous in vivo magnetic resonance imaging and radioactive measurements with the beta-MicroProbe. Eur. J. Nucl. Med. Mol. Imaging 34, 1868–1872.

Galineau, L., Wilson, A.A., Garcia, A., Houle, S., Kapur, S., Ginovart, N., 2006. In vivo characterization of the pharmacokinetics and pharmacological properties of [11C]-(+)-PHNO in rats using an intracerebral beta-sensitive system. Synapse 60, 172–183.

Ginovart, N., Sun, W., Wilson, A.A., Houle, S., Kapur, S., 2004. Quantitative validation of an intracerebral beta-sensitive microprobe system to determine in vivo drug-induced receptor occupancy using [11C]raclopride in rats. Synapse 52, 89–99.

Haigh, P.I., Glass, E.C., Essner, R., 2000. Accuracy of gamma probes in localizing radioactivity: in-vitro assessment and clinical implications. Cancer Biother. Radiopharm. 15, 561–569.

Haiss, F., Schwarz, C., 2005. Spatial segregation of different modes of movement control in the whisker representation of rat primary motor cortex. J. Neurosci. 25, 1579–1587.

Hume, S.P., Myers, R., 2002. Dedicated small animal scanners: a new tool for drug development? Curr. Pharm. Des. 8, 1497–1511.

Le Loirec, C., Champion, C., 2007. Track structure simulation for positron emitters of medical interest. Part I: the case of the allowed decay isotopes. Nucl. Instrum. Methods Phys. Res. Section A-Accel. Spectrom. Detect. Assoc. Equip. 582, 644–653.

Lindauer, U., Villringer, A., Dirnagl, U., 1993. Characterization of CBF response to somatosensory stimulation: model and influence of anesthetics. Am. J. Physiol. 264, H1223–1228.

Martin, C., Martindale, J., Berwick, J., Mayhew, J., 2006. Investigating neural–hemodynamic coupling and the hemodynamic response function in the awake rat. Neuroimage 32, 33–48.

Mikolajczyk, K., Szabatin, M., Rudnicki, P., Grodzki, M., Burger, C., 1998. A JAVA environment for medical image data analysis: initial application for brain PET quantitation. Med. Inform. (Lond) 23, 207–214.

Millet, P., Sallanon, M.M., Petit, J.M., Charnay, Y., Vallet, P., Morel, C., Cespuglio, R., Magistretti, P.J., Ibanez, V., 2004. In vivo measurement of glucose utilization in rats using a beta-microprobe: direct comparison with autoradiography. J. Cereb. Blood Flow Metab. 24, 1015–1024.

Nakao, Y., Itoh, Y., Kuang, T.Y., Cook, M., Jehle, J., Sokoloff, L., 2001. Effects of anesthesia on functional activation of cerebral blood flow and metabolism. Proc. Natl. Acad. Sci. U. S. A. 98, 7593–7598.

Pain, F., Besret, L., Vaufrey, F., Gregoire, M.C., Pinot, L., Gervais, P., Ploux, L., Bloch, G., Mastrippolito, R., Laniece, P., Hantraye, P., 2002a. In vivo quantification of localized neuronal activation and inhibition in the rat brain using a dedicated high temporal-resolution beta +-sensitive microprobe. Proc. Natl. Acad. Sci. U. S. A. 99, 10807–10812.

Pain, F., Laniece, P., Mastrippolito, R., Pinot, L., Charon, Y., Glatigny, A., Guillemin, M.T., Hantraye, P., Leviel, V., Menard, L., Valentin, L., 2002b. SIC, an intracerebral radiosensitive probe for in vivo neuropharmacology investigations in small laboratory animals: prototype design, characterization, and in vivo evaluation. IEEE Trans. Nucl. Sci. 49, 822–826.

Pain, F., Laniece, P., Mastrippolito, R., Charon, Y., Comar, D., Leviel, V., Pajol, J.F., Valentin, L., 2000. SIC, an intracerebral radiosensitive probe for in vivo neuropharmacology investigations in small laboratory animals. IEEE Trans. Nucl. Sci. 47, 25–32.

Paxinos, G., Watson, C., 1998. The Rat Brain in Stereotaxic Coordinates, 4th ed. Academic Press, San Diego.

Rowland, D.J., Cherry, S.R., 2008. Small-animal preclinical nuclear medicine instrumentation and methodology. Semin. Nucl. Med. 38, 209–222.

Sokoloff, L., Reivich, M., Kennedy, C., Des Rosiers, M.H., Patlak, C.S., Pettigrew, K.D., Sakurada, O., Shinohara, M., 1977. The [14C]deoxyglucose method for the measurement of local cerebral glucose utilization: theory, procedure, and normal values in the conscious and anesthetized albino rat. J. Neurochem. 28, 897–916.

Weber, S., Bauer, A., 2004. Small animal PET: aspects of performance assessment. Eur. J. Nucl. Med. Mol. Imaging 31, 1545–1555.

Weber, B., Burger, C., Biro, P., Buck, A., 2002a. A femoral arteriovenous shunt facilitates arterial whole blood sampling in animals. Eur. J. Nucl. Med. Mol. Imaging 29, 319–323.

Weber, B., Fouad, K., Burger, C., Buck, A., 2002b. White matter glucose metabolism during intracortical electrostimulation: a quantitative [(18)F]fluorodeoxyglucose autoradiography study in the rat. Neuroimage 16, 993–998.

Weber, B., Spath, N., Wyss, M., Wild, D., Burger, C., Stanley, R., Buck, A., 2003. Quantitative cerebral blood flow measurements in the rat using a beta-probe and H2 15O. J. Cereb. Blood Flow Metab. 23, 1455–1460.

Woody, C.L., Stoll, S.P., Schlyer, D.J., Shokouhi, S., Gerasimov, M., Dewey, S., Volkow, N., 2001. An intracerebral beta microprobe for studying radiotracer kinetics in freely moving animals. IEEE Nucl. Symp. Sci. Med. Imaging Conf. Rec. 3, 70–74.

Wyss, M.T., Ametamey, S.M., Treyer, V., Bettio, A., Blagoev, M., Kessler, L.J., Burger, C., Weber, B., Schmidt, M., Gasparini, F., Buck, A., 2007. Quantitative evaluation of 11C-

ABP688 as PET ligand for the measurement of the metabotropic glutamate receptor subtype 5 using autoradiographic studies and a beta-scintillator. Neuroimage 35, 1086–1092.
Wyss, M.T., Weber, B., Treyer, V., Heer, S., Pellerin, L., Magistretti, P.J., Buck, A., 2009. Stimulation-induced increases of astrocytic oxidative metabolism in rats and humans investigated with 1-11C-acetate. J. Cereb. Blood Flow Metab. 29, 44–56.
Zanzonico, P., Heller, S., 2000. The intraoperative gamma probe: basic principles and choices available. Semin. Nucl. Med. 30, 33–48.
Zimmer, L., Hassoun, W., Pain, F., Bonnefoi, F., Laniece, P., Mastrippolito, R., Pinot, L., Pujol, J.F., Leviel, V., 2002a. SIC, an intracerebral beta(+)-range-sensitive probe for radiopharmacology investigations in small laboratory animals: binding studies with (11)C-raclopride. J. Nucl. Med. 43, 227–233.
Zimmer, L., Pain, F., Mauger, G., Plenevaux, A., Le Bars, D., Mastrippolito, R., Pujol, J.F., Renaud, B., Laniece, P., 2002b. The potential of the beta-Microprobe, an intracerebral radiosensitive probe, to monitor the [(18)F]MPPF binding in the rat dorsal raphe nucleus. Eur. J. Nucl. Med. Mol. Imaging 29, 1237–1247.

NeuroImage

www.elsevier.com/locate/ynimg
NeuroImage 35 (2007) 1086–1092

Quantitative evaluation of ^{11}C-ABP688 as PET ligand for the measurement of the metabotropic glutamate receptor subtype 5 using autoradiographic studies and a beta-scintillator

Matthias T. Wyss,[a] Simon M. Ametamey,[b] Valerie Treyer,[a] Andrea Bettio,[b] Milen Blagoev,[b] Lea J. Kessler,[b] Cyrill Burger,[a] Bruno Weber,[a,c] Mark Schmidt,[d] Fabrizio Gasparini,[e] and Alfred Buck[a,*]

[a]*PET Center, University Hospital Zurich, Division of Nuclear Medicine, Rämistrasse 100, 8091 Zurich, Switzerland*
[b]*Center for Radiopharmaceutical Science of ETH, PSI and USZ, Department of Chemistry and Applied Biosciences of ETH, Zurich, Switzerland*
[c]*Institute of Pharmacology and Toxicology, University Zurich, Switzerland*
[d]*Novartis Pharma AG, Basel, Switzerland*
[e]*Novartis Institutes for Biomedical Research, Basel, Switzerland*

Received 9 May 2006; revised 5 January 2007; accepted 12 January 2007
Available online 24 January 2007

In this study we assessed the new glutamatergic ligand ^{11}C-ABP688 with regard to the following characteristics: (A) brain distribution, (B) first pass extraction fraction, (C) suitable model to describe tracer kinetics and (D) specificity for the mGlu5 receptor. These parameters were assessed using autoradiography and a beta-scintillator positioned in the striatum. The study included 13 male rats. In 2 animals cerebral blood flow was measured using $H_2{}^{15}O$. The ^{11}C-ABP688 data were analyzed using compartmental modeling. A two-tissue compartment model turned out to fit the data more adequately (parameters: K_1, k_2', k_3', k_4, total distribution volume $DV_{tot}=K_1/k_2'$ $(1+k_3'/k_4)$ than a one-tissue compartment model. The autoradiographic studies revealed high uptake in hippocampus, striatum and cortex and low accumulation in thalamus and cerebellum. The uptake was markedly reduced following blockade with the mGlu5 antagonist M-MPEP. The first pass extraction fraction exceeded 85%. Baseline DV_{tot} was 15.16 ± 2.67 ml plasma/ml tissue and decreased by 56, 67 and 72% following blockade with 1, 2 and 6 mg/kg M-MPEP, respectively. These results show that ^{11}C-ABP688 is a promising PET ligand for the quantification of mGlu5 receptors in humans and animals. It readily crosses the blood–brain barrier and binds with high specificity to the mGlu5 receptor. The study furthermore demonstrates the usefulness of a beta-scintillator, if necessary in connection with autoradiography, to evaluate new receptor tracers.

Keywords: Autoradiographic study; Beta-scintillator; Metabotropic glutamate receptor subtype 5

Introduction

Since the cloning of the first metabotropic glutamate receptor (mGlu1) in 1991 (Masu et al., 1991), seven additional subtypes of this receptor (mGlu2–8) have been cloned. Based on their amino-acids sequence, pharmacology and second messenger coupling these receptors have been classified into three groups (I–III) (Pin and Duvoisin, 1995). Group I includes mGlu1 and mGlu5 receptors, Group II includes mGlu2 and mGlu3 receptors, and Group III includes mGlu4, 6, 7 and 8 receptors. For the mGlu5 receptor subtype, based on the wide and consistent effects of selective non-competitive allosteric antagonists such as MPEP (2-Methyl-6-(phenylethynyl)pyridine) in animal models for anxiety (Gasparini et al., 1999; Kuhn et al., 2002), it has been hypothesized that this receptor could be a valuable target for the treatment of anxiety related disorders (Spooren et al., 2000; Tatarczynska et al., 2001; Spooren and Gasparini, 2004). Although a number of mGlu5 receptor antagonists have been successfully used *in vitro* to label mGlu5 receptors (Gasparini et al., 2002; Patel et al., 2003), the development of a PET tracer proved difficult (Hamill et al., 2003). Only recently a series of PET ligands, allowing the *in vivo* imaging in rhesus monkeys, has been described (Hamill et al., 2005). We have synthesized and profiled a series of derivatives using the prototypic antagonist MPEP as template. Unfortunately none of these derivatives proved to be a promising candidate for human PET imaging (Kokic et al., 2001; Ametamey et al., 2003). Recently, we identified a very promising ligand: ^{11}C-ABP688 (3-(6-methyl-pyridin-2-ylethynyl)-cyclohex-2-enone-*O*-[^{11}C]-methyl-oxime). This compound is a highly selective allosteric antagonist of the mGlu5 receptor *in vitro*, and initial studies have demonstrated a high specificity for mGlu5 receptors *in vivo* (Ametamey et al., 2005). The major purpose of this study was to

* Corresponding author. Fax: +41 44 255 44 14.
E-mail address: fred.buck@usz.ch (A. Buck).
Available online on ScienceDirect (www.sciencedirect.com).

1053-8119/$ - see front matter © 2007 Elsevier Inc. All rights reserved.
doi:10.1016/j.neuroimage.2007.01.005

further investigate the suitability of ^{11}C-ABP688 as a radiotracer for the study of mGlu5 receptors. Issues of interest were (A) the brain distribution of the tracer, (B) the first pass extraction fraction, (C) suitable models to describe tracer kinetics and (D) specificity for the mGlu5 receptor. These issues were addressed using autoradiographic studies and a beta-scintillator positioned in the rat striatum.

Materials and methods

Synthesis of ^{11}C-ABP688

The synthesis of ^{11}C-ABP688 has been described in detail elsewhere (Ametamey et al., 2005). Briefly, desmethyl ABP688 was reacted with ^{11}C-methyl iodide produced from the GE PET trace system at 90 °C for 5 min. The product was purified by semi-preparative HPLC using a reversed-phase column. Formulation of ^{11}C-ABP688 for *in vivo* administration into animals was accomplished using 0.15 M phosphate buffer and ethanol. The specific activities at the time of injection ranged from 11 to 437 GBq/μmol. The amount of stable ABP688 which was injected is indicated in Table 1.

Animal preparation

The beta-scintillator study included 11 male rats (Sprague–Dawley) weighing approximately 300 g (range: 266–366 g). Surgery was performed under isoflurane anesthesia and involved the placement of an arterio-venous shunt from the right femoral artery to the right femoral vein, tracheotomy for mechanical ventilation and craniotomy for the placement of the beta-scintillator. The actual experiments were performed under urethane anesthesia (1.4 g/kg bodyweight i.p.). The shunt was used for the continuous monitoring of arterial blood pressure, the injection of the radiotracers, the continuous measurement of the total arterial radioactivity and the administration of a lethal dose of pentobarbital at the end of the experiment. For the recording of the total blood radioactivity, the shunt was run through a coincidence counter. The on-line arterial sampling procedure is described in detail elsewhere (Weber et al., 2002).

Experiments

Beta-scintillator

The beta-scintillator is in detail described elsewhere (Weber et al., 2003; www.swisstrace.com). In short, it consists of a scintillation tip (Bicron, BF12, Newbury, OH, USA) with 0.8 mm length and 0.25 mm diameter that is attached to a high numerical aperture glass fiber. The probe was made light tight by applying a uniform coating of silver particles. Following each experiment the beta-probe was calibrated in a vial containing a known concentration of ^{11}C activity. The sensitivity ranged from 0.035 to 0.044 cps/kBq/ml. For data analysis all data were background-corrected (range of background count rates: 0–1 cps), decay-corrected to the time-point of injection and converted to kBq/ml. The scintillator was placed in the striatum using a stereotactic frame (David Kopf Instruments, Tujunga, CA, USA). The skull was exposed and a craniotomy was performed using a dental drill. Then the dura was carefully incised and the probe was carefully lowered to a depth of 5.5 mm for striatal recordings. Only one probe penetration was performed per animal.

Determination of the arterial plasma input curve

The total radioactivity in arterial blood was continuously recorded using the coincidence counter. Whole blood activity was then corrected for (a) the relative concentration of ^{11}C-ABP688 in plasma versus whole blood and (b) the concentration of labeled metabolites. The ratio “radioactivity concentration plasma/radioactivity concentration whole blood” was determined in 6 separate animals in a preceding pilot study at different time-points (2–4 blood samples (~100 μl) per animal). The data of all animals were then pooled and the time-course of the ratio was approximated by fitting a quadratic polynominal to the data. This function was subsequently used to convert radioactivity concentration in whole blood to radioactivity concentration in plasma.

In the same 6 animals, metabolite analysis was performed. For this purpose, 500 μl blood samples were taken at different time-points (a maximum of 4 samples per animal). In each sample the fraction of authentic ^{11}C-ABP688 in plasma was determined as described below. The data of all animals were then pooled and the

Table 1
Fitting results calculated with the two-tissue compartment model and fixed values for K_1/k_2 (1.6) and k_4 (0.05 min^{-1})

Baseline						Blockade with MMPEP						Blockade with cold ABP (3 mg/kg)			
Animal #	Cold ABP, pmol/g	α, ml blood/ml tissue	K_1, ml/min/ml	k_3, min^{-1}	DV_{tot}, ml plasma/ml tissue	M-MPEP	Cold ABP, pmol/g	α, ml blood/ml tissue	K_1, ml/min/ml	k_3, min^{-1}	DV_{tot}, ml plasma/ml tissue	α, ml blood/ml tissue	K_1, ml/min/ml	k_3, min^{-1}	DV_{tot}, ml plasma/ml tissue
1	0.90	0.09	0.93	0.55	16.21										
2	1.05	0.12	0.55	0.44	15.66										
3	0.79	0.15	0.88	0.47	16.62										
4	1.88	0.14	0.98	0.52	18.28										
5	2.10	0.12	0.68	0.38	13.61										
6	0.64	0.01	0.41	0.51	18.00										
7	0.84	0.02	0.67	0.34	12.60	1 mg/kg	7.47	0.05	0.63	0.12	5.55				
8	0.64	0.13	0.91	0.26	9.98	2 mg/kg	2.24	0.01	0.87	0.05	3.32				
9	4.51	0.01	0.98	0.47	15.48	6 mg/kg	14.3	0.07	0.74	0.09	4.41				
Mean		0.09	0.78	0.44	15.16	Mean		0.04	0.75	0.09	4.43				
SD		0.06	0.21	0.09	2.67	SD		0.03	0.12	0.04	1.12				
10						3 mg/kg		0.07	0.68	0.07	3.74	0.01	0.87	0.08	4.29
11						3 mg/kg		0.06	0.54	0.07	3.95	0.13	0.67	0.07	3.92

time-course of the fraction of authentic tracer was approximated by a decaying biexponential function starting at value 1 at time zero. This function was then used to convert the total plasma activity to the time-course of authentic ^{11}C-ABP688. Metabolite data acquired at baseline were also used for the blocking studies assuming that the blocking drug did not alter peripheral metabolism of the radioligand.

Metabolite analysis

To separate authentic tracer and metabolites in plasma, solid phase separation with extraction cartridges (Waters Sep-Pak® tC18) was performed. Plasma samples of 100 to 200 µl were diluted with 2.5 ml aqua and passed through the Sep-Pak® cartridges. In a second step the cartridges were eluted with 5 ml aqua and cleared with air to wash out the remaining metabolites, leaving only the adsorbed tracer in the cartridges. Both components were measured in the gamma counter, yielding the fraction of authentic tracer. The Sep-Pak® method had previously been validated with high-performance liquid chromatography (HPLC) as demonstrated in Fig. 1.

Experimental protocols

In 2 animals (nr5 and nr9), baseline cerebral blood flow (CBF) was determined using $H_2{}^{15}O$ and the methodology described previously (Weber et al., 2003). Briefly, 150–200 MBq $H_2{}^{15}O$ was injected into the shunt and data were recorded for 3 min. The striatal time–activity curve and the arterial input curve were then used to calculate quantitative CBF values. The analysis was based on a one-tissue compartment model (Fig. 2A). In these two animals the CBF values were then used for the calculation of the first pass extraction fraction EF of ^{11}C-ABP688 ($EF = K_1/CBF$).

In 6 (nr1–nr6) animals the time-course of ^{11}C-ABP688 was measured at baseline alone. In another 5 animals (nr7–nr11) the experiments involved a pharmacological intervention. In 3 animals (nr7–nr9) the baseline experiment was followed by blockade of the mGlu5 receptors using increasing doses of M-MPEP (1, 2 and 6 mg/kg), a selective allosteric antagonist of the mGlu5 receptor

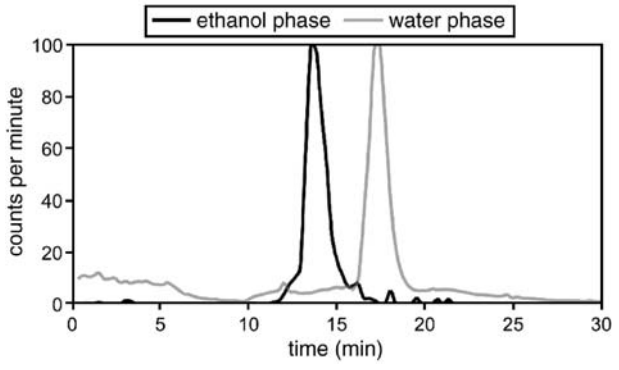

Fig. 1. High performance liquid chromatography (HPLC, BondClone, C18; 3.9×300; 5 µm; mobile phase, acetonitrile: 0.1% phosphoric acid [65:35]; flow late, 0.4 ml/min). The HPLC was performed to validate the Sep-Pak® method to separate authentic tracer from more polar metabolites. The peak in the ethanol phase (used to wash out the adsorbed compound) and in the water phase are clearly separated and there was only one peak per phase. A second experiment demonstrated that the ethanol peak represents ^{11}C-ABP688. These data demonstrate the suitability of the Sep-Pak® method.

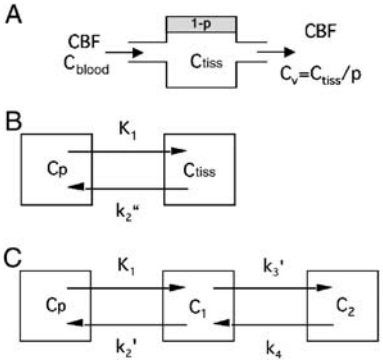

Fig. 2. One- and two-tissue compartment models used to analyze cerebral blood flow (CBF) using $H_2{}^{15}O$ (A) and the kinetics of ^{11}C-ABP688 (B, C), respectively.

(Gasparini et al., 1999). In each case (1.2 and 6 mg/kg respectively) the drug was intravenously injected 20 min after first ^{11}C-ABP688 injection and 10 min before the second radiotracer injection. Both injections were done sequentially using the same radiotracer synthesis. In 2 (nr10–11) animals it was investigated whether ^{11}C-ABP688 binds specifically to another site which cannot be blocked by M-MPEP. For this purpose the mGlu5 receptors were blocked with 3 mg/kg M-MPEP administered intravenously 10 min prior to a first tracer injection. Twenty minutes later, 3 mg/kg stable ABP688 was injected, and 10 min later another injection of ^{11}C-ABP688 was performed and data were recorded for another 20 min.

Injected activities were in the range of 41–108 MBq throughout all experiments and the injected mass of ABP688 was 0.64–14.30 pmol/g body weight (Table 1).

Model

The models used in this study are illustrated in Fig. 2.

CBF measurements

The basis of the calculation of the CBF measurements was the one-tissue compartment model including a partition coefficient for $H_2{}^{15}O$ (Fig. 2A). The change of the radioactivity concentration in tissue C_{tiss} is then defined by the following differential equation

$$dC_{tiss}/dt = CBF(C_{blood}(t) - C_{tiss}(t)/p) \quad (1)$$

where C_{blood} is the arterial blood tracer concentration and p is the tissue partition coefficient, e.g. that fraction of tissue that is permeable for $H_2{}^{15}O$. In this configuration C_{tiss} is the concentration of $H_2{}^{15}O$ in 1 ml of brain and it is assumed that $H_2{}^{15}O$ immediately reaches a homogeneous concentration in permeable space and no division into a vascular and a tissue compartment is necessary. The analytical solution of Eq. (1) is

$$C_{tiss} = CBF\exp(-CBF/pt) \otimes C_{blood} \quad (2)$$

where ⊗ signifies mathematical convolution.

Eq. (2) was fitted to the data using least squares fitting (Marquardt algorithm) implemented in the software PMOD (http://www.pmod.com; Mikolajczyk et al., 1998). Before fitting all data were corrected for decay and the input function for delay.

^{11}C-ABP688 experiments

In the experiments with 2 successive tracer injections the data following the second injection were confounded by counts from the first injection. This was corrected by the following procedure, illustrated in Fig. 3. The tissue data 20–30 min following the first tracer injection were fitted with a monoexponential which was then extrapolated to the end to the study (solid line). The value of the extrapolated exponential was then subtracted from the counts measured after the second injection. The same procedure was applied for the correction of the total arterial radioactivity concentration. All data were decay-corrected to the time-point of the first injection and expressed in kBq/ml and background corrected before this procedure.

Tracer kinetic model

The investigated methods consisted of standard compartmental modeling using an arterial input function. Tracer kinetic modeling was performed using the models depicted in Fig. 2. They contain one and two tissue compartments. The notation using primes is borrowed from Koeppe et al. (1991). The meaning of the parameters is as follows:

K_1:	Describes uptake of tracer across the blood brain barrier and is related to blood flow (CBF) and the first pass extraction fraction Ef (K_1=CBF Ef).
k_2'', k_2':	Represent backdiffusion from tissue to vascular space in the one- and two-tissue compartment model respectively
k_3':	Describes the transfer of the ligand to the receptor, $k_3' = \frac{k_3}{1+k_5/k_6} = \frac{k_{on}\ B_{max}'}{1+k_5/k_6}$

where k_5 and k_6 denote the exchange of ligand between the free and the nonspecific compartment in the full three-tissue compartment model. The term $\frac{1}{1+k_5/k_6}$ is equivalent to the term f2 used by Mintun et al. (1984) and others. B_{max}' is the density of free receptors and k_{on} denotes the association constant.

k_4:	Describes dissociation from receptor (k_{off})
DV″:	Total distribution volume of tissue activity calculated with the one-tissue compartment model (K_1/k_2'')
DV_{C1}:	Distribution volume of compartment C_1 (K_1/k_2')
DV_{C2}:	Distribution volume of compartment C_2 ($K_1/k_2'\ k_3'/k_4$)
DV_{tot}:	Total distribution volume of tissue activity calculated with the two-tissue compartment model ($DV_{C1}+DV_{C2}=K_1/k_2'\ (1+k_3'/k_4)$

Tracer exchange between the compartments is described by the following differential equations

$$\frac{dC_1}{dt} = K_1 C_p - (k_2' + k_3')C_1 + k_4 C_2 \quad (3)$$

$$\frac{dC_2}{dt} = k_3' C_1 - k_4 C_2 \quad (4)$$

$$\frac{dC_{tiss}}{dt} = K_1 C_p - k_2'' C_{tiss} \quad (5)$$

where C_p is the concentration of authentic tracer in arterial plasma. Eqs. (3) and (4) describe tracer exchange in the two-tissue compartment model, Eq. (5) in the one-tissue compartment model.

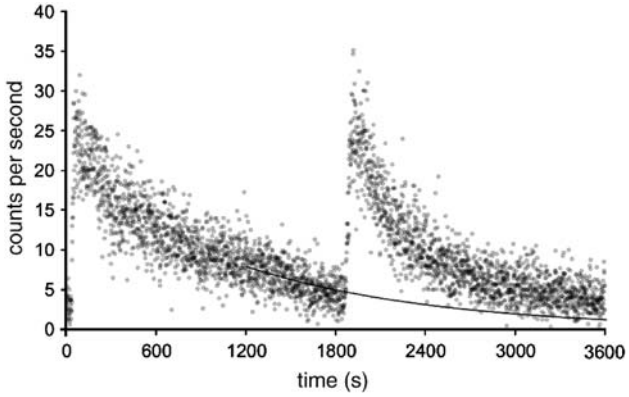

Fig. 3. Typical experiment with 2 tracer injections. Demonstrated is original beta-scintillator data (not decay corrected). The solid line represents the monoexponential fit to the last 10 min of data of the first experiment. The extrapolation of that fit was used to correct the second experiment for residual ^{11}C activity from the first experiment.

Since the total activity measured in a region is composed of counts from tissue and blood, all models contained a parameter (α) correcting for blood activity.

$$C_{probe} = (1-\alpha)C_{tiss} + \alpha C_{blood} \quad (6)$$

where:

C_{probe}:	Radioactivity registered by the beta probe α: Percentage of the counts originating from intravascular space
C_{tiss}:	Activity concentration in the extravascular compartment; with the two-tissue compartment model C_{tiss} is the sum of C_1 and C_2.
C_{blood}:	Radioactivity concentration in arterial whole blood

C_{tiss} was calculated by numerical integration of the differential equations.

Models B and C (Fig. 2) were fitted to the data from the time-point of injection to 20 min using Marquart's least squares fitting. The adequacy of the model was judged according to the Akaike information criterion (AIC) (Akaike, 1974). Model C was considered superior if there was a decrease in AIC compared to model B. DV_{tot} was taken as a measure for receptor density.

Autoradiographic studies

This study included 2 male rats (Sprague-Dawley) weighing approximately 307 and 311 g, respectively. To demonstrate the native distribution of ^{11}C-ABP688 in the brain and the effect of blockade with M-MPEP two autoradiographic studies were performed. Five minutes after the injection of 500 MBq ^{11}C-ABP688 (specific activities: 104 and 157 GBq/μmol; injected masses: 8.16 and 15.59 pmol/g body weight) into the tail vein, the animals were sacrificed by an intravenous overdose of pentobarbital (Nembutal; Abbott Laboratories, North Chicago, USA), the brains were quickly removed and frozen in chilled isopentane (Isopentan; Fluka Chemie GmbH, Buchs, Switzerland). The frozen brains were cut in 10 μm horizontal slices and thaw-mounted on glass slides. The slides were put on a phosphor imager screen (Fuji TR 2025; Fuji Photo Film Co., Ltd., Tokyo, Japan) for 2 h together with ^{14}C standards for quantification of tracer uptake. In a previous

calibration experiment, each ^{14}C standard had been assigned a value in kBq cm^{-3} of ^{11}C activity. This was achieved by exposing 10 µm sections of porcine brain paste with well defined amounts of ^{11}C activity for 2 h together with the ^{14}C standards. Finally the data were scanned (Fuji BAS 1900 II, pixelsize 50 µm; Fuji Photo Film Co., Ltd., Tokyo, Japan) and converted to kBq/ml. Dividing the tissue uptake by the decay-corrected injected activity per gram of body weight yielded standardized uptake values (SUVs). In the blocking experiment, M-MPEP (3 mg/kg i.v.) was injected intravenously 10 min prior to tracer injection.

Results

Autoradiographic studies

The brain distribution of ^{11}C-ABP688 is illustrated in the left autoradiograph of Fig. 4. High concentrations are observed in the striatum, cortex and hippocampus. Lower tracer uptake is seen in the thalamus and the white matter. The region with lowest uptake is the cerebellum. Following blockade with M-MPEP, the ^{11}C-ABP688 distribution pattern is homogeneous and the uptake value in all structures decreased to the level of the cerebellum. In striatum, SUV in the untreated animal was 3.15 versus 0.38 in the animal pretreated with M-MPEP, and SUV in the cerebellum was 0.45 and 0.38 under baseline and M-MPEP conditions, respectively.

Time-course of tracer in arterial plasma

The time-course of the fraction of authentic ^{11}C-ABP688 in arterial plasma is demonstrated in Fig. 5. Metabolism is rapid, and at 40 min the fraction of ^{11}C-ABP688 is 20%. The ratio of the ^{11}C-radioactivity concentration in plasma to whole blood decreased from 1.2 immediately after injection to 0.95 at 40 min.

Time-course of tracer in tissue and tracer kinetic modeling

An example of the time-course of the radioactivity concentration in striatum at baseline and following blockade with M-MPEP is demonstrated in Fig. 6. The model fit is superimposed. At

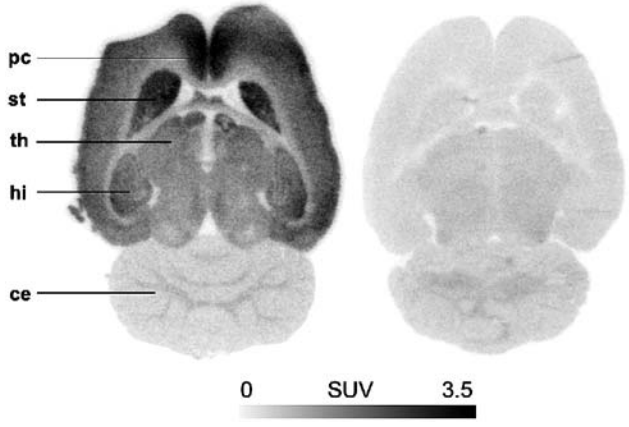

Fig. 4. ^{11}C-ABP688 autoradiographs demonstrating the ^{11}C distribution 5 min following injection of 500 MBq of tracer. On the left is a baseline experiment, on the right the animal was blocked with 3 mg/kg M-MPEP 10 min prior to tracer injection. pc: prelimbic cortex, st: striatum, hi: hippocampus, th: thalamus, ce: cerebellum.

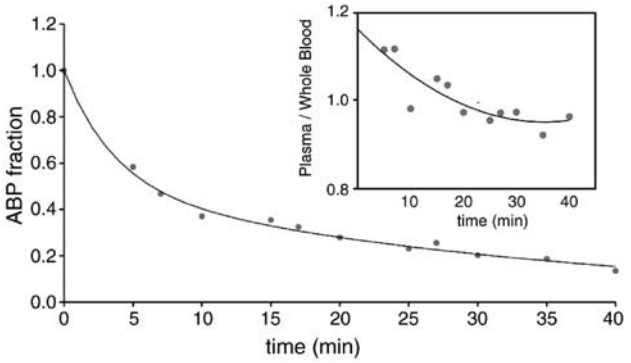

Fig. 5. The larger graph demonstrates the time-course of the fraction of authentic ^{11}C-ABP688 in arterial plasma. The filled circles are the mean of the measured data points obtained of 6 animals. In each animal, blood samples were processed at 2–4 different time-points. The line represents the biexponential fit to the data ($y=0.5\ \exp(-0.279*t)+0.5\ \exp(-0.029*t)$). The insert denotes the ratio of the total ^{11}C activity in plasma to whole blood. Again the filled circles represent measured data from 6 animals. The solid lines is a quadratic fit to the data ($y=0.00016t^2-0.01152t+1.15756$, t in minutes).

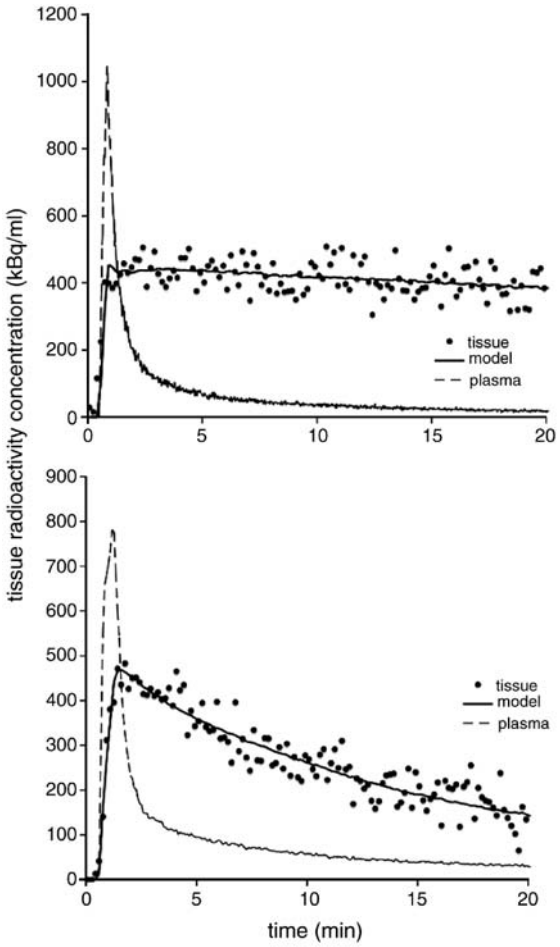

Fig. 6. Blockade experiment in animal nr9. Data recorded from the striatum at baseline are presented in the upper panel and following blockade with M-MPEP (6 mg/kg intravenous) in the lower panel. Washout of tracer is remarkably faster after blockade with M-MPEP. The dots represent the tissue time–activity curves, the solid line is the model fit and the broken line represents the ^{11}C-ABP688 activity concentration in arterial plasma.

baseline washout of tracer during the investigated 20 min is minimal. In contrast washout is remarkably faster following blockade with M-MPEP. The fitting results of all ^{11}C-ABP688 experiments are summarized in Table 1. In 5 of the 9 baseline experiments, the two-tissue compartment model was more adequate to fit the data based on a clear decrease in the AIC. In order to fit all experiments with one type of model, all data were then fitted using the two-tissue compartment model. To get stable fits K_1/k_2 was fixed to 1.6 and k_4 to 0.05 min^{-1} in both the baseline and the blocking experiments, corresponding to mean values of free fitting using two tissue compartments. Using this procedure we assumed that the blocking drug decreases the number of available receptors (k_3) but not the DV of compartment C_1 (K_1/k_2') and k_4. Blood flow in the 2 animals with CBF measurement was 0.63 and 0.69 ml/min/ml respectively. These values together with K_1 from ^{11}C-ABP688 experiments yielded a first pass extraction fraction of 97 and 87%, respectively. In the baseline experiments K_1 ranged from 0.41 to 0.98 ml/min/ml. The values of DV_{tot} were generally high, above 12 ml plasma/ml tissue in 8 of the 9 baseline experiments.

Blockade with M-MPEP

The blocking experiments nr7–9 demonstrate a marked reduction of DV_{tot}. The percentage reduction from baseline was 56, 67 and 72% for 1, 2 and 6 mg/kg M-MPEP, respectively. The effect of the blockade on K_1 was markedly less pronounced.

Sequential blockade with M-MPEP and stable ABP688

In the 2 experiments (nr10 and nr11) with a double blockade, there was no further decrease of DV_{tot} following cold ABP688.

Discussion

Qualitative assessment of the general distribution and specificity of the tracer using autoradiographic studies

Autoradiographic studies are very suitable to investigate the tissue distribution of a tracer. Spatial resolution is very high, but, as a disadvantage, only one time-point following tracer injection can be assessed per animal. It is furthermore important to note that tracer distribution assessed in a non-equilibrium state, as occurs after bolus injection, does not reflect receptor density in a quantitative manner, even if the tracer was 100% specifically bound. In order for the tracer distribution to reflect receptor density quantitatively one would have to image while tracer in brain and plasma are in complete equilibrium. Theoretically that would be possible using a "bolus and constant infusion" protocol as has been employed in human studies (Koeppe et al., 2005). However, it would be very difficult to do a ^{11}C autoradiographic study using such a protocol. Because of the rapid decay during the time to equilibration, not enough radioactivity would be available. Nevertheless, the comparison of the autoradiograph in Fig. 4 with previous studies (Shigemoto et al., 1993; Romano et al., 1995; Aoki et al., 2004) indicates, that the distribution of ^{11}C-ABP688 is related to the pattern of mGlu5 receptor distribution. Together with the blockade experiment, one can also get a first indication of the amount of specifically bound tracer. Since M-MPEP binds with high specificity to the allosteric binding site in the transmembrane portion of the mGlu5 receptor (Gasparini et al., 2002), the difference between the 2 autoradiographic studies represents specific binding of ^{11}C-ABP688 to the same site on the mGlu5 receptor.

First pass extraction fraction (EF)

This study demonstrates that the EF is exceptionally high, although probably somewhat overestimated because of a more pronounced underestimation of CBF relative to K_1. This is due to the larger free range of ^{15}O positrons leading to a more pronounced partial volume effect. With a high EF the tracer distribution early after injection will reflect blood flow. This opens the potential to assess CBF and receptor density with one tracer injection.

Specificity for the mGlu5 receptor

One measure for the specificity is the amount of tracer tissue binding which can be blocked by a ligand that binds to the same site. The allosteric antagonist M-MPEP displays high affinity binding to the mGlu5 receptor and has no relevant affinity for the other subtypes of the glutamate receptor family or other known receptors (Gasparini et al., 2002). The SUV values in the autoradiographs demonstrate an 88% reduction of ^{11}C-ABP688 binding in striatum following a blocking dose of M-MPEP, suggesting that this fraction of total tissue activity at the selected time-point was specific binding. More quantitative information on specific binding is obtained from the blocking experiments nr7–9. The reduction of DV_{tot} in the range of 56–72% indicates a high amount of specific binding. The percentage reduction seems related to the injected amount of M-MPEP; however, more experiments would be needed to establish a clear dose-dependence.

The high specificity of ^{11}C-ABP688 for the mGlu5 receptor is further demonstrated by the successive blockade with M-MPEP and stable ABP688 in experiments nr10 and 11. While the reduction of DV_{tot} following blockade with M-MPEP demonstrates the fraction of ^{11}C-ABP688 bound to the mGlu5 receptor, it does not exclude binding of ^{11}C-ABP688 to another specific (displaceable) binding site. This does not seem to be the case, since we observed no marked further reduction in DV_{tot} following the injection of stable ABP688.

General remarks

The combination of autoradiographic studies and beta-scintillator proved to be a valuable tool to evaluate important aspects of new receptor ligands. At this point it could be argued that the use of small animal PET would be preferable over the beta-scintillator. The advantage of the small animal PET method is that it is less invasive and that the tracer distribution can be assessed in the whole animal and not only at one location. However, there are points in favor of the beta-scintillator, e.g. it is considerably cheaper and its temporal resolution is superior. The latter point is important for quantitative perfusion imaging using $H_2{}^{15}O$ and the evaluation of tracer kinetic models.

Another point concerns the mass of injected stable ABP688. The number of stable ABP688 molecules per volume should be small relative to the available receptors, otherwise it will markedly alter the kinetics of the labeled ABP688 molecules due to relevant receptor binding. To evaluate this problem we took a B_{max} value of 83 nM (Hamill et al., 2005) and assumed that all ligands at peak activity were bound to receptors. This yielded a receptor occu-

pancy of 6±5% (mean±SD, all baseline experiments). This value is an upper limit, since not all ligands will be receptor bound. Another indication that receptor occupancy by stable ABP688 was low is the lacking correlation between the injected mass of stable ligand and DV_{tot} in the baseline experiments (Table 1). The vascular fraction α demonstrated in Table 1 displays quite a large variation. Part of this is probably noise, but some of it may be attributed to the location of vessels relative to the probe. A vessel located close to the probe will contribute more counts than a vessel 1 mm away.

Conclusion

^{11}C-ABP688 is a very promising ligand for the quantification of mGlu5 receptors in humans and animals. It readily crosses the blood–brain barrier and binds with high specificity to the mGlu5 receptor. The study furthermore demonstrates the usefulness of a beta-scintillator, if necessary in connection with autoradiographic studies, to evaluate new receptor tracers with regard to their usefulness in human PET studies.

Acknowledgments

The authors would like to acknowledge the support of René Amstutz, Head of Discovery Technologies, and Graeme Bilbe, Head of Neuroscience at the Novartis Institutes for Biomedical Research.

Matthias Wyss and Valerie Treyer were supported by the Swiss National Science Foundation.

References

Akaike, H., 1974. A new look at the statistical model identification. IEEE Trans. Automat. 716–723.

Ametamey, S.M., Kessler, L., Honer, M., Auberson, Y., Gasparini, F., Schubiger, P.A., 2003. Synthesis and evaluation of 11C-FPEP as a PET ligand for imaging the metabotropic glutamate receptor subtype 5 (mGluR5). J. Labelled Compd Radiopharm. 46, S188.

Ametamey, S.M., Kessler, L.J., Honer, M., Wyss, M.T., Hintermann, S., Auberson, Y.P., Gasparini, F.P.A.S., 2005. Radiosynthesis and preclinical evaluation of [11C]-ABP688 as a probe for imaging the metabotropic glutamate receptor subtype 5 (mGluR5). J. Nucl. Med. 47, 698–705.

Aoki, T., Narita, M., Shibasaki, M., Suzuki, T., 2004. Metabotropic glutamate receptor 5 localized in the limbic forebrain is critical for the development of morphine-induced rewarding effect in mice. Eur. J. Neurosci. 20, 1633–1638.

Gasparini, F., Lingenhohl, K., Stoehr, N., Flor, P.J., Heinrich, M., Vranesic, I., Biollaz, M., Allgeier, H., Heckendorn, R., Urwyler, S., Varney, M.A., Johnson, E.C., Hess, S.D., Rao, S.P., Sacaan, A.I., Santori, E.M., Velicelebi, G., Kuhn, R., 1999. 2-Methyl-6-(phenylethynyl)-pyridine (MPEP), a potent, selective and systemically active mGlu5 receptor antagonist. Neuropharmacology 38, 1493–1503.

Gasparini, F., Andres, H., Flor, P.J., Heinrich, M., Inderbitzin, W., Lingenhohl, K., Muller, H., Munk, V.C., Omilusik, K., Stierlin, C., Stoehr, N., Vranesic, I., Kuhn, R., 2002. [(3)*H*]-M-MPEP, a potent, subtype-selective radioligand for the metabotropic glutamate receptor subtype 5. Bioorg. Med. Chem. Lett. 12, 407–409.

Hamill, T.G., Seiders, T.J., Krause, S., Ryan, C., Sanabria, S., Gibson, R.E., Patel, S., Cosford, N., Roppe, J., Yang, J., King, C., Hargreaves, R.J., Burns, H.D., 2003. The synthesis and characterization of mGluR5 receptor PET ligands. J. Labelled Compd Radiopharm. 46, S184.

Hamill, T.G., Krause, S., Ryan, C., Bonnefous, C., Govek, S., Seiders, T.J., Cosford, N.D., Roppe, J., Kamenecka, T., Patel, S., Gibson, R.E., Sanabria, S., Riffel, K., Eng, W., King, C., Yang, X., Green, M.D., O'Malley, S.S., Hargreaves, R., Burns, H.D., 2005. Synthesis, characterization, and first successful monkey imaging studies of metabotropic glutamate receptor subtype 5 (mGluR5) PET radiotracers. Synapse 56, 205–216.

Koeppe, R.A., Holthoff, V.A., Frey, K.A., Kilbourn, M.R., Kuhl, D.E., 1991. Compartmental analysis of [11C]flumazenil kinetics for the estimation of ligand transport rate and receptor distribution using positron emission tomography. J. Cereb. Blood Flow Metab. 11, 735–744.

Koeppe, R.A., Gilman, S., Joshi, A., Liu, S., Little, R., Junck, L., Heumann, M., Frey, K.A., Albin, R.L., 2005. 11C-DTBZ and 18F-FDG PET measures in differentiating dementias. J. Nucl. Med. 46, 936–944.

Kokic, M., Honer, M., Ametamey, S.M., Gasparini, F., Andres, H., Bischoff, S., Flor, P.J., Heinrich, M., Vranesic, I.V., Spooren, W., Kuhn, R., Schubiger, P.A., 2001. Radiolabeling and in vivo evaluation of 11C-M-MPEP as a PET ligand for imaging the metabotropic glutamate receptor5 (mGluR5). Labelled Compd Radiopharm. 44, S231.

Kuhn, R., Pagano, A., Stoehr, N., Vranesic, I., Flor, P.J., Lingenhohl, K., Spooren, W., Gentsch, C., Vassout, A., Pilc, A., Gasparini, F., 2002. In vitro and in vivo characterization of MPEP, an allosteric modulator of the metabotropic glutamate receptor subtype 5: review article. Amino Acids 23, 207–211.

Masu, M., Tanabe, Y., Tsuchida, K., Shigemoto, R., Nakanishi, S., 1991. Sequence and expression of a metabotropic glutamate receptor. Nature 349, 760–765.

Mikolajczyk, K., Szabatin, M., Rudnicki, P., Grodzki, M., Burger, C., 1998. A JAVA environment for medical image data analysis: initial application for brain PET quantitation. Med. Inform. (Lond.) 23, 207–214.

Mintun, M.A., Raichle, M.E., Kilbourn, M.R., Wooten, G.F., Welch, M.J., 1984. A quantitative model for the in vivo assessment of drug binding sites with positron emission tomography. Ann. Neurol. 15, 217–227.

Patel, S., Krause, S.M., Hamill, T., Chaudhary, A., Burns, D.H., Gibson, R.A., 2003. In vitro characterization of [3*H*]MethoxyPyEP, an mGluR5 selective radioligand. Life Sci. 73, 371–379.

Pin, J.P., Duvoisin, R., 1995. The metabotropic glutamate receptors: structure and functions. Neuropharmacology 34, 1–26.

Romano, C., Sesma, M.A., McDonald, C.T., O'Malley, K., Van den Pol, A.N., Olney, J.W., 1995. Distribution of metabotropic glutamate receptor mGluR5 immunoreactivity in rat brain. J. Comp. Neurol. 355, 455–469.

Shigemoto, R., Nomura, S., Ohishi, H., Sugihara, H., Nakanishi, S., Mizuno, N., 1993. Immunohistochemical localization of a metabotropic glutamate receptor, mGluR5, in the rat brain. Neurosci. Lett. 163, 53–57.

Spooren, W., Gasparini, F., 2004. mGlu5 receptor antagonists: a novel class of anxiolytics? Drug News Perspect. 17, 251–257.

Spooren, W.P., Vassout, A., Neijt, H.C., Kuhn, R., Gasparini, F., Roux, S., Porsolt, R.D., Gentsch, C., 2000. Anxiolytic-like effects of the prototypical metabotropic glutamate receptor 5 antagonist 2-methyl-6-(phenylethynyl)pyridine in rodents. J. Pharmacol. Exp. Ther. 295, 1267–1275.

Tatarczynska, E., Klodzinska, A., Chojnacka-Wojcik, E., Palucha, A., Gasparini, F., Kuhn, R., Pilc, A., 2001. Potential anxiolytic- and antidepressant-like effects of MPEP, a potent, selective and systemically active mGlu5 receptor antagonist. Br. J. Pharmacol. 132, 1423–1430.

Weber, B., Burger, C., Biro, P., Buck, A., 2002. A femoral arteriovenous shunt facilitates arterial whole blood sampling in animals. Eur. J. Nucl. Med. Mol. Imaging 29, 319–323.

Weber, B., Spath, N., Wyss, M., Wild, D., Burger, C., Stanley, R., Buck, A., 2003. Quantitative cerebral blood flow measurements in the rat using a beta-probe and H2 15O. J. Cereb. Blood Flow Metab. 23, 1455–1460.

Section 2 –
Evaluation of PET tracers to establish clinical usefulness

Part II: Evaluation of radiotracers for the management of brain tumor patients

II.1. Uptake of ^{18}F-fluorocholine, ^{18}F-fluoroethyl-L-tyrosine, and ^{18}F-FDG in acute cerebral radiation injury in the rat: Implications for differentiation of radiation necrosis from tumor recurrence

Journal of Nuclear Medicine, 2004, Vol 45 (11), Pages 1931-1938

II.2. ^{18}F-choline in experimental soft tissue infection assessed with autoradiography and high-resolution PET

European Journal of Nuclear Medicine and Molecular Imaging, 2004, Vol 31 (3), Pages 312-316

II.3. Spatial heterogeneity of low-grade gliomas at the capillary level: A PET study on tumor blood flow and amino acid uptake

Journal of Nuclear Medicine, 2007, Vol 48 (7), Pages 1047-1052

II.4. Early metabolic responses in temozolomide treated low-grade glioma patients

Journal of Neurooncology, 2009, Vol 95 (1), Pages 87-93

Uptake of ^{18}F-Fluorocholine, ^{18}F-Fluoroethyl-L-Tyrosine, and ^{18}F-FDG in Acute Cerebral Radiation Injury in the Rat: Implications for Separation of Radiation Necrosis from Tumor Recurrence

Nicolas Spaeth, DVM[1]; Matthias T. Wyss, MD[1,2]; Bruno Weber, PhD[1]; Stephan Scheidegger, PhD[3]; Amelie Lutz, MD[4]; Jorn Verwey, MS[5]; Ivan Radovanovic, MD[6]; Jens Pahnke, MD[6]; Damian Wild, MD[1]; Gerrit Westera, PhD[2]; Dominik Weishaupt, MD[4]; Dirk M. Hermann, MD[7]; Barbara Kaser-Hotz, DVM[3]; Adriano Aguzzi, MD[6]; and Alfred Buck, MD, MS[1]

[1]PET Center, Division of Nuclear Medicine, University Hospital Zurich, Zurich, Switzerland; [2]Center for Radiopharmaceutical Science of ETH, PSI, and USZ, Paul Scherrer Institute, Villigen, und University Hospital Zurich, Zurich, Switzerland; [3]Section of Diagnostic Imaging and Radio-Oncology, Veterinary Hospital, University Zurich, Zurich, Switzerland; [4]Institute of Diagnostic Radiology, University Hospital Zurich, Zurich, Switzerland; [5]Division of Radiation Medicine, Paul Scherrer Institute, Villigen, Switzerland; [6]Institute of Neuropathology, Department of Pathology, University Hospital Zurich, Zurich, Switzerland; and [7]Department of Neurology, University Hospital Zurich, Zurich, Switzerland

Differentiation between posttherapy radiation necrosis and recurrent tumor in humans with brain tumor is still a difficult diagnostic task. The new PET tracers ^{18}F-fluoro-ethyl-L-tyrosine (FET) and ^{18}F-fluorocholine (*N,N*-dimethyl-*N*-^{18}F-fluoromethyl-2-hydroxyethylammonium [FCH]) have shown promise for improving diagnostic accuracy. This study assessed uptake of these tracers in experimental radiation injury. **Methods:** In a first model, circumscribed lesions were induced in the cortex of 35 rats using proton irradiation of 150 or 250 Gy. After radiation injury developed, uptake of ^{18}F-FET, ^{18}F-FCH, and ^{18}F-FDG was measured using autoradiography and correlated with histology and disruption of the blood–brain barrier as determined with Evans blue. In a second model, uptake of the tracers was assessed in acute cryolesions, which are characterized by the absence of inflammatory cells. **Results:** Mean ^{18}F-FET, ^{18}F-FCH, and ^{18}F-FDG standardized uptake values in the most active part of the radiation lesion and the contralateral normal cortex (in parentheses) were 2.27 ± 0.46 (1.42 ± 0.23), 2.52 ± 0.42 (0.61 ± 0.12), and 6.21 ± 1.19 (4.35 ± 0.47). The degree of uptake of ^{18}F-FCH and ^{18}F-FDG correlated with the density of macrophages. In cryolesions, ^{18}F-FET uptake was similar to that in radiation lesions, and ^{18}F-FCH uptake was significantly reduced. **Conclusion:** Comparison of tracer accumulation in cryolesions and radiation injuries demonstrates that ^{18}F-FET uptake is most likely due to a disruption of the blood–brain barrier alone, whereas ^{18}F-FCH is additionally trapped by macrophages. Uptake of both tracers in the radiation injuries is generally lower than the published uptake in tumors, suggesting that ^{18}F-FET and ^{18}F-FCH are promising tracers for separating radiation necrosis from tumor recurrence. However, the comparability of our data with the literature is limited by factors such as different species and acquisition protocols and modalities. Thus, more studies are needed to settle this issue. Nevertheless, ^{18}F-FCH and ^{18}F-FET seem superior to ^{18}F-FDG for this purpose.

Key Words: radiation necrosis; ^{18}F-fluorocholine; ^{18}F-fluoro-ethyl-L-tyrosine; ^{18}F-FDG; autoradiography

J Nucl Med 2004; 45:1931–1938

Over the last 20 y, PET has become indispensable for evaluating brain tumors. Indeed, diagnosis of brain tumors was the first oncologic application of ^{18}F-FDG PET (*1*). Differentiation of posttherapy radiation necrosis from recurrent tumor remains a challenging diagnostic problem. Correct diagnosis obviously has strong implications for disease management. Attempts with ^{18}F-FDG were only partially successful (*2–5*). One problem is the high intrinsic uptake of ^{18}F-FDG in normal brain cortex, often rendering differentiation of lesions from normal brain difficult. Another is the wide range of ^{18}F-FDG uptake in different brain tumors, leading to an overlap with the degree of uptake in radiation necrosis. Also, MRI and CT cannot reliably separate radiation necrosis from recurrent tumor (*6–8*).

Therefore, the development of more specific radiotracers is a major aim of nuclear medicine research. Radiolabeled choline or amino acid analogs such as ^{18}F-fluorocholine

Received Mar. 10, 2004; revision accepted May 21, 2004.

For correspondence or reprints contact: Alfred Buck, MD, Nuclear Medicine, University Hospital, Rämistrasse 100, 8091 Zürich, Switzerland.

E-mail: fred.buck@usz.ch

(*N,N*-dimethyl-*N*-^{18}F-fluoromethyl-2-hydroxyethylammonium [FCH]) and ^{18}F-fluoro-ethyl-L-tyrosine (FET) seem promising for separating radiation necrosis from tumor recurrence (*9–11*). The ideal tracer for this purpose would reproducibly demonstrate a different accumulation pattern in radiation necrosis from that in tumor, such as no accumulation in radiation necrosis and high accumulation in tumor—a pattern that has been demonstrated for ^{18}F-FET and ^{18}F-FCH.

^{18}F-FET is an amino acid analog that is not metabolized or incorporated into proteins. A specific Na^+-independent amino acid transport system, the L-system, is responsible for high ^{18}F-FET accumulation in tumor cells (*12*). Wester et al. introduced this tracer to clinical research (*13*). Further studies have demonstrated increased uptake of ^{18}F-FET in various brain tumors (*11,14,15*) and lack of uptake by inflammatory tissue (*16,17*). This is important, since radiation necrosis may contain inflammatory cells.

Choline is transported into mammalian cells by specific mechanisms and then phosphorylated by choline kinase. In a further step, choline is metabolized to phosphatidylcholine and incorporated into the cell membrane (*18,19*). The increased choline uptake in tumor cells is explained by upregulation of choline kinase (*20,21*). Initial studies with ^{11}C-choline demonstrated the diagnostic potential of this substance in different tumors (*22–26*). Degrado et al. introduced ^{18}F-FCH for brain tumor imaging (*27*). The major advantage of ^{18}F-labeled compounds, especially in clinical use, is the longer physical half-life of ^{18}F (110 min) than of ^{11}C (20 min). The tumor uptake patterns of ^{11}C-choline and ^{18}F-substituted choline analogs are very similar (*9*). Contrary to ^{18}F-FET, ^{18}F-FCH is accumulated by inflammatory cells (*28*).

The purposes of this study were, first, to assess uptake of ^{18}F-FET, ^{18}F-FCH, and, for comparison, ^{18}F-FDG in experimentally induced acute radiation injury in the rat brain. The tracer uptake pattern was assessed by autoradiography and correlated with histologic findings and disruption of the blood–brain barrier (BBB) as assessed with Evans blue. A second purpose was to evaluate the effect of BBB disruption alone on uptake of ^{18}F-FET and ^{18}F-FCH. For this purpose, ^{18}F-FET and ^{18}F-FCH accumulation was determined in cryolesions, which are characterized by a heavily disrupted BBB but, in contrast to radiation injury, absence of inflammatory cells. Finally, this study assessed the pattern of blood flow in radiation injuries and cryolesions. To this end, perfusion was determined in another group of animals using ^{14}C-iodoantipyrine autoradiography.

MATERIALS AND METHODS

Animals

This study used 35 male Sprague–Dawley rats weighing 250–400 g. All interventions were performed while the animals were under inhalation anesthesia using isoflurane (2–3 vol%, Forene; Abbott Laboratories). The experiments were approved by the local veterinary authorities of the Kanton of Zurich, Switzerland.

Radiopharmaceuticals

4-Iodo-*N*-methyl-^{14}C-antipyrine was obtained from American Radiolabeled Chemicals, Inc. ^{18}F-FDG was obtained from the commercial ^{18}F-FDG production of the University Hospital Zurich. ^{18}F-FET was produced using a method analogous to that of Wester et al. (*13*). ^{18}F-Fluoride (azeotropically dried with 0.7 mL of acetonitrile) was reacted with 10 mg of ethylene glycol-1,2-ditosylate in acetonitrile in the presence of Kryptofix(2.2.2) (Merck) at 110° to give ^{18}F-fluoroethyltosylate, which was purified by reversed-phase high-performance liquid chromatography (HPLC) (LiChrospher 100 RP-18 [Merck], 250 × 10 mm, MeOH/H_2O = 60/40). The product fraction was trapped on a polystyrene cartridge (LiChrolut EN; Merck), dried with nitrogen, and eluted with 0.7 mL of dimethyl sulfoxide into a second vial containing 10 mg of L-tyrosine and 7.5 mg of potassium methylate, where it was reacted for 5 min at 120°. The product was purified by reversed-phase HPLC (LiChrospher 100 RP-18, 10 μm, 250 × 10 mm, EtOH/H_2O/HAc = 8/89.5/2.5, 2.5 g of ammonium acetate per liter). The product peak was sterile filtered into a bottle containing 1 mL of saline and 0.1 mL of phosphate-buffered saline (0.6 mol/L, pH 4). Quality control was by reversed-phase HPLC over LiChrospher 100 RP-18, 5 μm, 250 × 4 mm, eluting with EtOH/H_2O/HAc = 8/89.5/2.5, with 2.5 g of ammonium acetate per liter. Radiochemical purity was >99%. In the ultraviolet trace, ^{18}F-FET was not visible and no quantifiable impurities were visible. Enantiomeric purity was determined by chiral ligand exchange HPLC over a Luna C18 column (250 × 4.6 mm, 5 μm) coated with L-penicillamine chiral selector, eluting with 30% methanol in 5 mmol of aqueous $CuSO_4$ per liter. Starting from L-tyrosine as the substrate, no D-(*R*)-*O*-^{18}F-fluoroethyltyrosine was detected.

^{18}F-FCH was produced by the reaction of ^{18}F-fluoromethyltriflate with diaminoethanol. ^{18}F-Fluoride (azeotropically dried with 2 × 0.7 mL of acetonitrile) was reacted with dibromomethane in acetonitrile in the presence of Kryptofix(2.2.2) at 110° to give ^{18}F-fluorobromomethane (*29*), which was purified over a series of 4 Sep-Pak Plus silica cartridges (Waters). ^{18}F-Fluoromethyltriflate was made by passing ^{18}F-bromofluoromethane over a silver triflate/Graphpac GC column (Alltech Associates Inc.) at 180°. ^{18}F-Fluoromethyltriflate was then used for the *N*-alkylation of 2-dimethylaminoethanol immobilized on a Sep-Pak Plus C-18 cartridge (a solution of 2-dimethylaminoethanol in ethanol [200 μL in 600 μL] was put on the cartridge), to quantitatively yield the desired product. For purification, ^{18}F-FCH was selectively trapped on a Sep-Pak Accel CM cartridge (Waters), washed with water, removed with saline, and, via a sterile filter, added to a patient bottle with 4 mL of saline, 0.5 mL of 10% NaCl, and 70 μL of $NaHCO_3$. Quality control was by HPLC over a cation exchange column (*30*). Supelcosil LC-SCX (Supelco, Inc.), 250 × 4.6 mm, 5 μm, eluting with a 0.15 mol/L concentration of NaH_2PO_4 in water/pyridine (1,000/0.08 v/v), was adjusted to pH 2.37 by 70% H_3PO_4. Radiochemical purity was >99%. In the ultraviolet trace, ^{18}F-FCH was not visible and no quantifiable impurities were visible.

Proton Irradiation

The rats were irradiated with a thin, collimated proton beam of 3-mm diameter at the Facility for Ocular Tumor Treatment (*31*) of the Paul Scherrer Institute. The energy of the protons was adapted to the required penetration depth of the beams or to the Bragg peak position. This position was evaluated using radiographs and CT scans of rats that were of a size typical of the irradiated animals. To ensure that the Bragg peak was at the same location for each

animal, a special holder was constructed. This holder was placed on the patient chair, which could be positioned with high precision. A laser beam, which marked the proton beam, guided the position of the irradiation point. The radiation was delivered as a single dose of 250 (n = 18) or 150 (n = 5) Gy.

MRI

Weekly sequential MRI examinations after the radiation treatment served for detection of radiation necrosis. MRI was performed on a 1.5-T system (Signa CV/i; General Electric Medical Systems). To maximize signal-to-noise ratio, animals were placed with their heads centrally located in a dedicated wrist coil. This coil was chosen because its design provides an optimal signal-to-noise ratio in relation to the relatively small diameter of a rat's skull. The imaging protocol included the following sequences: an unenhanced transaxial T1-weighted spin-echo sequence (repetition time [TR]/echo time [TE], 300 ms/13 ms; slice thickness, 3 mm, without an interslice gap) and a transaxial T2-weighted 3-dimensional fast spin-echo sequence (TR/TE, 3,000/128; slice thickness, 1.5 mm). In addition, the T1-weighted sequence was acquired in the transaxial plane after administration of gadopentetate dimeglumine (Magnevist [Schering AG], 0.1 mmol/kg of body weight) through a tail vein.

Cryolesions

Cryolesions (n = 12) were used as a model of pure BBB disruption without an inflammatory component. They were induced according to the method described by Hermann et al. (*32,33*). A liquid-nitrogen-cooled copper probe with a tip diameter of 2.5 mm and a tip temperature of −150°C was placed stereotactically through a burr hole onto the right parietal dura mater. Then, the probe was lowered another 200 μm to ensure contact with the cortical tissue and was left for 2 min. ^{18}F-FET and ^{18}F-FCH injections followed 30 min later.

Autoradiography with ^{18}F-FET, ^{18}F-FCH, and ^{18}F-FDG

After detection of radiation injuries on MRI, autoradiography was performed (12–20 d after irradiation in the 250-Gy group, 70–80 d in the 150-Gy group). Two hours before tracer injection, Evans blue was injected into a tail vein. Catheters were then placed in the right femoral artery to monitor blood pressure and in the femoral vein to allow intravenous application of the tracers. Fifteen (^{18}F-FCH and ^{18}F-FET) or 45 (^{18}F-FDG) minutes after injection of 150–200 MBq of tracer, the animals were sacrificed using an overdose of pentobarbital. The brain was removed and instantly frozen in cooled isopentane. For quantification, 10-μm brain slices (100-μm slice distance) were placed on a phosphor imaging screen together with ^{14}C standards and left for 240 min. Tritium-sensitive screens (TR2025; Fuji) were used, as their uncoated, thin, sensitive layer yields higher-resolution ^{18}F autoradiographs than do ordinary screens. The data were scanned (BAS 1800 II [Fuji]; pixel size, 50 μm) and converted to kBq/cm^3. For this conversion, the ^{14}C standards had previously been recalibrated using data from a 4-h exposure of 10-μm slices of brain homogenate containing a defined amount of ^{18}F activity.

For quantitative analysis, the activities were then decay corrected to the time of injection. Dividing these values by the amount of injected activity per gram of body weight yielded standardized uptake values (SUVs). Regions of interest were subsequently placed over the areas with highest and average tracer uptake in the lesions and over contralateral cortex.

4-Iodo-*N*-Methyl-^{14}C-Antipyrine Autoradiography for Evaluation of Perfusion

Two rats of each lesion model (n = 4) were injected with 1.85–2.0 MBq of ^{14}C-iodoantipyrine in 1 mL of saline and sacrificed 1 min later. The brain was removed and instantly frozen in chilled isopentane. Brain slices of 10-μm thickness (100-μm slice distance), together with ^{14}C standards, were placed on a phosphor-imaging screen for 24 h.

Histologic Examination and Evans Blue Fluorescence Imaging

Frozen sections 10 μm thick were fixed with 4% formalin and stained with hematoxylin–eosin for morphologic analysis. For Evans blue visualization, slices were fixed with 4% formalin and stained with 4′,6-diamidino-2-phenylindole (Molecular Probes). Images of the Evans blue distribution were then obtained using a fluorescence microscope. To assess the grade of gliosis, the brain slides were immunohistochemically stained with anti–glial fibrillary acidic protein (GFAP) (DAKO) and developed with the EnVision horseradish peroxidase rabbit system (DAKO).

Statistics

Differences in ^{18}F-FCH and ^{18}F-FET uptake in radiation injury and cryolesions were assessed using the Student 2-tailed unpaired t test.

RESULTS

Animals

In the 2 radiation groups, no animal experienced systemic side effects. Only a small oblong area of alopecia on the temporal skin corresponding to the beam line was discovered during the time of observation.

Radiation Injury

Development of Radiation Injury. Intracerebral lesions were detected on the MRI scans 12 and 70 d after irradiation in the 250- and 150-Gy groups, respectively. The diameter of the lesions ranged from 2 to 6 mm independent of the radiation dose.

Typical examples of MRI scans are demonstrated in Figure 1. The lesion was within the cortex of the right

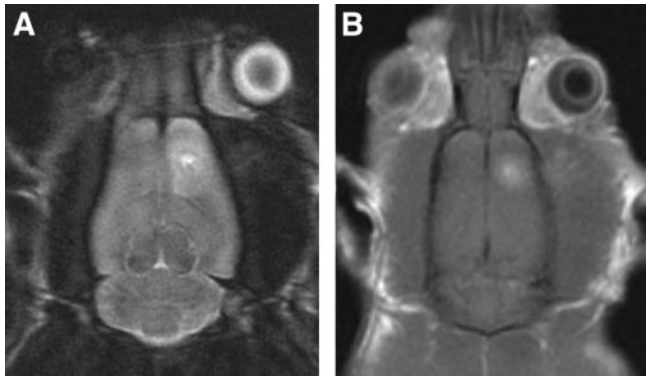

FIGURE 1. Axial MRI scans of rat brain clearly depict radiation lesion in frontoparietal right hemisphere. (A) T2-weighted 3-dimensional fast spin-echo sequence. (B) T1-weighted, gadolinium-enhanced spin-echo scan indicating disruption of the BBB.

frontoparietal region and extended into white matter. It presented as a hyperintense parenchymal signal alteration on the T2-weighted image. On the enhanced T1-weighted image after intravenous administration of gadolinium-diethylenetriaminepentaacetic acid (Magnevist; Schering AG), the entire lesion enhanced slightly, indicating leakage of the BBB.

Histology and Disruption of BBB. Images of a typical radiation injury are shown in Figure 2. Most lesions were characterized by a center of colliquation necrosis (area 1) consisting of cell debris, foamy macrophages, and sometimes calcifications. This center was surrounded by a layer (area 2) consisting of macrophages, reactive astrocytosis (evaluated by GFAP staining), dilated vessels, edema, and, occasionally, small hemorrhages.

Extravasation of Evans blue, indicating BBB disruption, was present in each case. In the example shown in Figure 2, the largest amount of Evans blue accumulated in parts of the necrotic center; smaller amounts were present in the surrounding inflammatory layer (area 2). A similar pattern is found in Figure 3B. In the ^{18}F-FDG example (Fig. 3D), no clear necrotic center was detectable. The small circumscribed area with increased Evans blue accumulation (area 4) did not correspond to the area with highest ^{18}F-FDG uptake (area 3 in Fig. 3C).

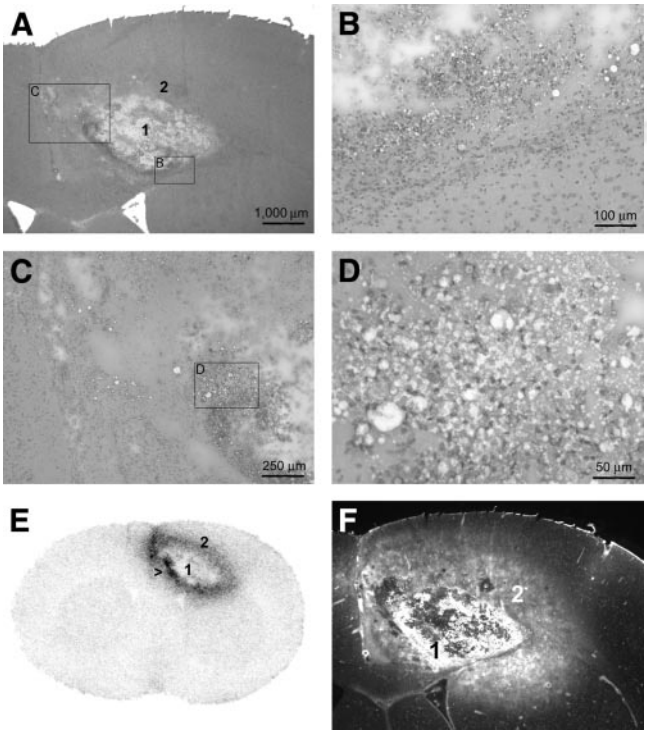

FIGURE 2. Images of radiation injury. (A–D) Hematoxylin- and eosin-stained histologic samples. The overview in panel A demonstrates the necrotic center (area 1) and the surrounding inflammatory layer (area 2). Panels B–D zoom in on layer 2, which is characterized by infiltration of macrophages and reactive astrocytosis. Panel D corresponds to the area with highest uptake of ^{18}F-FCH (arrow in E). The dense infiltrate of macrophages is clearly visible. Panel E depicts uptake of ^{18}F-FCH, which is concentrated in the area adjacent to the central necrosis. (F) Corresponding Evans blue fluorescent scan demonstrates disruption of the BBB.

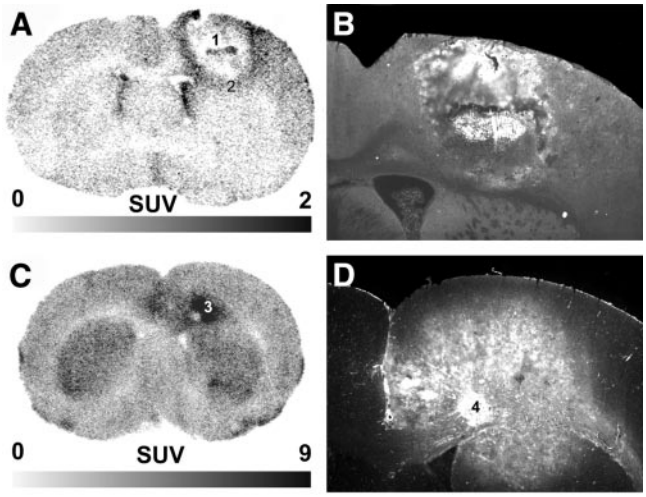

FIGURE 3. Uptake of ^{18}F-FET (A) and ^{18}F-FDG (C), together with the corresponding (B and D, respectively) Evans blue fluorescence scans.

Perfusion Pattern in Radiation Injury. ^{14}C-Iodoantipyrine autoradiography ($n = 2$) demonstrated reduced perfusion in the necrotic center. In the inflammatory layer adjacent to the necrotic center, where ^{18}F-FCH, ^{18}F-FET, and ^{18}F-FDG demonstrated increased uptake, perfusion was similar to that in normal cortex.

Uptake of ^{18}F-FET, ^{18}F-FCH, and ^{18}F-FDG. An autoradiograph demonstrating ^{18}F-FCH uptake is shown in Figure 2E. The highest degree of tracer accumulation was in the inflammatory layer (area 2) surrounding the central necrosis. Examples of ^{18}F-FET and ^{18}F-FDG autoradiographs are shown in Figure 3. ^{18}F-FET accumulation (Fig. 3A) was highest in the inflammatory layer (area 2). In the ^{18}F-FDG example (Fig. 3C), histologic examination revealed no clear necrotic center. The area with the highest ^{18}F-FDG uptake (area 3) was histologically characterized by increased macrophage density.

The SUVs of the various tracers are summarized in Table 1. ^{18}F-FDG displayed by far the highest uptake in the lesions. The SUVs for ^{18}F-FCH and ^{18}F-FET were similar and considerably smaller than for ^{18}F-FDG. The value of L/B (ratio of uptake in lesion to that in contralateral cortex) was highest for ^{18}F-FCH, followed by ^{18}F-FET and ^{18}F-FDG. This ratio to a high degree reflects the differing amounts of tracer accumulation in healthy cortex: least for ^{18}F-FCH, followed by ^{18}F-FET and ^{18}F-FDG.

Cryolesions

Histology and Disruption of BBB. Representative photomicrographs are shown in Figure 4. Cryolesions were characterized mainly by edema. There were no inflammatory cells or reactive astrocytes. Evans blue extravasation is demonstrated in Figure 4A. BBB disruption was present in the entire lesion.

TABLE 1
SUV in Animals with Induced Radiation Necrosis

Animal no.	Tracer	Radiation dose (Gy)	Nec1	Nec2	Ctx	Nec1/Ctx	Nec2/Ctx
1	^{18}F-FCH	250	2.18	1.38	0.58	3.76	2.38
2	^{18}F-FCH	250	2.62	1.43	0.54	4.85	2.65
3	^{18}F-FCH	250	2.18	1.43	0.53	4.11	2.70
4	^{18}F-FCH	250	2.11	1.12	0.54	3.91	2.07
5	^{18}F-FCH	250	2.44	1.25	0.59	4.14	2.12
6	^{18}F-FCH	150	3.22	1.99	0.60	5.37	3.32
7	^{18}F-FCH	150	2.92	1.92	0.86	3.40	2.23
Mean			2.52	1.50	0.61	4.22	2.50
SD			0.42	0.33	0.12	0.67	0.44
8	^{18}F-FET	250	1.25	0.90	0.73	1.71	1.23
9	^{18}F-FET	250	2.13	1.29	1.20	1.78	1.08
10	^{18}F-FET	250	2.64	1.39	1.56	1.69	0.89
11	^{18}F-FET	250	2.52	1.82	1.70	1.48	1.07
12	^{18}F-FET	250	2.40	1.80	1.27	1.89	1.42
13	^{18}F-FET	250	2.44	1.92	1.08	2.26	1.78
14	^{18}F-FET	150	1.77	1.52	1.57	1.13	0.97
15	^{18}F-FET	150	1.98	1.69	1.54	1.29	1.10
Mean			2.27	1.63	1.42	1.64	1.19
SD			0.46	0.34	0.23	0.36	0.29
16	^{18}F-FDG	250	4.82	3.66	4.29	1.12	0.85
17	^{18}F-FDG	250	4.93	4.35	3.62	1.36	1.20
18	^{18}F-FDG	250	6.59	4.48	4.38	1.50	1.02
19	^{18}F-FDG	250	6.50	5.28	5.07	1.28	1.04
20	^{18}F-FDG	250	6.39	3.93	4.24	1.51	0.93
21	^{18}F-FDG	150	8.01	6.11	4.47	1.79	1.37
Mean			6.21	4.64	4.35	1.43	1.07
SD			1.19	0.91	0.47	0.23	0.19

Nec1 = area of highest SUV in necrosis; Nec2 = area of average SUV in necrosis; Ctx = contralateral cortex.

Perfusion in Cryolesions. An example of the perfusion pattern as assessed with ^{14}C-iodoantipyrine is shown in Figure 4B. Perfusion in the lesion was reduced but not absent.

Uptake of ^{18}F-FET and ^{18}F-FCH. Typical ^{18}F-FCH and ^{18}F-FET autoradiographs are shown in Figures 3C and 3D. Accumulation of both tracers was homogeneously increased in the cryolesion, compared with the adjacent and contralateral normal brain tissue.

Table 2 summarizes the SUVs of ^{18}F-FCH and ^{18}F-FET. In lesions, ^{18}F-FET SUVs were on the order of 85% higher than ^{18}F-FCH SUVs. Compared with uptake in radiation injury, ^{18}F-FCH uptake was significantly lower in cryolesions (0.99 ± 0.18 vs. 1.50 ± 0.33, $P = 0.006$). In contrast, ^{18}F-FET accumulation was similar in both types of lesions (1.85 ± 0.34 vs. 1.63 ± 0.34, $P = 0.14$).

DISCUSSION

The main purpose of this study was to evaluate accumulation of the investigated tracers in an acute model of radiation injury so as to assess their ability to separate radiation necrosis from tumor recurrence in humans with brain tumors. All 3 investigated tracers have demonstrated usefulness in the evaluation of brain tumors with PET. ^{18}F-FET and ^{18}F-FCH usually display increased uptake in tumors relative to normal gray matter. Because ^{18}F-FDG is avidly taken up in normal gray matter, one commonly relates tumor uptake to white matter. The ideal tracer to separate tumor recurrence from radiation necrosis would show high uptake in tumors and no uptake in radiation necrosis. That ideal is clearly not met by any of the examined compounds. Three major components determine tracer uptake in lesions. The first is blood flow, which is responsible for tracer delivery. However, the normal or decreased blood flow that is found in areas with increased ^{18}F-FET or ^{18}F-FCH uptake indicates that blood flow is of minor importance. One can therefore concentrate on the other 2 factors: crossing of the BBB, which may be mediated by some regulated process if the BBB is intact or by pure leakage if the BBB has been disrupted, and accumulation in cellular elements. Of note with regard to the latter, a major histologic hallmark of tissue surrounding the necrotic center in radiation injury is macrophage invasion. Previous studies have shown that ^{18}F-FET is not taken up by these cells but is taken up by tissue outside the brain. One of these previous studies addressed ^{18}F-FET uptake in experimentally induced abscesses in the rat thigh muscle (*16*), and the other investigated ^{18}F-FET uptake in murine lymph nodes (*17*). Be-

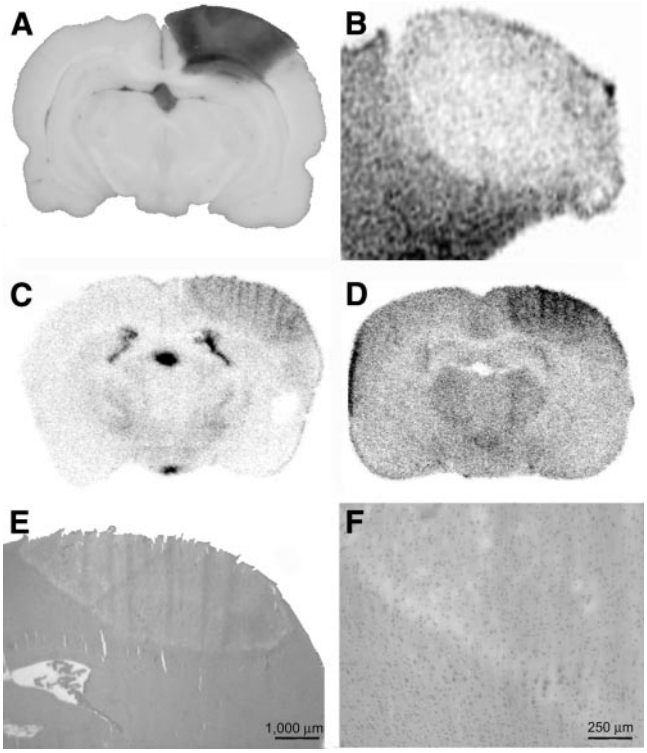

FIGURE 4. Examples of cryolesions. Extravasation of Evans blue, demonstrating disruption of the BBB, is already clearly visible on native images (A). Perfusion in the lesion is decreased relative to that in normal cortex but not absent, as is demonstrated by autoradiography with ^{14}C-iodoantipyrine (B). In contrast, ^{18}F-FCH (C) and ^{18}F-FET (D) uptake is increased in the cryolesion. Hematoxylin–eosin staining (E and F) demonstrate that edema characterizes the histology. There are no signs of inflammatory infiltration.

cause ^{18}F-FET is not taken up by macrophages, the increased uptake in radiation injury is most likely due to leakage of the BBB. This hypothesis was tested in the cryolesions, which served as a model of severe BBB disruption without inflammatory cells. The finding that ^{18}F-FET SUV was similar in radiation injury and cryolesions strongly supports the assumption that ^{18}F-FET uptake in acute radiation injury is indeed driven mainly by leakage across the disturbed BBB. In this context, it is important to note that blood flow in cryolesions was decreased (Fig. 4C). Increased blood flow could have been another reason for the observed increased ^{18}F-FET uptake.

The situation is different for ^{18}F-FCH, which displayed significantly higher uptake in radiation injury than in cryolesions. This finding is consistent with the hypothesis that ^{18}F-FCH uptake in radiation injury is determined by leakage across the BBB and incorporation mainly in macrophages. Because macrophages are missing from cryolesions, ^{18}F-FCH probably diffuses back from tissue into blood in cryolesions but is incorporated into macrophages in radiation injury. That ^{18}F-FCH is indeed incorporated mainly into macrophages and not other cells is suggested by the finding that the areas with highest ^{18}F-FCH uptake coincided with the areas of densest macrophage infiltration. Furthermore, we already demonstrated in a previous study that ^{18}F-FCH is taken up by macrophages (*28*).

There remains the important question of the suitability of the investigated tracers for differentiating radiation necrosis from tumor tissue. We address this question by comparing our data with published data on uptake of ^{18}F-FET, ^{18}F-FCH, and ^{18}F-FDG in brain tumors. However, a direct comparison of our data with the literature is limited by factors such as different acquisition protocols and modalities and interspecies differences.

^{18}F-FET

A direct comparison is possible of our ^{18}F-FET data with the tumor data of Langen et al., who inoculated F98 glioma cells into the brains of 13 CDF Fisher rats and evaluated ^{18}F-FET uptake by autoradiography. They reported a mean L/B of 5.26 ± 1.30 (*34*). This L/B is markedly higher than the values for radiation injury (1.19 ± 0.29, average areas) found by our study.

Weber et al. investigated ^{18}F-FET uptake in 16 patients with various tumors and radiation necrosis (*11*). SUV in the 2 patients with radiation necrosis was 1.1 and 0.8, and L/B was 1.2 and 1.1. These values are smaller than in our study.

TABLE 2
SUVs in Animals with Induced Cryolesions

^{18}F-FCH				^{18}F-FET			
Animal no.	Lesion	Ctx	Lesion/Ctx	Animal no.	Lesion	Ctx	Lesion/Ctx
1	1.29	0.71	1.82	6	1.6	1.10	1.45
2	0.84	0.36	2.33	7	1.52	1.10	1.38
3	0.89	0.45	1.98	8	1.88	1.19	1.58
4	0.97	0.40	2.43	9	1.87	1.21	1.55
5	0.98	0.59	1.66	10	2.38	1.69	1.41
Mean	0.99	0.50	2.04		1.85	1.26	1.47
SD	0.18	0.15	0.33		0.34	0.25	0.09

Ctx = contralateral cortex.

A possible reason is that radiation necrosis in the human study was of a more chronic type. Furthermore, SUVs measured with PET tend to underestimate the true values because of the limited resolution of PET. In the 14 patients with tumors, the L/B was 2.27 ± 0.65. In other studies, this value ranged from 2.0 to 3.3 (*13–15,35,36*). These values are higher than those found by our study, but there is some overlap. With regard to SUV, Weber et al. reported values of 2.67 ± 0.91 and 1.17 ± 0.16 in tumor lesions and normal cortex, respectively. Direct comparison of SUVs in humans and rats is limited, since the magnitude of the SUV depends on the distribution in all tissues that accumulate the tracer, and this distribution may differ between species. In addition, PET SUVs tend to be too small. These factors may be why SUVs in normal cortex were 18% smaller in the human study of Weber et al. than in our animal study. Considering all the available data, and especially the rat study by Langen et al. (*34*), ^{18}F-FET seems promising for separating radiation necrosis from tumor tissue.

Radiolabeled Choline Analogs

For ^{18}F-FCH, the comparison of our data with the literature is less conclusive, since no data are available on ^{18}F-FCH uptake in a rat model of brain tumor. Shinoura et al. measured ^{11}C-choline uptake in C6 glioma cells implanted under the skin of rats. Tumor uptake was 3- to 4-fold higher than brain uptake (*26*). This is higher than the L/B ratio of 2.50 ± 0.44 found by our study. Although Shinoura et al. used ^{11}C-choline, the data should at least in part be comparable, since Hara described similar uptake characteristics for ^{11}C-choline and ^{18}F-labeled choline compounds (*9*). Some data are available from human studies. Degrado et al. also used ^{18}F-FCH and reported an L/B of 10.0 in a single patient with recurrent anaplastic astrocytoma (*27*). Using another ^{18}F-labeled choline analog, ^{18}F-fluoroethyl-dimethyl-2-hydroxyethylammonium, Hara et al. found an L/B in the range of 12–21 for high-grade gliomas (n = 8) and 0–4.8 for grade II astrocytomas (n = 2) (*10*). Ohtani et al. investigated ^{11}C-choline uptake in 20 patients with different brain tumors and calculated tumor–to–white matter ratios in the range of 0.98–29.10 (*37*). The above studies indicate that ^{18}F-FCH in the radiation injury of our study is generally lower than in tumors. However, more studies using ^{18}F-FCH in tumors are needed to settle the issue.

^{18}F-FDG

In our study, accumulation of ^{18}F-FDG in radiation injury was generally on the same order as accumulation in normal cortex (mean L/B = 1.07 ± 0.19, average regions). For comparison, a rat study of Takeda et al. showed a maximum ^{14}C-FDG L/B of approximately 1.2 in intracerebral C6 gliomas (*38*). This is in the same range as the ^{18}F-FDG uptake in our study and leads to the conclusion that ^{18}F-FDG is of questionable suitability for separating radiation necrosis from tumor.

General Remarks

Some differences between our model and human studies are important to mention. The dose and type of irradiation (single dose, 150–250 Gy) used in our study differ from those used on humans. In addition, our model represents acute radiation injury. In humans, a more chronic phase of radiation injury is seen, referred to in the clinical literature as radiation necrosis. In radiation necrosis, the accumulation of inflammatory cells and degree of BBB disruption is probably less pronounced than in acute radiation injury. Typical alterations include wall thickening, fibrinoid necrosis, hyalinization of the vessel walls, and extensive gliosis adjacent to the necrotic focus (*39*). Therefore, uptake of all investigated tracers in such lesions is likely to be smaller. The low ^{18}F-FET uptake found by Weber et al. (*11*) for 2 cases of human radiation necrosis points in this direction. A lower uptake would increase the specificity for diagnosing radiation necrosis, especially for ^{18}F-FET and ^{18}F-FCH. However, more studies on ^{18}F-FCH and ^{18}F-FET uptake in chronic radiation lesions are needed to settle this issue.

CONCLUSION

The presented data elucidate the mechanism of ^{18}F-FET and ^{18}F-FCH uptake by acute radiation injuries and acute cryolesions. ^{18}F-FET uptake is determined mainly by disruption of the BBB, whereas ^{18}F-FCH is additionally trapped by inflammatory cells. Uptake of both tracers in radiation injuries was generally lower than published uptake values in tumors, suggesting that ^{18}F-FET and ^{18}F-FCH are promising for separating radiation necrosis from tumor recurrence. However, the comparability of our data with the literature is limited by factors such as differences in species and acquisition protocols and modalities. Thus, more studies are needed to settle this issue. Nevertheless, ^{18}F-FCH and ^{18}F-FET seem superior to ^{18}F-FDG for this purpose.

ACKNOWLEDGMENTS

This study was supported by the Radium-Stiftung and the OPO Stiftung in Zurich. The authors thank Hans Blattmann and Gustav K. von Schulthess for valuable discussions, Emanuel Egger for support with the proton gantry, Kerstin Goepfert for assistance with MRI, Susanne Hess for superb photographic work, and Tibor Cservenyak and Rolf Hesselmann for tracer production.

REFERENCES

1. Di Chiro G, DeLaPaz RL, Brooks RA, et al. Glucose utilization of cerebral gliomas measured by [^{18}F] fluorodeoxyglucose and positron emission tomography. *Neurology.* 1982;32:1323–1329.
2. Chao ST, Suh JH, Raja S, Lee SY, Barnett G. The sensitivity and specificity of FDG PET in distinguishing recurrent brain tumor from radionecrosis in patients treated with stereotactic radiosurgery. *Int J Cancer.* 2001;96:191–197.
3. Kahn D, Follett KA, Bushnell DL, et al. Diagnosis of recurrent brain tumor: value of ^{201}Tl SPECT vs ^{18}F-fluorodeoxyglucose PET. *AJR.* 1994;163:1459–1465.
4. Ricci PE, Karis JP, Heiserman JE, Fram EK, Bice AN, Drayer BP. Differentiating recurrent tumor from radiation necrosis: time for re-evaluation of positron emission tomography? *AJNR.* 1998;19:407–413.
5. Thompson TP, Lunsford LD, Kondziolka D. Distinguishing recurrent tumor and

radiation necrosis with positron emission tomography versus stereotactic biopsy. *Stereotact Funct Neurosurg.* 1999;73:9–14.
6. Del Sole A, Falini A, Ravasi L, et al. Anatomical and biochemical investigation of primary brain tumours. *Eur J Nucl Med.* 2001;28:1851–1872.
7. Dooms GC, Hecht S, Brant-Zawadzki M, Berthiaume Y, Norman D, Newton TH. Brain radiation lesions: MR imaging. *Radiology.* 1986;158:149–155.
8. Mikhael MA. Radiation necrosis of the brain: correlation between computed tomography, pathology, and dose distribution. *J Comput Assist Tomogr.* 1978;2:71–80.
9. Hara T. ^{11}C-Choline and 2-deoxy-2-[^{18}F]fluoro-D-glucose in tumor imaging with positron emission tomography. *Mol Imaging Biol.* 2002;4:267–273.
10. Hara T, Kondo T, Kosaka N. Use of ^{18}F-choline and ^{11}C-choline as contrast agents in positron emission tomography imaging-guided stereotactic biopsy sampling of gliomas. *J Neurosurg.* 2003;99:474–479.
11. Weber WA, Wester HJ, Grosu AL, et al. O-(2-[^{18}F]fluoroethyl)-L-tyrosine and L-[methyl-^{11}C]methionine uptake in brain tumours: initial results of a comparative study. *Eur J Nucl Med.* 2000;27:542–549.
12. Heiss P, Mayer S, Herz M, Wester HJ, Schwaiger M, Senekowitsch-Schmidtke R. Investigation of transport mechanism and uptake kinetics of O-(2-[^{18}F]fluoroethyl)-L-tyrosine in vitro and in vivo. *J Nucl Med.* 1999;40:1367–1373.
13. Wester HJ, Herz M, Weber W, et al. Synthesis and radiopharmacology of O-(2-[^{18}F]fluoroethyl)-L-tyrosine for tumor imaging. *J Nucl Med.* 1999;40:205–212.
14. Baum RP, Calcagni M, Dimitrakopoulou-Strauss A, Strauss LG. Pharmakokinetic analysis of O-2-[^{18}F]fluorethyl-L-tyrosin (^{18}F-FET) by dynamic PET in the differential diagnosis of malignant gliomas [abstract]. *J Nucl Med.* 2003;44(suppl):63P.
15. Cheon GJ, Ahn SH, Cho YS, et al. Correlation of ^{18}F-FET uptake and histologic grades of primary brain tumors [abstract]. *J Nucl Med.* 2003;44(suppl):367P.
16. Kaim AH, Weber B, Kurrer MO, et al. (18)F-FDG and (18)F-FET uptake in experimental soft tissue infection. *Eur J Nucl Med Mol Imaging.* 2002;29:648–654.
17. Rau FC, Weber WA, Wester HJ, et al. O-(2-[(18)F]Fluoroethyl)-L-tyrosine (FET): a tracer for differentiation of tumour from inflammation in murine lymph nodes. *Eur J Nucl Med Mol Imaging.* 2002;29:1039–1046.
18. Kennedy EP, Weiss SB. The function of cytidine coenzymes in the biosynthesis of phospholipids. *J Biol Chem.* 1956;222:193–214.
19. Zeisel SH. Dietary choline: biochemistry, physiology, and pharmacology. *Annu Rev Nutr.* 1981;1:95–121.
20. Haeffner EW. Studies on choline permeation through the plasma membrane and its incorporation into phosphatidyl choline of Ehrlich-Lettre-ascites tumor cells in vitro. *Eur J Biochem.* 1975;51:219–228.
21. Katz-Brull R, Degani H. Kinetics of choline transport and phosphorylation in human breast cancer cells: NMR application of the zero trans method. *Anticancer Res.* 1996;16:1375–1380.
22. Hara T, Inagaki K, Kosaka N, Morita T. Sensitive detection of mediastinal lymph node metastasis of lung cancer with ^{11}C-choline PET. *J Nucl Med.* 2000;41:1507–1513.
23. Hara T, Kosaka N, Kishi H. PET imaging of prostate cancer using carbon-11-choline. *J Nucl Med.* 1998;39:990–995.
24. Hara T, Kosaka N, Shinoura N, Kondo T. PET imaging of brain tumor with [methyl-^{11}C]choline. *J Nucl Med.* 1997;38:842–847.
25. Kobori O, Kirihara Y, Kosaka N, Hara T. Positron emission tomography of esophageal carcinoma using (11)C-choline and (18)F-fluorodeoxyglucose: a novel method of preoperative lymph node staging. *Cancer.* 1999;86:1638–1648.
26. Shinoura N, Nishijima M, Hara T, et al. Brain tumors: detection with C-11 choline PET. *Radiology.* 1997;202:497–503.
27. DeGrado TR, Baldwin SW, Wang S, et al. Synthesis and evaluation of (18)F-labeled choline analogs as oncologic PET tracers. *J Nucl Med.* 2001;42:1805–1814.
28. Wyss MT, Weber B, Honer M, et al. ^{18}F-choline in experimental soft tissue infection assessed with autoradiography and high-resolution PET. *Eur J Nucl Med Mol Imaging.* 2004;31:312–316.
29. Bergman J, Eskola O, Lehikoinen P, Solin O. Automated synthesis and purification of [^{18}F]bromofluoromethane at high specific radioactivity. *Appl Radiat Isot.* 2001;54:927–933.
30. Vassiliev D, Krasikova R, Kuznetsova O, Fedorova O, Nader M. Simple HPLC method for the detection of N,N-dimethylaminoethanol in the preparation of [N-methyl-^{11}C]choline. *Eur J Nucl Med.* 2003;30(suppl):S311.
31. Egger E, Zografos L, Perret C. Proton beam irradiation of choroidal melanomas at PSI: technique and results. In: Sagerman RH, Alberti WE, eds. *Medical Radiology: Diagnostic Imaging and Radiation Oncology—Radiotherapy of Intraocular and Orbital Tumors.* New York, NY: Springer-Verlag; 1993:57–72.
32. Hermann DM, Kilic E, Kugler S, Isenmann S, Bahr M. Adenovirus-mediated glial cell line-derived neurotrophic factor (GDNF) expression protects against subsequent cortical cold injury in rats. *Neurobiol Dis.* 2001;8:964–973.
33. Hermann DM, Mies G, Hossmann KA. Effects of a traumatic neocortical lesion on cerebral metabolism and gene expression of rats. *Neuroreport.* 1998;9:1917–1921.
34. Langen KJ, Jarosch M, Muhlensiepen H, et al. Comparison of fluorotyrosines and methionine uptake in F98 rat gliomas. *Nucl Med Biol.* 2003;30:501–508.
35. Pauleit DO, Floeth F, Hamacher K, et al. Influence of blood-brain barrier disruption on FET uptake in cerebral gliomas [abstract]. *J Nucl Med.* 2003;44(suppl):244P.
36. Poepperl G, Goetz C, Rachinger W, et al. Value of [^{18}F]fluoroethyltyrosine PET for the diagnosis of recurrent malignant astrocytomas [abstract]. *J Nucl Med.* 2003;44(suppl):166P.
37. Ohtani T, Kurihara H, Ishiuchi S, et al. Brain tumour imaging with carbon-11 choline: comparison with FDG PET and gadolinium-enhanced MR imaging. *Eur J Nucl Med.* 2001;28:1664–1670.
38. Takeda A, Tamano H, Enomoto S, Oku N. Zinc-65 imaging of rat brain tumors. *Cancer Res.* 2001;61:5065–5069.
39. The pathology of central nervous system radiation injury. In: Gutin PH, Leibel SA, Sheline GE, eds. *Radiation Injury to the Nervous System.* New York, NY: Raven Press; 1991:191–208.

^{18}F-choline in experimental soft tissue infection assessed with autoradiography and high-resolution PET

Matthias T. Wyss[1, 2], Bruno Weber[1], Michael Honer[2], Nicolas Späth[1], Simon M. Ametamey[2], Gerrit Westera[2], Beata Bode[4], Achim H. Kaim[3], Alfred Buck[1]

[1] PET Center, Division of Nuclear Medicine, University Hospital Zurich, Zurich, Switzerland
[2] Center for Radiopharmaceutical Science of ETH, PSI and USZ, Paul Scherrer Institute, Villigen, Switzerland
[3] Klinik Im Schachen, Aarau, Switzerland
[4] Institute of Pathology, University Hospital, Zurich, Switzerland

Received: 3 June 2003 / Accepted: 27 July 2003 / Published online: 20 November 2003

Abstract. For each oncological tracer it is important to know the uptake in non-tumorous lesions. The purpose of this study was to measure the accumulation of fluorine-18 choline (FCH), a promising agent for the evaluation of certain tumour types, in infectious tissue. Unilateral thigh muscle abscesses were induced in five rats by intramuscular injection of 0.1 ml of a bacterial suspension (*Staphylococcus aureus*, 1.2×10^9 CFU/ml). In all animals, FCH accumulation was measured with high-resolution positron emission tomography (PET) on day 6. Autoradiography of the abscess and ipsilateral healthy muscle was performed on day 7 (three animals) and day 11 (two animals) and correlated with histology. In addition, ^{18}F-fluorodeoxyglucose (FDG) PET was performed on day 5. Increased FCH uptake was noted in specific layers of the abscess wall which contained an infiltrate of mainly granulocytes on day 7 and mainly macrophages on day 11. The autoradiographic standardised uptake values in the most active part of the abscess wall were 2.99 on day 7 (n=3) and 4.05 on day 11 (n=2). In healthy muscle the corresponding values were 0.99 and 0.64. The abscesses were clearly visualised on the FCH and FDG PET images. In conclusion, this study demonstrated avid FCH accumulation in inflammatory tissue, which limits the specificity of FCH for tumour detection. Future studies are now needed to determine the degree of this limitation in human cancer patients.

Keywords: Soft tissue infection – ^{18}F-choline – ^{18}F-fluorodeoxyglucose – Autoradiography – PET – Tumour imaging

Alfred Buck (✉)
PET Center, Division of Nuclear Medicine,
University Hospital Zurich, Rämistrasse 100,
8091 Zurich, Switzerland
e-mail: buck@nuklearmed.unizh.ch
Tel.: +41-1-2553547, Fax: +41-1-2554414

Eur J Nucl Med Mol Imaging (2004) 31:312–316
DOI 10.1007/s00259-003-1337-4

Introduction

Whole-body positron emission tomography (PET) has developed into an invaluable tool for the evaluation of tumours. By far the largest number of examinations are performed with fluorine-18 fluorodeoxyglucose (FDG). However, FDG has several disadvantages. One is the reduced specificity for tumour cells due to FDG uptake in inflammatory lesions. A promising candidate for higher tumour specificity was ^{18}F-ethyl tyrosine (FET), which does not accumulate in inflammatory lesions [1] and which had shown promising potential in the evaluation of brain tumour patients [2]. Unfortunately, FET proved to be less sensitive than FDG in whole-body imaging of certain tumours [3]. Another substantial disadvantage of FDG is the minimal or lacking uptake in certain tumours, such as prostate carcinoma, the most common cancer in elderly men. Promising results for staging patients with prostate carcinoma have been reported with labelled choline compounds. Some studies have used carbon-11 labelled choline [4, 5, 6], whose clinical usefulness is limited by the short half-life of ^{11}C. This problem is overcome by ^{18}F-labelled choline (FCH), which has recently been introduced and has also shown promising results in the evaluation of patients with prostate cancer [7, 8, 9, 10]. For every tumour imaging compound it is important to know the accumulation characteristics in non-tumorous lesions, of which inflammatory/infectious foci are among the most important. Thus, the purpose of this study was to assess the FCH uptake in infected tissue. As in our previous studies, we used a rat model with experimentally induced abscesses in a leg muscle [1, 10]. FCH accumulation was determined using high-resolution PET

and autoradiography. In addition, FDG PET was performed in each animal.

Materials and methods

Animals and abscess model. This study was performed according to the guidelines of the National Institutes of Health and the recommendations of the committee on animal research at our institution. The protocol was approved by the local institutional review committee on animal care.

The study included five Sprague-Dawley rats (weight 250–300 g). All the animals were kept in cages with standardised conditions of light and free access to water and food. Using general inhalation anaesthesia (isoflurane, Forene, Abbott Laboratories), a unilateral deep calf muscle abscess was induced by intra muscular inoculation (25G needle) of 0.1 ml of a bacterial suspension (*Staphylococcus aureus*, clinical strain 10B, Novartis Pharma, Inc., Switzerland). The bacterial concentration (1.2109 CFU/ml) was measured by optical density (McFarland Standard, bioMerieux, Inc., USA).

All animals developed a palpable fluctuating mass in the left calf muscle within 36 h after bacterial inoculation. No systemic infection occurred.

Positron emission tomography with FCH and FDG. Examination were performed on a high-resolution PET system (16 Module quad Hidac PET System). The resolution at the centre of the field of view was 1.0 mm. FDG PET was performed 5 days after the induction of the abscess. Twenty minutes of data were acquired in list mode starting 40 min following the injection of 10–19 MBq FDG into the tail vein. FCH PET was performed 1 day later. Forty-five minutes of data were acquired immediately following injection of 8–20 MBq FCH into the tail vein. The list mode data were then rebinned into nine frames of 5 min duration. Injection and imaging with both tracers were done under isoflurane inhalation anaesthesia. To quantify tracer uptake a 10-ml syringe filled with an ^{18}F solution of known concentration (0.5–1.5 MBq/ml) was imaged immediately following the animal examination. The raw data were reconstructed using the iterative one pass list-mode–expectation maximisation (OPL-EM) algorithm (0.5 mm bin size, 200×200×440 matrix size) incorporating resolution recovery. Volumes of interest (VOIs) were subsequently placed on various tissue areas using the software PMOD [11]. The uptake values were expressed in kBq/ml using the syringe calibration. Dividing the tissue uptake by the injected activity per gram of body weight yielded the standardised uptake value (SUV).

Autoradiography with FCH. Autoradiography was performed 7 days (three animals) and 11 days (two animals) following induction of the abscess. For injection of the radiotracer a catheter was put into the right femoral vein under isoflurane anaesthesia. Ten minutes following the injection of 100–200 MBq FCH, the animals were sacrificed by an intravenous overdose of pentobarbital. Infected calf muscle and ipsilateral normal calf muscle were dissected immediately and frozen in isopentane cooled to −50°C. The frozen samples were cut (10 µm thickness) and thaw-mounted on glass slides. The slides were then put on a phosphor imager screen (Fuji TR 2025) for 4 h together with ^{14}C standards for quantification of tracer uptake. The data were scanned (Fuji BAS 1800 II, pixel size 50 µm) and converted to kBq/mg. For histological examination the slices were stained using haematoxylin-eosin (H-E).

Quantitative analysis. In a previous calibration experiment, each ^{14}C standard was assigned a value in kBq/ml of ^{18}F activity. For this purpose, 10-µm-thick slices of tissue homogenate that contained defined amounts of ^{18}F activity (kBq/mg) were exposed on the phosphor imaging screen together with the ^{14}C standard for 4 h. Using this calibration allowed conversion of the gray values into absolute uptake values (kBq/ml) at the beginning of screen exposure. To calculate standardised uptake values (SUVs) the injected activity was also decay-corrected to the same time point. The SUVs were then obtained by dividing the tissue uptake by the injected activity per gram of body weight. Regions of interest were subsequently placed on several tissue areas using the software PMOD [11].

Histology. After the autoradiographic measurements with the phosphor imaging system, the same slices were stained with H-E for histological examination.

Results

Histomorphological correlation to FCH autoradiography

A typical autoradiograph of an abscess formation on day 7 is shown together with the histology in Fig. 1. The acute abscess formation is histologically characterised by central necrosis surrounded by a layer consisting mostly of necrotic granulocytes. Adjacent to this layer is a zone of granulation tissue with an active inner part and a more mature outer part. The inner layer contains granulocytes, macrophages, myofibroblasts, blood capillaries and bacteria. The outer part is composed of the same elements but contains fewer inflammatory cells (granulocytes and macrophages) and more mature collagen. Superposition of the histological and autoradiographic image of the identical slice clearly demonstrated that the highest FCH concentration was in layer 3; no FCH at all was noted in layer 2. On day 11, layer 2 was even more necrotic and granulocytes were no longer present in layers 3 and 4.

The SUVs (mean) of layers 3 and 4 are summarised in Table 1. In the three animals examined 7 days and the

Table 1. FCH SUV determined by autoradiography

Animal	Day[a]	Abscess wall[b]		Muscle SUV
		Inner	Outer	
1	7	2.96	2.13	0.85
2	7	2.94	2.02	0.95
3	7	3.07	2.12	1.16
4	11	4.02	2.82	0.61
5	11	4.07	2.95	0.67

[a] Day of autoradiography following induction of abscess
[b] Inner: layer 3 in Fig. 1; outer: layer 4 in Fig. 1

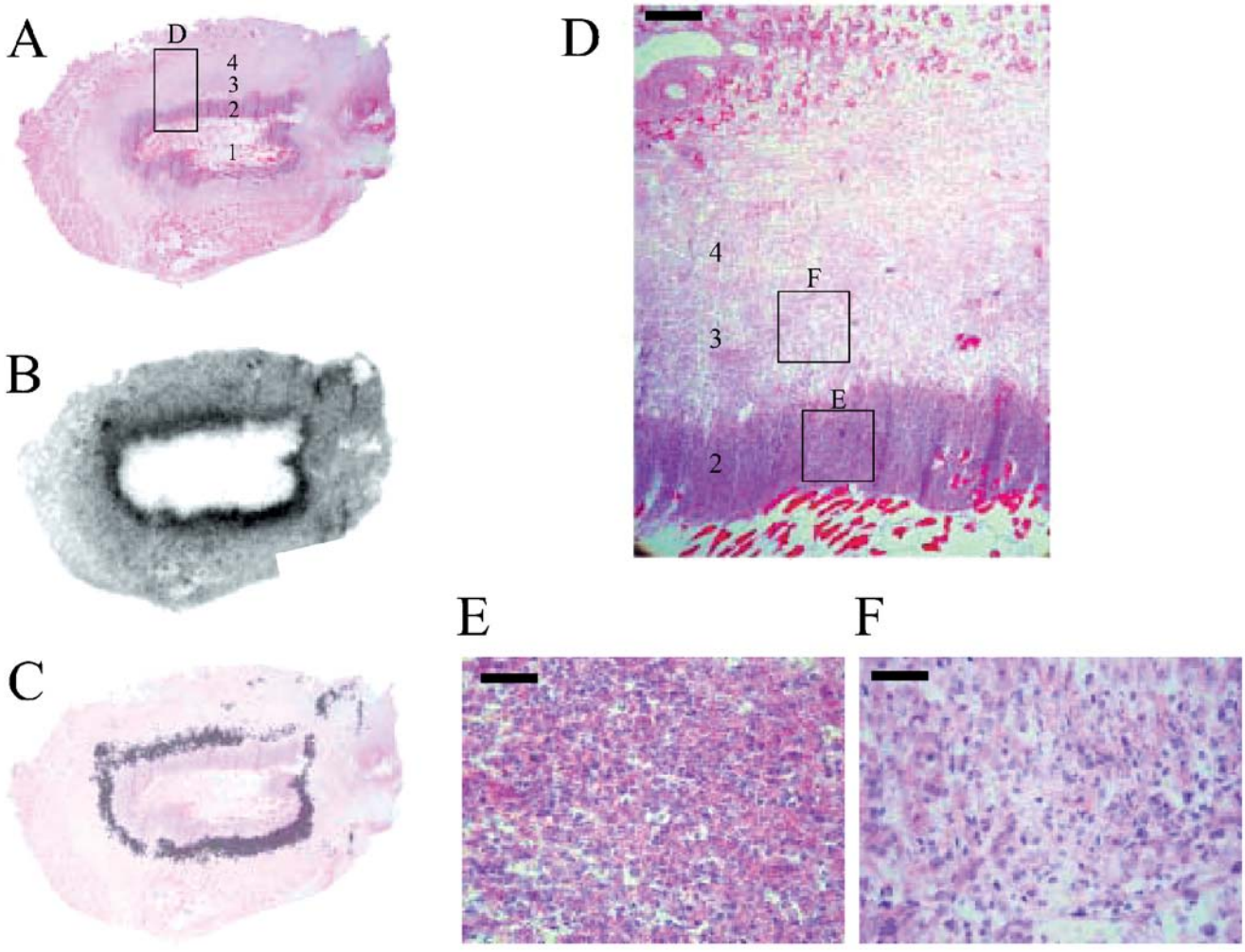

Fig. 1A–F. Histology of the abscess formation on day 7 (H-E staining, **A**), FCH autoradiography of the identical slice (**B**) and superposition of the two (**C**). The abscess wall (**D**) is characterised by a necrotic centre (*1*), which is surrounded by a layer consisting mainly of necrotic granulocytes (*2*; for higher magnification see **E**). Adjacent is a zone with granulation tissue, which can be subdivided into a more active inner (*3*, for higher magnification see **F**) and a more mature outer part (*4*). The highest concentration of FCH is found in layer 3, while layer 2 does not take up any FCH. Further details are reported in the text. The *bar* represents 400 µm in **D** and 100 µm in **E** and **F**

Table 2. SUV of tracer uptake determined with PET

Animal	FCH PET, day 6			FDG PET, day 5		
	Abscess	Normal ipsilateral	Muscle contralateral	Abscess	Normal ipsilateral	Muscle contralateral
1				4.12	1.72	2.10
2	1.06	0.45	0.30	4.53	0.95	0.55
3	1.17	0.38	0.28	2.36	0.86	0.42
4				2.36	0.81	0.44
5	1.13	0.35	0.29	3.45	1.29	0.63
Mean	1.12	0.39	0.29	3.37	1.13	0.83
SD	0.06	0.05	0.01	0.99	0.38	0.72

two animals examined 11 days following induction of the abscess, the mean SUV in layer 3 was 2.99 and 4.05 respectively. The corresponding values for layer 4 were 2.09 and 2.89 and for healthy muscle, 0.99 and 0.64.

FCH and FDG PET

The SUVs of tracer uptake determined with FCH and FDG PET are demonstrated in Table 2. In animals 1 and

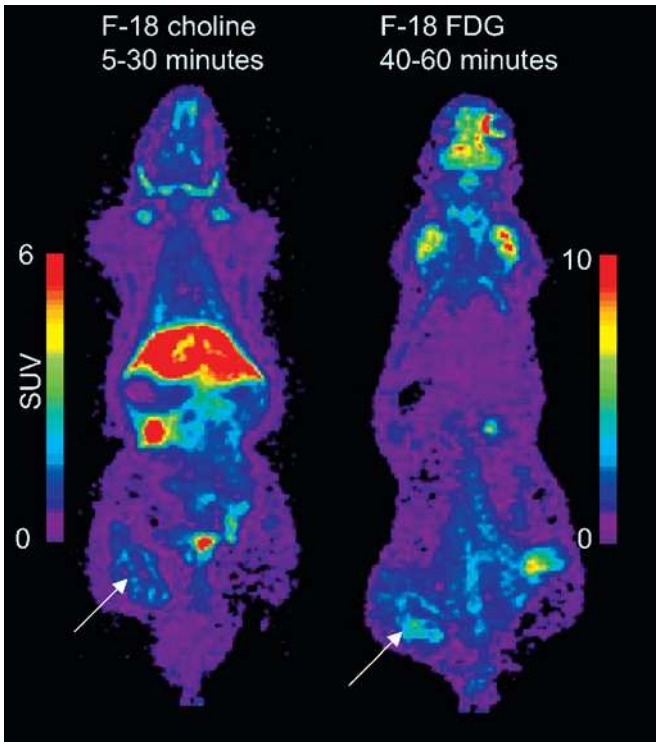

Fig. 2. FCH and FDG PET. Shown is a slice with a thickness and pixel size of 0.5 mm. The abscess (*arrows*) is clearly visualised with FCH (on the *left*) and FDG (on the *right*). With FCH the highest uptake is in the liver and kidney

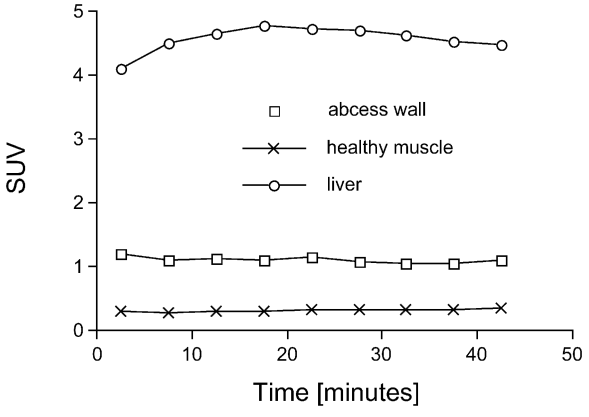

Fig. 3. Time course of the FCH concentration in different structures (mean of three animals)

4, tracer uptake was sluggish owing to partial paravenous injection of FCH. SUV values were therefore not calculated. In the other three animals the mean SUV in the abscess wall was 2.8 and 3.9 times higher than in ipsilateral and contralateral normal muscle respectively. With FDG, the abscess wall accumulated three to four times more tracer than normal muscle.

A slice of an FCH and an FDG PET scan are shown in Fig. 2. The abscess wall is clearly delineated with both tracers. With FCH the highest uptake is present in the liver and kidney. The time course of FCH concentration is illustrated in Fig. 3. In the abscess wall and in muscle tissue there was only minimal change between 5 and 45 min following injection. In the liver a maximum SUV of 4.75 was reached after 15–20 min.

Discussion

The most important result of this study is the demonstration of avid FCH uptake in inflammatory lesions. Such uptake will potentially limit the specificity of FCH in tumour evaluations. In the abscess wall the autoradiographically measured FCH SUV was 3 and 4 at days 7 and 11 respectively. This is somewhat lower than the FDG SUV determined with the same methods in one of our earlier experiments [12]. In that study the FDG SUV in the abscess wall was 5 and 8 at days 5 and 9 respectively. However, the important issue is how FCH SUV in infectious lesions compares with FCH uptake in tumours. In a study by Price et al. in patients with prostate cancer, the FCH SUV was between 2 and 8 in the prostate gland and between 3 and 8 in metastatic lymph nodes and bone metastasis [10]. Zhang et al. assessed the usefulness of ^{11}C-choline in separating benign from malignant lesions in bone and soft tissue tumours in 43 patients [13]. The SUV was 4.9±2.1 and 2.5±1.7 in malignant and benign lesions respectively. The data of both studies demonstrate that the SUV in certain tumorous lesions is in the same range as the SUV in the infectious tissue of our study (range 3–4).

Correlation of the FCH autoradiographs with the histology clearly demonstrated that the highest FCH uptake is found in the active granulation tissue (layer 3). The resolution of autoradiography does not allow identification of which cell types within this area incorporate FCH. However, since the main difference between the inner and the outer layer of the granulation tissue is the number of inflammatory cells, it seems likely that these cells accumulate a major part of the FCH. On day 11, FCH uptake in layers 3 and 4 is even higher than on day 7, with granulocytes no longer present. This suggests that a major part of the FCH is incorporated in macrophages at that stage, pointing to an upregulation of choline kinase in these cells, as has been demonstrated for tumour cells. Choline is transported into cells by specific mechanisms and then phosphorylated by choline kinase. In a further step it is metabolised to phosphatidylcholine and incorporated into the cell membrane. The increased choline uptake in tumours is explained by upregulation of choline kinase.

It is interesting that the layer with the highest cell density (layer 2) does not take up any FCH. This may be because this layer contains only dead cells or because it is not perfused, or a combination of the two. Another question is to what degree the observed FCH uptake pattern is determined by blood flow, which may vary in the different layers of the abscess wall.

The abscesses were clearly delineated by FCH and FDG PET. The contrast relative to surrounding tissue seemed similar for both tracers. Comparison of the SUVs determined with PET and autoradiography demonstrated an underestimation of the FCH SUVs by PET. This is most probably due to the limited spatial resolution of PET and the resultant underestimation of radioactivity concentration in small structures. Another factor may be the lack of attenuation correction, which is not implemented on the present system. Also the FDG SUVs in the abscess wall at day 5 were somewhat lower than the autoradiographically determined values in our previous study (3.3 vs 5 in the previous study [12]).

In summary, FCH is avidly accumulated in inflammatory infiltrates. This finding limits the specificity of labelled choline compounds for tumour detection. Future studies are now required to determine the degree of this limitation in human cancer patients. This includes the evaluation of FCH uptake in different acute and chronic inflammatory lesions.

Acknowledgements. The authors would like to thank Claudia Keller for the help with the data acquisition and Tibor Cservenjak for the radiotracer synthesis. This project was supported by the Wilhelm Sander Foundation.

References

1. Kaim AH, Weber B, Kurrer MO, Westera G, Schweitzer A, Gottschalk J, von Schulthess GK, Buck A. ^{18}F-FDG and ^{18}F-FET uptake in experimental soft tissue infection. *Eur J Nucl Med Mol Imaging* 2002; 29:648–654.
2. Weber WA, Wester HJ, Grosu AL, Herz M, Dzewas B, Feldmann HJ, Molls M, Stocklin G, Schwaiger M. *O*-(2-[^{18}F]fluoroethyl)-L-tyrosine and L-[methyl-^{11}C]methionine uptake in brain tumours: initial results of a comparative study. *Eur J Nucl Med* 2000; 27:542–549.
3. Hustinx R, Lemaire C, Jerusalem G, Moreau P, Cataldo D, Duysinx B, Aerts J, Fassotte MF, Foidart J, Luxen A. Whole-body tumor imaging using PET and 2-^{18}F-fluoro-L-tyrosine: preliminary evaluation and comparison with ^{18}F-FDG. *J Nucl Med* 2003; 44:533–539.
4. Hara T, Kosaka N, Kishi H. PET imaging of prostate cancer using carbon-11-choline. *J Nucl Med* 1998; 39:990–995.
5. de Jong IJ, Pruim J, Elsinga PH, Vaalburg W, Mensink HJ. Preoperative staging of pelvic lymph nodes in prostate cancer by ^{11}C-choline PET. *J Nucl Med* 2003; 44:331–335.
6. de Jong IJ, Pruim J, Elsinga PH, Vaalburg W, Mensink HJ, Visualization of prostate cancer with ^{11}C-choline positron emission tomography. *Eur Urol* 2002; 42:18–23.
7. DeGrado TR, Baldwin SW, Wang S, Orr MD, Liao RP, Friedman HS, Reiman R, Price DT, Coleman RE. Synthesis and evaluation of (18)F-labeled choline analogs as oncologic PET tracers. *J Nucl Med* 2001; 42:1805–1814.
8. DeGrado TR, Coleman RE, Wang S, Baldwin SW, Orr MD, Robertson CN, Polascik TJ, Price DT. Synthesis and evaluation of ^{18}F-labeled choline as an oncologic tracer for positron emission tomography: initial findings in prostate cancer. *Cancer Res* 2001; 61:110–117.
9. DeGrado TR, Reiman RE, Price DT, Wang S, Coleman RE. Pharmacokinetics and radiation dosimetry of ^{18}F-fluorocholine. *J Nucl Med* 2002; 43:92–96.
10. Price DT, Coleman RE, Liao RP, Robertson CN, Polascik TJ, DeGrado TR. Comparison of [^{18}F]fluorocholine and [^{18}F]fluorodeoxyglucose for positron emission tomography of androgen dependent and androgen independent prostate cancer. *J Urol* 2002; 168:273–280.
11. Mikolajczyk K, Szabatin M, Rudnicki P, Grodzki M, Burger C. A JAVA environment for medical image data analysis: initial application for brain PET quantitation. *Med Inform (Lond)* 1998; 23:207–214.
12. Kaim AH, Weber B, Kurrer M, Gottschalk J, von Schulthess GK, Buck A. Autoradiographic quantification of ^{18}F-FDG uptake in experimental soft tissue abscesses in rats. *Radiology* 2002; 223:446–451.
13. Zhang H, Tian M, Oriuchi N, Higuchi T, Watanabe H, Aoki J, Tanada S, Endo K. ^{11}C-choline PET for the detection of bone and soft tissue tumours in comparison with FDG PET. *Nucl Med Commun* 2003; 24:273–279.

Spatial Heterogeneity of Low-Grade Gliomas at the Capillary Level: A PET Study on Tumor Blood Flow and Amino Acid Uptake

Matthias T. Wyss[1], Silvia Hofer[2], Martin Hefti[3], Esther Bärtschi[4], Catrina Uhlmann[4], Valerie Treyer[1], and Ulrich Roelcke[5]

[1]PET Center, Division of Nuclear Medicine, University Hospital, Zürich, Switzerland; [2]Department of Oncology, University Hospital, Zürich, Switzerland; [3]Department of Neurosurgery, Cantonal Hospital, Aarau, Switzerland; [4]Department of Oncology and Hematology, Cantonal Hospital, Aarau, Switzerland; and [5]Department of Neurology, Cantonal Hospital, Aarau, Switzerland

Many low-grade gliomas (World Health Organization grade II) respond to chemotherapy. Cerebral blood flow (CBF) and microvessel density may be critical for drug delivery. We used PET with ^{18}F-fluoro-ethyl-L-tyrosine (FET) to measure the spatial distribution of the amino acid carrier, which is located at the brain capillaries, and ^{15}O-H_2O to measure tumor CBF. **Methods:** Seventeen patients with low-grade glioma were studied. Region-of-interest (ROI) analysis was used to quantify tumor tracer uptake, which was normalized to cerebellar uptake (tumor-to-cerebellum ratio). ''Active'' tumor was defined as tumor having a radioactivity concentration that was at least 110% of the cerebellar activity. This threshold provided measures of active tumor volume, global and peak tumor CBF, and ^{18}F-FET uptake. Trace ROIs were applied to create voxelwise profiles of CBF and ^{18}F-FET uptake across tumor and brain. Standard MRI sequences were used for spatial correlations. **Results:** Fourteen of 17 tumors showed increased global CBF and ^{18}F-FET uptake. Active tumor volumes ranged between 3 and 270 cm^3 for ^{18}F-FET and between 1 and 41 cm^3 for CBF. Global ^{18}F-FET uptake in tumors corresponded to CBF increases (Spearman rank $\rho = 0.771$, $P < 0.01$). The volumes of increased CBF and ^{18}F-FET uptake spatially coincided and were also correlated ($\rho = 0.944$, $P < 0.01$). Trace ROIs showed that irrespective of increased ^{18}F-FET uptake at the tumor periphery, CBF increases were more confined to the tumor center. Within individual tumors, spatial heterogeneity was present. Particular tumors infiltrating the corpus callosum showed low CBF and ^{18}F-FET uptake in this tumor region. The patterns observed with PET were not reflected on MRI of the tumors, all of which presented as homogeneous non–gadolinium-enhancing lesions. **Conclusion:** Low-grade gliomas are heterogeneous tumors with regard to the distribution of amino acid uptake and CBF. Both are coupled in the tumor center. At the tumor periphery, where tumor infiltration of surrounding brain occurs, CBF may be low irrespective of increased ^{18}F-FET uptake. An ongoing study is investigating the effect of chemotherapy on these observations.

Key Words: low-grade glioma; fluoro-ethyl-L-tyrosine; blood flow; positron emission tomography

J Nucl Med 2007; 48:1047–1052
DOI: 10.2967/jnumed.106.038489

Most low-grade gliomas affect adults in their third to fifth decades of life. According to the classification of the World Health Organization (WHO), low-grade gliomas (WHO grade II) comprise diffuse astrocytoma, oligodendroglioma, and oligoastrocytoma (*1*). Although the tumors are considered slowly progressing, an annual increase in tumor size of 4.1 mm has been estimated (*2*). Surgery is the standard treatment at the time of first presentation. Subsequent radiotherapy remains controversial (*3,4*). Low-grade gliomas have long been regarded as resistant to chemotherapy; however, several studies published over the last few years showed remarkable responses to regimens such as procarbazine, *N*-(2-chloroethyl)-*N′*-cyclo-hexyl-*N*-nitrosourea, and vincristine or to the alkylating agent temozolomide (*5,6*). There is evidence that loss of heterozygosity on chromosomes 1p and 19q might be predictive of chemotherapy response, but large, prospective randomized studies on this issue are lacking (*6*). On the other hand, the effectiveness of chemotherapy depends on adequate delivery of drugs to tumor cells, and this delivery is a function of drug concentration in the blood, blood flow through tumor microvasculature, and the flux of drugs across tumor capillaries. Our study aimed at the in vivo characterization with PET of microvessel distribution and of cerebral blood flow (CBF) in low-grade gliomas. We used ^{15}O-H_2O as a standard tracer for CBF measurement. To investigate microvessel distribution, we used ^{18}F-fluoro-ethyl-L-tyrosine (FET) as a tracer for amino acid transport (*7*). Several PET studies on human brain tumors showed that the uptake of radiolabeled amino acids is governed by increased influx across the blood–brain barrier (*8–10*). Experimental studies revealed that this influx is mediated by active transendothelial amino acid transport (*11,12*). Accordingly, the signal measured with

Received Nov. 29, 2006; revision accepted Mar. 20, 2007.
For correspondence contact: Ulrich Roelcke, MD, Department of Neurology, Cantonal Hospital, CH 5001 Aarau, Switzerland.
E-mail: roelcke@ksa.ch

^{18}F-FET PET in tumors reflects the magnitude of amino acid transport and its distribution over tumors.

MATERIALS AND METHODS

Patients

We enrolled 17 patients with either progressive or recurrent supratentorial WHO grade II gliomas. At the time of the first surgery (2–127 mo before the PET study), all tumors were histologically verified WHO grade II gliomas and included 5 fibrillary astrocytomas, 7 oligoastrocytomas, and 5 oligodendrogliomas. Recurrence or progression was defined clinically and on MRI and occurred at a mean of 30 mo (range, 2–127 mo; Table 1) after the first tumor surgery. We included only patients who, at the time of our PET study, did not show any gadolinium enhancement on MRI, because this finding may indicate the presence of a more malignant glioma (WHO grade III or IV). The clinical details are presented in Table 1. PET studies were performed within 2 wk of the MRI studies. Written informed consent was obtained from all patients. The study protocol was approved by the local ethics committee.

Image Acquisition and Processing

MRI included standard procedures on a 1.5-T Siemens Magnetom. We obtained digitized pre- and postgadolinium T1- and T2-weighted, proton-density, and fluid-attenuated inversion recovery (FLAIR) sequences (slice thickness, 4.8 mm). Following the methods of recent studies on low-grade gliomas, we used the FLAIR sequences to calculate the tumor volume, because these sequences best delineate between the lesion and adjacent brain (*6,13*).

PET studies were performed on a whole-body PET/CT scanner (Discovery LS; GE Healthcare) and were acquired in 3-dimensional mode with a 14.6-cm axial field of view and a reconstructed in-plane resolution of 7 mm (voxel size, 0.018 cm^3; slice thickness, 4.25 mm). Immediately before the CBF PET study, a low-dose CT scan for attenuation correction was obtained. For the CBF studies, 600–800 MBq of ^{15}O-H_2O were administered using an automatic injection device that delivers the bolus over 20 s. After arrival of the bolus in the brain, acquisition of a series of eighteen 10-s frames was initiated. The ^{15}O-H_2O PET images were transformed according to a previously described approach yielding absolute CBF values without arterial blood sampling (*14*). ^{18}F-FET studies were performed subsequent to the CBF studies within the same session. ^{18}F-FET was produced according to the method of Wester et al. (*15*). For the ^{18}F-FET studies, 140–250 MBq were injected intravenously and tracer accumulation was recorded over 60 min as a series of twelve 5-min frames. To avoid movement of the head during the acquisition, the head was slightly fixed, and PET images were visually assessed for movement artifacts. Attenuation-corrected PET images were reconstructed with standard Fourier rebinning backprojection, including standard calibration factors to receive kBq/mL of tissue and corrections for randoms, scatters, geometry, decay, and dead time. As in other reports (*16*), our patients showed a plateau phase with a relatively stable tissue radioactivity concentration later than 40 min after intravenous tracer injection. Therefore, our ^{18}F-FET PET data were analyzed on averaged activity images acquired 50–60 min after tracer injection. Dividing these activities by the amount of injected activity per kilogram of body weight yielded standardized uptake values.

Data Analysis

PET data were analyzed with PMOD (*17*). As a standard procedure in nuclear medicine, tumor uptake values can be normalized to the contralateral normal brain, allowing easy data analysis

TABLE 1
Patients Ranked by WHO Grade II Histologic Subgroups According to Global ^{18}F-FET T/Cb Ratio

Patient no.	Age (y)	Sex	Histology*	Resection type†	Location	Interval‡ (mo)	Lesion volume (cm^3)			Global T/Cb ratio		Peak T/Cb ratio	
							MRI FLAIR	Active ^{18}F-FET	Active CBF	^{18}F-FET	CBF	^{18}F-FET	CBF
1	39	M	FIAC	b	Temporal, R	19	34	—	—	0.77	0.77	—	—
2	49	F	FIAC	p	Frontoparietal, L	127	46	29	12	1.24	1.25	1.39	1.45
3	46	F	FIAC	p	Temporooccipital, R	9	40	6	1	1.24	1.21	1.40	—
4	51	F	FIAC	p	Frontotemporal, L	79	88	65	9	1.24	1.39	1.38	1.69
5	34	M	FIAC	p	Temporal, L	27	44	6	1	1.25	1.19	1.39	—
6	55	M	OA	b	Temporal, R	12	56	—	—	0.70	0.59	—	—
7	56	M	OA	gt	Frontal, R	81	91	3	1	1.21	1.31	1.24	—
8	31	F	OA	p	Frontal, L	40	14	11	5	1.32	1.34	1.58	1.61
9	27	M	OA	p	Temporal, L	6	23	18	1	1.42	1.25	1.78	—
10	39	M	OA	b	Temporal, L	9	79	64	16	1.44	1.33	1.93	1.59
11	42	M	OA	p	Frontotemporal, R	50	44	23	10	1.50	1.51	2.18	1.96
12	28	M	OA	b	Parietal, L	5	90	79	28	1.59	1.49	2.17	1.93
13	50	F	OD	p	Frontal, L	26	23	—	—	0.61	0.45	—	—
14	54	F	OD	b	Temporal, L	2	42	6	1	1.28	1.23	1.46	—
15	37	M	OD	b	Frontal, L, R	13	140	270	41	1.33	1.25	1.62	1.41
16	45	F	OD	b	Frontal, L	2	25	27	3	1.40	1.20	1.75	—
17	34	M	OD	b	Temporal, L	6	23	28	9	1.65	1.35	2.25	1.76

*FIAC = fibrillary astrocytoma; OA = oligoastrocytoma; OD = oligodendroglioma.
†b = biopsy; p = partial; gt = gross total resection.
‡Between surgery and PET.
— = no active tumor volume (in those patients, ROIs for calculation of global uptake ratio were drawn from MRI FLAIR images).

and reliable interindividual comparisons. However, normalization to contralateral brain depends on the location of the tumor in the brain and may thus infer substantial variation, particularly as 2 tumors in our series crossed the midline. We therefore chose the cerebellum as the reference region because it is a large and homogeneous structure and was distant from the tumor. Regions of interest (ROIs) were first placed over both sides of the cerebellum on 3 subsequent slides. The mean activity of all cerebellar ROIs was used to set the threshold for normalization of tumor tracer uptake (tumor-to-cerebellum [T/Cb] ratio). This thresholding procedure has recently been proposed to provide an observer-independent evaluation, which is particularly important for follow-up PET studies during tumor treatment (*18*). In a first step, we used thresholds between 100% and 120% of cerebellar activity. Increasing the threshold produced moderate decreases of active tumor volumes and small increases of T/Cb ratios. We finally chose a threshold that gave a volume of active voxels close to what was the "visibly increased" ^{18}F-FET uptake. For our low-grade gliomas, we found this threshold to be 110%. This threshold was also applied for the quantification of CBF. Accordingly, tumor ROIs were placed covering all voxels with activity values above 110% of the mean activity in the cerebellum, thus yielding the active tumor volume for CBF and ^{18}F-FET uptake. The activity in these tumor ROIs was then used for the calculation of global T/Cb ratios (all active voxels) and peak T/Cb ratios (all voxels that were 75% or more of the maximum radioactivity in the tumor ROI). In tumors with inactive tumor volumes (below 110% of the mean activity in the cerebellum), digitized MRI FLAIR images were coregistered with the PET studies to define the placement of tumor ROIs according to the FLAIR lesion volume.

To more precisely investigate the spatial relationship between ^{18}F-FET uptake and CBF, we placed linear trace ROIs that spanned from normal cortex through white matter and tumor and created CBF and ^{18}F-FET profiles across the brain (Fig. 1, yellow line). First, trace ROIs were placed on the 3 adjacent planes that showed the highest tumor tracer uptake. For each of these planes, 3 adjacent parallel trace ROIs were created per plane in the ^{18}F-FET study and were then also used at the same position for the coregistered CBF studies. Depending on the individual tumor location, a single trace ROI consisted of up to 64 voxels (voxel size, 0.018 cm^3). At this step, 9 single ^{18}F-FET and CBF profiles per patient were available. Second, the activity of the spatially corresponding voxels derived from these 9 profiles was averaged and yielded a mean trace ROI profile for ^{18}F-FET and CBF activity for each patient. Then, the mean activity for each voxel was normalized to the cerebellum. Accordingly, the data points of these profiles represent voxel averages of T/Cb ratios for CBF and ^{18}F-FET uptake (*y*-axis) and the distance (mm) across the brain (*x*-axis).

Statistics

The Spearman rank test was used to search for correlations between the active tumor volumes of CBF and ^{18}F-FET uptake, between tumor uptake of ^{18}F-FET and tumor CBF, and between these measures and the MRI FLAIR lesion.

RESULTS

The results are summarized in Table 1. Relative to normal brain, we found increased ^{18}F-FET uptake and CBF in 14 of 17 tumors. ^{18}F-FET uptake and CBF were not homogeneously increased across these tumors but rather showed a variable distribution. The peaks of CBF and ^{18}F-FET uptake were spatially colocalized. In 3 tumors, both ^{18}F-FET uptake and CBF were decreased relative to normal brain. The heterogeneity of ^{18}F-FET uptake and CBF within individual

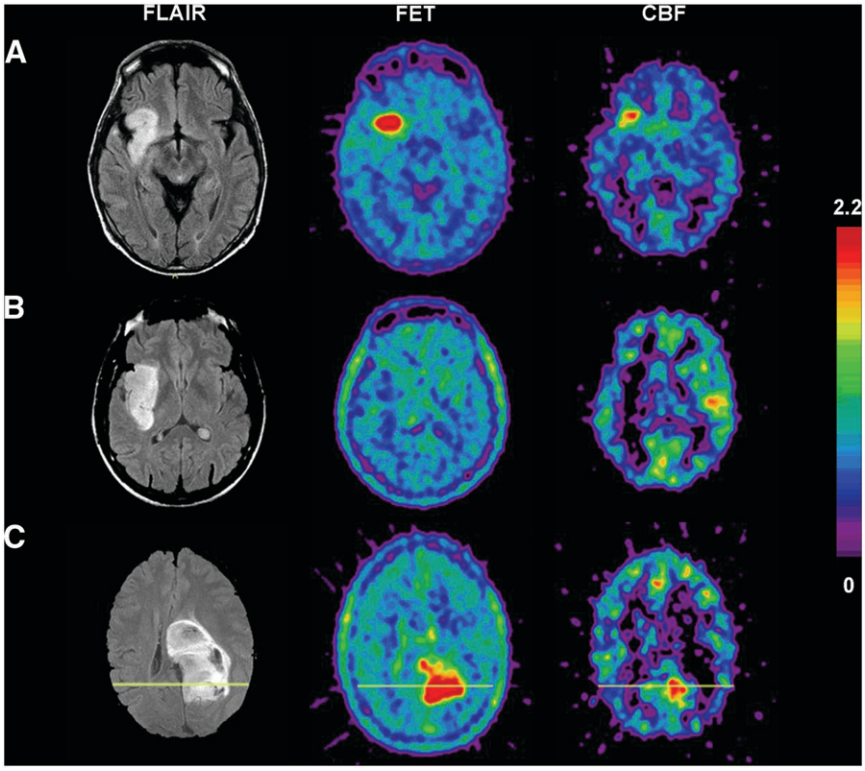

FIGURE 1. Heterogeneity of ^{18}F-FET uptake and CBF in 3 low-grade gliomas. Corresponding axial slices are presented. Color scale represents T/Cb ratio of ^{18}F-FET and CBF. (A) Oligoastrocytoma shows markedly increased ^{18}F-FET uptake and CBF in right frontoinsular region (patient 11 in Table 1). ^{18}F-FET and CBF peak uptake regions coincide; however, active volume of CBF is smaller than active ^{18}F-FET volume. (B) Reduced ^{18}F-FET uptake and CBF in fibrillary astrocytoma (patient 1). (C) Oligoastrocytoma (patient 12). Anterior tumor part involves corpus callosum and shows substantially reduced CBF and ^{18}F-FET uptake when compared with posterior tumor part. This heterogeneity is not evident from any MRI sequences. Yellow line through posterior part of brain and tumor illustrates positioning of trace ROI (Fig. 4).

tumors and within our group of low-grade gliomas is illustrated in Figure 1.

Tumor tracer uptake was quantified by normalizing the tumor radioactivity concentration to the activity of the cerebellum (uptake ratio). Cerebellar ^{18}F-FET uptake and CBF were calculated as the mean value of both cerebellar hemispheres. Asymmetry between the hemispheres ("crossed cerebellar diaschisis") was less than 5% for ^{18}F-FET and less than 9% for CBF. For the cerebellum, the ^{18}F-FET standardized uptake value was 1.22 ± 0.32 (mean ± SD). The cerebellar CBF was 36.4 ± 8.6 mL/min/100 mL. At a 110% cutoff of cerebellar tracer uptake, tumor uptake ratios varied between 0.61 and 1.65 for global ^{18}F-FET uptake and between 1.24 and 2.25 for peak ^{18}F-FET uptake. For CBF, these values ranged from 0.45 to 1.50 for the global ratio and from 1.41 to 1.96 for the peak ratio. At lower ^{18}F-FET uptake ratios (global), smaller variations in CBF ratios were observed, whereas for higher ^{18}F-FET uptake ratios (peak), the variation in CBF ratios increased (Fig. 2). Uptake ratios tended to be higher in oligodendroglial tumors than in fibrillary astrocytoma. No correlation between MRI lesion volume and tracer uptake was observed (^{18}F-FET: Spearman rank $\rho = 0.023$, $P = 0.931$; CBF: Spearman rank $\rho = 0.262$, $P = 0.309$) (Table 1). Over the whole study population, ^{18}F-FET uptake and CBF correlated (Fig. 2): For global uptake ratios, the Spearman rank correlations were $\rho = 0.771$, $P < 0.01$ ($n = 17$). Because of the small number of pairs, the correlation of peak uptake ratios did not reach statistical significance ($\rho = 0.571$, $P = 0.139$).

In most tumors, the volume of increased ^{18}F-FET uptake was smaller than the corresponding tumor volume on MRI FLAIR images. Active tumor volumes of ^{18}F-FET and CBF were colocalized within 1 tumor (Fig. 1); however, the CBF volume was always smaller than the ^{18}F-FET uptake volume. The active tumor volumes ranged from 3 to 270 cm^3 for ^{18}F-FET and from 1 to 41 cm^3 for CBF. The correlation between active global tumor volumes is presented in Figure 3 (Spearman rank $\rho = 0.944$, $P < 0.01$). To address this spatial relationship between intratumoral tracer uptake, we created CBF and ^{18}F-FET profiles across tumor and brain. The positioning of trace ROIs is illustrated for a single patient (patient 12) in Figure 1. The resulting profile of ^{18}F-FET and CBF distribution is exemplified in Figure 4. The presented pattern was observed in all 14 tumors with increased ^{18}F-FET uptake and CBF—that is, the peak coincidence of ^{18}F-FET uptake and CBF. Reflective of our active volume data, the area under the curve in the trace ROIs was smaller for the tumor CBF than for the tumor ^{18}F-FET uptake profiles. Along the profiles, the mean distance between increase of intratumoral ^{18}F-FET uptake and CBF was 6.3 mm (range, 2.2–13.6 mm). At the position where the CBF ratio in tumors started to exceed 1.0, the mean ^{18}F-FET ratio was 1.51 (1.01–2.24).

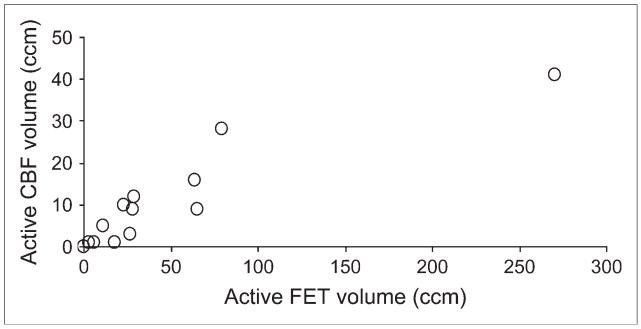

FIGURE 3. Correlation of global active tumor volumes of ^{18}F-FET and CBF (Spearman rank $\rho = 0.944$, $P < 0.01$). Significant correlation is maintained if outlier is excluded from analysis ($\rho = 0.885$, $P < 0.01$).

DISCUSSION

Our study demonstrated a substantial heterogeneity in CBF and ^{18}F-FET uptake over the whole series of low-grade gliomas that, on MRI, appeared as homogeneous

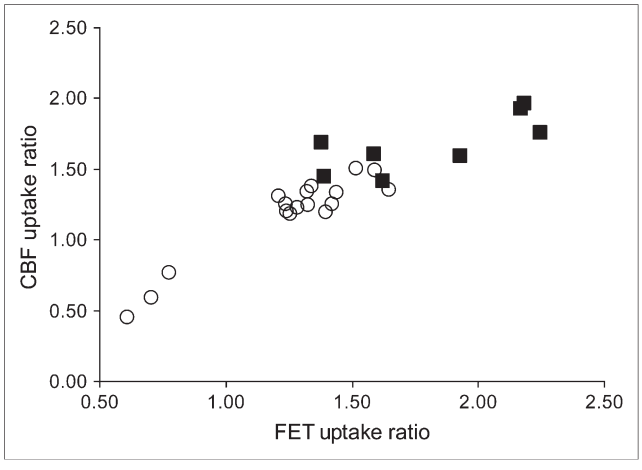

FIGURE 2. Distribution of global (○) and peak (■) ^{18}F-FET uptake and CBF. Values represent T/Cb ratios.

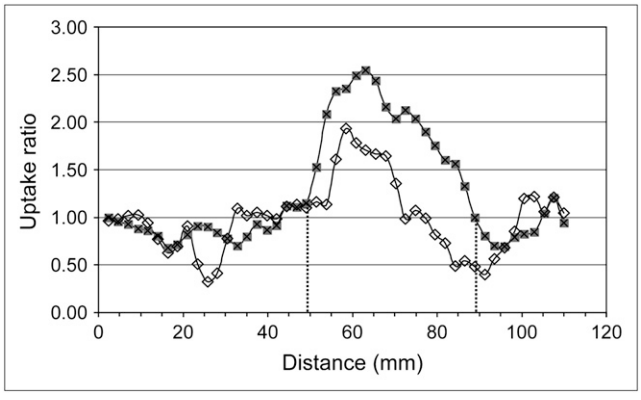

FIGURE 4. Trace ROI analysis in a single patient (patient 12). Pixelwise profiles of ^{18}F-FET uptake (■) and CBF (◇) span from normal cortex over white matter and tumor. Vertical dashed lines represent tumor borders on MRI (patient 12; Fig. 1C). Increases of tumor CBF (T/Cb ratio > 1.0) are more confined to tumor center. T/Cb ratio increases in this patient at a ratio of approximately 2.1 of ^{18}F-FET uptake.

non–gadolinium-enhancing lesions. In many patients, we also observed intratumoral heterogeneity on the PET studies, possibly indicating that subregions of tumors could behave differentially with respect to tumor evolution and treatment response. Knowledge of the individual tumor vasculature is of particular interest with regard to angiogenetic tumor potential and targeted treatment. The total intravascular volume, which comprises all sizes of tumor vessels, can be used as an in vivo marker of angiogenesis and can be studied by following the changes in the MRI signal after administration of gadolinium (*19,20*). If the point of interest is the distribution of the capillaries themselves, where solutes and drugs are exchanged, markers should exclusively trace mechanisms located at that anatomic level. Such is the case for radiolabeled amino acids that bind to and are transported by the amino acid carriers located in the endothelial cells of the blood–brain barrier (*21*). In brain tumors of various WHO grades, uptake of ^{11}C-methyl-L-methionine correlates with the microvascular density (MVD) as validated by immunohistochemistry (*22*). ^{18}F-FET is a nonmetabolized tyrosine analog and behaves similarly to methionine (*16*). ^{18}F-FET was evaluated for the clinical investigation of gliomas (*7,16*). We found an ^{18}F-FET uptake ratio of between 0.61 and 1.65 for the whole tumor and peak values of between 1.24 and 2.25. These ratios are in the range of the data presented by Kracht et al. (*22*). Taking these findings together, our results provide evidence that ^{18}F-FET, like methionine, is a surrogate marker of MVD. To validate this assumption, we initiated a study on ^{18}F-FET PET–guided biopsies and determination of MVD in patients with low-grade gliomas.

In our series, 3 of 17 tumors showed neither increased tyrosine uptake nor increased CBF. In addition, tumor areas contacting or infiltrating the corpus callosum exhibited normal or reduced CBF and ^{18}F-FET uptake, whereas in the same tumor, distant cortical or subcortical areas showed increases of these measures (Fig. 1). Our finding of reduced ^{18}F-FET uptake in some tumors would be in line with immunohistochemical results on microvessel counts in astrocytomas. In particular, low-grade astrocytomas may show MVDs below the level of normal cortex or white matter (*23*). Studies have shown that microvessels in these tumors are native cerebral vessels co-opted by tumor cells and that the formation of new vessels ("neo-angiogenesis") and higher vessel densities occur in more malignant tumors (*23,24*).

Earlier studies on CBF in gliomas reported a similar range for tumors (7–102 mL/100 mL/min) and for normal white matter and cortex (15–59 mL/100 mL/min) (*25–27*). The magnitude of CBF in these studies did not discriminate between glioma types or WHO grade. Across our series, tumor CBF and ^{18}F-FET uptake correlated (Fig. 2). Our data therefore suggest a coupling between blood flow and microvascular distribution in low-grade gliomas. This coupling is different from known perfusion patterns in more malignant gliomas (WHO grades III and IV), in which, irrespective of the high vascularity, low CBF is considered to be responsible for the formation of hypoxia (*28*). In addition, we found a significant correlation between active ^{18}F-FET and perfused tumor volumes (Fig. 3). ^{18}F-FET and CBF volumes showed a close spatial coincidence and were independent of lesion size on MRI (Fig. 1). Interestingly, the active CBF volumes were smaller than the corresponding ^{18}F-FET volumes (Table 1), as is explained by the characteristic intratumoral rises in ^{18}F-FET uptake and CBF as presented in the trace ROI analysis (Fig. 4). Our data revealed that CBF increases occurred when uptake of ^{18}F-FET exceeded a certain level (mean ratio, 1.50). Assuming that ^{18}F-FET uptake is related to MVD, our results can be transferred into absolute numbers of tumor MVD by comparison with the data presented by Kracht et al. (*22*). They reported global ^{11}C-methyl-L-methionine uptake ratios of 1.30 ± 0.20 for astrocytic tumors and 2.30 ± 0.35 for oligodendroglial tumors (WHO grade II)—values that are similar to our ^{18}F-FET uptake values (Table 1). Correlating ^{11}C-methyl-L-methionine uptake and histopathologically proven MVD, an amino acid uptake ratio of 1.50 equals 10 microvessels/0.763 mm^2 (*22*). If we extrapolate a median ^{18}F-FET uptake ratio of 1.50 as calculated from our trace ROIs, an approximate MVD of 13 microvessels/mm^2 would result. At this level, CBF starts to increase above the level in normal brain. In view of that fact, we assume that CBF increases follow the formation of new microvessels and therefore represent a subsequent phenomenon.

Intratumoral heterogeneity of tumor CBF and amino acid uptake has been reported in several animal studies. In opposition to our findings, CBF progressively increased from the tumor center to the tumor periphery and to brain surrounding the tumor (*29*). A corresponding increase in MVD was reported for large tumors of the same tumor model (tumor center, 245/mm^2, vs. surrounding brain, 689/mm^2) (*30*). With regard to a cortical or subcortical tumor location, variable amino acid uptake values were found in more "malignant" tumor models (*11*). In humans, intratumoral variations have not been recognized so far. Overall, we detected in our study no differences in ^{18}F-FET uptake or CBF with regard to cortical or subcortical tumor location. However, we noted intratumoral heterogeneity, particularly in tumor regions infiltrating the corpus callosum. Low CBF and capillary density may initiate the development of a mismatch between metabolic demand and energy supply and may promote hypoxia, possibly making these tumors prone to behaving more aggressively than tumors with the same histopathologic features located outside the corpus callosum (*31*).

CONCLUSION

Taking our observations together, we found that tumor CBF and amino acid uptake varied substantially in nonenhancing WHO grade II gliomas. This variation was evident within the whole group of tumors and within individual tumors and did not depend on lesion size on MRI. All patients were studied at the time of clinical or radiologic progression, making tumor therapy necessary after initial

surgery and observation. Because MVD constitutes a significant independent prognostic factor (*32,33*), it is tempting to validate whether ^{18}F-FET PET provides a robust means for the in vivo measurement of MVD. Our results in this study led us to initiate a prospective PET study that will address the effect of chemotherapy on regional tumor blood flow and amino acid uptake, with particular emphasis on the tumor-to-brain border zone, because this is the area most critical to tumor cell infiltration of the surrounding brain and to tumor progression and the prognosis of patients with low-grade gliomas.

ACKNOWLEDGMENTS

This study was supported by grants from the Swiss Group for Clinical Cancer Research (SAKK) and by Essex Chemie AG, Luzern, Switzerland. We thank Tibor Cservenyak for radiotracer production.

REFERENCES

1. Kleihues P, Cavanee WK. *Pathology and Genetics of Tumours of the Nervous System*. Lyon, France: IARC Press; 2000:10–21.
2. Mandonnet E, Delattre JY, Tanguy ML, et al. Continuous growth of mean tumor diameter in a subset of grade II gliomas. *Ann Neurol.* 2003;53:524–528.
3. Van den Bent MJ, Afra D, de Witte O, et al. Long-term efficacy of early versus delayed radiotherapy for low-grade astrocytoma and oligodendroglioma in adults: the EORTC 22845 randomised trial. *Lancet.* 2005;366:985–990.
4. Van den Bent MJ. Advances in the biology and treatment of oligodendrogliomas. *Curr Opin Neurol.* 2004;17:675–680.
5. Brada M, Viviers L, Abson C, et al. Phase II study of primary temozolomide chemotherapy in patients with WHO grade II gliomas. *Ann Oncol.* 2003;14: 1715–1721.
6. Hoang-Xuan K, Capelle L, Kujas M, et al. Temozolomide as initial treatment for adults with low-grade oligodendrogliomas or oligoastrocytomas and correlation with chromosome 1p deletions. *J Clin Oncol.* 2004;22:3133–3138.
7. Weckesser M, Langen KJ, Rickert CH, et al. O-(2-[^{18}F]fluorethyl)-L-tyrosine PET in the clinical evaluation of primary brain tumours. *Eur J Nucl Med Mol Imaging.* 2005;32:422–429.
8. Wienhard K, Herholz K, Coenen HH, et al. Increased amino acid transport into brain tumors measured by PET of L-(2-^{18}F)fluorotyrosine. *J Nucl Med.* 1991;32: 1338–1346.
9. Roelcke U, Radu E, Ametamey S, Pellikka R, Steinbrich W, Leenders KL. Association of rubidium and C-methionine uptake in brain tumors measured by positron emission tomography. *J Neurooncol.* 1996;27:163–171.
10. Heiss P, Mayer S, Herz M, Wester HJ, Schwaiger M, Senekowitsch-Schmidtke R. Investigation of transport mechanism and uptake kinetics of O-(2-[^{18}F]fluoroethyl)-L-tyrosine in vitro and in vivo. *J Nucl Med.* 1999;40:1367–1373.
11. Miyagawa T, Oku T, Uehara H, et al. "Facilitated" amino acid transport is upregulated in brain tumors. *J Cereb Blood Flow Metab.* 1998;18:500–509.
12. Langen KJ, Jarosch M, Mühlensiepen H, et al. Comparison of fluorotyrosines and methionine uptake in F98 rat gliomas. *Nucl Med Biol.* 2003;30:501–508.
13. Husstedt HW, Sickert M, Kostler H, Haubitz B, Becker H. Diagnostic value of the fast-FLAIR sequence in MR imaging of intracranial tumors. *Eur Radiol.* 2000;10:745–752.
14. Treyer V, Jobin M, Burger C, Teneggi V, Buck A. Quantitative cerebral $H_2{}^{15}O$ perfusion PET without arterial blood sampling, a method based on washout rate. *Eur J Nucl Med Mol Imaging.* 2003;30:572–580.
15. Wester HJ, Herz M, Weber W, et al. Synthesis and radiopharmacology of O-(2-[^{18}F]fluoroethyl)-L-tyrosine for tumor imaging. *J Nucl Med.* 1999;40:205–212.
16. Weber WA, Wester HJ, Grosu AL, et al. O-(2-[^{18}F]fluoroethyl)-L-tyrosine and L-[methyl-^{11}C]methionine uptake in brain tumours: initial results of a comparative study. *Eur J Nucl Med.* 2000;27:542–549.
17. Mikolajczyk K, Szabatin M, Rudnicki P, Grodzki M, Burger CA. JAVA environment for medical image data analysis: initial application for brain PET quantitation. *Med Inform (Lond).* 1998;23:207–214.
18. Tang BN, Sadeghi N, Branle F, De Witte O, Wikler D, Goldman S. Semiquantification of methionine uptake and flair signal for the evaluation of chemotherapy in low-grade oligodendroglioma. *J Neurooncol.* 2005;71:161–168.
19. Rosen BR, Belliveau JW, Vevea JM, Brady TJ. Perfusion imaging with NMR contrast agents. *Magn Reson Med.* 1990;14:249–265.
20. Abu-Hajir M, Rand SD, Krouwer HG, Schmainda KM. Noninvasive assessment of neoplastic angiogenesis: the role of magnetic resonance imaging. *Semin Thromb Hemost.* 2003;29:309–315.
21. Christensen HN. Role of amino acid transport and countertransport in nutrition and metabolism. *Physiol Rev.* 1990;70:43–77.
22. Kracht LW, Friese M, Herholz K, et al. Methyl-[^{11}C]-L-methionine uptake as measured by positron emission tomography correlates to microvessel density in patients with glioma. *Eur J Nucl Med Mol Imaging.* 2003;30:868–873.
23. Wesseling P, van der Laak JA, Link M, Teepen HL, Ruiter DJ. Quantitative analysis of microvascular changes in diffuse astrocytic neoplasms with increasing grade of malignancy. *Hum Pathol.* 1998;29:352–358.
24. Fischer I, Gagner JP, Law M, Newcomb EW, Zagzag D. Angiogenesis in gliomas: biology and molecular pathophysiology. *Brain Pathol.* 2005;15:297–310.
25. Lammertsma AA, Wise RJ, Cox TC, Thomas DG, Jones T. Measurement of blood flow, oxygen utilisation, oxygen extraction ratio, and fractional blood volume in human brain tumours and surrounding oedematous tissue. *Br J Radiol.* 1985;58:725–734.
26. Mineura K, Sasajima T, Kowada M, et al. Perfusion and metabolism in predicting the survival of patients with cerebral gliomas. *Cancer.* 1994;73:2386–2394.
27. Mineura K, Shioya H, Kowada M, Ogawa T, Hatazawa J, Uemura K. Blood flow and metabolism of oligodendrogliomas: a positron emission tomography study with kinetic analysis of ^{18}F-fluorodeoxyglucose. *J Neurooncol.* 1999;43:49–57.
28. Bruehlmeier M, Roelcke U, Schubiger PA, Ametamey SM. Assessment of hypoxia and perfusion in human brain tumors using PET with ^{18}F-fluoromisonidazole and ^{15}O-H_2O. *J Nucl Med.* 2004;45:1851–1859.
29. Blasberg RG, Kobayashi T, Horowitz M, et al. Regional blood-to-tissue transport in ethylnitrosourea-induced brain tumors. *Ann Neurol.* 1983;14:202–215.
30. Schlageter KE, Molnar P, Lapin GD, Groothuis DR. Microvessel organization and structure in experimental brain tumors: microvessel populations with distinctive structural and functional properties. *Microvasc Res.* 1999;58:312–328.
31. Pignatti F, van den Bent M, Curran D, et al. Prognostic factors for survival in adult patients with cerebral low-grade glioma. *J Clin Oncol.* 2002;20:2076–2084.
32. Leon SP, Folkerth RD, Black PM. Microvessel density is a prognostic indicator for patients with astroglial brain tumors. *Cancer.* 1996;77:362–372.
33. Abdulrauf SI, Edvardsen K, Ho KL, Yang XY, Rock JP, Rosenblum ML. Vascular endothelial growth factor expression and vascular density as prognostic markers of survival in patients with low-grade astrocytoma. *J Neurosurg.* 1998;88: 513–520.

J Neurooncol
DOI 10.1007/s11060-009-9896-2

CLINICAL STUDY - PATIENT STUDY

Early metabolic responses in temozolomide treated low-grade glioma patients

Matthias Wyss · Silvia Hofer · Matthias Bruehlmeier · Martin Hefti · Catrina Uhlmann · Esther Bärtschi · Ulrich Wolf Buettner · Ulrich Roelcke

Received: 28 November 2008 / Accepted: 6 April 2009

Abstract Amino acid transport and protein synthesis are important steps of tumor growth. We investigated the time course of tumor metabolism in low-grade gliomas (LGG) during temozolomide chemotherapy, and compared metabolic responses as measured with positron emission tomography (PET) with volume responses as revealed by magnetic resonance imaging (MR). A homogeneous population of 11 patients with progressive non-enhancing LGG was prospectively studied. Imaging was done at 6-months intervals starting six months, and in a second series starting three months after treatment initiation. F-18 fluoro-ethyl-L-tyrosine (FET) uptake was quantified with PET as metabolically active tumor volume, and was compared with the tumor volume on MR. Response was defined as $\geq$10% reduction of the initial tumor volume. Eight patients showed metabolic responses. Already 3 months after start of chemotherapy the active FET volumes decreased in 2 patients to a mean of 44% from baseline. First MR volume responses were noted at 6 months. Responders showed a volume reduction to 31 $\pm$ 23% (mean $\pm$ SD) from baseline for FET, and to 73 $\pm$ 26% for MR. The time to maximal volume reduction was 8.0 $\pm$ 4.4 months for FET, and 15.0 $\pm$ 3.0 months for MR. The initial metabolic response correlated with the best volume response on MR (Spearman Rank $P = 0.011$). Deactivation of amino acid transport represents an early indicator of chemotherapy response in LGG. Response assessment based on MR only has to be reconsidered. The time window obtained from PET may assist for individual treatment decisions in LGG patients.

Keywords Low-grade glioma · Chemotherapy · Temozolomide · Positron emission tomography · Tyrosine

M. Wyss
PET Center, Division of Nuclear Medicine,
University Hospital, 8091 Zurich, Switzerland

S. Hofer
Department of Oncology, University Hospital,
8091 Zurich, Switzerland

M. Bruehlmeier
Department of Nuclear Medicine, Cantonal Hospital,
5001 Aarau, Switzerland

M. Hefti
Department of Neurosurgery, Cantonal Hospital,
5001 Aarau, Switzerland

C. Uhlmann · E. Bärtschi
Department of Oncology and Hematology, Cantonal Hospital,
5001 Aarau, Switzerland

U. W. Buettner · U. Roelcke (✉)
Department of Neurology, Cantonal Hospital,
5001 Aarau, Switzerland
e-mail: roelcke@ksa.ch; ulrich.roelcke@ksa.ch

Introduction

Chemotherapy represents a treatment option in low-grade glioma patients (LGG) [1]. This may be particularly important if tumors are not amenable to gross resection or irradiation. Several retrospective studies have shown that chemotherapy (either temozolomide or PCV regimen) was active in LGG. Using magnetic resonance (MR) imaging chemotherapy yielded response rates up to 61% [2–6] which were mainly determined by Macdonald's criteria [7], although these criteria are not validated for LGG. The median time to reach a morphological response in the largest series was 12 months [4]. As many LGG grow very

Published online: 18 April 2009

slowly the inhibition of tumor metabolism may be detected earlier than structural volume changes. Early identification of treatment response by molecular imaging may be promising. Positron emission tomography (PET) allows to quantitatively measure several biochemical and physiological alterations in brain tumors. Increased amino acid transport and protein synthesis represent essential and early steps of tumor growth [8]. In our present study we used PET with the radiolabeled amino acid analogue tyrosine (F-18 fluoro-ethyl-L-tyrosine, FET) to characterize metabolic responses in LGG patients treated with the alkylating agent temozolomide (TMZ).

Methods

Patients

A homogeneous population of 11 patients (median age 34 years, range 23–49 years, 3 female and 8 male) with progressive supratentorial LGG WHO II consented to participate in our study (3 oligodendrogliomas, 4 fibrillary astrocytomas and 4 oligoastrocytomas [9]). Progression was defined on MR as an increase in tumor size of >25% and/or clinical deterioration (according to the EORTC study protocol on low-grade gliomas, 22033-26033 [10]), and occurred at a median of 27 months after the first tumor surgery (range 2–127 months). No patient had received previous radio- or chemotherapy. We included only patients which did not show any gadolinium enhancement on MR as the latter may be suggestive for transformation to malignant glioma. The clinical data are presented in Table 1. Patients received 75 mg/m^2 TMZ per day over 3 weeks, followed by one week off (21q/28d = one cycle, according to EORTC protocol 22033-26033 [10]). Patients were scheduled to receive 12 cycles of chemotherapy. TMZ chemotherapy was discontinued at the time of tumor progression or due to inacceptable side effects. Following the baseline scans the imaging protocol consisted of PET and MR scans at six-month intervals, starting after six cycles of chemotherapy in group A ($n = 8$). Due to the magnitude of PET responses observed at six months in group A the first follow-up scans in three subsequent patients (group B, Table 1) started after three cycles of chemotherapy. Further follow-up scans in group B patients were scheduled 9 and 15 months after initiation of treatment. Based on the clinical judgement several patients received more than 12 cycles (up to 24). The study protocol was approved by the local Ethical Committee. Written consent was obtained from all patients.

Imaging

MR imaging included standard sequences on a 1.5 Tesla Siemens Magnetom. Amino acid imaging with PET was done with F-18-fluoro-ethyl-L-tyrosine (FET). 3D PET data were acquired with a whole-body PET/CT Scanner (Discovery LS, GE Medical Systems, Waukesha, WI, USA,

Table 1 Clinical and imaging data

#(group)	Histology[a], resection type[b]	Gender	Age (years)	Baseline tumor volume (ccm)		Baseline T:CBL ratio[c]	Response type[d]	Best volume response (% from baseline)		Time to best volume response (months)	
				MR[e]	FET[f]	FET		MR	FET	MR	FET
1 (B)	FIAC, pr	f	49	46	29	1.24	R	96	49	–	3
2 (A)	FIAC, pr	m	23	52	52	1.52	R	91	6	–	12
3 (A)	OA, b	m	28	90	78	1.57	R	65	15	12	12
4 (A)	OA, pr	f	28	14	11	1.32	R	65	8	18	6
5 (B)	OA, pr	m	27	23	18	1.45	R	90	38	15	3
6 (A)	OD, b	m	34	23	29	1.64	R	39	40	12	12
7 (A)	OD, pr	f	45	25	27	1.40	R	33	18	18	12
8 (A)	OD, pr	m	36	284	273	1.33	R	102	71	–	6
9 (B)	FIAC, pr	m	32	44	6	1.25	NR	109	121	–	–
10 (A)	FIAC, b	m	38	66	0	1.10	NR	99	100	–	–
11 (A)	OA, B	m	39	79	69	1.43	NR	99	93	–	–

[a] Histology: *FIAC* fibrillary astrocytoma, *OA* oligoastrocytoma, *OD* oligodendroglioma

[b] Resection type: *b* biopsy, *pr* partial resection

[c] T:CBL ratio = uptake of the active tumor volume normalized to the mean uptake of the crebellum

[d] Response type according to FET PET follow up results (see Methods): *R* responding patients, *NR* non-responding patients

[e] MR = FLAIR sequence

[f] FET = active tumor volume of amino acid uptake

14.6 cm axial field of view, in-plane resolution 7 mm). FET was intravenously administered as bolus injection of 140–250 MBq. FET uptake was measured on PET images acquired from 50 to 60 min after tracer injection [11].

Data analysis

Quantification of PET and MR data was done using PMOD [12] on digitized images as described in detail in our recent publication [13]. For calculation of the MR tumor volume we used the FLAIR sequence which provides the best delineation between tumor and adjacent brain [3, 14]. Following manual outlining of the tumor boundaries the areas of all tumor containing MR slices were summed up to yield the whole tumor volume. For quantification of the FET PET data the cerebellum was used as reference region. Regions of interest (ROI) covering the whole cerebellum were drawn for each slice. The ROI counts of all PET slices which contained the cerebellum were then averaged to produce the mean cerebellar FET uptake (counts). For tumors two measures were calculated. First, the 'active volume' (ccm) was quantified as the tumor volume containing pixels >110% of the mean cerebellar FET uptake. This threshold corresponds well to the visual impression of active LGG [13, 15]. Second, the tumor FET uptake (counts) of the active volume was normalized to the mean FET uptake of the cerebellum (T:CBL ratio, unit-less). This uptake ratio is routinely used in nuclear medicine, and is robust with regard to intra- and inter-individual comparisons. For the one patient who showed no active FET tumor volume (#10) the T:CBL ratio was calculated using the tumor area derived from the MR FLAIR images. As TMZ-induced reductions of FET uptake were better detectable by active volumes than by T:CBL ratios, we defined treatment response as a $\geq$10% reduction of the initial tumor volume (active PET, MR FLAIR) on at least two subsequent time points after the initiation of chemotherapy. Defining treatment response as a 20% volume reduction produced the same number of metabolic, but a lower number of MR responders. The Spearman rank test (SPSS, version 10.0.7) was applied to test whether baseline tumor FET uptake, or metabolic responses during treatment, were correlated with treatment response on MR.

Results

In total 172 cycles of TMZ were administered (mean 16, range 6–24 per patient). The initially scheduled TMZ dose could be maintained in 9 patients, in the two other patients the dose had to be reduced by 20% and 30% respectively due to hematotoxicity (CTCAE v3.0, grade 2 and 3). In group A 3 patients completed 4 follow-up PET-MR scans, 3 patients completed 3 scans, and 2 patients completed 1 scan. In group B each 1 patient completed 4, 3, and 2 follow-up scans.

Tumor volumes

At baseline a variable active FET tumor volume was found in 10/11 patients (range 6–273 ccm). This is line with earlier reports which describe a lack of increased amino acid uptake in a proportion of LGG [16]. The absolute numbers of the baseline active FET and MR volumes are presented in Table 1. Overall 8/11 patients were metabolic responders. Among these only five patients also showed a MR volume response (Table 1). Examples of individual responses are presented in Figs. 1 and 2. At three months 2/3 patients (group B, #1, 5) showed a substantially reduced active FET volume (38% and 49% of baseline volume), whereas no MR volume change was observed. In one patient the metabolic response persisted until 15 months (#5, Fig. 1c and bottom Fig. 2). At that time also a small volume response was noted on MR (90% of baseline). In group A patients (first follow-up study at six months) 6/8 patients showed a reduced active FET volume (range 7–71% of baseline volume). At that time 4/8 MR volume reductions were observed. The delay

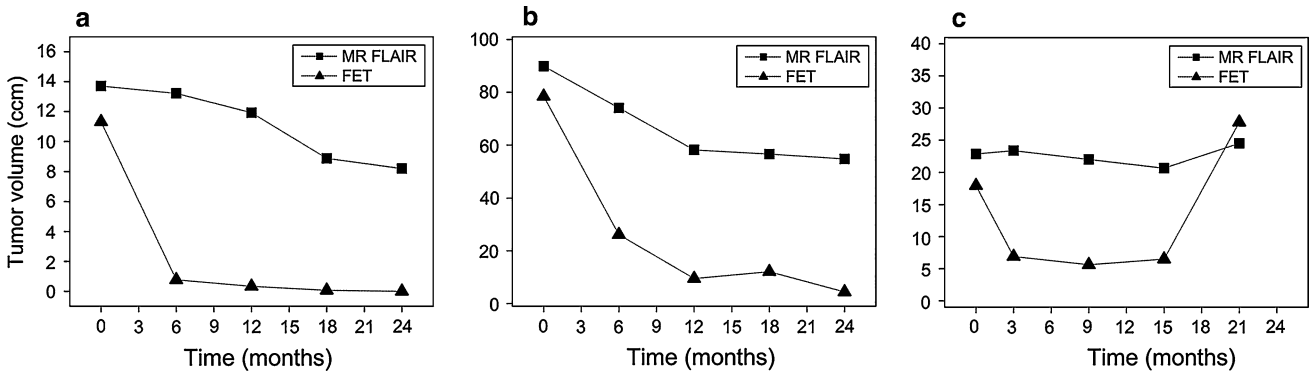

Fig. 1 Treatment responses of MR FLAIR (*square*) are compared with the active FET tumor volume (*triangle*) in patient #4 **a**, #3 **b**, and #5 **c**. C: the increase of the active FET volume at 21 months was associated with tumor progression to anaplastic oligoastrocytoma WHO III

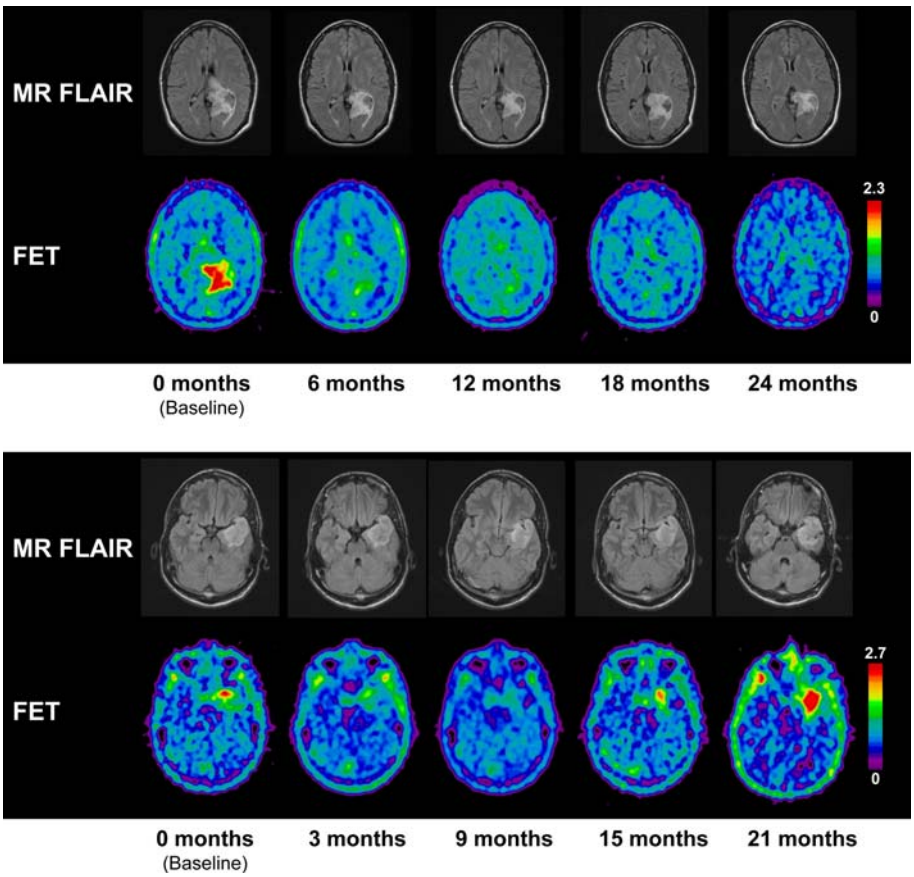

Fig. 2 Top: Patient #3 (Fig. 1a). Imaging studies were done before (*left*), and 6, 12, 18, 24 months after initiation of chemotherapy. *Bottom*: Patient #5 (Fig. 1c). Imaging studies were done before (left), and 3, 9, 15, 21 months after initiation of chemotherapy. At the time of clear metabolic tumor progression (21 months) a small increase of the MR FLAIR tumor volume was noted compared to the volume at 15 months (25 vs. 21 ccm). No tumor gadolinium enhancement was observed. The increase of the active FET tumor volume (27.8 vs. 6.5 ccm) was paralleled by an increase of the FET uptake ratio (1.98 vs. 1.51) which is compatible with progression from WHO II towards WHO III. The color scale represents the tumor:cerebellum uptake ratio

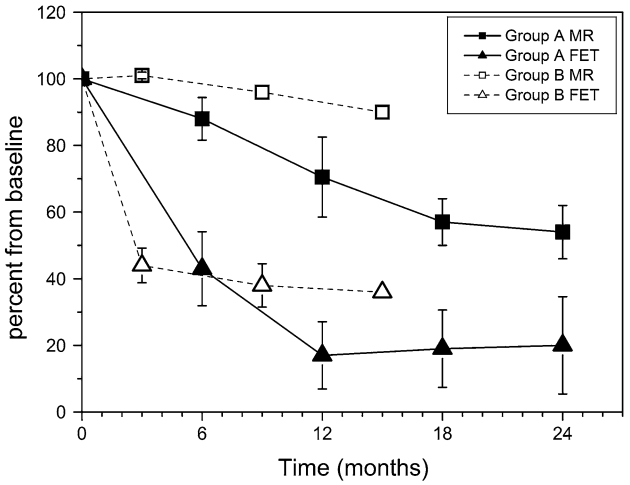

Fig. 3 The time course of FET (*triangle*) and MR (*square*) volumes in metabolic responders is plotted until tumor progression or study termination ($n = 8$, mean ± SEM). Follow up data points: group B at 3, 9, 15 months ($n = 2, 2, 1$ patients), group A at 6, 12, 18, 24 months ($n = 6, 5, 4, 3$ patients)

between FET and MR volume reductions is illustrated in Fig. 3. Whereas the maximal reduction of the active FET volume was observed between 3 and 12 months (8.0 ± 4.4, mean ± SD), the delay to maximum MR volume reduction was 15.0 ± 3.0 months. The best FET response reached a mean of 31 ± 23% from baseline (Table 1), whereas the best volume response on MR reached a mean of 73 ± 26% from baseline.

Uptake ratios

The range of baseline FET T:CBL ratios was 1.10–1.64 (Table 1). In responders the maximal reduction of FET uptake ratios was 76% from baseline. Similar to the active volume the maximal response of FET uptake ratios was reached until 12 months.

Response prediction

Before treatment neither the active tumor volume nor the uptake ratio predicted the response to TMZ chemotherapy (Spearman rank $P > 0.68$). However, the FET volume response measured at the time of the *first* follow up study correlated with the *best* MR volume response obtained later during the course of chemotherapy (Spearman Rank 0.731, $P = 0.01$, Fig. 4). Vice versa, patients who did not show a reduction of the active FET volume in their first follow up study also did not show PET or MR responses at later time points. With regard to tumor histology 6/7 oligodendroglial tumors showed a FET volume response, and 5/7 a MR

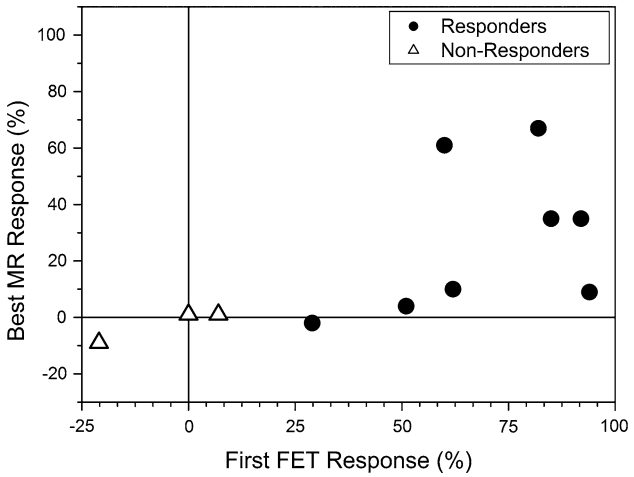

Fig. 4 The metabolic response at the *first* FET PET follow up (ΔBaseline FET—first FET response (%)) is plotted against the *best* MR volume response (ΔBaseline MR—maximum MR response (%)). *Circles*: metabolic responders, *triangles*: non-responders. In non-responders the MR volume at the last MR scan is taken

volume response. 2/4 fibrillary astrocytomas showed a FET volume responses in the absence of any MR volume response. The magnitude of metabolic responses did not correspond to the duration of chemotherapy.

Clinical follow up, tumor progression

A clinical benefit emerged for two patients which were seizure-free after four and six months of chemotherapy respectively. Those patients with PET and MR responses showed the longest progression-free survival (PFS; 38 ± 3 months). At the time of last follow up 3/8 metabolic responders were still free of progression. In patients without MR response variable PFS periods were noted (15 ± 8 months). 5/8 metabolic responders progressed 19 ± 7 months after initiation of chemotherapy. Four progressive patients underwent re-operation between 6 and 21 months after initiation of chemotherapy, which yielded unchanged histology (#8), anaplastic oligoastrocytoma WHO III (#5), anaplastic astrocytoma (#9), and glioblastoma WHO IV (#2). In those three patients with progression towards WHO grade III or IV a prominent increase particularly of the uptake ratio was observed (1.98, 1.37, 1.69 compared to an uptake ratio of 1.24, 1.24, 1.16 at best response). Also the active FET volume increased (28, 47, 23 ccm compared to 6, 3, 8 ccm at best response). This is examplified by Fig. 1c and bottom panel of Fig. 2.

Discussion

LGG tend to grow slowly. A mean tumor diameter increase of 4.1 mm per year was reported in oligodendrogliomas or mixed gliomas on serial MR [17]. TMZ chemotherapy reversed this increase and led to an average tumor diameter decrease of 9.1 mm per year in one series [18]. The key finding of our study is that a substantial proportion of patients initially showing stable MR volumes are 'early' metabolic responders during chemotherapy, and that metabolic responses are more pronounced than MR volume responses. Of note none of the patients included in our series showed blood-brain barrier disruption as revealed by gadolinium enhanced MR. Interestingly, not only oligodendroglial tumors but also fibrillary astrocytomas showed metabolic responses, which preceded MR volume reductions by several months. These responses were particularly evident from the reduction of the active FET tumor volume. In contrast, the uptake indices (T:CBL ratios) in responders decreased only slightly. This suggests a decrease in tumor cell density, and indicates that the residual viable tumor has a metabolic activity similar to the untreated tumor, which is compatible with an unchanged histology and WHO tumor grade during chemotherapy.

Discrepancies between changes in amino acid uptake (C-11 methionine) and MR volume reductions were also reported in pure oligodendrogliomas WHO II [15]. That study addressed the magnitude of metabolic and MR volume response after completion of 4–6 cycles of PCV chemotherapy, and also found that responses are more pronounced on metabolic compared to MR imaging. Various other treatment modalities also produced reductions of amino acid uptake in LGG (radio-chemotherapy [19], external beam radiotherapy [20], interstitial brachytherapy with I125-Iodine seeds [21]). Extrapolating our data in responding patients toward earlier time points (Fig. 3) suggests that metabolic responses may be observed as early as one month after treatment initiation. Vice versa we also found that tumor progression was earlier evident on metabolic imaging compared with MR (Fig. 1c and bottom Fig. 2). Our data therefore underline the role of PET imaging with amino acids as a sensitive tool for early response assessment in LGG.

Upregulation of amino acid transporters in human astrocytomas can be demonstrated by immunohistochemistry and correlates with the WHO grade [22, 23]. In accordance, increased amino acid transport as measured in vivo with PET also correlates with the WHO grade of gliomas [24, 25]. The importance of amino acid transport for tumor growth is illustrated by experiments which show that specific transport inhibitors produce a rapid suppression of cell growth, and prolong survival of rats treated with C6 glioma cells [22]. Also successful chemotherapy with the alkylating agent TMZ decreases amino acid transport as shown in our study. As long as amino acid transport was deactivated no tumor progression was evident. Moreover, volume expansion on MR as sign of tumor

progression was paralleled by substantially increased amino acid transport (Fig. 1c and bottom Fig. 2). These findings suggest that tumor growth in LGG is maintained by amino acid supply and does not escape towards other metabolic pathways.

With regard to identify patients who benefit from treatment the prediction of treatment response in individual patients would have major impact on patient care. Several studies suggested that histological features of LGG (fibrillary astrocytoma versus oligodendroglial tumors) and molecular profiles (e.g. status of loss-of-heterozygosity, LOH, on 1p/19q, methylation of O6-methylguanine-methyltransferase, MGMT) are associated with treatment response and survival. In individual patients, however, treatment response cannot be predicted yet [26, 27], and molecular markers are not implemented into clinical practice. Actually our data may lead to the concept that individual patient management should be optimized by early response identification in addition to response prediction. We clearly demonstrate the advantage of molecular over structural imaging in LGG particularly with regard to the time window (Fig. 3). FET PET data may therefore assist to define the maximal duration of chemotherapy. Due to our small sample size we cannot draw final conclusions as to whether the magnitude of PET and MR responses relate to the subsequent clinical course and to the time until tumor progression. This has to be addressed in larger prospective studies. We conclude that the early identification of non-responders will help to minimize any negative impact of chemotherapy on quality of life. Finally, individually optimized treatment will also have economical impact since the costs of PET imaging must be weighted against the expenses of chemotherapy and the management of adverse effects.

Acknowledgements This work was supported by grants of the Swiss Group for Clinical Cancer Research (SAKK) and by Essex Chemie AG, Luzern, Switzerland.

References

1. Schiff D, Brown PD, Giannini C (2007) Outcome in adult low-grade glioma: the impact of prognostic factors and treatment. Neurology 69:1366–1373. doi:10.1212/01.wnl.0000277271.47601.a1
2. Brada M, Viviers L, Abson C et al (2003) Phase II study of primary temozolomide chemotherapy in patients with WHO grade II gliomas. Ann Oncol 14:1715–1721. doi:10.1093/annonc/mdg371
3. Hoang-Xuan K, Capelle L, Kujas M et al (2004) Temozolomide as initial treatment for adults with low-grade oligodendrogliomas or oligoastrocytomas and correlation with chromosome 1p deletions. J Clin Oncol 22:3133–3138. doi:10.1200/JCO.2004.10.169
4. Kaloshi G, Benouaich-Amiel A, Diakite F et al (2007) Temozolomide for low-grade gliomas: predictive impact of 1p/19q loss on response and outcome. Neurology 68:1831–1836. doi:10.1212/01.wnl.0000262034.26310.a2
5. Pouratian N, Gasco J, Sherman JH et al (2007) Toxicity and efficacy of protracted low dose temozolomide for the treatment of low grade gliomas. J Neurooncol 82:281–288. doi:10.1007/s11060-006-9280-4
6. Quinn JA, Reardon DA, Friedman AH et al (2003) Phase II trial of temozolomide in patients with progressive low-grade glioma. J Clin Oncol 21:646–651. doi:10.1200/JCO.2003.01.009
7. Macdonald DR, Cascino TL, Schold SC Jr et al (1990) Response criteria for phase II studies of supratentorial malignant glioma. J Clin Oncol 8:1277–1280
8. Miyagawa T, Oku T, Uehara H et al (1998) "Facilitated" amino acid transport is upregulated in brain tumors. J Cereb Blood Flow Metab 18:500–509. doi:10.1097/00004647-199805000-00005
9. Kleihues P, Louis DN, Scheithauer BW et al (2002) The WHO classification of tumors of the nervous system. J Neuropathol Exp Neurol 61:215–225
10. EORTC (European Organization of Research and Treatment of Cancer) Intergroup study 22033-26033: Primary chemotherapy with temozolomide vs. radiotherapy in patients with low grade gliomas after stratification for genetic 1p loss: a phase III study (http://groups.eortc.be/brain/html/trials.html)
11. Weckesser M, Langen KJ, Rickert CH et al (2005) O-(2-[18F]fluorethyl)-L-tyrosine PET in the clinical evaluation of primary brain tumours. Eur J Nucl Med Mol Imaging 32:422–429. doi:10.1007/s00259-004-1705-8
12. Mikolajczyk K, Szabatin M, Rudnicki P et al (1998) A JAVA environment for medical image data analysis: initial application for brain PET quantitation. Med Inform (Lond) 23:207–214. doi:10.3109/14639239809001400
13. Wyss MT, Hofer S, Hefti M et al (2007) Spatial heterogeneity of low-grade gliomas at the capillary level: a PET study on tumor blood flow and amino acid uptake. J Nucl Med 48:1047–1052. doi:10.2967/jnumed.106.038489
14. Husstedt HW, Sickert M, Kostler H et al (2000) Diagnostic value of the fast-FLAIR sequence in MR imaging of intracranial tumors. Eur Radiol 10:745–752. doi:10.1007/s003300050997
15. Tang BN, Sadeghi N, Branle F et al (2005) Semi-quantification of methionine uptake and flair signal for the evaluation of chemotherapy in low-grade oligodendroglioma. J Neurooncol 71:161–168. doi:10.1007/s11060-004-9654-4
16. Herholz K, Holzer T, Bauer B et al (1998) 11C-methionine PET for differential diagnosis of low-grade gliomas. Neurology 50:1316–1322
17. Mandonnet E, Delattre JY, Tanguy ML et al (2003) Continuous growth of mean tumor diameter in a subset of grade II gliomas. Ann Neurol 53:524–528. doi:10.1002/ana.10528
18. Ricard D, Kaloshi G, Amiel-Benouaich A et al (2007) Dynamic history of low-grade gliomas before and after temozolomide treatment. Ann Neurol 61:484–490. doi:10.1002/ana.21125
19. Ribom D, Schoenmaekers M, Engler H et al (2005) Evaluation of 11C-methionine PET as a surrogate endpoint after treatment of grade 2 gliomas. J Neurooncol 71:325–332. doi:10.1007/s11060-004-2031-5
20. Nuutinen J, Sonninen P, Lehikoinen P et al (2000) Radiotherapy treatment planning and long-term follow-up with [(11)C] methionine PET in patients with low-grade astrocytoma. Int J Radiat Oncol Biol Phys 48:43–52. doi:10.1016/S0360-3016(00)00604-0
21. Voges J, Herholz K, Holzer T et al (1997) 11C-methionine and 18F-2-fluorodeoxyglucose positron emission tomography: a tool for diagnosis of cerebral glioma and monitoring after brachytherapy with 125I seeds. Stereotact Funct Neurosurg 69:129–135. doi:10.1159/000099864

22. Asano S, Kameyama M, Oura A et al (2007) L-type amino acid transporter-1 expressed in human astrocytomas, U343MGa. Biol Pharm Bull 30:415–422. doi:10.1248/bpb.30.415
23. Nawashiro H, Otani N, Shinomiya N et al (2006) L-type amino acid transporter 1 as a potential molecular target in human astrocytic tumors. Int J Cancer 119:484–492. doi:10.1002/ijc.21866
24. Roelcke U, Radu E, Ametamey S et al (1996) Association of rubidium and C-methionine uptake in brain tumors measured by positron emission tomography. J Neurooncol 27:163–171. doi:10.1007/BF00177480
25. Wienhard K, Herholz K, Coenen HH et al (1991) Increased amino acid transport into brain tumors measured by PET of L-(2-18F)fluorotyrosine. J Nucl Med 32:1338–1346
26. van den Bent MJ, Kros JM (2007) Predictive and prognostic markers in neuro-oncology. J Neuropathol Exp Neurol 66:1074–1081. doi:10.1097/nen.0b013e31815c39f1
27. Yip S, Iafrate AJ, Louis DN (2008) Molecular diagnostic testing in malignant gliomas: a practical update on predictive markers. J Neuropathol Exp Neurol 67:1–15. doi:10.1097/nen.0b013e31815f65fb

Own publications referred with this work

Spaeth N, Wyss MT, Weber B, Scheidegger S, Lutz A, Verwey J, Radovanovic I, Pahnke J, Wild D, Westera G, Weishaupt D, Hermann DM, Kaser-Hotz B, Aguzzi A, Buck A (2004) Uptake of 18F-fluorocholine, 18F-fluoroethyl-L-tyrosine, and 18F-FDG in acute cerebral radiation injury in the rat: implications for separation of radiation necrosis from tumor recurrence. J Nucl Med 45:1931-8.

Weber B, Spath N, Wyss M, Wild D, Burger C, Stanley R, Buck A (2003) Quantitative cerebral blood flow measurements in the rat using a beta-probe and H2 15O. J Cereb Blood Flow Metab 23:1455-60.

Wyss M, Hofer S, Bruehlmeier M, Hefti M, Uhlmann C, Bartschi E, Buettner UW, Roelcke U (2009a) Early metabolic responses in temozolomide treated low-grade glioma patients. J Neurooncol 95:87-93.

Wyss MT, Weber B, Honer M, Spath N, Ametamey SM, Westera G, Bode B, Kaim AH, Buck A (2004) 18F-choline in experimental soft tissue infection assessed with autoradiography and high-resolution PET. Eur J Nucl Med Mol Imaging 31:312-6.

Wyss MT, Ametamey SM, Treyer V, Bettio A, Blagoev M, Kessler LJ, Burger C, Weber B, Schmidt M, Gasparini F, Buck A (2007a) Quantitative evaluation of 11C-ABP688 as PET ligand for the measurement of the metabotropic glutamate receptor subtype 5 using autoradiographic studies and a beta-scintillator. Neuroimage 35:1086-92.

Wyss MT, Hofer S, Hefti M, Bartschi E, Uhlmann C, Treyer V, Roelcke U (2007b) Spatial heterogeneity of low-grade gliomas at the capillary level: a PET study on tumor blood flow and amino acid uptake. J Nucl Med 48:1047-52.

Wyss MT, Obrist NM, Haiss F, Eckert R, Stanley R, Burger C, Buck A, Weber B (2009b) A beta-scintillator for surface measurements of radiotracer kinetics in the intact rodent cortex. Neuroimage 48:339-47.

Wyss MT, Weber B, Treyer V, Heer S, Pellerin L, Magistretti PJ, Buck A (2009c) Stimulation-induced increases of astrocytic oxidative metabolism in rats and humans investigated with 1-11C-acetate. J Cereb Blood Flow Metab 29:44-56.

Wyss MT, Jolivet R, Buck A, Magistretti PJ, Weber B (2011) *In vivo* evidence for lactate as a neuronal energy source. *J Neurosci* 31:7477-85.

Additional references

Abdulrauf SI, Edvardsen K, Ho KL, Yang XY, Rock JP, Rosenblum ML (1998) Vascular endothelial growth factor expression and vascular density as prognostic markers of survival in patients with low-grade astrocytoma. *J Neurosurg* 88:513-20.

Ambrosini V, Quarta C, Nanni C, Pettinato C, Franchi R, Grassetto G, Al-Nahhas A, Fanti S, Rubello D (2009) Small animal PET in oncology: the road from bench to bedside. *Cancer Biother Radiopharm* 24:277-85.

Ametamey SM, Kessler LJ, Honer M, Wyss MT, Buck A, Hintermann S, Auberson YP, Gasparini F, Schubiger PA (2006) Radiosynthesis and preclinical evaluation of 11C-ABP688 as a probe for imaging the metabotropic glutamate receptor subtype 5. *J Nucl Med* 47:698-705.

Ametamey SM, Treyer V, Streffer J, Wyss MT, Schmidt M, Blagoev M, Hintermann S, Auberson Y, Gasparini F, Fischer UC, Buck A (2007) Human PET studies of metabotropic glutamate receptor subtype 5 with 11C-ABP688. *J Nucl Med* 48:247-52.

Attwell D, Laughlin SB (2001) An energy budget for signaling in the grey matter of the brain. *J Cereb Blood Flow Metab* 21:1133-45.

Barros LF, Deitmer JW (2010) Glucose and lactate supply to the synapse. *Brain Res Rev* 63:149-59.

Bell C. (1802). *The anatomy of the brain, explained in a series of engravings*. London: Longman, T.N. Rees, O., Cadell T., Davies W., 87pp.

Chen W (2007) Clinical applications of PET in brain tumors. *J Nucl Med* 48:1468-81.

Del Sole A, Falini A, Ravasi L, Ottobrini L, De Marchis D, Bombardieri E, Lucignani G (2001) Anatomical and biochemical investigation of primary brain tumours. *Eur J Nucl Med* 28:1851-72.

Di Chiro G, DeLaPaz RL, Brooks RA, Sokoloff L, Kornblith PL, Smith BH, Patronas NJ, Kufta CV, Kessler RM, Johnston GS, Manning RG, Wolf AP (1982) Glucose utilization of cerebral gliomas measured by [18F] fluorodeoxyglucose and positron emission tomography. *Neurology* 32:1323-9.

Dunn AK, Bolay H, Moskowitz MA, Boas DA (2001) Dynamic imaging of cerebral blood flow using laser speckle. *J Cereb Blood Flow Metab* 21:195-201.

Dunn AK, Devor A, Bolay H, Andermann ML, Moskowitz MA, Dale AM, Boas DA (2003) Simultaneous imaging of total cerebral hemoglobin concentration, oxygenation, and blood flow during functional activation. *Opt Lett* 28:28-30.

Dupont P, Warwick J (2009) Kinetic modelling in small animal imaging with PET. *Methods* 48:98-103.

Grosu AL, Astner ST, Riedel E, Nieder C, Wiedenmann N, Heinemann F, Schwaiger M, Molls M, Wester HJ, Weber WA (2011) An Interindividual Comparison of O-(2- [(18)F]Fluoroethyl)-L-Tyrosine (FET)- and L-[Methyl-(11)C]Methionine (MET)-PET in Patients With Brain Gliomas and Metastases. *Int J Radiat Oncol Biol Phys*.

Heiss WD (2009) The potential of PET/MR for brain imaging. *Eur J Nucl Med Mol Imaging* 36 Suppl 1:S105-12.

Heiss WD, Raab P, Lanfermann H (2011) Multimodality assessment of brain tumors and tumor recurrence. *J Nucl Med* 52:1585-600.

Helmchen F, Denk W (2005) Deep tissue two-photon microscopy. *Nat Methods* 2:932-40.

Hoang-Xuan K, Capelle L, Kujas M, Taillibert S, Duffau H, Lejeune J, Polivka M, Criniere E, Marie Y, Mokhtari K, Carpentier AF, Laigle F, Simon JM, Cornu P, Broet P, Sanson M, Delattre JY (2004) Temozolomide as initial treatment for adults with low-grade oligodendrogliomas or oligoastrocytomas and correlation with chromosome 1p deletions. *J Clin Oncol* 22:3133-8.

Hounsfield GN (1973) Computerized transverse axial scanning (tomography). 1. Description of system. *Br J Radiol* 46:1016-22.

Kaim AH, Weber B, Kurrer MO, Gottschalk J, Von Schulthess GK, Buck A (2002a) Autoradiographic quantification of 18F-FDG uptake in experimental soft-tissue abscesses in rats. *Radiology* 223:446-51.

Kaim AH, Weber B, Kurrer MO, Westera G, Schweitzer A, Gottschalk J, von Schulthess GK, Buck A (2002b) (18)F-FDG and (18)F-FET uptake in experimental soft tissue infection. *Eur J Nucl Med Mol Imaging* 29:648-54.

Kracht LW, Friese M, Herholz K, Schroeder R, Bauer B, Jacobs A, Heiss WD (2003) Methyl-[11C]- l-methionine uptake as measured by positron emission tomography correlates to microvessel density in patients with glioma. *Eur J Nucl Med Mol Imaging* 30:868-73.

Lauterbur PC (1973) Image Formation by Induced Local Interactions: Examples Employing Nuclear Magnetic Resonance. *Nature* 242:190-1.

Leon SP, Folkerth RD, Black PM (1996) Microvessel density is a prognostic indicator for patients with astroglial brain tumors. *Cancer* 77:362-72.

Magistretti PJ, Pellerin L, Rothman DL, Shulman RG (1999) Energy on demand. *Science* 283:496-7.

Magistretti PJ (2008) Brain Energy Metabolism. In: *Fundamental Neuroscience* (Squire L, Berg D, Bloom FE, du Lac S, Ghosh A, Spitzer N, eds), Vol. 3rd Edition: Academic Press, 271-93.

Mankoff DA (2007) A definition of molecular imaging. *J Nucl Med* 48:18N, 21N.

Mullins ME, Barest GD, Schaefer PW, Hochberg FH, Gonzalez RG, Lev MH (2005) Radiation necrosis versus glioma recurrence: conventional MR imaging clues to diagnosis. *AJNR Am J Neuroradiol* 26:1967-72.

Okamoto S, Shiga T, Hattori N, Kubo N, Takei T, Katoh N, Sawamura Y, Nishijima K, Kuge Y, Tamaki N (2011) Semiquantitative analysis of C-11 methionine PET may distinguish brain tumor recurrence from radiation necrosis even in small lesions. *Ann Nucl Med* 25:213-20.

Oldendorf WH (1961) Isolated flying spot detection of radiodensity discontinuities--displaying the internal structural pattern of a complex object. *Ire Trans Biomed Electron* BME-8:68-72.

Pellerin L, Magistretti PJ (1994) Glutamate uptake into astrocytes stimulates aerobic glycolysis: a mechanism coupling neuronal activity to glucose utilization. *Proc Natl Acad Sci U S A* 91:10625-9.

Pellerin L, Magistretti PJ (2011) Sweet sixteen for ANLS. *J Cereb Blood Flow Metab*.

Petersen CC, Sakmann B (2001) Functionally independent columns of rat somatosensory barrel cortex revealed with voltage-sensitive dye imaging. *J Neurosci* 21:8435-46.

Peyre M, Cartalat-Carel S, Meyronet D, Ricard D, Jouvet A, Pallud J, Mokhtari K, Guyotat J, Jouanneau E, Sunyach MP, Frappaz D, Honnorat J, Ducray F (2010) Prolonged response without prolonged chemotherapy: a lesson from PCV chemotherapy in low-grade gliomas. *Neuro Oncol* 12:1078-82.

Phelps ME, Hoffman EJ, Mullani NA, Ter-Pogossian MM (1975) Application of annihilation coincidence detection to transaxial reconstruction tomography. *J Nucl Med* 16:210-24.

Phelps ME, Mazziotta JC (1985) Positron emission tomography: human brain function and biochemistry. *Science* 228:799-809.

Pierre K, Magistretti PJ, Pellerin L (2002) MCT2 is a major neuronal monocarboxylate transporter in the adult mouse brain. *J Cereb Blood Flow Metab* 22:586-95.

Piroth MD, Pinkawa M, Holy R, Klotz J, Nussen S, Stoffels G, Coenen HH, Kaiser HJ, Langen KJ, Eble MJ (2011) Prognostic value of early [18F]fluoroethyltyrosine positron emission tomography after radiochemotherapy in glioblastoma multiforme. *Int J Radiat Oncol Biol Phys* 80:176-84.

Riemann B, Schafers KP, Schober O, Schafers M (2008) Small animal PET in preclinical studies: opportunities and challenges. *Q J Nucl Med Mol Imaging* 52:215-21.

Röntgen WC (1898) Ueber eine neue Art von Strahlen 300:1-11.

Schiepers C, Dahlbom M, Chen W, Cloughesy T, Czernin J, Phelps ME, Huang SC (2010) Kinetics of 3'-deoxy-3'-18F-fluorothymidine during treatment monitoring of recurrent high-grade glioma. *J Nucl Med* 51:720-7.

Sokoloff L (1999) Energetics of functional activation in neural tissues. *Neurochem Res* 24:321-9.

Terakawa Y, Tsuyuguchi N, Iwai Y, Yamanaka K, Higashiyama S, Takami T, Ohata K (2008) Diagnostic accuracy of 11C-methionine PET for differentiation of recurrent brain tumors from radiation necrosis after radiotherapy. *J Nucl Med* 49:694-9.

von Schulthess GK. (2007). *Molecular Anatomic Imaging: PET-CT and SPECT-CT integrated modality imaging*. Philadelphia: Lippincott Williams & Wilkins.

Waldman AD, Jackson A, Price SJ, Clark CA, Booth TC, Auer DP, Tofts PS, Collins DJ, Leach MO, Rees JH (2009) Quantitative imaging biomarkers in neuro-oncology. *Nat Rev Clin Oncol* 6:445-54.

Waniewski RA, Martin DL (1998) Preferential utilization of acetate by astrocytes is attributable to transport. *J Neurosci* 18:5225-33.

Weber WA, Wester HJ, Grosu AL, Herz M, Dzewas B, Feldmann HJ, Molls M, Stocklin G, Schwaiger M (2000) O-(2-[18F]fluoroethyl)-L-tyrosine and L-[methyl-11C]methionine uptake in brain tumours: initial results of a comparative study. *Eur J Nucl Med* 27:542-9.

Zimmer L, Hassoun W, Pain F, Bonnefoi F, Laniece P, Mastrippolito R, Pinot L, Pujol JF, Leviel V (2002) SIC, an intracerebral beta(+)-range-sensitive probe for radiopharmacology investigations in small laboratory animals: binding studies with (11)C-raclopride. *J Nucl Med* 43:227-33.